Unravelling the mechanism of axonal degeneration in Hereditary Spastic Paraplegia type 7

Inaugural-Dissertation

zur

Erlangung des Doktorgrades

der Mathematisch-Naturwissenschaftlichen Fakultät

der Universität zu Köln

vorgelegt von

Carolina Montoro Gámez

aus Malaga, Spanien

Köln, 2022

Berichterstatter:

Prof. Dr. Elena I. Rugarli

Prof. Dr. Natalia Kononenko

Tag der Mündlichen Prüfung: 19.09.2022

Para mi abuela Valentina,

Abstract

Hereditary spastic paraplegia (HSP) is an inherited neurodegenerative disease which affects mainly the upper motor neuron axons in the corticospinal tract. Due to mutations in any of the more than 80 genes that are known to cause the disease, these long axons get compromised and undergo a dying-back phenomenon, whereby the axonal distal part degenerates while the soma maintains its integrity. Mutations in *SPG7* are among the most common causes of autosomal recessive HSP, yet the mechanisms underlying its pathogenesis are still not clear. *SPG7* encodes for paraplegin, a protein that assembles in mouse with AFG3L2 and AFG3L1 to build up the *m*-AAA protease in the inner membrane of the mitochondria. These ATP-dependent proteases constitute a quality control system that ensures organellar homeostasis by degrading misfolded or damaged proteins and by processing specific substrates. In this thesis I aimed to decipher the function of paraplegin within the CNS and shed light on the mechanisms that lead to axonal degeneration in HSP. In order to investigate this, a new mouse model lacking both paraplegin and AFG3L1 was generated (DKO model). This model recapitulates closely the human SGP7-HSP condition, as it displayed early motor deficits, abnormal mitochondria in anterior spinal cord tracts, cerebellar axonal fibers and cerebellar granule cells, and a prominent axonal degeneration at 28 weeks of age. The ER compartment appeared also altered, in form of transverse, swollen structures in spinal cord tracts. Both astroglia and microglia displayed a reactive morphology in the affected areas indicating a contribution of neuroinflammation to the SPG7 pathology. Proteomic analysis at 16 weeks revealed the accumulation of certain inner-membrane mitochondrial proteins, such as UQCC2, suggesting a potential role of the paraplegin/AFG3L1 *m*-AAA proteases in their processing. Moreover, metabolite analysis revealed an increase of cADPR and a dysregulated NAD^+/NADH ratio upon paraplegin/AFG3L1 loss. Indeed, deletion of the NADase SARM1 partially rescued the *in vivo* DKO phenotype, improving early weight and motor impairments up to 32 weeks of age. As opposed to most evidence, SARM1 absence did not improve the abnormal mitochondria nor the axonal degeneration observed in DKO spinal cord. However, it restored the mitochondrial phenotype of the granule cells and the loss of parallel fibers in the cerebellum. Proteomic analyses at 28 weeks revealed an alteration of a great amount of OXPHOS subunits and protein import components, as well as an alteration of the actin cytoskeleton, cell adhesion and synaptic transmission in DKO tissue. Interestingly, these protein changes were either not observed or showed an opposite direction in absence of SARM1. Moreover, this study reveals tissue-specific differences within the CNS of both paraplegin/AFG3L1 complexes and SARM1. The loss of SARM1 in absence of damage rewired the cellular proteome, particularly in the cerebellum, where proteomic analysis showed a substantial amount of OXPHOS subunits altered as well as proteins involved in cell adhesion, the immune system and neuronal morphogenesis.

I. Table of contents

II. Abbreviations

AAA	ATPase associated with various cellular Activities
Acetyl CoA	acetyl CoenzymeA
AD	autosomal dominant
ADP	adenosine diphosphate
ADPR	adenosine diphosphate ribose
AFG3L1	AFG3-like gene 1
AFG3L2	AFG3-like gene 2
ANOVA	analysis of Variance
AR	autosomal recessive
ARM	armadillo repeat motif
ATP	adenosine triphosphate
BP	biological processes
cADPR	cyclic adenosine diphosphate ribose
CaMKII	calmodulin-dependent protein kinase II
CamKK1	calcium/Calmodulin Dependent Protein Kinase Kinase 1
CamKmt	calmodulin-Lysine N-Methyltransferase
CCCP	carbonyl cyanide m-chlorophenyl hydrazone
CI	complex I
ClpXP	ATP-dependent Clp protease
CNS	central nervous system
CRC	calcium retention capacity
CST	corticospinal tract
CypD	cyclophilin D
DKO	double knock-out
DNA	deoxyribonucleic acid
EAAT	excitatory amino acid transporter
EDTA	ethylene diaminetetraacetic acid
EM	electron microscopy

EMRE	essential MCU regulator
ER	endoplasmic reticulum
ETC	electron transport chain
FAD	flavin adenine dinucleotide (oxidized form)
FADH2	flavin adenine dinucleotide (reduced form)
GABA	gamma-aminobutyric acid
GAPDH	glyceraldehyde phosphate dehydrogenase
GC	granule cell
GFAP	glial fibrillary acidic protein
gl	granular layer
GO	gene ontology
GSEA	gene set enrichment analysis
GTP	guanosine triphosphate
HSP	hereditary spastic paraplegia
IBA-1	ionized calcium binding adaptor molecule 1
IF	immunofluorescence
IL	interleukin
IMM	mitochondrial inner membrane
IMS	mitochondrial intermembrane space
IP3	inositol 1,4,5-trisphosphate
JNK	c-Jun N-terminal kinases
KO	knockout
m-AAA	mitochondrial matrix-ATPase
MAPK	mitogen-activated protein kinase
MCU	mitochondrial calcium uniporter
MEF	mouse embryonic fibroblasts
MICU	mitochondrial calcium uptake protein
MKK4	mitogen-activated protein kinase kinase 4
ml	molecular layer
MPC1	mitochondrial pyruvate Carrier 1

MPC2	mitochondrial pyruvate Carrier 2
mPTP	mitochondrial permeability transition pore
mPTP	mitochondrial permeability transition pore
MRPL	mitochondrial ribosomal protein, large subunit
MRPS	mitochondrial ribosomal protein, small subunit
MT	mitochondrial
Hsp60	heat shock protein, 60 kDa
Hsp70	heat shock protein, 70 kDa
MTS	mitochondrial targeting sequence
NAD+	nicotinamide adenine dinucleotide (oxidized form)
NADH	nicotinamide adenine dinucleotide (reduced form)
NADP	nicotinamide adenine dinucleotide phosphate (oxidized form)
NADPH	nicotinamide adenine dinucleotide phosphate (reduced form)
NAM	nicotinamide
NAMPT	nicotinamide phosphoribosyltransferase
NES	normalized enrichment factor
NMN	nicotinamide mononucleotide
NMNAT	nicotinamide mononucleotide adenylyltransferases
NMNDA	N-methyl-D-aspartate receptors
O/N	overnight
OCR	oxygen consumption rate
OMM	mitochondrial outer membrane
OXPHOS	oxidative phosphorylation
PAGE	polyacrylamide gel electrophoresis
PB	phosphate buffer
PBS	phosphate buffer saline
PC	Purkinje cell
PCR	polymerase chain reaction
PFA	paraformaldehyde
PHB	prohibitin

PINK1	PTEN-induced kinase 1
QPRT	quinolinate phosphoribosyl transferase
RNA	ribonucleic acid
ROS	reactive oxygen species
RT	room temperature
RT-PCR	real-time PCR
SARM1	Sterile Alpha and Toll Interleukin Receptor Motif-containing protein 1
SCA	spinocerebellar ataxia
SD	standard deviation
SEM	standard error of the mean
SIRT	sirtuin
SLC	solute carrier
SNARE	soluble NSF attachment proteins (SNAP) receptor
SPG	spastic paraplegia gene
TCA	tricarboxylic acid
TIM	mitochondrial inner membrane translocase
TIR	toll-interleukin-1 receptor
TKO	triple knockout
TLR	toll-like receptors
TNF	tumour necrosis factor
UQCC	ubiquinol-cytochrome c reductase complex assembly factor
VDAC	voltage-dependent anion-selective channel proteins
w/v	weight/volume
WD	Wallerian degeneration
WLSS	Wallerian degeneration slow mutant
WT	wildtype

III. List of Figures

Supplementary Figures:

IV. List of Tables

Supplementary Tables:

1. Introduction

1.1. The mouse nervous system

Out of all anatomical structures, the nervous system stands out as one of the most compelling, not only for its complex organization and cellular diversity, but also for its ability to govern the entire body. Its main component, the central nervous system (CNS), is formed by the brain, including cerebellum, and the spinal cord. They are responsible for integrating all sensory inputs collected through the body and sending a coordinated response back. Peripheral information can be conveyed to the brain in ascending tracts through the spinal cord, whereas the processed output uses the descending tracts to reach musculature and execute the brain´s response. Specific regions of the CNS integrate the information differently depending on the nature of the somatic process. Since this thesis will mainly refer to motor control, only the concepts relevant to it will be described.

1.1.1. Neurons and glial cells

Neurons have been long considered to be the unit of the nervous system. Although there is a great variability of neuron shapes, most CNS neurons are multipolar neurons. They exhibit a unique polarized morphology formed by a soma (cell body), which hosts most of the organelles including the nucleus, and two types of processes emerging from it: a long thin axon and a multitude of branched dendrites. Axons are of particular importance, since they not only serve a structural role but are also the platforms in which electric signals -the action potentials- originate, allowing neurons to communicate with each other. Structurally, axons rely on microtubule arrangements to grow and maintain their rounded-thin shape. These microtubules also act as railways along which proteins synthesised in the soma and other cell cargos, including organelles such as mitochondria, are transported to the periphery. This axonal anterograde transport becomes particularly relevant at the distal locations, where specific deliveries are needed to maintain synaptic transmission and therefore, neuronal function (Kelliher et al., 2019). However, certain cellular structures such as autophagosomes must be transported retrogradely to the soma, where they are either removed or recycled. Thus, any impairment of this cytoskeletal organisation would impact neuronal function and compromise its survival, leading generally to neurodegenerative diseases (Sen et al., 2022).

Glial cells make up roughly half of the total CNS cells. They held a crucial role from early embryonic development, as they regulate neuronal migration, axon guidance and synaptic communication. In fact, they provide neurons with functional and structural support throughout their entire life (Allen & Lyons, 2018). Glial cells constitute very heterogeneous populations,

which can be classified in four main groups: astrocytes, microglia, oligodendrocytes and oligodendrocyte progenitor cells.

Astrocytes provide essential metabolic support to neurons. They are able to monitor oxygen demand by wrapping the blood-barrier vessels with their end feet, influencing blood flow depending on the energy demand. Their projections also surround pre- and postsynaptic neuron domains, forming what is known as the “tripartite synapse” (Perea et al., 2009), where they uptake neurotransmitters and release their own, modulating synaptic function. An example of this is the glutamate-glutamine cycle, by which astrocytes uptake neuronal-released glutamate from the synaptic cleft and help preventing glutamate-induced excitotoxicity. Glutamate enters the astrocytic cell via EAAT transporters, being transformed to glutamine in the cytosol via the glutamine synthetase pathway. Glutamine is then released to the extracellular space and uptaked by the neighbouring neurons to regenerate glutamate and replenish the neurotransmitter synaptic pools (**Fig. 1.1**) (Mahmoud et al., 2019).

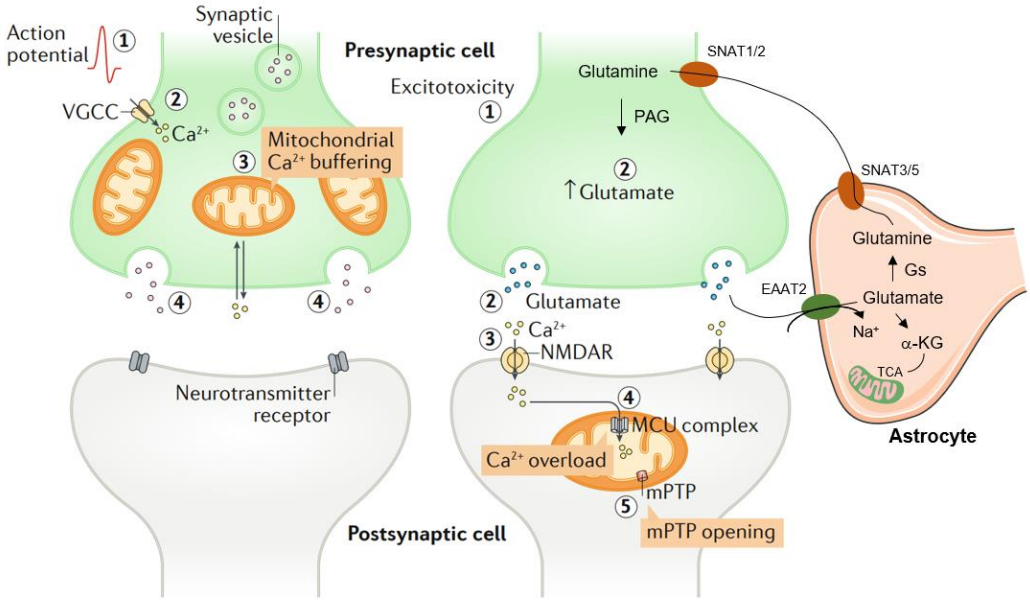

Figure 1.1. Glutamate-mediated excitotoxicity and the glutamate-glutamine cycle. Left synapsis represents synaptic transmission under normal stimulation, where mitochondria efficiently buffer calcium and glutamate is quickly cleared from the synaptic cleft. Right scheme indicates a situation of excitotoxicity, during which glutamate is highly present in the synaptic cleft inducing excessive activation of the NMNDARs, an overload of calcium in the cytoplasm and mitochondria, which leads to the opening of the mitochondrial transition pore (mPTP) and apoptosis. Astrocytes help clearing synaptic glutamate, which can be either converted into α-ketoglutarate (KG) and enter the TCA cycle or mostly converted to glutamine by astrocytic glutamine synthase (GS), which is then shuttle back to neurons where is transformed into glutamate via the phosphate-activated glutaminase (PAG). Modified from (Giorgi, Marchi, et al., 2018).

In this synaptic environment, astrocytes can also release numerous neuroactive metabolites, such as prostaglandins, GABA, glutamate, ATP and lactate, in a process known as gliotransmission (Perea et al., 2009). Lactate is of particular interest, as it is released by astrocytes to fuel neuronal energy metabolism and to induce intracellular signaling cascades important for the regulation of gene expression to support long-term memory formation (Suzuki et al., 2011). Together with microglial cells, astrocytes also respond to extracellular insults and participate in neuroinflammatory processes (Giovannoni & Quintana, 2020).

Unlike the other glial cells, microglia derive from primitive macrophages and constitute the immune cells of the CNS (Ginhoux et al., 2010). Nonetheless, in their "resting" state, they also contribute to brain homeostasis and affect cognitive processes. For instance, microglia participate in the synaptic pruning taking place during neurodevelopment, they are able to respond to a variety of neuronal signals to influence neurogenesis and memory formation and, together with astrocytes, their projections take part and monitor mature synapses (Augusto-Oliveira et al., 2019). Most known is their role in neural environment sensing and response to injury or toxic insults. Depending on these factors, microglia are able to shift their metabolic profile towards different activated states: anti-inflammatory (neuroprotective) or pro-inflammatory (neurotoxic) (Jurga et al., 2020). In many neurodegenerative diseases, microglia become "reactive", proliferating in damage areas, generally adopting a ameboid morphology, and releasing pro-inflammatory cytokines such as IL-1β, IL-6, reactive oxygen species (ROS) and Tumour Necrosis Factor alpha (α-TNF) (Chitnis & Weiner, 2017). These features are common to reactive astrocytes, with both cell types establishing a bidirectional communication to modulate the inflammatory processes (Linnerbauer et al., 2020). Thus, a chronic inflammatory state hampers the function glia have in neuronal homeostasis, leading to metabolic and synaptic impairments and neuronal death (Skaper et al., 2018).

Mature oligodendrocytes constitute the CNS cells responsible for axonal myelination. They spread their projections to tightly wrap several times the axonal fibers, generating a multi-layered stack known as the myelin sheaths (**Fig. 1.2**). In contrast to most biological membranes, these layers are formed mainly by lipids, such as cholesterol and galactosylceramide, and a small portion of proteins (20%) (Poitelon et al., 2020). As such, myelin isolate axons allowing for a high-speed transmission of action potentials and, at the same time, it provides structural and metabolic support to neurons (Simons & Nave, 2016).

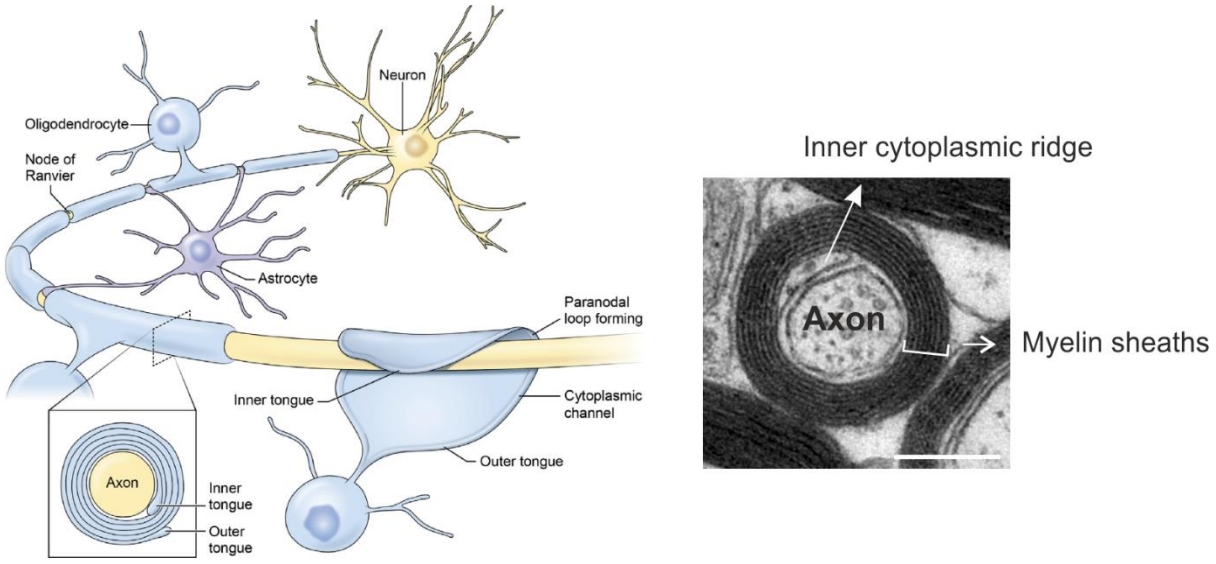

Figure 1.2. Structure and generation of myelin by oligodendrocytes in the CNS. Cartoon from (Fields & Dutta, 2019). Scale bar: 250 nm.

1.1.2. Motor control pathways

The spinal cord constitutes the central hub connecting the brain with the periphery. In adult mice, this structure runs along the dorsal part of the body, from the caudal brain to the sacral area, with a total of 34 segments. Within these, thoracic and lumbar parts comprise the biggest regions taking up each ca. 35% of the total length. If transversally sectioned, spinal cord shows an internal butterfly-shaped region which groups several neuronal cell bodies, including the spinal cord motor neurons, and unmyelinated axons (grey matter). In the surrounding area, many myelinated axons gather in bundles making up the white matter of the spinal cord. These tracts are separated anteriorly by a ventral median fissure and posteriorly by a dorsal median septum, clearly dividing the structure into two symmetrical halves (**Fig. 1.3**) (Sengul & Watson, 2012).

In primates, the corticospinal tract (CST) is the main motor pathway for skilled voluntary movements, connecting the motor cortex directly to spinal cord motor neurons (Welniarz et al., 2017). In adult rodents, however, this connection is polysynaptic, with the motor commands being transmitted by the CST to propriospinal neurons and interneurons before they reach the spinal cord motor neurons. In fact, in this species, the CST seems to have a minor role in motor regulation, which instead is controlled to a great extent by the following pathways (**Fig. 1.3**) (Lemon, 2008; Sengul & Watson, 2012):

- **The cortico-reticulospinal pathway**: several pyramidal neurons from the motor cortex send their information to the spinal cord via the reticular formation of the brain stem. From this region, a set of reticular fibers descend along the ventral spinal cord to convey information about limb movement initiation and postural control to spinal cord motor neurons.
- **The vestibulospinal tract**: neurons from the vestibular system in the brain stem also project their axons through the anterior part of the spinal cord influencing posture, balance, and movement. Particularly, the lateral vestibulospinal tract acts as the main regulator of the extensor tone, modulating the mouse walk cycle.
- **The spinocerebellar tract:** this pathway is formed by fibers of the periphery of the spinal cord which project to the cerebellum carrying information from the hindlimbs. Those axons located dorsally transmit proprioceptive inputs from muscle spindles, Golgi tendon organs and joints, whereas ventral tracts are involved in coordinated movement and posture.

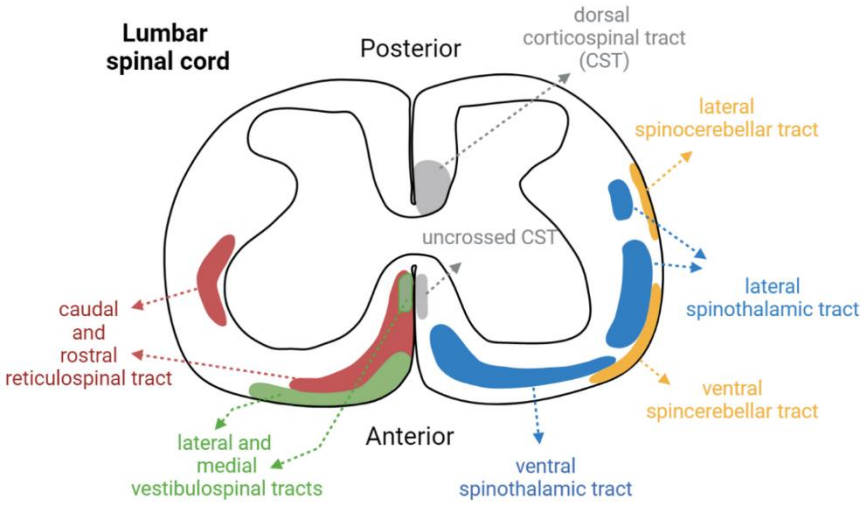

Figure 1.3. Lumbar spinal cord with estimated location of the major ascending and descending tracts. All described pathways, but the spinothalamic tract (STT), are involved in motor control. The STT, however, carries pain and temperature information to the brain. Created with BioRender 2022. Adapted from (Sengul & Watson, 2012).

Right above the brainstem, in between the spinal cord and the brain, is located the cerebellum. This highly folded region constitutes a crucial structure for motor processing, being involved in motor learning, posture, and balance maintenance. Anatomically, it is divided in two big zones: a central area called vermis, which is thought to mostly receive input from spinal cord ascendent fibers, and two hemispheres, which connect the cerebellum with cerebral areas (Sillitoe et al., 2012). The external part of these regions, known as the cerebellar cortex, contains a variety of cell types structured into three regular well-defined layers. From the outer to the inner part, the molecular layer stands as the most diverse area as it is formed by dendrites of the Purkinje cells (PCs), axons of the granule cells and two cell types: stellate cells and basket cells. The PC layer appears in between the molecular and the granule layer, and it consists of a single layer of PC bodies. The axons of these GABAergic neurons constitute the only efferent fibers projected into the deep cerebellar nuclei. The granular layer is located internally and contains Golgi cells and many, densely clustered granule cells (GC). In fact, GC represent most cerebellar cells (99%) (Consalez et al., 2021). These tiny neurons project their axons, the parallel fibers, to the outer molecular layer with a characteristic T shape and establish glutamatergic synapses with the dendrites of the PCs. Moreover, GC receive excitatory inputs from the mossy fibers, one of the two afferent fibers of the cerebellum, which originate in nuclei of the brainstem and spinal cord. Climbing fibers, the other principal input to the cerebellum, originate instead from the inferior olive and synapse on PC dendrites through the molecular layer (**Fig. 1.4**) (Apps & Garwicz, 2005).

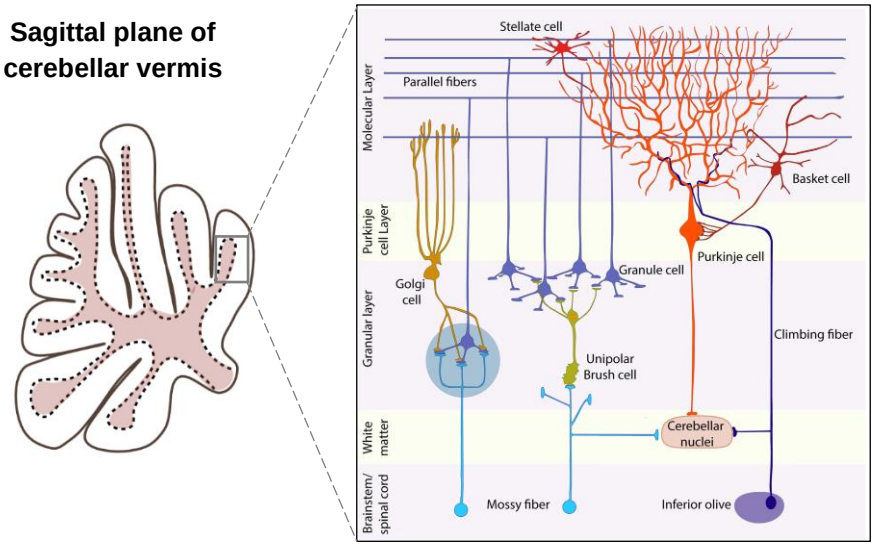

Figure 1.4. Cerebellar cytoarchitecture. Cerebellar tissue presents a foliate appearance consisting of different layers, represented in the left scheme. Cerebellar diagram created with BioRender 2022. Right cartoon modified from (Consalez et al., 2021).

1.2. Mitochondria

Mitochondria are crucial organelles carrying out very important metabolic activities in eukaryotic cells. These organelles, which originated two billions years ago through an endosymbiotic process (Wallin, 1927), have kept from its prokaryotic ancestors the double membrane morphology, the ability to produce ATP and lots of copies of its own circular genome (mtDNA). However, as part of the evolution process, most of the genes were transferred to the nuclear genome, remaining as of today only 37 mitochondrial genes in humans. Out of these, 13 constitute protein-encoding genes, codifying information for the respiratory chain complexes part of the oxidative phosphorylation (OXPHOS). Additionally, the ~16-kilobase human mtDNA encodes for 22 transfer RNAs (tRNAs) and 2 ribosomal RNAs (rRNAs), required for the mitochondrial translation machinery (Anderson et al., 1981). In mouse, a similar sequence and gene organization was observed (Maureen et al., 1981). The rest of the mitochondrial proteins are synthesized in the cytoplasm as precursors containing mitochondrial targeting signals (MTS) recognized by mitochondrial-surface receptors. Depending on the signal, the polypeptides can reach different mitochondrial subcompartments: the outer membrane (OMM), the inner membrane (IMM) which forms very specialized invaginations named cristae, the intermembrane space (IMS) or the matrix (**Fig. 1.5**) (Schmidt et al., 2010). The fact that the mitochondrial proteome is encoded by the nuclear and the mitochondrial genome implies a high simultaneous synchronization and regulation of both systems.

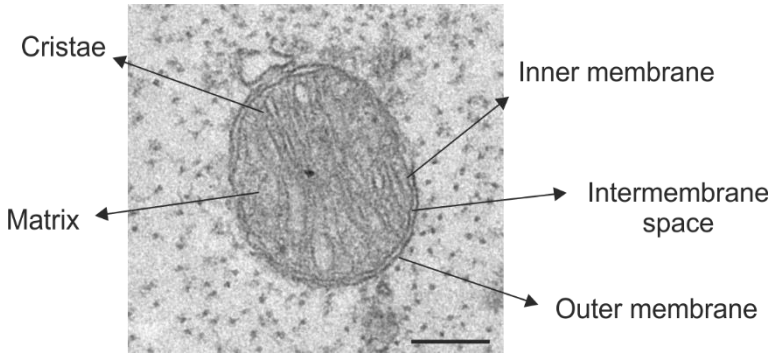

Figure 1.5. Mitochondrial structure. Electron micrograph from a mitochondria in an anterior spinal cord axon of a *wild-type* mouse. Scale bar: 200 nm.

1.2.1. Mitochondrial function and network in neurons

Mitochondria constitute versatile cellular compartments, whose functions include calcium buffering, apoptotic regulation and, most importantly, ATP production. In fact, most of the energy requirements of the brain are supplied by mitochondria through a metabolic network that involves different pathways, particularly the tricarboxylic acid (TCA) cycle, OXPHOS and the fatty acid β-oxidation. Energy demands becomes notably higher at the sites of action potential generation and synapses, where mitochondria are strategically located to provide localized ATP efficiently (Devine & Kittler, 2018). To do this, after glucose is converted into pyruvate via glycolysis, mitochondria uptake cytosolic pyruvate via mitochondrial pyruvate carries (MPC1 and MPC2), being then decarboxylated to form acetyl CoenzymeA (acetyl CoA). Once acetyl CoA is generated in the mitochondrial matrix, it fuels the TCA cycle, where it is oxidized in a series of enzymatic reactions to two CO_2 molecules while generating 1 GTP, 3 NADH and 1 $FADH_2$ molecules (**Fig. 1.6**). These metabolites transfer their electrons to the electron transport chain (ETC), where they are oxidized back to FAD and NAD^+ to keep the TCA cycle functioning. Thus, the TCA cycle and the OXPHOS work tightly together to effectively cover the cell energy demands (Martínez-Reyes & Chandel, 2020).

OXPHOS constitutes the system coupling the ETC respiration with the ATP production. It is formed of 5 multi-subunit complexes and 2 electron carriers located in the cristae of the IMM. During respiration, NADH cedes the electrons to complex I (NADH-ubiquinone reductase) whereas $FADH_2$ does it to complex II (succinate-ubiquinone reductase). Afterwards, the electrons are transferred to complex III (cytochrome c oxidoreductase) and complex IV (cytochrome c oxidase) via two diffusible small components: a lipid-soluble ubiquinone (CoQ, from I to II) and a water-soluble cytochrome c (cyt c, from II to IV). Finally, the cytochrome c receives them to produce water from oxygen. During these processes, complexes I, III and IV translocate protons (hydrogen ions) across the IMM creating a membrane potential used by the F_1-F_0-ATP synthase (complex V) to produce ATP (**Fig. 1.6**). This protonmotive force is also utilized by many transporters to translocate mitochondrial proteins, metabolites and positive charged ions, such as calcium, into the mitochondrial matrix (S. Papa et al., 2012). As a collateral effect, OXPHOS also constitutes the main source of ROS of the cell in form of hydrogen peroxide and superoxide. The levels of ROS are tightly controlled by antioxidant systems and their dysregulation has been linked to many neurodegenerative conditions including amyotrophic lateral sclerosis, Alzheimer's disease and different forms of ataxia (Barnham et al., 2004; Lupoli et al., 2018). In line with this, mutations in OXPHOS assembly and structural genes also give rise to a great variety of diseases (Koopman et al., 2013).

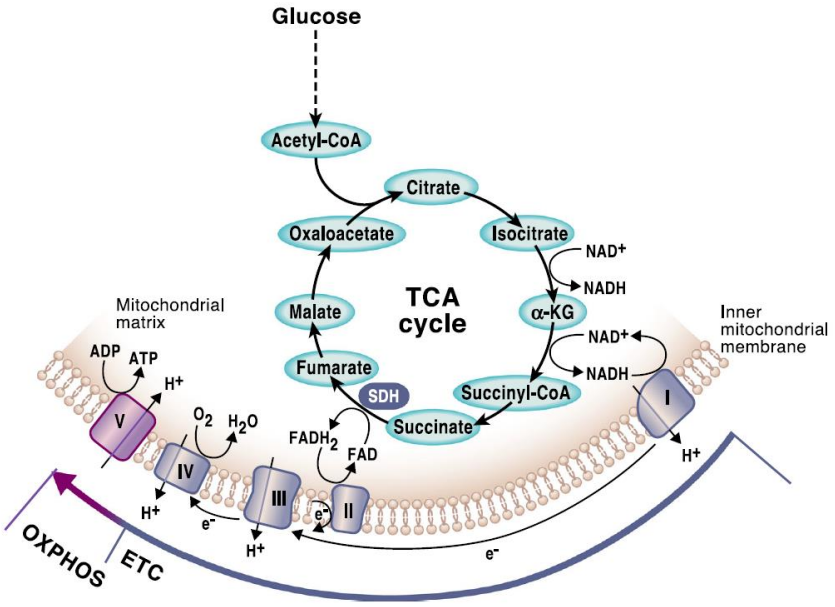

Figure 1.6. Schematic of TCA cycle and OXPHOS. Image taken from (Martínez-Reyes & Chandel, 2020).

Although glucose stands as the best oxidative substrate to produce ATP in the brain, approximately 20% of the total brain energy demands are covered via oxidation of fatty acids, taking place predominantly in astrocytes (Ebert et al., 2003). This catabolic process consists of four repeated reactions that take place in the mitochondrial matrix by which the fatty acids, previously converted to fatty acyl CoAs, are sequentially oxidized to produce $FADH_2$, NADH and acetyl CoA. Same as for those produced by the TCA cycle, the first two act as electron donors to the ETC whereas acetyl CoA directly enters the TCA cycle for further energy production (Tracey et al., 2018).

Nonetheless, although ATP generation via OXPHOS constitutes a more efficient mean of utilizing glucose as energy substrate (one molecule of glucose yields approx. 30 molecules of ATP) than glycolysis (2 molecules of ATP per glucose molecule), in cases of high synaptic activity, for example during synaptic formation, some neurons are able to rewire their metabolism towards aerobic glycolysis, an event known as the Warburg effect (Magistretti, 2014). This shift in favor of lactate synthesis, even in presence of enough oxygen availability, is thought to be an adaptation to enhance the rate of ATP synthesis whilst rapidly supplying carbon chains for molecule biosynthesis. Moreover, this effect may exert a neuroprotective role as mitochondrial burden can be mitigated and, thus, the consequent oxidative damage as well (Bas-Orth et al., 2017).

Calcium buffering constitutes another well-known function of mitochondria. This ability becomes especially significant in neurons as calcium serves as secondary messenger and contributes decisively to synaptic activity. During synaptic transmission, action potentials trigger a rapid increase of cytosolic calcium levels through voltage gated calcium channels, which leads to the release of neurotransmitter containing vesicles into the synaptic cleft. In respond to this, mitochondria exert a dual role, supporting calcium clearance by transiently uptaking it from the cytosol, while stimulating the TCA cycle and OXPHOS activity (Ashrafi et al., 2020). In fact, mitochondria can accumulate, by using the ATP-derived force, up to 10- to 20-fold more calcium than the cytosol (100-200 nM). This buffering helps maintaining cytosolic calcium homeostasis and prevents presynaptic terminals from excitotoxicity (Devine & Kittler, 2018).This function is also important in postsynaptic terminals, where postsynaptic currents lead to a quick release of calcium from the smooth endoplasmic reticulum (ER), which is then taken up by the closely located mitochondria. In fact, the largest source of intracellular calcium is the ER compartment (Raffaello et al., 2016). Therefore, the close proximity between ER and mitochondria at the contact sites determines the quick response and coordination of the machineries of both organelles towards many calcium signaling pathways (Hirabayashi et al., 2017; Raffaello et al., 2016).

In this context, either cytoplasmatic calcium ions or those released from the ER can be taken up by mitochondria through voltage-dependent anion-selective channel proteins (VDACs) and mitochondrial calcium uniporter (MCU) complexes. VDACs form voltage-dependent channels along the OMM and they are known to interact with ER IP3 receptors, which enhance and facilitate the calcium flux between the ER and the IMS. After reaching the IMS, the principal way towards the mitochondrial matrix is through the MCU complexes. These uniporters are located in the IMM and, in non-neuronal cells, they have low calcium affinity, requiring high levels of cytosolic calcium to open. Nonetheless, in neurons, they have been demonstrated to have a much lower calcium uptake threshold (Ashrafi et al., 2020). Moreover, they exist as macromolecular complexes comprising different subunits and several regulatory proteins (Fan et al., 2020). Its gatekeeper component is the mitochondrial calcium uniporter protein (MICU), which acts as a calcium sensor inducing the opening of the MCU complex when cytosolic concentrations of calcium are high. MICU proteins are connected to the essential MCU regulator (EMRE), an indispensable component without which MCU complexes are not able to transport calcium (Fan et al., 2020). The efflux of calcium to the cytosol is guaranteed by two proteins, the Na+/Ca2+/Li+ exchanger and the mitochondrial permeability transition pore (mPTP). The mPTP is crucial for the maintenance of calcium homeostasis as it opens when mitochondria undergo calcium overload. Indeed, a long-lasting opening state of

the channel contributes to increased oxidative stress, decreased mitochondrial membrane potential and swellings that lead ultimately to apoptosis (Giorgi et al., 2018).

The regulation of mitochondrial bioenergetics also relies on a proper mitochondrial transport along the neurites. Since these neuronal structures are constantly changing, the entire mitochondrial system must rapidly adapt and rearrange itself to allow its transport and redistribution to these areas with increased energy requirements. Therefore, mitochondria, far from constituting individual organelles, create an interconnected network controlled by mitochondrial dynamics. These processes are based on a balance between fusion and fission events. For instance, in order to be transported throughout the axons, mitochondria must undergo fission, a process mostly mediated by ER-mitochondria contact sites, dynamin-related protein 1 (DRP1) and the mitochondrial fission factor (MFF). Once these organelles arrive at their destination, it is likely they fuse again, an event coordinated by mitofusins (MFN1 and MFN2), responsible for OMM fusion, and the optic atrophy 1 protein (OPA1), mediating IMM fusion (Misgeld & Schwarz, 2017). An impairment of the fusion process leads to mitochondrial fragmentation whereas a fission disruption triggers hyperfused mitochondria. Both alterations highlight the relevance of these processes in neurons, as they are associated with many neurological disorders (Burté et al., 2015).

1.2.2. Mitochondria quality control systems

Mitochondria, as the energy converters of the cell and key players of many signaling pathways, need to have its network thoroughly controlled and regulated. Elaborate quality control systems have evolved within eukaryotic cells to maintain mitochondria homeostasis by detecting and repairing mitochondrial damage. Thus, survival is ensured through different lines of defense at various levels, comprehending organellar and molecular quality control (QC) systems.

At an organelle-level scale, defective mitochondria are removed following a specific autophagy pathway known as mitophagy. Although different pathways have been proven to be involved in this process, one the most studied mechanism is the PINK1-Parkin-mediated pathway (Gladkova et al., 2018). It starts with the accumulation of the serine/threonine kinase PINK1 at the OMM, which occurs as a result of depolarized, and thus, malfunctional, mitochondria. This leads to the recruitment and phosphorylation of Parkin, a cytosolic E3 ubiquitin ligase. When phosphorylated, Parkin ubiquitinates several OMM proteins from the autophagic machinery such as p62, whose sequence is recognized by the microtubule associated protein 1A/1B light chain 3 (LC3) located on the phagophore membrane. This interaction triggers the formation of the autophagosome, which fuses with lysosomes to finally

degrade the organelle. This process may be especially relevant in neurons, which distally rely on mitochondria to ensure synaptic transmission and whose loss of function is linked to many neurodegenerative diseases (Fang et al., 2019; Fivenson et al., 2017) . Although there is still controversy about how mitochondria are recycled in axons *in vivo*, local mitophagy seems to be a decisive way to ensure distal mitochondrial homeostasis (Doxaki & Palikaras, 2021).

At a molecular level, mitochondrial proteins are continuously exposed to ROS with a high risk of being damaged. This can have a great impact on the whole cell system as mitochondrial proteome constitute approx. 10% of the entire cell proteome (Calvo & Mootha, 2010). Thus, to preserve mitochondria function and avoid further cell damage, rigorous pathways exist. Among these, chaperones and proteases appear as the first line of defense (Song et al., 2021). Nuclear encoded proteins are synthesized in the cytosol -as unfolded preproteins- and need to cross the different mitochondrial compartments to finally reach its mitochondrial destination. To prevent misfolding of these polypeptides, and thus its aggregation, various classes of chaperones exist and bind to them on their way to the matrix. Two key chaperones are mtHsp70 and mtHsp60, which facilitate protein import into mitochondria while using the energy of ATP to stabilize and promote the native structure of the newly imported mitochondrial proteins (Jebara et al., 2017).

In concert with chaperones, highly conserved proteases remove proteins that fail to fold or assemble properly. Many of them are ATP dependent and localize across the mitochondria to maintain organelle proteostasis. One important group of proteases is the AAA+ (ATPase Associated with various cellular Activities) family which harbors an AAA ATPase domain with chaperone-like activities. Within these, the Lon protease stands as one of the most decisive QC systems in the matrix, performing proteolytic functions under healthy and pathological conditions in addition to support mitochondrial gene expression (Pinti et al., 2015). The protease ClpXP is also present in the matrix to help removing oxidatively damaged proteins (Baker & Sauer, 2012). Nonetheless, it is important to highlight the crucial role the IMM proteases execute. The inner mitochondrial compartment is highly exposed to oxidative damage caused by close-produced ROS and needs to be especially regulated. There, this function is mainly ensured by two complexes, the *i*-AAA (intermembrane space-ATPase) and *m*-AAA (matrix-ATPase) proteases. Both are inserted in the IMM but facing opposite sites; while the *i*-AAA protease has its proteolytic site in the IMS, the *m*-AAA protease directs it to the matrix. Apart from targeting misfolded proteins to prevent the accumulation of toxic aggregates, they also clear specific substrates as a way of regulating metabolic pathways (Glynn, 2017).

Furthermore, upon different proteotoxic stresses, the levels of these chaperones and proteases increase in response to the unfolded protein response activation. This pathway not only emerges to upregulate those genes involved in proteostasis but also to alleviate mitochondrial stress by shifting metabolism towards cytoplasmic glycolysis (Nargund et al., 2015).

1.3. The *m*-AAA protease

1.3.1. Composition and functions

The *m*-AAA protease forms ring hexamers organized along the IMM. These complexes are made up of different isoforms, which are ubiquitously expressed and highly conserved from yeast to mammals. In humans, *m*-AAA proteases are built up of two subunits: paraplegin and AFG3L2 (AFG3-like gene 2), which can assemble in either heterooligomeric or, only in the case of AFG3L2, homooligomeric complexes. Murine *m*-AAA proteases harbour a third isoform: AFG3L1 (AFG3-like gene 1), which, as AFG3L2, is able to form both types of oligomeric complexes (**Fig. 1.7**). This protein is encoded by a pseudogene in humans (Kremmidiotis et al., 2001).

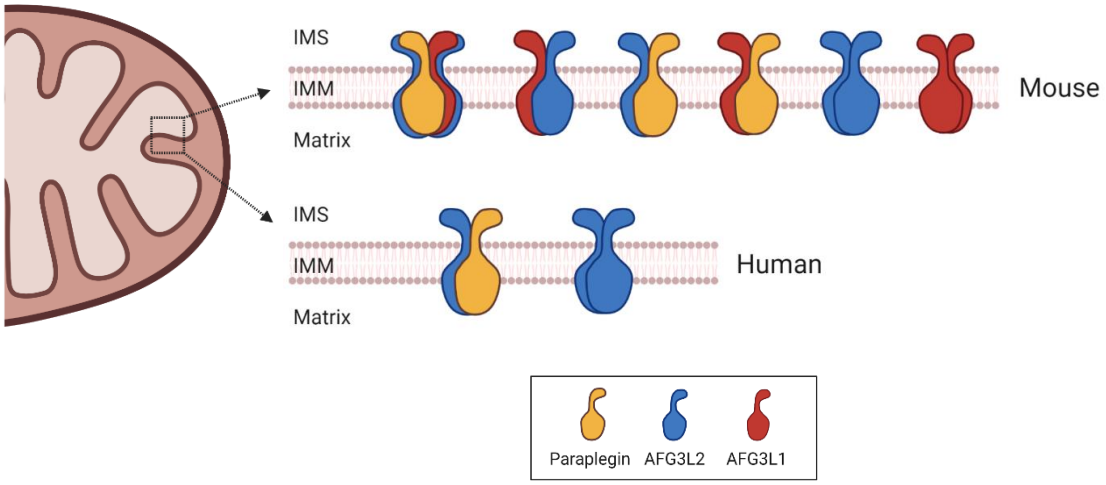

Figure 1.7. The different isoenzymes of the *m*-AAA protease. Whereas mice present three different subunits, humans only present two: paraplegin and AFG3L2. These subunits can form heterooligomeric complexes, composed of different subunits, or, only for AFG3L2 and AFG3L1, assemble among themselves to form homooligomeric hexamers. Image created with BioRender 2022.

Despite the redundancy among the different *m*-AAA protease subunits, they exhibit tissue-specific expression patterns. AFG3L2 and paraplegin protein levels were shown to be 10 and 4-fold higher, respectively, in mouse brain than in the liver compared to AFG3L1 expression in those tissues (Koppen et al., 2007). Within the brain, *in situ* hybridization and RT-PCR studies revealed a particularly high presence of both *Afg3l2* and *Spg7* transcripts in the mouse cerebellum (Martinelli et al., 2009). Interestingly, *Spg7* -the gene encoding for paraplegin- was also found to be highly expressed in neocortical pyramidal cells and motor neurons (Sacco et al., 2010). In line with previous findings, *Afg3l1* expression was in general the least measured (Martinelli et al., 2009). These studies highlight a variability in the subunit composition of the *m*-AAA protease in the different tissues that might ultimately determine the diverse roles these proteases have within mitochondria.

As other AAA+ family members, *m*-AAA proteases contain a specific ATPase domain that couples the hydrolysis of ATP with the proteolytic cleavage of the polypeptides, and, at the same time, also favours the oligomer assembly (Glynn, 2017). However, a study carried out with their yeast homologous showed that interactions between the M41 zinc metalloprotease regions, those responsible for the peptidase activity, are also required for the correct assembly of the *m*-AAA proteases (Lee et al., 2011). Apart from these two domains, they also present two transmembrane sequences, which drive their anchoring to the IMM, an N-terminal domain, whose function in the mature protein is still poorly understood, and a C-terminal coiled-coil domain, which appears to be influencing substrate recognition (Truscott et al., 2010).

The *m*-AAA protease is situated in close association with membrane scaffolds such as the prohibitins (PHB1 and PHB2). In fact, PHB subunits form ring-like complexes that surround the IMS domain of the *m*-AAA protease (Deshwal et al., 2020). In yeast, PBHs have been shown to negatively regulate *m*-AAA protease functions as their deletion enhanced *m*-AAA mediated proteolysis of IMM proteins (Steglich et al., 1999). However, this function has not been demonstrated in mammals yet. Interestingly, the *m*-AAA protease also interacts with MAIP1, a matrix protein that helps inserting the MCU regulator EMRE in the IMM thereby preventing its degradation by QC proteases. Therefore, this interaction is vital for MCU-dependent calcium signaling (König et al., 2016).

Functions of the m-AAA protease

As part of the quality control machinery, *m*-AAA proteases carry out housekeeping functions by removing non-assembled or misfolded mitochondrial proteins and mediating protein turnover. In yeast, these substrates include subunits of the ETC from complexes III and IV (Arlt et al., 1996; Guélin et al., 1996) and the peripheral membrane protein Atp7, a subunit of the F_1-F_0-ATP synthase (Korbel et al., 2004). In humans, paraplegin-containing *m*-AAA proteases

have also been associated with an ETC activity impairment, as their loss causes reduced CI activity and a higher sensitivity to oxidant stress (Atorino et al., 2003). Furthermore, mitochondria from brain and spinal cord of *Spg7*$^{ko/ko}$ *Afg3l2*$^{ko/wt}$ mice seem to display problems in complex I, III and IV stability (Martinelli et al., 2009). Studies performed with AFG3L2 demonstrated indeed that this subunit specifically processes the OXPHOS components COX1 (Hornig-Do et al., 2012), ND1 (Zurita Rendon & Shoubridge, 2012) and ATP6 (Richter et al., 2015), although none have been proven a direct substrate of the paraplegin-containing *m*-AAA complexes so far.

The *m*-AAA protease also degrades unassembled EMRE, regulating proper MCU activity. In resting cellular conditions, EMRE and the MCU gatekeepers MICU1 and MICU2 ensure proper regulation of MCU complexes in response to calcium levels. However, an increase of non-assembled EMRE due to *m*-AAA protease absence leads to the accumulation of MCU-EMRE complexes which lack the gatekeeper subunits. These aberrant complexes are constitutively active, promoting the opening of the mPTP due to calcium overload with the consequent neuronal death (König et al., 2016). In this study, they measured the calcium retention capacity (CRC), an indicator of the maximum calcium overload of mitochondria preceding mPTP opening. While mitochondria isolated from human *SPG7* KO HEK293 cells did not alter the CRC, mitochondria from *Spg7* KO mouse embryonic fibroblasts (MEFs) showed a significantly reduced CRC and earlier mPTP opening. Another study from Hurst et al., 2019 also found a role of SPG7 in modulating mPTP opening, although in an opposite manner, as they showed an increased CRC via regulation of MCU regulator 1 (MCUR1) upon SPG7 deletion. SPG7 was even proposed to be an essential component of the mPTP via interaction with cyclophilin D (CypD) and VDAC (Shanmughapriya et al., 2015). However, this study has been highly criticized due to a misinterpretation of their own scientific findings (Bernardi & Forte, 2015). Because recent studies have also reported opposite results upon SPG7 absence, the modulation of mPTP by SPG7 is still a controversial topic. For example, while Klutho et al., 2020 claimed that paraplegin does not regulate the mPTP in MEFs, the study from Sambri et al., 2020 attributes this protein a role in hampering the transient openings of the mPTP via increased expression of sirtuin 3 and lower levels of acetylated CypD.

In addition to the aforementioned functions, these proteases can also act as regulatory systems by specifically processing certain preproteins under physiological conditions. A regulatory substrate of the yeast and mouse *m*-AAA protease is the large ribosomal subunit MRPL32. Under physiological conditions, MRPL32 is imported into the matrix via the TOM and TIM complexes in an unfolded state, bearing a long unstructured N-terminal presequence. After translocation, the newly imported MRPL32 adopts a folded state which prompts the binding of the *m*-AAA protease to its N-terminal region to subsequently cleave its mitochondrial

targeting sequence. Mature MRPL32 is then recruited to ribosomes allowing synthesis of mitochondrial encoded proteins, such as the ETC subunits. Thus, impaired *m*-AAA protease leads to the accumulation of unmature MRPL32, impacting mitochondrial ribosome biogenesis and translation (Koppen et al., 2009; Nolden et al., 2005). Indeed, further studies with AFG3L2 also demonstrated an impaired mitoribosome assembly and a reduced protein synthesis rate in mitochondrial from *Afg3l2* constitutive KO brain (Almajan et al., 2012) and in fruit fly *Drosophila melanogaster* (Pareek & Pallanck, 2020).

In yeast, the *m*-AAA protease also mediates the processing of the cytochrome c peroxidase (Ccp1). Strikingly, although this function has still not been investigated in mammals, it suggests a new role for *m*-AAA proteases, as Ccp1 processing was driven by ATP-dependent membrane dislocation, independently of the protease's peptidase activity (Tatsuta et al., 2007).

1.3.2. Role of the m-AAA protease dysfunction in neurodegeneration

The importance of an appropriate mitochondrial proteostasis, specially in neurons, is further underscored by the appearance of neurodegenerative diseases associated with *m*-AAA protease subunit alterations. Mutations in *AFG3L2* are the cause of two different neurodegenerative conditions: autosomal recessive (AR) spastic ataxia neuropathy syndrome (SPAX5) (Pierson et al., 2011) and autosomal dominant (AD) spinocerebellar ataxia type 28 (SCA28), whereas mutations in *SPG7* give rise to AR hereditary spastic paraplegia (HSP).

1.3.2.1. Spinocerebellar ataxia type 28 (SCA28)

SCA28, which accounts for 1 to 3% of European families diagnosed with SCAs, is an AD form of SCA associated with standing imbalance, gait impairments with lower limb hyperreflexia, nystagmus and ophthalmoparesis. It was first described in a four-generation Italian family in 2006 (Cagnoli et al., 2006), and four years later, mutations in *Afg3l2* were discovered to be behind its development (di Bella et al., 2010). Up to date, other missense mutations have also been described (Cagnoli et al., 2010; Zühlke et al., 2015).

Mice carrying mutations in both *Afg3l2* alleles show a severe neuromuscular syndrome which begins seven days after birth and leads to death generally one week after. These mice show a prominent axonal development impairment of the whole CNS with delayed myelination (Maltecca et al., 2008). This mouse model was the first to be reported linking axonal development to a mitochondrial protein, which emphasizes the essential role AFG3L2 carries within the CNS. Notwithstanding, *Afg3l2* KO mouse phenotype does not mimic the progressive ataxia SCA28 patients display. This recapitulation was, however, achieved by mutating only

one of the *Afg3l2* alleles (Maltecca et al., 2009). *Afg3l2* haploinsufficient mice show a progressive decline in motor coordination caused by PC dark degeneration, a type of cell death between necrosis and apoptosis. It is worth noting that these mice only show cerebellar alterations with minimal repercussion on spinal cord processes. Although the underlying pathogenetic mechanisms are still under study, it seems to involve an early proteotoxic stress due to the accumulation of misfolded substrates, which leads to impaired mitochondrial bioenergetics, mitochondrial axonal transport, and an ineffective calcium handling (Maltecca et al., 2015; Mancini et al., 2019; Tulli et al., 2019). A disruption in the mitochondrial nascent chain synthesis caused by AFG3L2 mutations has been postulated as a proteotoxic trigger initiating the cellular stress response (Richter et al., 2019).

Recently, a mouse model with an astrocytic-specific deletion of *Afg3l2* drew the attention to the role of glial cells within SCA28 pathology. These mice also displayed late-onset motor defects along with inflammation and metabolic stress responses, which ultimately alter PC morphology and electrophysiological properties (Murru et al., 2019).

1.3.2.2. SPG7-linked Hereditary spastic paraplegia

HSP comprises a genetically heterogeneous family of inherited neurodegenerative disorders that share a common clinical manifestation: lower limb weakness and spastic gait disturbance. However, “complicated” forms of the disease can appear that are associated with a variety of clinical features such as cognitive deficits, cerebellar ataxia, peripheral neuropathy, optic atrophy, bladder dysfunction and epilepsy (Blackstone et al., 2011). The neuropathological shared feature of all HSPs is the progressive degeneration of upper cortical motor neurons, whose axons get compromised and experiment a dying-back phenomenon whereby the axonal distal part degenerates while the soma maintains its integrity. To date, mutations in over 200 genetic loci have been described, from which only a subset of genes has been numerically denoted SPG1 to SPG80 (Blackstone, 2020). Two of the major mechanisms implicated in autosomal forms of HSP are intracellular transport and organelle shaping, caused to a large extend by mutations in the microtubule-severing protein spastin (SPG4), but also in atlastin (SPG3A), the Kinesin heavy chain KIF5A (SPG10) and the receptor expression-enhancing protein1 REEP1 (SPG31) (Blackstone, 2018; Klebe et al., 2015).

Few genes related to mitochondrial regulation have been also identified in HSP. Two of them are involved in mitochondrial quality control: the chaperonin mtHSP60 (SPG13) (Bross et al., 2008) and paraplegin (SPG7). Indeed, paraplegin was first discovered while mapping the locus of a new HSP autosomal recessive form (Casari et al., 1998). Up to now, several mutations have been identified within the *SPG7* loci, with their associated pathogenesis and

manifestation depending on the region of the protein they affect (Hewamadduma et al., 2018; van Gassen et al., 2012). For instance, those carrying an homozygous mutation in the M41 peptidase region display an earlier onset of symptoms whereas mutations in other regions do not seem to affect age at disease onset. Pathogenic nonsense, frameshift, splice site and missense mutations have been identify throughout *SPG7*, with missense variants occurring most frequently. These mutations are mainly loss-of-function mutations, leading to the absence of paraplegin protein (Atorino et al., 2003; Hewamadduma et al., 2018). However, increased paraplegin expression has also been reported (Pfeffer et al., 2014; Thal et al., 2015).

As a matter of fact, many mutations in *SPG7* are clinically classified not only as HSP forms but also as cerebellar ataxia, as these patients show a prominent cerebellar dysarthria (Synofzik & Schüle, 2017). Moreover, although females seem to present an earlier age at onset, male patients outnumber female patients and generally show a more severe symptomatology (Hewamadduma et al., 2018; van Gassen et al., 2012).

In order to investigate the role of paraplegin in the appearance of HSP, in 2004, a *Spg7* KO mouse model was generated and characterised (Ferreirinha et al., 2004). These homozygous mice present a mild, late-onset phenotype, showing mitochondrial abnormalities with disrupted cristae in a subset of spinal cord axons at 4.5 months of age, with an accumulation of organelles and neurofilaments at late stages. Furthermore, *Spg7* KO mice develop a progressive axonal degeneration of spinal cord anterior tracts, prominent only from 15 months on, an optic neuropathy, a peripheral axonopathy, and a mild muscular involvement. Despite the fact that *Spg7* KO mouse model shows some similarities with the human HSP pathology, it still expresses *Afg3l1*, which could be compensating the absence of paraplegin and therefore, contributing to the mild phenotype observed. Moreover, a variant of paraplegin is also present in these mice, which arises from an alternative splicing that skips the first exons encoding for the MTS (Mancuso et al., 2012). This variant is expressed at a very low level and localizes to the ER, suggesting that paraplegin might be exerting its role beyond the mitochondrial compartment. Although the function of this isoform is still unclear, it may be implicated in the Spg7 KO mouse pathogenesis.

The underlying pathogenic mechanisms causing the mitochondrial abnormalities and the axonal degeneration are still unresolved. Crucial mitochondrial functions, such as respiration and ATP production, were only seen slightly impaired in late stages of the pathogenesis, indicating that OXPHOS alterations are not a primary defect of paraplegin deficiency (Ferreirinha et al., 2004). Like AFG3L2, an accumulation of unfolded protein aggregates might be a trigger for proteotoxic stress, however, these aggregates have never been observed in the *Spg7* KO model. Defects in ribosome assembly have previously been reported upon *Spg7*

deletion, as the *m*-AAA protease processes MRPL32, affecting mitochondrial translation (Nolden et al., 2005). Thus, an impairment of ribosome biogenesis could be one of the factors contributing to the *Spg7*-associated phenotype. Nonetheless, this hypothesis would imply wide phenotypic manifestations, not only neurological, as translation constitutes a housekeeping function in mitochondria. The variable expression of *m*-AAA subunits in the different tissues might explain this specific phenotype, as the levels of paraplegin are quite high in neuronal tissues (Koppen et al., 2007; Sacco et al., 2010). Therefore, the identification of paraplegin-specific substrates is crucial to bring new insights into underlying molecular events causing HSP. In this context, the study of Sambri et al., 2020, which used the above describe *Spg7* mouse model, proposed SIRT3 as a substrate of paraplegin, linking an increase of SIRT3 at both transcriptional and protein levels to an impaired mPTP flickering via low levels of acetylated CypD. These findings suggest hindered synaptic transmission upon paraplegin deficiency due to a dysfunctional calcium handling at presynaptic terminals.

1.4. NAD metabolism and homeostasis

Nicotinamide adenine dinucleotide (NAD^+) is a crucial molecule governing many metabolic pathways. It serves as both an essential redox cofactor and a substrate of non-redox NAD^+-dependent enzymes. NAD^+ accepts hydride from various metabolic processes to generate NADH. Additionally, it can also be phosphorylated to $NADP^+$, which can also accept hydride to form NADPH. The $NADP^+$/NADPH redox couple mainly participates in those metabolic processes that require reducing power, such as fatty acid and nucleic acid biosynthesis, whereas NAD^+ and its reduced form -NADH- are critical regulators of catabolic pathways, such as fatty acid oxidation, glycolysis and OXPHOS (Xiao et al., 2018).

Several NAD^+-consuming enzymes have been so far described, including poly (ADP-ribosyl) transferases (PARP1-2), the sirtuin family of deacetylases (SIRT1-7) and cADPR-ribose synthases (for instance: SARM1, CD38). The pathways these enzymes affect include DNA repair, transcription, cytoskeleton stability, calcium signaling and immune response (Cantó et al., 2015).

1.4.1. NAD^+ biosynthesis and distribution

Due to its importance in all biological processes, NAD^+ is always in high demand and its regeneration becomes an indispensable process to ensure cell homeostasis and survival. In fact, low NAD^+ levels have been linked to metabolic and neurodegenerative diseases (Lautrup et al., 2019; Okabe et al., 2019) as well as to the aging process (Camacho-Pereira et al., 2016).

NAD^+ levels can be maintained via different cellular routes which involve *de novo* synthesis and metabolite recycling (**Fig. 1.8**).

NAD^+ can be synthesised from various vitamin B_3 precursors. Nicotinic acid constitutes the main dietary supplier of NAD^+, a conversion that occurs in the cytosol following the Preiss-Handler pathway. Dietary nicotinamide riboside (NR) is transformed to nicotinamide mononucleotide (NMN) in either the extracellular milieu or after being imported in the cell. NMN originating both from the diet and the NR conversion is then metabolized to NAD^+ by nicotinamide mononucleotide adenylyltransferases (NMNATs). Tryptophan can also be transformed into NAD^+ via *de novo* kynurenine pathway (Covarrubias et al., 2021). However, this transformation seems to be tissue-specific, as most of this amino acid is metabolized to nicotinamide (NAM) in the liver (L. Liu et al., 2018). NAM can then be released into systemic circulation to reach other organs, where is converted to NAD^+ via activity of nicotinamide phosphoribosyltransferase (NAMPT). Interestingly, the brain appears to rely on circulating NAM, as NR and NMN may not be crossing the brain blood barrier (L. Liu et al., 2018).

Most of the cellular NAD^+ is, however, recycled from NAM via the salvage pathway. This recycling is crucial for NAD^+ homeostasis as NAM constitutes a by-product generated from the activity of NAD^+-consuming enzymes. The salvage pathway begins with the conversion of NAM to NMN by NAMPT, followed by the transformation of NMN into NAD^+ via NMNATs (Covarrubias et al., 2021). To date, three different NMNAT isoforms have been identified: NMNAT1 in the nucleus, NMNAT2 in the cytosol and NMNAT3 in the mitochondrial matrix (Berger et al., 2005). These compartments constitute the three main subcellular NAD^+ pools, with the mitochondria harbouring the majority of intracellular NAD^+. Apart from NMNAT3, mitochondrial NAD^+ equilibrium is affected by the recently discovered NAD^+ transporter -Slc25a51- (Kory et al., 2020; Luongo et al., 2020) and the redox balance of the mitochondrial metabolic reactions (Cambronne et al., 2016).

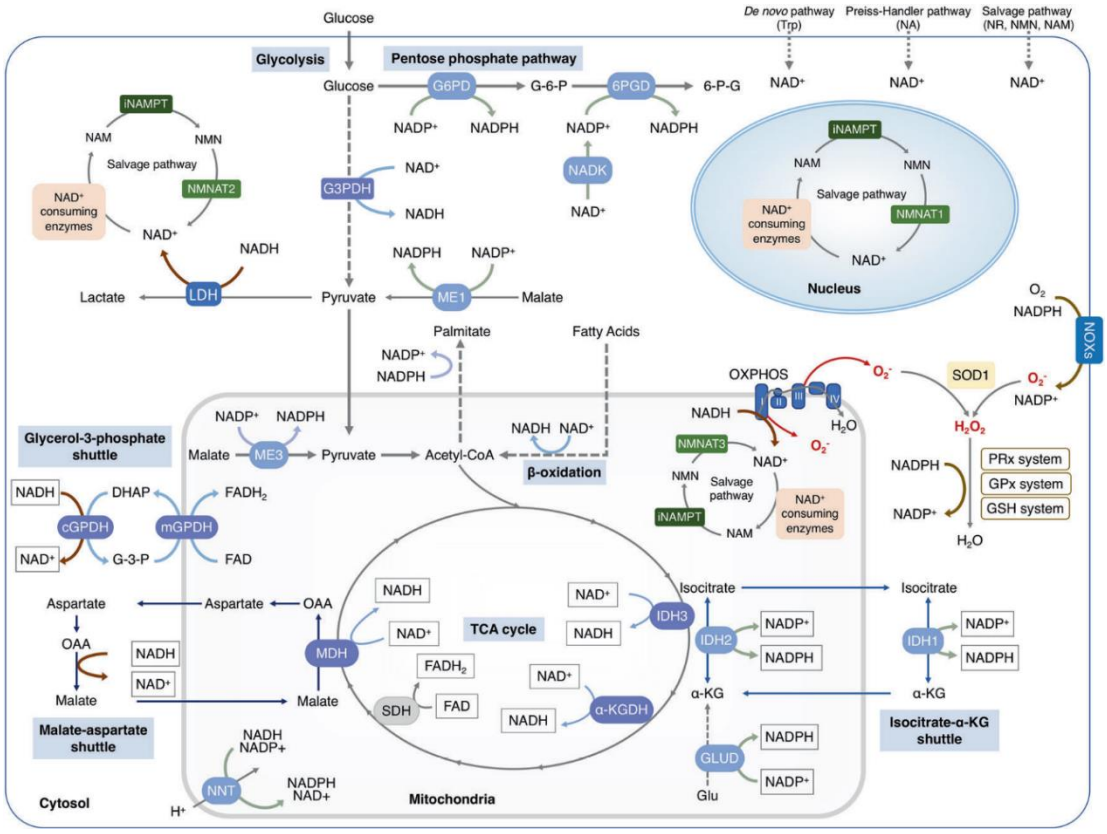

Figure 1.8. Cellular NAD⁺ homeostasis. Different cellular pathways coordinate together to maintain the NAD⁺ subcellular equilibrium. These processes involve the *novo* synthesis, metabolite recycling and its consumption. NAD⁺ is also key for metabolism, acting as hydride receptor to form NADH. This redox pair greatly regulates the intracellular redox state of the cell, being particularly relevant in glycolysis, the TCA cycle, OXPHOS and the fatty acid β-oxidation. Image from (Xie et al., 2020).

1.4.2. NAD⁺ and energy metabolism

NAD⁺ can modulate cytosolic energy metabolism via different pathways, including glycolysis, where it acts as cofactor of the glyceraldehyde phosphate dehydrogenase (GAPDH) and the lactase dehydrogenase. In the mitochondria, the NAD⁺/NADH redox pair is particularly relevant, as it connects the TCA cycle substrate oxidation to the OXPHOS activity. NADH molecules generated as by-products of the glycolysis enter the mitochondria through two shuttles: the malate-aspartate (MA) and the glycerol-3-phospate (G3P) shuttle, as the IMM is impermeable to NADH. In the matrix, the MA shuttle provides the ETC with NADH molecules, whereas G3P shuttle generates $FADH_2$ molecules. Additionally, mitochondrial NAD⁺ is used by the TCA cycle to generate NADH through three rate-limiting enzymes: isocitrate dehydrogenase 3 (IDH3), malate dehydrogenase (MDH2) and α-ketoglutarate dehydrogenase (KGDH). Resulting NADH is then utilized as an electron donor by complex I, which regenerates

NAD^+ and contributes to mitochondrial NAD^+ pool, whereas $FADH_2$ facilitates OXPHOS activity by transferring its electrons to complex II (**Fig. 1.8**) (Xiao et al., 2018).

NAD^+ also mediates oxidative metabolism via sirtuin activity (Imai & Guarente, 2016). Mitochondrial SIRT3 can deacetylate and activate acetyl-CoA synthetase 2 (Hallows et al., 2006), which generates acetyl-CoA from acetate, and long-chain coenzyme A dehydrogenase, modulating fatty acid oxidation (Hirschey et al., 2010). Moreover, together with SIRT1, SIRT3 activity orchestrates the mitochondrial UPR and mitophagy (L. Papa & Germain, 2014). In neurons, SIRT3 carry an important role in adaptive responses to bioenergetic, oxidative, excitatory stress (Cheng et al., 2016) and intermittent fasting (Y. Liu et al., 2019).

1.4.3. SARM1

The Sterile Alpha and Toll Interleukin Receptor Motif-containing protein 1 (SARM1) was originally identified in 2001 by Mink et al., in a genome-wide screen study. They showed that SARM1 is evolutionary conserved in *Drosophila*, mouse, *C. elegans* and humans (Mink et al., 2001). SARM1 is a member of the TLR adaptor family, which mediates innate immunity. In fact, the first function that was attributed to TIR-1, the SARM1 *C. elegans* homologue was the regulation of the innate immune response, due to its Toll-interleukin 1 receptor (TIR) domain (Liberati et al., 2004). However, the same study found no effect of human SARM1 in nuclear factor κB-dependent transcription. A couple of years later, Carty et al., (2006) paradoxically showed that human SARM1 negatively regulates TLR signaling and, therefore, innate immune response. This proinflammatory role was further demonstrated in HEK cells (Peng et al., 2010), in mouse macrophages upon bacterial infection (Pudla et al., 2011) and after spinal cord injury (H. Liu et al., 2021). Furthermore, SARM1 has been shown to influence cytokine production in neurons under normal conditions (Lin et al., 2014) and upon viral infection (Szretter et al., 2009). SARM1 seems to also mediate neuronal stress responses, as neurons without SARM1 are protected from death after deprivation of glucose and oxygen (Kim et al., 2007). In hepatocytes, SARM1 deletion seems not only to reduce inflammation and oxidative stress, but also to generally impact cell bioenergetics via TLR signaling (Pan & An, 2018).

Beyond its role in immune responses, very little is known about its function in the brain under physiological conditions. In *C. elegans*, TIR-1 regulates the expression of olfactory receptors via the ASK1–MKK–JNK pathway (Chuang & Bargmann, 2005). Similarly, in mammalian hippocampal neurons, SARM1 seems to modulate microtubule stability, axonal outgrowth, dendritic arborisation and neuronal polarity via interaction with syndecan-2 and through the MKK4–JNK pathway (Chen et al., 2011). However, a recent study in sensory neurons suggests a negative regulation of SARM1 in axonal cytoskeletal dynamics, including

microtubules and actin filaments, as axons lacking SARM1 showed increased axonal filopodia dynamics, with less mitochondrial motility, and branch formation along axons (Ketschek et al., 2022). Remarkably, SARM1 has also been associated with mitophagy, as it was shown to stabilize PINK1 on depolarized mitochondria in different cell lines (Murata et al., 2013).

An novel role of SARM1 was uncovered in 2012 while performing a mutant screening in *Drosophila* to block Wallerian degeneration (Osterloh et al., 2012). In this study, Sarm1$^{ko/ko}$ mice whose axons were severed showed a remarkable delay in the degeneration process

1.4.3.1. Wallerian degeneration

Wallerian degeneration constitutes an injury-induced axon degeneration program, which is triggered upon axon severing and active in the distal part to the injury site (Waller, 1850). It is characterised by a series of molecular changes grouped in three different phases: an initiation phase right after injury, a latent phase with no changes in axon morphology and a final execution phase when the axon fragments itself and disintegrates. During the first hours after nerve transection the axons remain physically intact, but they present two major molecular differences: a decline in NMNAT2 levels and the phosphorylation of MKK4 (Gerdts et al., 2016). During these hours, cytokines and growth factors also start to be released. These events trigger a whole degeneration cascade -the execution phase- characterised by NAD and ATP loss, SARM1 activation, increased calcium influx, calpain activation and neurofilament proteolysis, leading to the final death of the axon (Gerdts et al., 2016; Loring & Thompson, 2020).

Contrary to the belief that degeneration after physical injury is a passive phenomenon, the discovery of the Wallerian degeneration slow mutant (WLD^S) pointed out that Wallerian degeneration is rather an active phenomenon. In fact, WLD^S axons are able to survive weeks after axotomy (Mack et al., 2001) and WLD^S confers protection against axonal degeneration in different species including mice, flies, zebrafish and humans (Beirowski et al., 2009; Kitay et al., 2013; Martin et al., 2010), and in models of neurodegenerative diseases (Fischer et al., 2005; Hasbani & Omalley, 2006). However, this protection might not be long-lasting, as WLD^S mice show a progressive hindlimb motor impairment starting at 3 months of age (Gilley et al., 2017).

Conforti et al. revealed that the *Wld^S* gene encodes for a chimeric fusion protein which contains a non-enzymatic fragment of the ubiquitin conjugation factor E4B (Ube4B) and the full-length sequence of the NMNAT1 enzyme (Conforti et al., 2000). Although at that time it was unclear which part of the protein was responsible for the neuroprotection, it is now known that it is due to the NMNAT1 activity (Conforti et al., 2009). NMNAT1 normally localizes to the

nucleus, however, the WLD^S fusion protein is also found in axons where it converts NAM into NAD^+ (Coleman & Freeman, 2010). In fact, it is believed that NMNAT1 protects axons from degenerating by replacing for NMNAT2 (Gerdts et al., 2016). NMNAT2, the cytoplasmatic isoform of NMNATs, is very short-lived and it has to be transported from the soma in order to provide NAD^+ in the distal axonal regions. As such, it is considered to be a "survival factor" whose depletion is a determining step that triggers the fatal degeneration cascade (Gilley & Coleman, 2010). Its relevance is further underlined by the fact that $NMNAT2^{ko/ko}$ mice die perinatally (Hicks et al., 2012). Unlike NMNAT2, WLS^S protein levels remain unaltered after axotomy and can support NAD^+ local synthesis (Gerdts et al., 2016).

Sarm1 was the first endogenous gene whose deletion was found to delay Wallerian degeneration (Osterloh et al., 2012). It was confirmed later that SARM1 absence prevents axonal degeneration and perinatal lethality in mouse neurons upon axotomy (Gerdts et al., 2013), and that this absence has benefits over the WLD^S, as Sarm1 KO mice offer higher long-term axonal protection (Gilley et al., 2017). Indeed, SARM1 deficiency is able to rescue the extreme mouse $NMNAT2^{ko/ko}$ phenotype for several months (Gilley et al., 2015).

1.4.3.2. SARM1 structure and activity

The mouse *Sarm1* gene is located at chromosome 11 and encodes for a protein 724 amino acid long, which shares around 40% identity with its human homologous. *Sarm1* is highly expressed in neurons and macrophages, although it can also be found in other cell types such as astrocytes, hepatocytes, and kidney cells (H. Liu et al., 2021; Mink et al., 2001; Pan & An, 2018). SARM1 protein is formed of different domains: a mitochondrial targeting sequence (MTS), an N-terminal autoinhibitory armadillo/HEAT motif (ARM) domain, two tandem SAM (SAM1-SAM2) regions, a toll/interleukin-1 receptor (TIR) domain, and a C-terminal TIR domain (**Fig. 1.9**). SAM domains constitute the oligomerization sites promoting the assembly of SARM1 in octameric rings (Sporny et al., 2019). Moreover, the MTS positions it in association with the outer membrane of the mitochondria, which seems to be important for its role in microtubule stability and cell death (Kim et al., 2007; Panneerselvam et al., 2012). However, cytosolic SARM1 lacking the MTS triggers equally the degeneration cascade upon axotomy and mitochondrial dysfunction (Gerdts et al., 2013; Summers et al., 2014). Surprisingly, another group has demonstrated the presence in non-neuronal cells *in vitro* of SARM1 in the mitochondrial matrix, a localisation that seems to be necessary to induce apoptosis (Killackey et al., 2019).

Unlike other TLR adaptors, the TIR domain of SARM1 exhibits enzymatic activity (Essuman et al., 2017), for which an interaction with the rest of TIR domains of the octameric ring is required (Horsefield et al., 2019). It presents both ADP-Ribosyl cyclase and glycohydrolase activity, as it converts NAD^+ into cADPR, ADPR and NAM. This NADase activity is necessary to promote a NAD^+ decline and the subsequent axonal degeneration (Essuman et al., 2017). Shortly after that, it was discovered that NAD^+ is able to bind to the ARM domain and mediate self-inhibition (Jiang et al., 2020). Additionally, NMN, the substrate of NMNATs, also acts as a ligand of the ARM domains, a binding that is required to induce SARM1 pro-degenerative activity (di Stefano et al., 2015, 2017). Indeed, SARM1 acts as a metabolic sensor which gets activated by an increased NMN/NAD^+ ratio (Figley et al., 2021). In recent years, new studies have supported this model and shed light on its structural basis (**Fig. 1.9**) (Bratkowski et al., 2020; Loring et al., 2021; Shi et al., 2022; Sporny et al., 2020). In the inactive or "locked" structure, ARM domains directly interact with TIR domains to keep them apart, in a way that the TIR catalytic sites are partially hidden and not fully formed. In this scenario, given that NAD^+ and NMN compete for the same ARM binding site, good levels of NAD^+ maintain the TIR domain locked via NAD^+-ARM binding. However, an increase of NMN/NAD^+ ratio, for example due to NMNAT2 depletion, promotes allosteric activation of SARM1. In the active structure, ARM regions experience a conformational change driven by NMN binding, which frees the TIR domains to self-associate into a two-stranded active assembly now able to bind and consume NAD^+. Per SARM1 octamer, there are up to six catalytically-competent active sites (Shi et al., 2022).

Furthermore, SARM1 can also be inhibited by NAM, which highlights the tight control among metabolites of the NAD savage pathway (Bratkowski et al., 2020), free pyridines, pyridine ribosides and NADP (Angeletti et al., 2022). In fact, this recent study from Angeletti et al., attributes two new enzymatic activities to SARM1: base exchange, catalysing the formation of the calcium release signal NaADP, and NADP hydrolysis and cyclization, to form ADPRP and cADPRP, respectively.

Interestingly and contrary to the belief that SARM1 was inactive under physiological conditions, Sasaki et al., have shown that it has basal activity in brain, sciatic nerve and dorsal root ganglion neurons, being the main producer of the neuronal cADPR in healthy conditions (Sasaki et al., 2020).

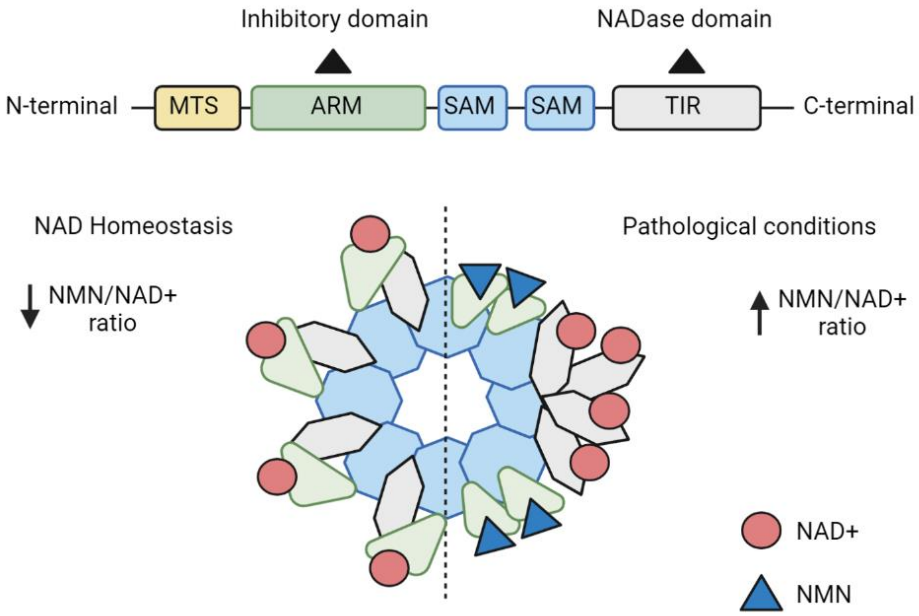

Figure 1.9. SARM1 protein domains, structure and activation mechanism. SARM1 protein is formed of different domains: MTS (mitochondrial targeted sequence), ARM (the armadillo-repeat containing domain), SAMs (two tandem regions) and TIR (toll/interleukin-1 receptor). SARM1 oligomerizes into octameric rings, which are able to change their conformation depending on the NMN/NAD^+ cellular ratio. In presence of good NAD^+ levels, Sarm1 activity is inhibited *via* binding of NAD^+ to the ARM inhibitory regions. Upon injury or damage, NMN binds to the allosteric sites of the ARM domains and triggers a conformational change that exposes the NADase TIR domains to the remaining NAD^+ available. Image created with BioRender 2022 and adapted from (DiAntonio et al., 2021).

1.4.3.3. SARM1-associated axonal degeneration

While Wallerian degeneration (WD) constitutes a concrete axonal program in response to injury, SARM1-associated axonal degeneration has been proven a general mechanism in many disorders characterised by axonal loss (Crawford et al., 2022; Finnegan et al., 2022; Li et al., 2022; Maynard et al., 2020; Viar et al., 2020; White et al., 2019). This process, termed Sarmoptosis (Summers et al., 2014), tightly links NAD^+ metabolism with axonal degeneration via the activation of SARM as the central executioner.

As for WD, the classical accepted model for SARM1-mediated degeneration starts with a decline in NMNAT2 levels (**Fig. 1.10**) (Loring & Thompson, 2020). This depletion leads to reduced levels of NAD^+ and an accumulation of NMN, which subsequently triggers SARM1 activation. Different insults have been associated with a decline in NMNAT2 levels, including

the activation of MAPK signaling (Walker et al., 2017), impaired axonal transport and mitochondrial dysfunction (Loreto et al., 2020). Mitochondria hold a special role within sarmoptosis as it has been found to be both an initiator and a downstream component of the programmed axonal death (Benarroch, 2022). As a trigger, mitochondrial impairment caused by CCCP and rotenone increases oxidative stress and leads to Sarm1-dependent cell death (Hughes et al., 2021; Summers et al., 2014), a process that was also previously shown to be mediated by NMNAT (Press & Milbrandt, 2008). Nonetheless, SARM1 activation can also drive mitochondrial dysfunction due to decreased NAD^+ levels. This is further supported by the fact that deleting SARM1 seems to be beneficial for mitochondrial function (Lai et al., 2022; Murata et al., 2018; Ward et al., 2022).

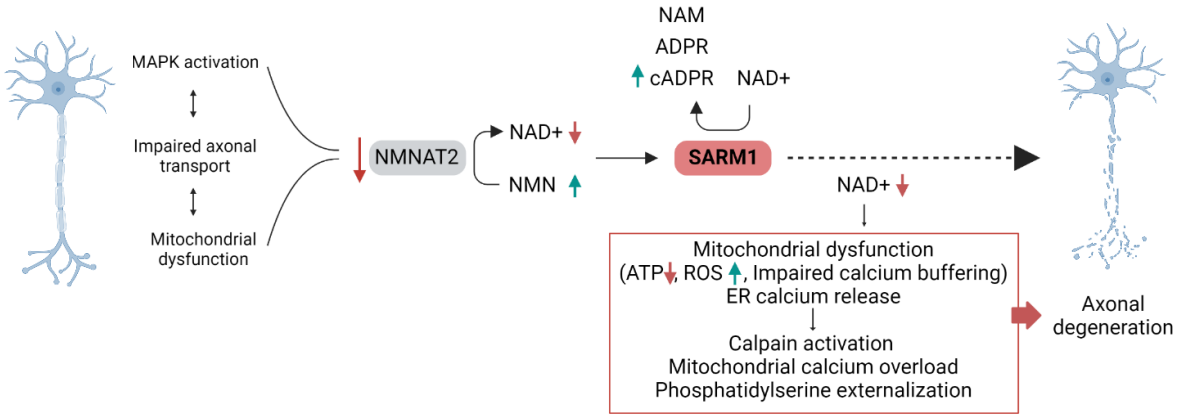

Figure 1.10. Current model for SARM1-mediated axonal degeneration. Image created with BioRender 2022 and adapted from (Ko et al., 2021).

Following the model for sarmoptosis, the activation of SARM1 drastically reduces NAD^+ levels while accumulating cADPR and ADPR. On one hand, as mentioned previously, NAD^+ alteration directly impacts mitochondrial metabolism leading to a decrease in ATP production followed by mitochondrial stalling, depolarization and inability to buffer calcium (Ko et al., 2021). On the other hand, cADPR and ADPR trigger the opening of calcium channels, such as ER ryanodine receptors and the transient receptor potential melastatin 2 (TRPM2), leading to a first wave of intra-axonal calcium (Li et al., 2022; Villegas et al., 2014). A prolonged calcium rise together with ATP loss inhibits membrane flippases, contributing to the externalization of phosphatidylserine and compromising membrane integrity (Ko et al., 2021). Shortly after these events, a final calcium wave takes place which appears to be a determining step precipitating

the axonal fragmentation (Vargas et al., 2015). This disintegration can happen due to two events: an activation of calpains, which break down microtubules and neurofilaments, and a mitochondrial calcium overload with the subsequent mPTP opening (Vargas et al., 2015).

In addition to this non-apoptotic broadly accepted model, SARM1 has also been implicated in other types of cell death. Various studies have demonstrated a role of SARM1 in neuronal (Mukherjee et al., 2015) and T-cell (Panneerselvam et al., 2013) apoptosis, mediated either by TLR7/ TLR9 signaling or Bcl-2 family proteins, respectively. Interestingly, Ko et al., have also shown a link between necroptosis and SARM1 activation (Ko et al., 2020). They propose a noncanonical necroptotic mechanism by which MLKL and RIPK3 factors trigger NMNAT2 depletion and the subsequent SARM1-mediated axonal degeneration.

Surprisingly, a recent study performed in *C. elegans* attributed SARM1 a protective role against mitochondrial-associated axonal degeneration, suggesting that the activation of SARM1 might depend on different environmental factors (Ding et al., 2022). This protective function seems to be mediated by calcium and calmodulin-dependent protein kinase II (CaMKII), whose activation trigger a downstream SARM1/MAPK signaling that suppresses axon degeneration.

2. Aims

Paraplegin deficiency leads to mitochondrial impairments associated with the development of HSP, a neurodegenerative condition characterised by the degeneration of the corticospinal axons. Nonetheless, why paraplegin absence causes such mitochondrial phenotype and axonal degeneration remains an open question. Therefore, this thesis aims to unravel the underlying mechanisms of mitochondrial dysfunction and the subsequent axonal degeneration observed upon paraplegin deficiency.

The specific questions that this thesis addresses are the following:

- ***How does the lack of paraplegin impact mitochondrial function?***

The role of paraplegin has been previously studied by using a *Spg7* KO mouse model. Although these mice recapitulate the motor impairments observed in HSP patients, they show a very late-onset phenotype. Moreover, they still present AFG3L1 and paraplegin-2. Therefore, a new mouse line lacking both paraplegin isoforms and AFG3L1 should be generated and extensively characterised, from behavioural to neuropathological aspects. Moreover, by using affected tissue from this mouse model, I sought to identify key proteins and pathways altered upon paraplegin deficiency and explore their role in the neurodegeneration observed in the HSP pathology. Since ER-targeted paraplegin-2 should be also absent in this DKO model, not only mitochondria but also ER should be assessed.

- ***Is an excess of calcium influx a relevant factor contributing to the HSP pathology?***

It is known that an impaired *m*-AAA protease leads to defects in mitochondrial calcium handling. However, previous studies mainly consider AFG3L2 but not paraplegin. Furthermore, the inability to handle calcium appears to be a factor underlying SCA28 pathology, as treatment with ceftriaxone, an antibiotic promoting the clearance of glutamate from the synaptic cleft, thereby reducing calcium influx, improves the phenotype of *Afg3l2*$^{wt/ko}$ mice. Since AFG3L2 assembles with paraplegin, one goal of this thesis is to identify whether a similar calcium-mediated mechanism is a determining factor in the SPG7-HSP pathology.

- ***Is the lack of paraplegin triggering SARM1-mediated axonal degeneration?***

In recent years, SARM1 activation has been found to mediate the axonal degeneration of many neurodegenerative disorders. However, it has never been investigated in HSP. In order to study this *in vivo*, an additional mouse model lacking all *Sarm1*, *Spg7* and *Afg3l1* genes should be generated. The resultant mouse line should be analysed based on the Spg7/Afg3l1 model characterisation as to determine if a rescue occurs, and if so, as to what extent.

3. Material and Methods

3.1. Generation of mouse lines and husbandry

For the generation of the *Spg7*/*Ag3l1* KO line (DKO), CRISPR-Cas9 technology was applied in *Afg3l1*$^{wt/ko}$ single-cell stage zygotes. In mouse, the *Spg7* gene locates to the qE1 region of the chromosome 8 (Chr8), only 0,4 Mb upstream of the *Afg3l1* gene (**Fig. 4.1, A**). Due to the proximity of these two genes, the obtention of a DKO mouse by crossing the *Spg7* KO and *Afg3l1* KO mice is quite challenging, as it is very unlikely that they recombine during meiosis. Therefore, CRISPR gene-editing system arose as the best tool to easily modify our gene of interest. In collaboration with Simon Tröder from the CECAD *in vivo* facility, gRNAs were designed to target the beginning of the *Spg7* exon 8 creating a frameshift deletion of 86 bp, which disrupts the AAA domain of both paraplegin 1 and paraplegin 2 isoforms (**Fig. 4.1, C**). Furthermore, the mutation was introduced slightly upstream the region where patients frequently present mutations (Klebe et al., 2012; Wilkinson et al., 2004), resembling the human condition. Microinjected zygotes were transferred into pseudopregnant host females to later obtain the first gene-edited mice (founders). Founders (F0) were genotyped, and those which carried both *Spg7* and *Afg3l1* mutations were crossed with *wild-type* (WT) C57BL6/N mice. F1 DKO mice were then selected for sub-cloning analysis (Section 3.3). Although the chosen gRNAs did not show any predicted off-targets in exons of Chr8, F1 mice carrying the desired frameshift mutation were bred with WT C57BL6/N mice for at least two generations prior to analysis (**Fig. 3.1, A**).

Sarm1 *knockout* (Sarm1KO) line, previously described (Kim et al., 2007), was purchased from The Jackson Laboratory (strain #018069, IMSR_JAX:018069). KO mice carry a NEO cassette which disrupts exons 3 to 6 of the *Sarm1* gene. In order to generate a *Spg7/Afg3l1/Sarm1* mouse line, heterozygous *Sarm1* animals were crossed with *Spg7*/*Afg3l1*$^{wt/ko}$ mice. Once *Sarm1*$^{ko/ko}$ *Spg7*/*Afg3l1*$^{wt/ko}$ individuals were obtained, they were bred for the maintenance of the line and for the generation of both Sarm1KO and *Sarm1*$^{ko/ko}$ *Spg7*/*Afg3l1*$^{ko/ko}$ (TKO) mice (**Fig. 3.1, B**). The original Sarm1KO mice were on a C57BL/6N genetic background (Kim et al., 2007), however, at The Jackson Laboratory they were bred with C57BL/6J least once to establish the colony. Upon generation of the TKO mouse line, the mice that were subjected to analysis were on a mixed background: 88% C57BL6/N, 12% C57BL6/J.

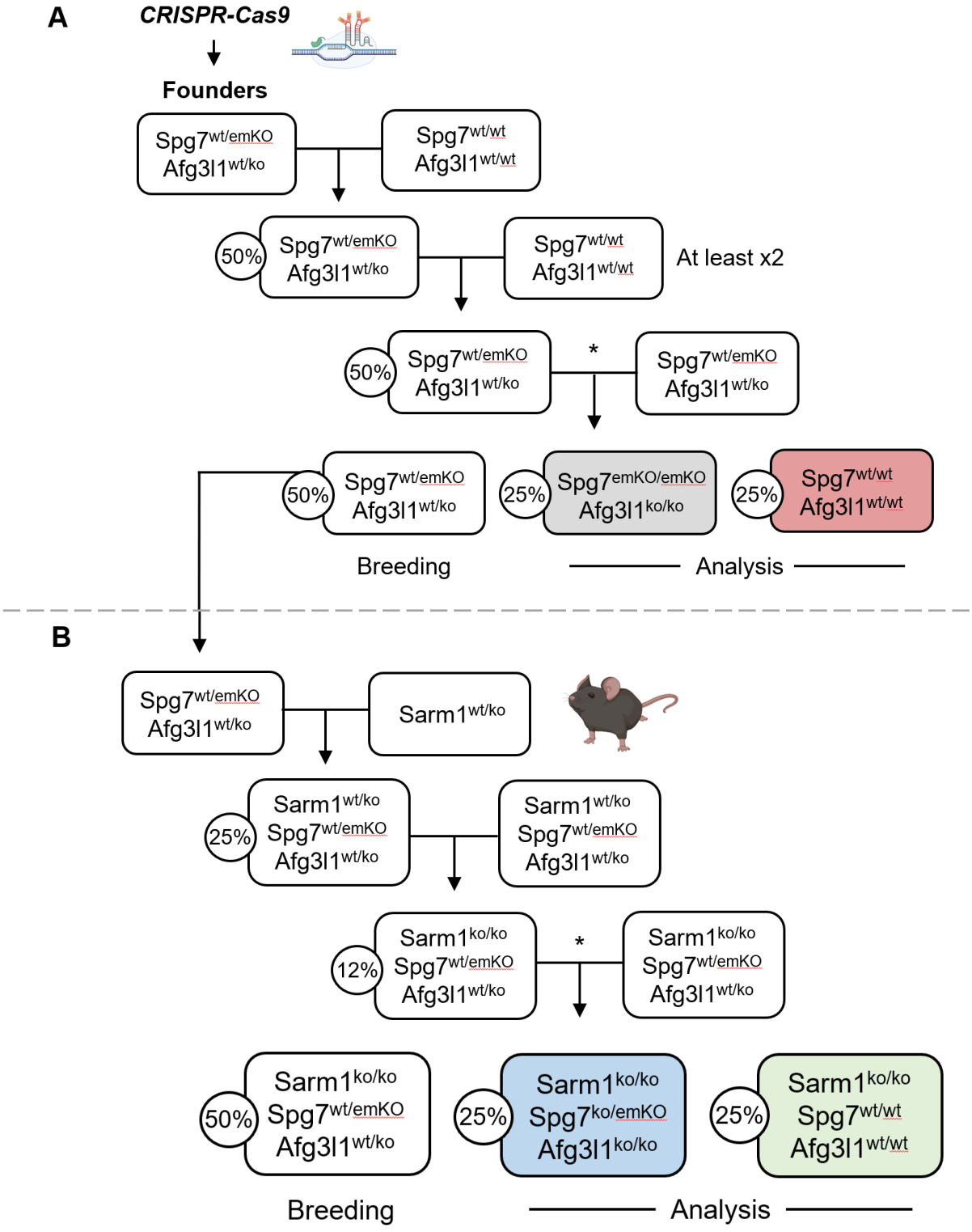

Figure 3.1. Scheme showing the breeding strategies employed in the generation and maintenance of the different mouse lines. (A) Crossings used after performing CRISPR-Cas9 technology to establish the DKO model. (B) Generation of the Sarm1/Spg7/Afg3l1 KO line. Asterisks (*) denote maintenance breedings and the percentage value indicates the probability of a mouse to inherit the specified genotype. Drawings from BioRender 2022.

Animals were kept in ventilated cages within the CECAD *in vivo* research facility, under 12h day/night cycles and with *ab libitum* access to food (V1554, Ssniff Spezialdiäten GmbH) and fresh water. Moreover, mice were closely monitored for signs of distress and motor impairments. All animal studies were approved by the Landesamt für Natur, Umwelt und Verbraucherschutz Nordrhein-Westfalen, Germany (LANUV, license 81-02.04.2019.A115 and 81-02.04.2019.A145), and were carried out following current local and institutional guidelines (Tierschutzgesetz) as well as European regulations (EU directive 86/609/EEC).

3.1.1. Genotyping

3.1.1.1. *DNA extraction*

Mouse DNA from either ear-punches or tails was incubated first in cutting lysis buffer containing 50 mM Tris-HCl (pH 8), 100 mM EDTA (pH 8), 100 mM NaCl, 0,5% SDS and fresh proteinase K (#03115852001, Roche) at 55°C overnight (O/N). The following day, samples were shortly vortex and centrifuged at 10000 g for 10 min at room temperature (RT). The supernatant was transferred to a new tube where cold 100% ethanol was added to precipitate the DNA. Tubes were then inverted 5 to 6 times following 20 minutes of 20000 g centrifugation at 4°C. Afterwards, tubes were washed with cold 70% ethanol and centrifuged for 10 minutes at 15000 g at 4°C. The DNA was resuspended in TE buffer containing 10 mM Tris-HCl (pH 8) and 1 mM EDTA (pH 8), incubated O/N at 55°C with continuous shaking and then stored at 4°C.

3.1.1.2. *PCR and gel electrophoresis*

In order to determine the allele inheritance of the pups, specific DNA regions covering, in particular, *knock-out* mutations, were amplified via the polymerase chain reaction (PCR). Briefly, 0.5 μL of each sample were mixed with 7.5 μL of EmeraldAmp® Master Mix (RR320Q, Takara), 0.2 μM of both reverse and forward primers (**Table 3.1**) and adjusted to 15 μL with autoclaved water. The PCR program specifications are described in **Table 3.2**. In some cases, such as for *Afg3l1*, a forward primer was commonly used for amplifying both WT and KO fragments (to avoid redundancy, only described for WT in **Table 3.1**). PCR samples were then run in 1.5% agarose gels at constant voltage in TAE buffer (1 mM EDTA, 40 mM Tris-HCl and 20 mM acetic acid). As a marker, a 100 bp DNA ladder (Generuler™, Fisher Scientific) was used.

Table 3.1. List of primers used for PCR, with sequences represented from 5' to 3', and the size of the bands of the PCR products.

Name	Forward	Reverse
Spg7	TTCTCCGTTAAATGCTGAGTCCT	CTCCTTGAAGAGGCTTCGCAC
Afg3l1 KO	-	TGGACAGGGCATTATGATGC
Afg31 WT	GCATTGCACAGTCATTTCAGG	GCCGTGGGTAATGTTTGTTCC
Sarm1 KO	-	TGTGGTTTCCAAATGTGTCAG
Sarm1 WT	GAAATGCATGGAGGGGTTG	CCACCAAACGTGTCCAATC

Gene	Band size of PCR products
Spg7	WT: 750 bp; KO: 670 bp
Afg3l1	WT: 250 bp; KO: 500 bp
Sarm1	WT: 302 bp; KO: 248 bp

Table 3.2. **PCR program used for genotyping.**

Temperature	Time	Number of cycles
98°C	10 s	35 cycles
58°C	30 s	
72°C	1 min	
72°C	5 min	
4°C	hold	

3.1.2. Subcloning analysis

PCR was performed as described previously by using extracted mouse DNA and specific forward and reverse primers containing Pst1 and BamHI restriction sites, respectively (**Table 3.3**). DNA was extracted by mixing the PCR products with phenol/chloroform and centrifuging at 10000 g for 3 minutes at 4°C. DNA precipitation occurred after incubating the samples with 1 μL of glycogen, 0.3 M Na-Acetate (pH 5.3) and 100% ethanol. Final mixture was incubated for 10 minutes at 20°C followed by centrifugation at 20000 g for 30 minutes at 4°C. Purified DNA pellet was air dried and resuspended in digest solution containing 2 μL of NE Buffer™ r3.1 (NEB), 1 μL of Pst1 and BamHI restriction enzymes (#140S and #R0136S,

respectively, NEB) and 16 μL of autoclaved water. Plasmid used (pBluescriptKS) was also incubated in parallel with the same solution. Both preparations were incubated at 37°C for 2 hours.

The restricted vector and samples were then run on 1.5% agarose gels with the KO bands excised after clear separation from the WT products. DNA was extracted with Gel Extraction Kit (#740609.250, Macherey-Nagel) according to manufacturer´s instructions.

Ligation step was carried out by gently mixing T4 DNA ligase (M0202, NEB), ligase buffer 10X (B0202, NEB), restricted plasmid and inserts. As control, the plasmid was also incubated with the same solution lacking the DNA inserts. Incubation was performed for 2 hours at RT.

Bacterial transformation took place by using *E. Coli* competent cells. Bacteria was incubated with ligation solution on ice for 30 minutes and heat shocked for 2 minutes at 42°C. After being on ice for 2 minutes, Luria broth (LB) medium was added and samples were centrifuged at 4000 g for 3 minutes with the supernatant carefully discarded afterwards. The pellet was resuspended in the remaining solution and whole samples were spread on LB agar plates containing 100 μg/mL of ampicillin. Plates were incubated O/N at 37°C. On the next day, ca. 2-3 selected bacteria colonies were inoculated into LB-medium with 100 μg/mL of ampicillin and grown O/N at 37°C in continuous shaking. DNAs were later extracted by performing Miniprep according to protocol (#740609.250, Macherey-Nagel). For each sample, DNA was measured using NanoDrop and final preparations were sent for sanger sequencing to Eurofins Genomics. The obtained sequence readouts were processed using the free-available FinchTV 1.5 and Serial Cloner 2.5 software.

Table 3.3. Primers used for subcloning analysis. Restriction sites for the respective enzymes are highlighted in grey.

Name	Sequence 5´to 3´
***Spg7* forward (Pst1)**	ATCTGCAGTTCTCCGTTAAATGCTGAGTCCT
***Spg7* reverse (BamHI)**	ATGGATCCCTCCTTGAAGAGGCTTCGCAC

3.2. Treatment with Ceftriaxone

DKO mice were injected intraperitoneally with either ceftriaxone solution (C5793-1G, Sigma) or vehicle (0.9% w/v saline, control group) for 5 consecutive days at both 16 and 20 weeks of age (**Fig. 3.2**). These specific time points were chosen in order to monitor the capacity of this drug to block or delay axonal degeneration. Before starting each treatment, mice were weighed to adjust the volume of injection to 200 mg/kg/day of ceftriaxone. The same volume was then administer for the control group. All treatments and experiments were performed in blind.

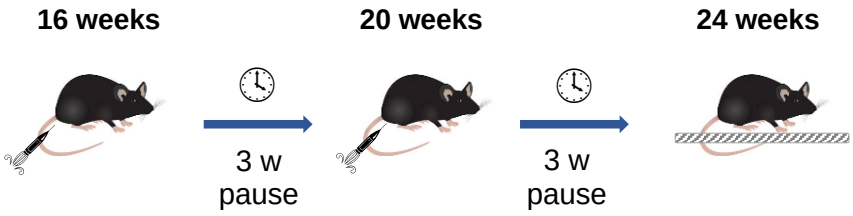

Figure 3.2. Timeline of the ceftriaxone treatment. To assess the effectiveness of this drug in delaying or blocking the motor impairment in this mouse model, behavioural tests were performed three weeks after the last injection.

3.3. Behavioural tests

3.3.1. Rotarod

In order to analyse motor coordination, mice from both DKO and TKO lines were subjected to the Rotarod test. Animals were first acclimated to their cages in the behavioural room for at least 15 minutes prior to the test. Then, mice were trained to balance themselves on top of a rotating rod (TSE systems) for 1-2 minutes at constant speed of 4 rpm. The actual test consisted on three different trials, taking place 15 minutes apart, where the mice had to walk on the rod with a starting speed of 4 rpm and a constant acceleration of 7.2 rpm, up to a maximum of 300 seconds. For each mouse and trial, the latency to fall from the rod was recorded

3.3.2. Walking beam

To assess subtle motor deficits and balance alterations the walking beam was used. The beam set up consists of a 90 cm long beam elevated 30 cm over its fixed platform. During the two training days, after a period of acclimation in the experimental room, animals were

instructed to walk three times across a 3 cm width beam until they reached a little safety box, where they could rest ca. 15 second before starting the next trial. On the third day, each mouse performed the test similarly but crossing a 1 cm beam instead, and their performance during the three trials was recorded. The time to cross and the number of foot slips were quantified.

3.3.3. Foot-base angle

To evaluate gait alterations, a rear view of the mice crossing the walking beam during the training days was recorded. Video sequences were analysed with the Tracker software to select 4-5 frames per mice in which they were seen in defined phases of step cycle. In particular, when the ipsilateral paw was at to-off position with the sole parallel to the beam and the contralateral foot was in a stance position (Fey et al., 2010; Irintchev et al., 2005). The angle formed by the horizontal line and the line dividing the sole into two symmetrical halves was measured in each frame.

3.4. Fat measurements

Total body composition including fat and lean mass was examined with nuclear magnetic resonance (NMR) in the CECAD in vivo animal facility.

3.5. Tissue harvesting

For immunofluorescence or electron microscopy analyses, animals from 16, 28 and 48 weeks of age were sacrificed by transcardial perfusion. They were anesthetized intraperitoneally with ketamine/xylazine at a dose of 20 mg/100 mg per kg of body weight. Once the animals were fully asleep with no toe pinch reflex, the thoracic cavity was open and the heart exposed. A thin needle (18 G, Ecoflo) was inserted in the left ventricle followed by a thin cut in the right atrium to allow the efflux of blood and the systemic circulation of first, phosphate buffer saline (PBS) for 4-5 minutes and then the fixative (4% paraformaldehyde (PFA) in PBS) for another 5 minutes. Afterwards, brain, cerebellum and spinal cord tissues were collected and post-fixed in either 4% PFA in PBS or 2% glutaraldehyde in 0.12 phosphate buffer (PB). Then, tissues were kept at 4°C in 0.12 M PB.

For molecular analysis, mice were euthanized *via* cervical dislocation. Tissues were quickly removed and snap frozen in liquid nitrogen. Then, they were stored at -80°C until analysed.

3.6. Histopathological techniques

3.6.1. Electron microscopy

After 24 hours (cerebellum) or one week (spinal cord) of post-fixation in freshly prepared 2% glutaraldehyde in 0.12 M PB (pH 7.4), samples were dissected and cut into 2-3 mm pieces. They were then immerse in 1% osmium tetroxide (Sigma, #75632) for 5 hours at 4°C in shaking, followed by 10 min dehydration steps in 50-70-90-100% ethanol. Samples were later on incubated with propylene oxide (three times, 10 min each) and embedded in a 1:1 solution of propylene oxide (Sigma, #82320) and epoxy resin (Sigma, #45359-1EA-F) for 24 h. Afterwards, the pieces were included in epoxy resin for 2 days at 60°C. Tissue samples were trimmed with a diamond knife on an ultramicrotome (EM-UC7, Leica) and cut into 900 nm semithin sections, which were stained with 1% toluidine blue in 0.12 PB for light microscopy. Ultrathin sections of 70 nm were then obtained and contrasted with 2% uranyl acetate (Plano GMBH) and a Reynold's solution of 3.52% sodium citrate (Sigma, W302600), 160 mM sodium hydroxide and 2.66% lead citrate (Sigma, #228621). Images were acquired with a JEOL JEM-2100Plus transmission electron microscope and an GATAN OneView 4K camera.

EM quantifications were carried out manually on acquired images (2500X). In spinal cord tissue, the number of axons degenerating were counted in 15 to 25 images per animal, taking up each image a total area of 319 μm^2. The resulting sum was averaged and normalized per 100 μm^2. Between 200 and 400 axons from the anterior areas were counted per mouse to analyse the percentage of axons showing abnormal mitochondria and ER. Axons where no mitochondria of any kind were visible were excluded from the analysis. Male animals were used for all time-points (16, 28 and 48 weeks), whereas females were only analysed at 28 weeks. In the cerebellum, over 100 granule cells were counted per animal to calculate the percentage of cells displaying abnormal mitochondria. Only those cells showing any kind of mitochondria were considered. Moreover, only the cerebellum from males were analysed (16 and 28 weeks).

3.6.2. Immunofluorescence on free floating sections

PFA-fixed samples were placed into silicon molds and embedded in 6% agar (company) in dH_2O. They were left on ice until solidified, after which they were cut with a vibratome (VT1200 S, Leica) into 30 µm sagittal slices. Sections were washed three times in TBS (Tris buffered saline; 20 mM Tris-HCl pH 7.4, 150 mM NaCl) for 10 min, permeabilized and blocked in 10% goat serum and 0.4% Triton X-100 in TBS for 1 h at RT. Primary antibodies (**Table 3.4**) were incubated overnight at 4°C in TBS with 5% goat serum, followed by three additional washes with TBS and a secondary antibody (**Table 3.5**) incubation for 2 h at RT in constant shaking.

DAPI was added in the second wash at a concentration of 1:2000. Stained sections were mounted on slides using Fluorsave medium (345789, Calbiochem). After 24 hours at 4°C, samples were kept at -20°C. Immunofluorescence (IF) images were acquired with a confocal laser microscope (TCS SP8, Leica Microsystems) and visualized using LASX software (Leica) or Fiji (ImageJ).

To quantify the area occupied by GFAP and IBA-1 positive cells in cerebellar vermis and distal spinal cord IF sections of DKO, TKO, and WT, 2-4 images (20X) per section were selected and processed in Fiji. They were similarly thresholded and the particles automatically counted with the Analyze Particles menu command. The resultant area fraction and the average size of all measured particles of the biological replicates (n=4) were then normalized over the control (WT). These IF analyses were only performed in male animals.

Table 3.4. Primary antibodies used for immunofluorescence

Antibody	Company	Catalogue number	Dilution
Calbindin	SWANT	300	1:500
GFAP	Cell signaling	3670	1:1000
IBA-1	Wako	019-19741	1:2000
NMNAT2	Santa Cruz	sc-515206	1:800
SMI31	BioLegend	801601	1:500

Table 3.5. Secondary antibodies employed for immunofluorescence

Antibody	Company	Catalogue number	Dilution
Alexa Fluor 488 α-mouse	Molecular Probes	A-11029	1:1000
Alexa Fluor 546 α-rabbit	Molecular Probes	A-21143	1:1000

3.7. Molecular analyses

3.7.1. Lysate preparation and Western blot

Cerebella and spinal cord frozen tissues were transferred into a 15 cm^2 Potter homogeniser (Sartorius) on ice and lysed in RIPA buffer (50 mM Tris–HCl pH 7.4, 5 mM EDTA, 150 mM NaCl, 1% sodium deoxycholate, 1% Triton X-100, 0.1% SDS) provided with fresh protease inhibitor (P2714, Sigma). Afterwards, samples were kept for 30 min on ice and centrifuged at 20 000g for 30 min at 4°C. The Bradford assay (Bio-Rad Laboratories) was performed to determine protein concentrations. Eighty grams of proteins were mixed with RIPA and Laemmli

sample buffer (Bio-Rad), boiled for 5 min and resolved in 10-15% sodium dodecyl sulphate polyacrylamide gel electrophoresis (SDS-PAGE) gels in running buffer (0.1% SDS, 25 mM Tris, 192 µM glycine) at constant current of 20 mA per gel. To identify protein band sizes, a protein marker was also loaded (PageRuler™ Plus Prestained Protein ladder, Thermo Fisher Scientific). Gel proteins were transferred onto PVDF membranes (GE Healthcare), previously activated with pure methanol, by wet transfer in blotting buffer (25 mM Tris, 192 µM glycine and 20% methanol) at a constant current of 300 mA for 90 min at 4°C. As a control for the transfer, membranes were incubated with Ponceau solution (0.1% Ponceau S and 5% acetic acid). Ponceau was then washed by reactivating the membrane first with methanol, followed by quick washes in TBS-T (0.1% of Tween 20 in TBS). Membranes were blocked with 5% non-fat milk in TBS-T for 30 min at RT, after which they were incubated with primary antibodies (**Table 3.6**) diluted in either 5% BSA or 5% milk in TBS-T at 4°C either for 4 h or O/N. Afterwards, membranes were washed with TBS-T three times for 10 min and placed in secondary antibodies (**Table 3.7**) diluted in 5% milk in TBS-T for 2 h at RT. After three 10 min washes in TBS-T, the antibody signal was detected by incubating the membranes with enhanced chemiluminescent (ECL) reagent (GE Healthcare) and developing them using X-ray films (FUJIFILM) in the dark. Quantification of western blot results was performed using select and plot lanes commands of Fiji.

Table 3.6. List of primary antibodies used for Western blot.

Antibody	Company	Catalogue number	Dilution
Paraplegin	Homemade, Rugarli lab	(Ferreirinha et al., 2004)	1:500
UQCC1	Thermo Fisher Scientific	PA5-57087	1:1000
UQCC2/MNF1	Thermo Fisher Scientific	PA5-97321	1:1000
MKK4/SEK1	Cell signaling	9156	1:1000
pMKK4/pSEK1	Cell signaling	9156	1:1000
JNK/SAPK	Millipore	06-748	1:1000
pJNK/SAPK	Cell signaling	9251	1:1000
GAPDH	Millipore	MAB374	1:1000
ACTIN	Milipore	MAB1501	1:1000

Table 3.7. List of secondary antibodies employed for Western blot

Antibody	Company	Catalogue number	Dilution
HRP linked α-rabbit IgG	Sigma-Aldrich	A0545	1:10000
HRP linked α-mouse IgG	Sigma-Aldrich	A9044	1:20000

3.7.2. Metabolites measurements (performed by Susanne Brodesser)

Levels of cADPR, NAD^+ and NADH in mouse spinal cord and cerebellum were determined at the CECAD Lipidomics/Metabolomics Facility (University of Cologne, Germany) by Liquid Chromatography coupled to Electrospray Ionization Tandem Mass Spectrometry (LC-ESI-MS/MS) using a QTRAP 6500 triple quadrupole/linear ion trap mass spectrometer (SCIEX) coupled to a Nexera X2 UHPLC System (Shimadzu).

3.8. Multi-omic analyses

3.8.1. Transcriptomics

RNA isolation was performed in frozen DKO and WT mouse spinal cord using TRIzol (Thermo Fisher Scientific). Tissue were homogenized in a hand homogenizer on ice and incubated at RT for 5 min. 200 μL of chloroform was then added to each sample, which were mixed by inverting and incubated at RT for 3 min. Following centrifugation at 12000 g for 15 min at 4°C, the aqueous phase was transferred to a new tube together with 500 μL of isopropanol. After a 10-min incubation at RT, samples were centrifuged at 12000 g for 10 min at 4°C. Supernatant was then removed and the RNA pellet washed with 75% EtOH by centrifuging at 12000 g for 5 min at 4°C. After the resulting pellet was air dried, samples were dissolved in nuclease-free H_2O and incubated at 55°C for 10 min. For each sample, the concentration of RNA was measured using NanoDrop.

RNA sequencing (Poly A+ selection) was carried out by Janine Altmüller and Christian Becker from the Cologne Center for Genomics (CCG). Samples were prepared according to the CCG preparation guide for Next Generation Sequencing, with a final RNA concentration of 150 ng/μL, and sequenced with 35 million reads per sample by Illumina paired-end sequencing. The results were analysed by Alexander Dilthey from the CECAD bioinformatic facility (University of Cologne, Germany) using the QuickNGS system (Wagle et al., 2015).

3.8.2. Proteomics (performed by Hendrik Nolte)

3.8.2.1. Protein digestion

For lysis, 4% SDS in 100 mM HEPES pH 8.5 was used in a Percellys 24 homogenizer and the protein concentration was determined. A total of 20 µg of protein was subjected for tryptic digestion. Proteins were reduced (10 mM TCEP) and alkylated (20 mM CAA) in the dark for 45 min at 45°C. Samples were subjected to SP3 based digestion (Hughes et al., 2014). Washed SP3 beads (SP3 beads (Sera-Mag (TM) Magnetic Carboxylate Modified Particles (Hydrophobic), Sera-Mag (TM) Magnetic Carboxylate Modified Particles (Hydrophylic) from

Thermo Fisher Scientific) were mixed equally, and 3 µL of bead slurry were added to each sample. Acetonitrile was added to a final concentration of 50% and washed twice using 70 % ethanol (V=200 µL) on an in-house made magnet. After an additional acetonitrile wash (V=200 µL), 5 µL digestion solution (10 mM HEPES pH 8.5 containing 0.5 µg Trypsin (Sigma) and 0.5µg LysC (Wako)) was added to each sample and incubated overnight at 37°C. Peptides were desalted on a magnet using 2 x 200 µL acetonitrile. Peptides were eluted in 10 µL 5% DMSO in LC-MS water (Sigma Aldrich) in an ultrasonic bath for 10 min. Formic acid and acetonitrile were added to a final concentration of 2.5% and 2%, respectively. Samples were frozen until subjected to LC-MS/MS analysis.

3.8.2.2. Liquid Chromatography and Mass Spectrometry

LC-MS/MS instrumentation consisted of an Easy-LC 1200 (Thermo Fisher Scientific) coupled via a nano-electrospray ionization source to an Exploris 480 mass spectrometer (Thermo Fisher Scientific). For peptide separation an in-house packed column (inner diameter: 75 µm, length: 40 cm) was used. A binary buffer system (A: 0.1 % formic acid and B: 0.1 % formic acid in 80% acetonitrile) was applied to achieve 95 min total gradient length as follows: Linear increase of buffer B from 4% to 27% within 69 min, followed by a linear increase to 45% within 5 min. The buffer B content was further ramped to 65 % within 5 min and then to 95 % within 6 min. 95 % buffer B was kept for further 10 min to wash the column. Prior each sample, the column was washed using 5 µL buffer A and the sample was loaded using 8 µL buffer A.

For MS spectra acquisition, the RF Lens amplitude was set to 55%, the capillary temperature was 275°C and the polarity was set to positive. MS1 profile spectra were acquired using a resolution of 60,000 (at 200 m/z) at a mass range 320 - 1150 m/z and an AGC target of 1 × 106. For MS/MS independent spectra acquisition, 48 windows were acquired at an isolation m/z range of 15 Th and the isolation windows overlapped by 1 Th. The fixed first mass was to 200. The isolation center range covered a mass range of 350 – 1065 m/z. Fragmentation spectra were acquired at a resolution of 15,000 at 200 m/z using a maximal injection time of 22 ms and stepped normalized collision energies (NCE) of 26, 28, 30. The default charge state was set to 3. The AGC target was set to 900%. MS2 spectra were acquired as centroid spectra.

3.8.2.3. Data analysis

For the analysis of DIA (Data independent acquisition), we utilized DIA-NN version 1.8 (Demichev et al., 2020). The library-free approach was used based on the mouse uniport (Mus musculus) reference proteome which predicts MS2 spectra using neuronal network. The deep-

learning option was enabled. Quantification strategy was set to ‘robust LC (high accuracy)’. The precursor range was adjusted to 330 – 1200 m/z. The RT profiling option was enabled. Otherwise, default settings were used. To identify significantly different proteins, a two-sided t-test was applied. The FDR was controlled to 5% using a permutation-based approach in the Perseus software (Tyanova et al., 2016).

3.8.3. Pathway analyses

Pathway enrichment of 16 weeks proteomics was carried out by Hendrik Nolte using the Gene Ontology (GO) data base for cellular components (CC), molecular function (MF) and biological processes (BP). Analyses of the pathways of 28 week proteomics were performed using STRING network analysis (Szklarczyk et al., 2021) and GSEA software (Mootha et al., 2003; Subramanian et al., 2005). For GSEA processing, proteins (Uniprot IDs) were ranked based on t statistic considering both the fold change and the *P* value. Reported datasets were defined using the GOBP database with categories considered significant at q value < 0.2. Enrichr was used for transcriptomic pathway analysis (Chen et al., 2013; Kuleshov et al., 2016; Xie et al., 2021).

3.9. Statistical analyses

Statistical analysis were carried out using GraphPad Prism v.8.0.2. Unpaired Student’s t-test analyses were performed for two group comparisons. For comparisons with more than two genotypes, one-way ANOVA followed by a Tukey’s post-hoc test was applied to data sets and two-way ANOVA or mixed ANOVA analysis to define significant curves (behavioural tests). Statistical values are indicated in the respective graphs when statistically significant.

4. Results

4.1. The DKO mouse model exhibits a worsening of the HSP-like phenotype

The function of paraplegin was previously investigated by employing a *Spg7* KO mouse model. However, these mice present few disadvantages, such as the presence of paraplegin-2 and AFG3L1, and a very late-onset phenotype. Therefore, to recapitulate more accurately the human HSP pathology, a *Spg7*/*Afg3l1* KO (hereon referred to as DKO) mouse line was generated. For that, CRISPR-Cas9 technology was applied, which targeted the *Spg7* gene in an *Afg3l1* KO background (pure C57BL/6N). The induced mutation consisted of a 86 bp deletion at the beginning of the *Spg7* exon 8 (**Fig. 4.1, A**). To investigate whether this deletion was successfully created in the DKO mice, the first generation of DKO mice was genotyped, and those carrying both *Afg3l1* and *Spg7* KO alleles selected for sub-cloning analysis (**Fig. 4.2, A**). I performed alignment analysis with the final DKO sequence readouts and a complementary *wild-type* (WT) sequence, where I could see that DKO mice presented indeed the desired mutation (**Fig. 4.1, B**). Moreover, in order to see to what extend this mutation affects the domains of paraplegin, I also aligned DKO-WT protein sequences. The mutation leads to a frameshift after V341, which results in a premature STOP codon affecting both the AAA and the peptidase domain (**Fig. 4.1, C**). Although both domains are required for oligomer assembly and therefore, to form functional complexes, a truncated protein fragment might still be present. To check this, I performed western blot analysis with a polyclonal paraplegin antibody that detects epitopes before the deletion (raised against amino acids 50-397 of the mouse protein, Ferreirinha et al., 2004). No band was detected for DKO mice at any height, indicating that paraplegin protein was successfully removed with no truncated fragments present (**Fig. 4.2, B**).

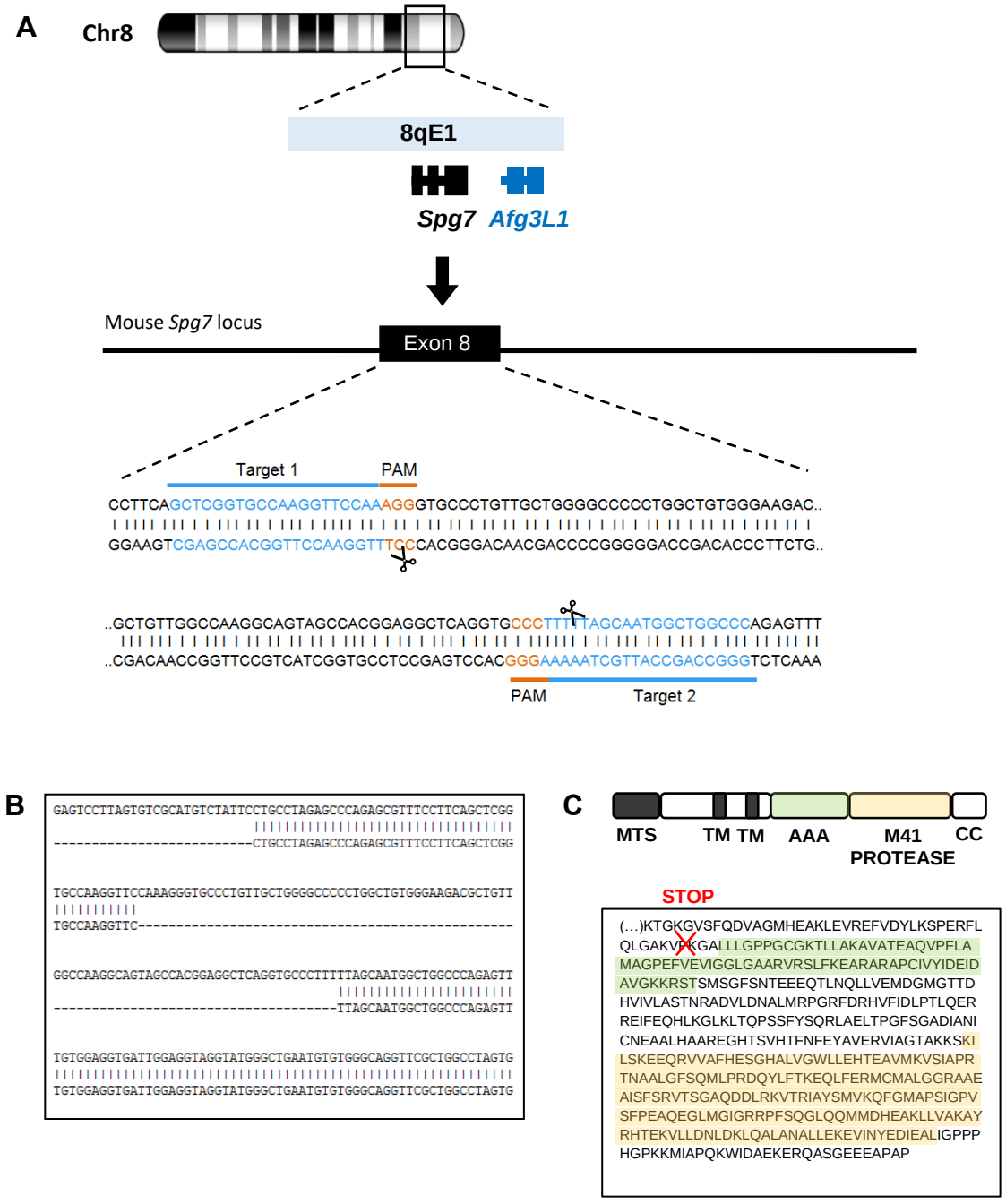

Figure 4.1. Schematic representation of deletion induced in the *Spg7* locus. (A) Within the mouse genome, *Spg7* appears to be in the 8th chromosome, only 0,4 Mb upstream of *Afg3l1*. CRISPR-Cas9 technology was used in *Afg3l1* KO zygotes to generate the DKO mouse model, targeting a specific sequence within the exon 8 of *Spg7*. (B) Alignment analysis of the WT-DKO DNA sequence to confirm the 86 bp deletion. (C) Paraplegin domains and protein sequence, indicating how the mutation affects both the AAA domain of the mitochondrial protease (green) and the proteolytic center (yellow). MTS: mitochondrial targeting sequence, TM: transmembrane domain, AAA: ATPase domain, CC: C-terminal, PAM: protospacer adjacent motif. Chromosome drawing from U.S. NIH webpage.

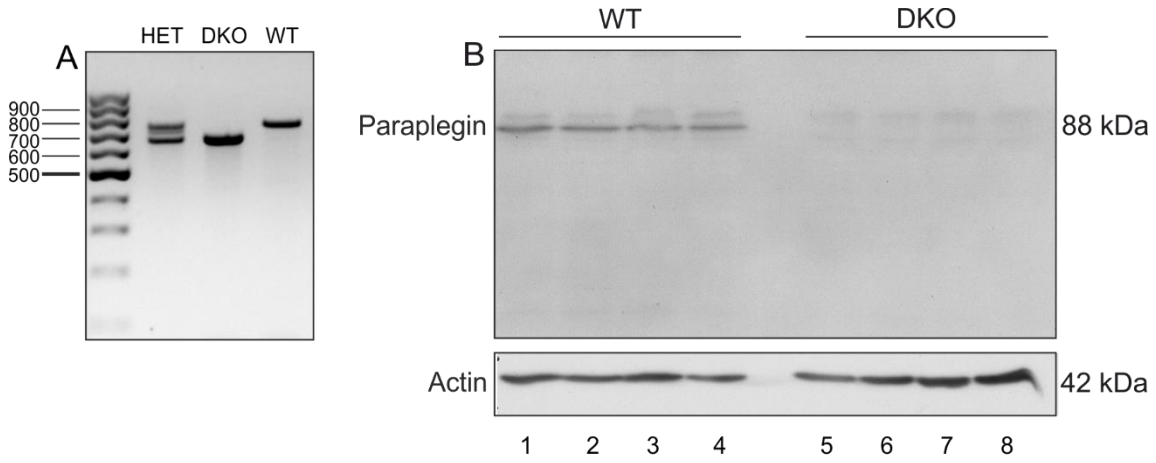

Figure 4.2. *Spg7* was successfully mutated with no paraplegin protein present in DKO mice. (A) Genotyping results from heterozygous animals (HET, two bands of 750 and 670 bp), DKO (only lower band) and WT (only upper band). (B) Western blot analysis of cerebellar lysates confirming the absence of paraplegin in DKO animals, with actin used as loading control (n=4 per genotype).

4.1.1. DKO mice display early weight reduction and motor deficits

Previously-developed *Spg7* KO mice display a late onset phenotype, with an inability to gain weight from 12 months of age and kyphosis at 17 months (Ferreirinha et al., 2004). In order to see whether the newly-generated DKO model showed these phenotypic characteristics at earlier time-points, I closely monitored physical and weight changes since the first month of age in WT and DKO littermates. Despite the fact that young DKO males are physically indistinguishable from their WT controls, they showed a significant body weight reduction at 4 weeks of age (**Fig. 4.3, B**). Between 2 and 4 months of age, however, their weight briefly matched that of the WT littermates, after which they exhibited a permanent inability to gain weight (**Fig. 4.3, A**). Although DKO females did not present significant differences in body weight during the first months, they also exhibited a significant body weight reduction from 4 months on (**Fig. 4.3, C-D**). Despite weighing less, DKO males exhibited a similar cerebellar weight to the WT control (**Fig. 4.3, E**), which resulted in a higher cerebellum-to-body weight ratio in DKO males at 28 weeks (**Fig. 4.3, F**). Moreover, DKO mice also presented a similar body composition to the WT animals, as they did not present significant changes in relative fat and lean body mass (**Fig. 4.3, E-F**). Furthermore, both DKO males and females presented a distinctive kyphosis prominent at 28 weeks, earlier than the previous *Spg7* KO mice.

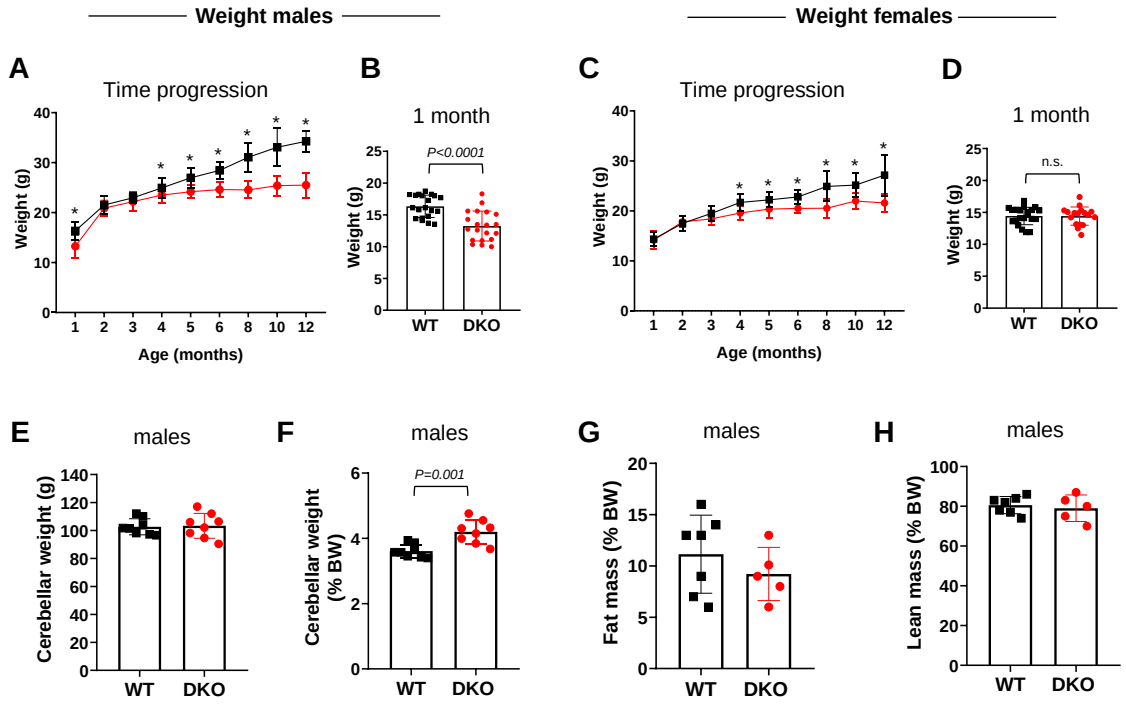

Figure 4.3. Body weight alterations induced by the loss of paraplegin and AFG3L1. (A, C) Analysis of weight with n=20 males per genotype and n=14-20 females per genotype and age. Data represent mean ± SD. Asterisks indicate significance with Student´s t-test (*P* value < 0.05). (B, D) body weight at one month of age extracted from progression graph A and C. Each dot represent one animal. (E) Males cerebellar weight at 28 weeks. (F) Same cerebellar weight as in E but represented as percentage of body weight; mean ± SD. *P* value from Student's t-test. (G-H) Fat and lean masses of males at 28 weeks. Represented values in are expressed as percentage of body weight; mean ± SD. No significant difference was observed by Student's t-test.

Upon visual inspection, WT littermates appeared to be more fidgety, constantly moving around and inspecting the cage, whereas DKO animals often stayed inside the paper houses and if going around, they would avoid to run and rather move calmly. To assess to what extent these mice have a compromised ability to stand and walk, different behavioural tests were performed at 16, 24 and 32 weeks of age. In order to analyse general motor coordination, WT and DKO mice from both sexes were subjected to the Rotarod test. For that, mice were placed on top of a rotating shaft with constant speed and trained to stand on it walking for at least one minute. After this training period, however, they had to maintain themselves on the rotating rod while it accelerated. In general, WT mice were able to endure ca. two minutes of walking without falling, whereas DKO were falling after approximately one minute. At 16 weeks, these performance differences were already significant in the three trials measured. This decreased latency to fall was also seen at 24 and 32 weeks. Furthermore, males and females behaved

quite similarly, with a slightly worse performance of DKO males at the latest time-point measured (**Fig. 4.4, C-D**).

The walking beam assay was used to study subtle motor impairments, since it has been demonstrated to be a more sensitive tool over the Rotarod test, and particular useful to detect early signs of ataxia (Hoxha et al., 2017; Luong et al., 2011; Stanley et al., 2005). This test consists of a narrow elevated beam, through which mice have to walk until they reach a little cage at the end, where they can rest. After two training days, both the time to cross and the number of foot slips were quantified. In line with the rotarod test results, DKO males and females displayed a gait instability already at 16 months, as represented by longer time to cross the beam (**Fig. 4.4, A-B**) and an increased number of slips (**Suppl. S1, A-B**). These motor deficiencies got slightly bigger over time, reflecting the progressive motor phenotype.

To further investigate these gait alterations, the foot-base angle (FBA), which has been previously demonstrated to be a highly sensitive method to detect gait abnormalities in HSP models (Beetz et al., 2013; Khundadze et al., 2013), was measured at 24 weeks of age in males. The FBA was calculated for both right and left limbs. However, in order to detect an alteration of the FBA during step cycle and assuming that we do not expect a side-specific impairment, I only considered the hind leg that seemed affected the most for both genotypes. Following this, DKO mice showed a significant increase of the FBA compared to their WT mates (**Fig. 4.4, E, G**). Moreover, frequently their ipsilateral foot reached the maximal plantar flexion before the contralateral foot was firmly placed on the ground, so that when the latter occurred, their soles were more visible than those from WT mice at the same step cycle (**Fig. 4.4, G red line**). To quantify that, I measured the length of the sole in this stance position from the ankle to the other visible end, with a line symmetrically dividing the sole into two parts. As for the FBA, the length of the visible sole was significantly higher for DKO mice than for the respective WT controls (**Fig. 4.4, F-G red line**).

Altogether, these behavioural findings point towards a motor deficient phenotype with hindered gait, balance, coordination, and fine movement control skills, which, similarly to human HSP patients, get progressively worse over time.

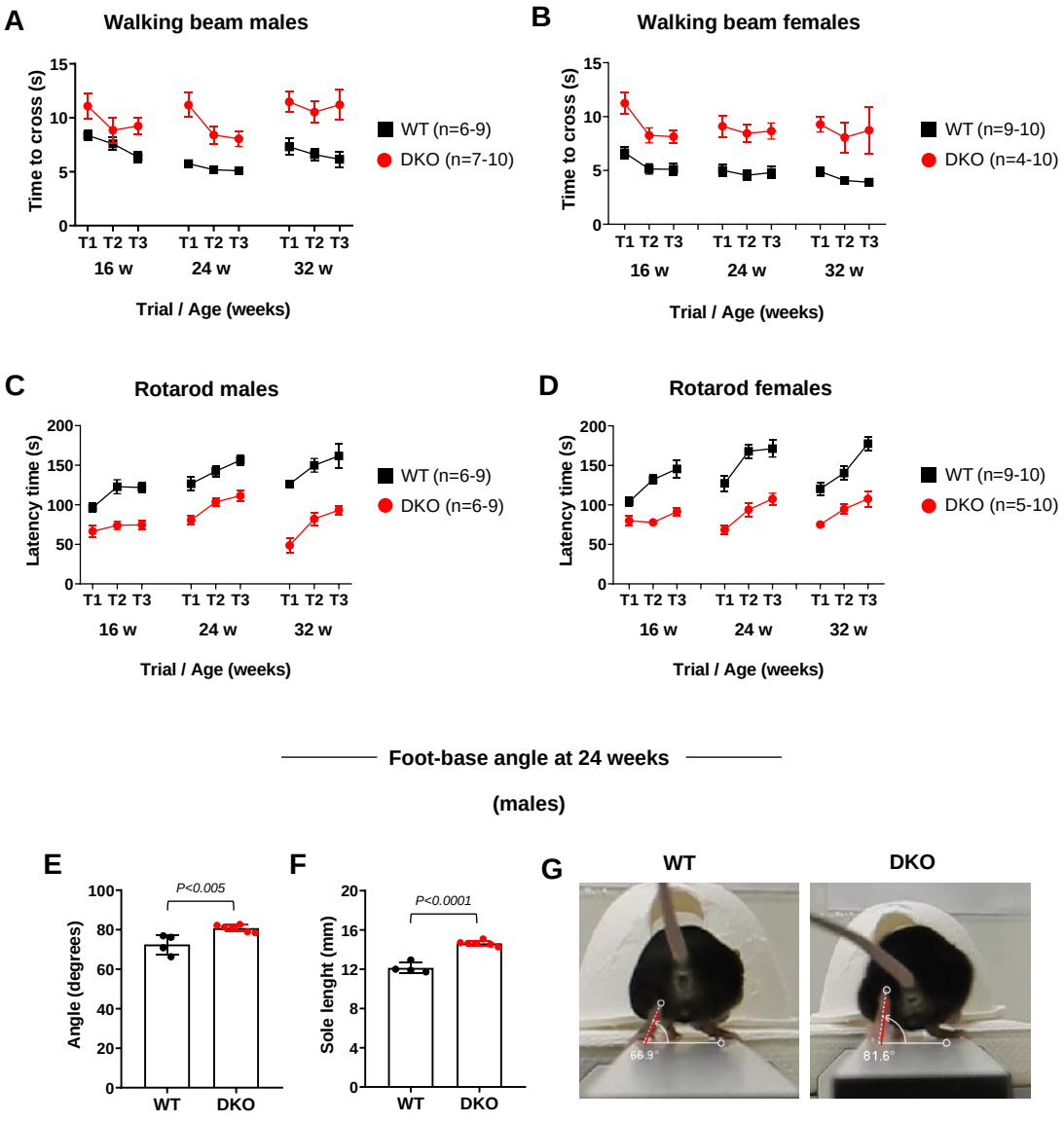

Figure 4.4. The loss of paraplegin and AFG3L1 causes unbalance, gait alterations and incoordination. (A-B) Analysis of motor abilities by testing their time to cross the walking beam or (C-D) their latency to fall in the rotarod test. Three consecutive trials (T) were performed at the different time points. Data represent mean ± SEM. The number of animals appears indicated in the legend, for each genotype and time points. Mixed model test was performed for each time point ($p<0.0001$). Gait analysis were carried out by measuring (E) the FBA and (F) sole length in the stance position. Each dot represent one mouse (WT n=4, DKO n=6). Data shown as mean ± SD. *P* value from Student's t-test. (G) Representative video frames of WT and DKO mice while crossing the walking beam. Red lines indicate the sole length quantified in F.

4.1.2. A deficiency of paraplegin and AFG3L1 leads to an accumulation of abnormal mitochondria and axonal degeneration in spinal cord

Impairments in the *m*-AAA protease subunits are known to be associated with abnormal mitochondrial morphology and altered cristae distribution (Ferreirinha et al., 2004; Murru et al., 2019; Richter et al., 2019). Moreover, previous paraplegin-deficient mice showed a delay of neuronal retrograde transport, suggesting that mitochondria might not be efficiently transported back to the soma to be recycled (Ferreirinha et al., 2004). These neuropathological marks together with the fact that DKO mice display motor deficits, prompted me to investigate ultrastructural changes in the lumbar spinal cord of the recently-generated DKO mouse model by electron microscopy (EM). EM is a widely used technique to visualize high resolution images of samples in the range of micro- and nanometres, which is very convenient to obtain detail information of cellular organelles such as mitochondria. Sample processing for EM requires several steps involving the embedding of the tissue in resin and later cutting of the samples with a ultramicrotome. In a first step, semithin sections with a thickness of 900 nm are obtained and analysed with a light microscope to have a first impression of the quality of the tissue. Semithin sections of lumbar spinal cord of DKO males were very comparable to WT at 16 and 28 weeks. However, at 48 weeks many degenerating axons appeared close to the ventral median fissure and peripherally in anterior areas of the white matter (**Fig. 4.5, A, B arrows**). There, different descending tracts are located such as vestibulospinal and corticospinal fibers which carry motor information but also ascending tracts, such as the spinothalamic and spinocerebellar fibers, both carrying sensory information (Sengul & Watson, 2012).

Last step in the EM procedure is the preparation of ultrathin sections (70 nm) with which the samples are observed by a transmission electron microscope. Surprisingly, already at 16 weeks many abnormal mitochondria were present in lumbar DKO spinal cord compared to WT samples, particularly in the antero-medial areas previously mentioned (**Fig. 4.5, C-D**). These mitochondria showed a different range of impairments, from slightly disorganized cristae, occasionally swollen, to mitochondria with cristae displaced at the periphery of the organelle sometimes hardly identifiable. At 28 weeks, the percentage of axons that displayed these mitochondrial abnormalities (**Fig. 4.5, H**) as well as the percentage of axons that accumulate material inside and degenerate (**Fig. 4.5, I**) significantly increased. These changes were not only observed in males but also in females to the same extend (**Suppl. S2, B-D**), but they were not present in AFG3L1 KO mice (**Suppl. S2, A, C-E**). The difference between WT and DKO mice became quite remarkable at 48 weeks, when almost 50% of axons analysed in the anterior spinal cord accumulated these abnormal organelles. The fact that these altered mitochondria get stuck there suggest a problem in mitophagy and/or mitochondrial transport (**Fig. 4.5, D arrows**).

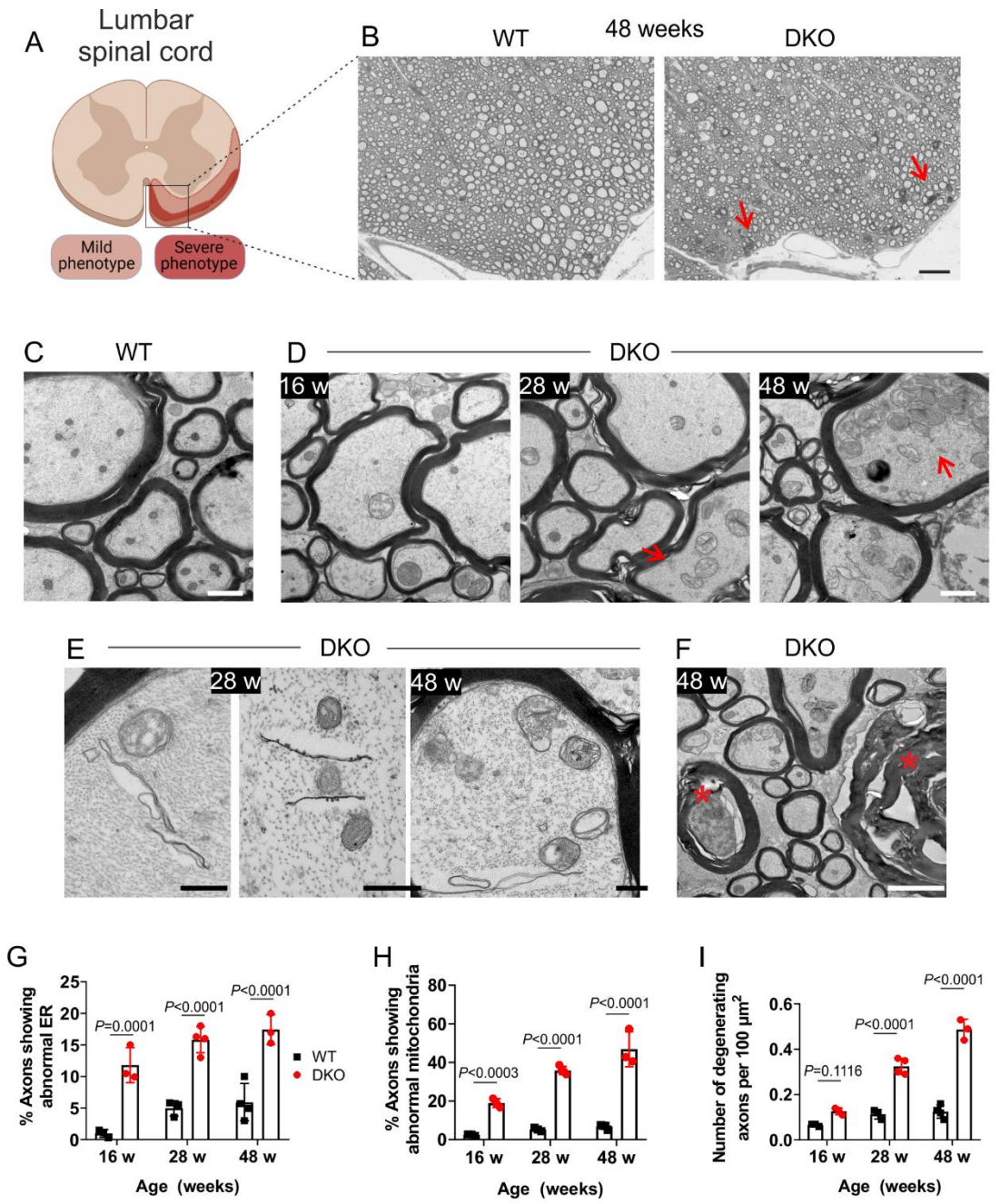

Figure 4.5. DKO mice show altered mitochondria and ER structures together with axonal degeneration in anterior tracts of the spinal cord. (A) Spinal cord drawing indicating the affected areas in DKO animals. Created with BioRender. (B) Representative semithin sections highlighting the loss of big-diameter axons and the axonal degeneration (black dots) in DKO samples at 48 weeks. (C) EM image from WT spinal cord at 28 weeks. (D) Electron micrographs showing the time progression of the mitochondrial phenotype leading to stuck mitochondria in affected distal axons (arrows). (E) Transverse ER structures very distinguishable in spinal cord tracts at 28 and 48 weeks, which also appear in a time-dependent manner. (F) EM images of DKO mice at 48 weeks showing prominent axonal degeneration (asterisks). (G) Quantification of the percentages of axons showing abnormal ER over time. (H) Quantification of the percentages of axons displaying abnormal mitochondria. Between 200 to 400 axons were counted per mouse in G and H analysis. (I) Number of degenerating axons per 100 µm^2. Data represented in graphs as mean ± SD, with each dot being one mouse, all males (n=3-4 per genotype). Student's t-test performed for significance. Scale bar: 20 µm in B, 1 µm in C-D, 0.5 µm in E and 2 µm in F.

Unexpectedly, the same axonal fibers also presented from 16 weeks on, long, swollen one-membrane structures which resemble impaired ER (**Fig. 4.5, E-G**). As for mitochondria, axons presenting these abnormal structures were more frequent at late stages. Moreover, as observed in the semithin sections, these impaired fibers appeared mostly peripherally and to a less extend in inner areas of the anterior white matter.

All these semithin and ultrathin sample analysis indicate that, in line with the motor phenotype observed, these mice present an affectation of anterior spinal cord motor tracts, with a possible involvement of sensorial innervations, which displayed not only abnormal mitochondria but also long transverse structures resembling the endoplasmic reticulum.

4.1.3. Cerebellar tissue is also affected upon paraplegin absence

An impairment of limb movements may also be a consequence of cerebellar damage. In fact, many SPG7-HSP patients very often present ataxic symptoms, which is not surprising given that *SGP7* is highly expressed in this tissue (GTEx Human brain dataset). Similarly, *Spg7* mouse gene is also quite expressed in cerebellar cells (Martinelli et al., 2009; Sacco et al., 2010). However, cerebellar tissue integrity was never studied in paraplegin-deficient mice. Therefore, to investigate the contribution of cerebellar impairment to the phenotype observed in DKO mice, 16, 28 and 48 week old cerebellar samples were processed and observed by EM.

DKO cerebellum general structure observed in the semithin sections was indistinguishable from WT samples, with well-structured and easy-to-differentiate cerebellar layers (**Fig. 4.6, A-B**). In the ultrathin sections, the cellular network of Purkinje cells (PC) seemed similar to wild type (**Fig. 4.6, C, D arrows**), with an exception of few slightly abnormal mitochondria appearing in dendritic ramifications at 48 weeks of age (**Fig. 4.6, D**). Next to this dendrites in the molecular layer (ML), however, some altered mitochondria appeared scattered through the layer at 28 weeks, which were characterised by a loss of electron density and rounded cristae (**Fig. 4.6, D arrowhead**). More strikingly, already at 16 weeks, granule cells (**Fig. 4.6, E**) and several fibers of the cerebellar white matter (**Fig. 4.6, F**) showed hypertrophic mitochondria with disorganized cristae (**Fig. 4.6, G**). At 28 weeks, approximately 40% of the granule neurons displayed these mitochondria with altered morphology, suggesting also a progressive cerebellar impairment over time (**Fig. 4.6, H**). Furthermore, at this time-point, a few axons degenerating were spotted within the DKO cerebellar fibers (**Fig. 4.6, F asterisk**).

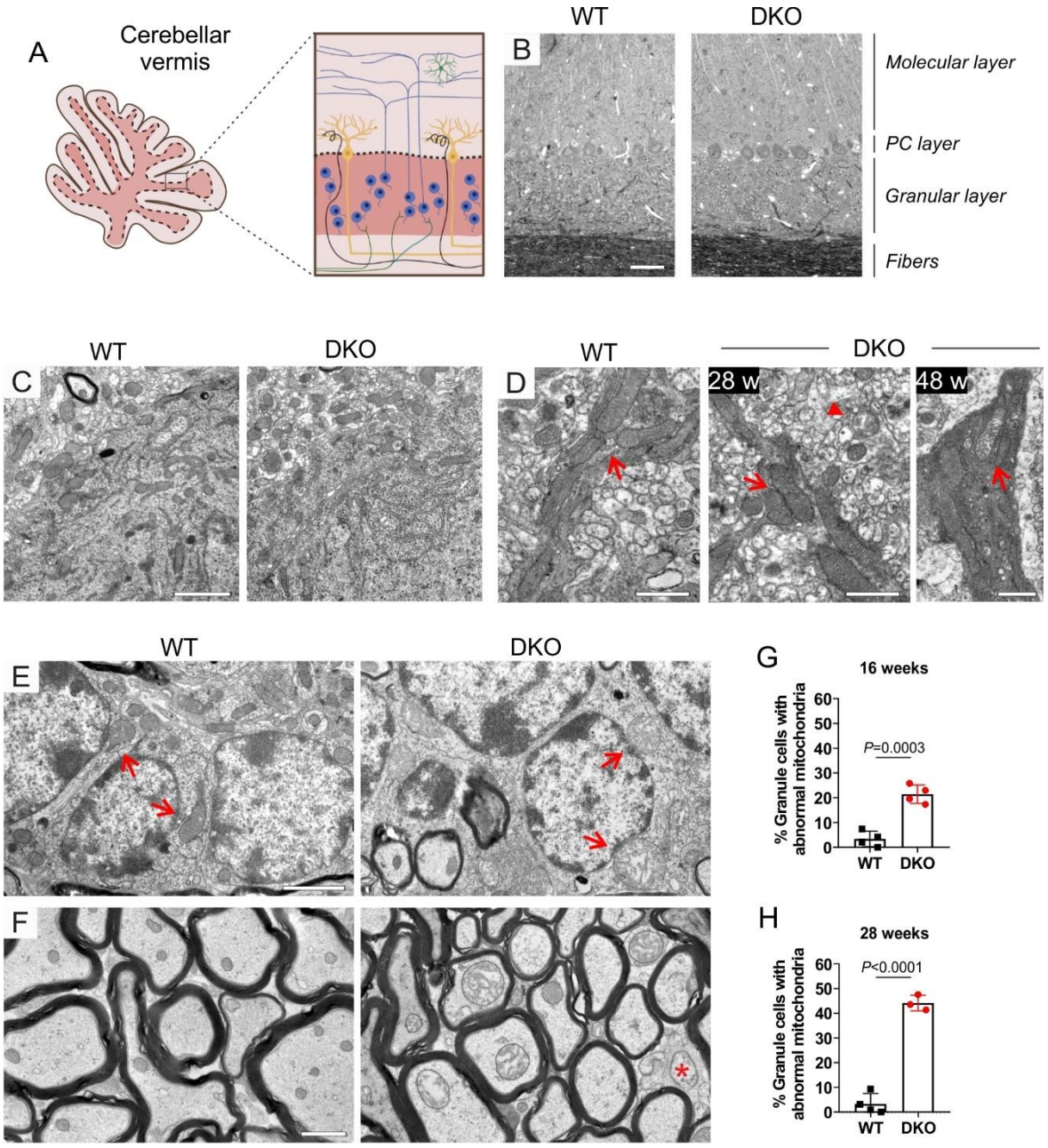

Figure 4.6. Cerebellar ultrastructural analysis reveal many abnormal mitochondria in granule cells and axonal fibers. (A) Cerebellar scheme of the different tissue layers (PCs in yellow, granule cells in blue, mossy fibers in green, climbing fibers in black) as a reference for WT and DKO semithin sections from the same region (B). Drawing created with BioRender. (C) Ultrathin sections of PC soma and (D) dendrites in the ML with mitochondrial network indicated with arrows. Arrowhead in D highlights the presence of abnormal mitochondria along the ML. (E) Electron micrographs of granule cells and (F) axonal fibers (mitochondria indicated by arrows; axonal degeneration with an asterisk). (G-H) Quantification of granule cells showing abnormal mitochondria at 16 and 28 weeks, correspondingly. Over 100 granule cells were counted per animal. All images and data come from male animals. Data indicated by mean ± SD, with each dot being one male (n=3-4 per genotype). Student's t-test performed for significance. Scale bar: 40 µm in B, 2 µm in C-E, and 1 µm in D-F.

To complement this analysis, PCs were stained with calbindin D28k, a calcium-binding protein highly expressed in their cell body and dendrites, to have a qualitative assessment of any pathological alteration. At 28 weeks, DKO animals showed a well-organized PC layer with packed cell bodies and dendrites projected straight towards the ML (**Suppl. S3, A**). This structure was also maintained at 48 weeks in DKO cerebellum, with no difference detected when compared to WT litter controls (**Suppl. S3, B**).

To summarize, DKO mice show a cerebellar phenotype characterized by the presence of abnormal mitochondria in granule cells and axonal fibers of the cerebellar white matter.

4.1.4. Spinal cord and cerebellum exhibit reactive glial cells in DKO mice

Glial cells constitute key components in maintaining brain homeostasis and synaptic transmission, not only by offering structural support and regulating nutrient flux but also by phagocyting pathogens and cellular debris of the extracellular space, regulating ion and metabolite uptake and even removing disused synapses (Allen & Lyons, 2018). Neuronal damage often leads to a pro-inflammatory glial activation, particularly microglia and astrocytes, which aims to protect neurons from the insult by initiating inflammatory responses. During these responses, glial cells are recruited to injury sites, where they adopt characteristic shapes (Stevenson et al., 2020). Astrocytes increase cell size and upregulate the glial fibrillary acidic protein (GFAP), whereas microglia frequently retract their long ramifications to exhibit an ameboid shape. This neuroinflammation has been demonstrated to be crucial in the development of many neurodegenerative diseases (Chitnis & Weiner, 2017). In fact, diverse studies have also revealed a role for glial cells in a subtype of HSP known as SPG2 (Ip et al., 2006; Lüders et al., 2017). Therefore, to investigate the pathogenic implication of neuroinflammation in SPG7-HSP, microglia and astrocytes were analysed by using vibratome free-floating slices from 16 and 28 week old mice.

GFAP staining was used to specifically label astrocytes and was hardly detectable in WT samples from cerebellum or spinal cord. Contrary to this, DKO mice displayed increased levels of GFAP at both time points, mainly in the fibers and granular cell layer of the cerebellum (**Fig 4.7, A, green**) and in the anterior tracts of the spinal cord (**Fig 4.7, B, green**), which correspond to those areas showing abnormal mitochondria and degeneration by EM. Likewise, microglia, labelled with the microglia-specific calcium binding protein IBA-1, presented in WT tissues a nice ramified morphology with small cell bodies, equally distributed across the tissues (**Fig. 4.7 A-B, red).** This shape became thicker in DKO tissues, particularly the cerebellum, with shorter processes and higher number of microglial cells (**Fig. 4.7, A-B, red**). These parameters were also assessed in brain slices containing motor cortex areas, where the soma

of the motor corticospinal neurons are located. There, neither GFAP nor IBA-1 gave a detectable signal in DKO samples (**Fig 4.7, C**), indicating an absence of neuronal damage in these brain regions.

Therefore, an impairment of the *m*-AAA protease due to the loss of paraplegin and AFG3L1 in mice leads to neuroinflammation in cerebellum and spinal cord, but not in the brain.

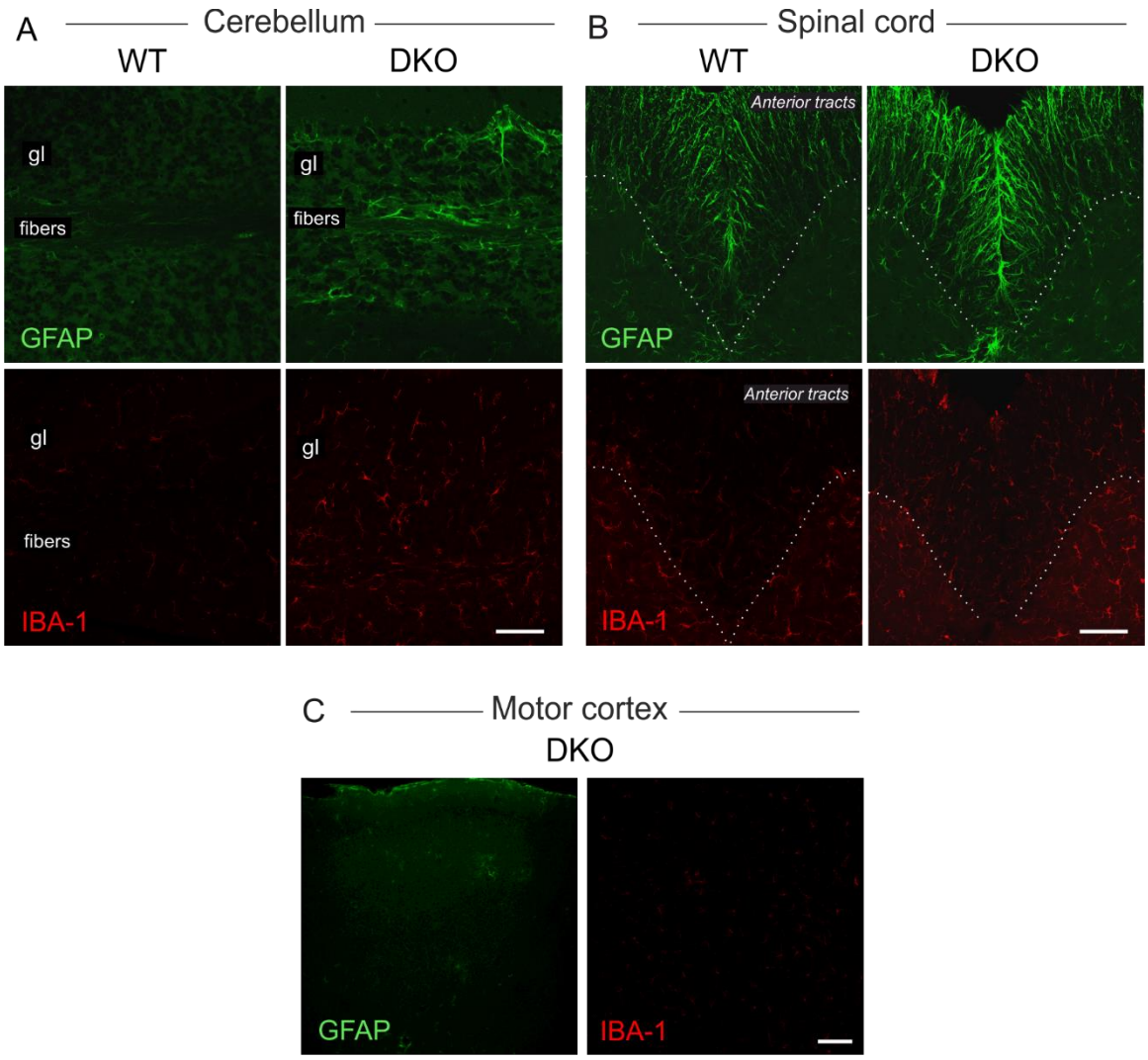

Figure 4.7. Presence of neuroinflammation in cerebellum and spinal cord, but not brain, of DKO mice. (A) Representative immunofluorescence images of cerebellum, (B) spinal cord and (C) brain stained with GFAP to label astrocytes and IBA-1 to mark microglial cells. Images obtained as maximal projections from same-size Z-stacks. A total number of 4 male animals per genotype were analysed. gl: granular cell layer. Scale bar: 20 µm in A-B and 40 µm in C.

4.2. Proteomic analyses reveal perturb mitochondrial and extra-mitochondrial pathways in DKO mice

Despite the fact that previous studies have shed light into the role of *m*-AAA proteases in mitochondrial function, such as the maturation of MRPL32, thereby ribosome assembly and translation (Nolden et al., 2005), how these enzymes impact more broadly mitochondrial metabolism is not completely understood. Moreover, most of the investigations only focus on AFG3L2, which can form both homo- and heterooligomeric *m*-AAA complexes, whereas paraplegin has been so far only seen to form complexes in association with AFG3L2. One hypothesis is that both types of multimers have completely independent functions and substrates, which can translate into the involvement of *m*-AAA proteases in different cellular pathways. The tissue-specific expression of *m*-AAA protease subunits (Koppen et al., 2007) can also influence the balance between homo- and heterooligomers, further determining how they specifically regulate the mitochondrial system. In order to get insights into paraplegin-containing *m*-AAA protease specific substrates within the CNS *in vivo* and identify dysregulated pathways upon its absence, proteomics was performed in DKO and WT spinal cord and cerebellar samples at 16 weeks of age by Hendrik Nolte.

Out of 6710 proteins detected on average in the spinal cord, only 95 proteins were significantly changed in DKO mice (n=8) compared to control samples (n=8) (**Fig. 4.8, A-B; Suppl. Table S2**) (q value < 0.1). In fact, principal component analysis (PCA) did not show any apparent segregation (**Suppl. S4, B**). Of the total changed proteins, approximately 59% were mitochondrial proteins (predicted by Mitocarta 3.0 from a total of 882 mitochondrial proteins), highlighting the importance of paraplegin-containing *m*-AAA proteases within the mitochondrial spinal cord proteome. Proteomic analysis in this tissue also detected six proteins exclusively present in DKO samples and two in WT samples (**Table 4.1**), including proteins involved in gene expression changes and DNA damage, highlighting, in general, processes undergoing in the spinal cord during the HSP-like pathology.

Table 4.1. **List of proteins exclusively found in either WT or DKO spinal cord proteomics** (source: UniProt Consortium).

Genotype	Protein	Description
WT	**ARAP2**	GTPase-activating protein modulating actin cytoskeleton
	DNAAF4	Dynein assembly factor involved in neuronal migration during development
DKO	**NIPBL**	Promotes the loading of cohesins at sites of DNA damage
	FOXO1	Transcription factor regulating metabolic homeostasis in response to oxidative stress
	KMT2D	Part of the chromatin remodelling machinery mediating H3K4me1 methylation
	PGBD5	Transposase that mediates sequence-specific genomic rearrangements
	PLEK	Major protein kinase C substrate of platelets
	OSBPL5	Involved in the lipid countertransport between ER and plasma membrane

Cerebellum proteomics, on the other side, only revealed 38 proteins with an altered abundance in DKO mice (n=8) compared to controls (n=8) (**Fig. 4.8, C-D; Suppl. Table S1**) out of more than 7000 total proteins analysed (less than 0.01% change) [q value < 0.1]. Indeed, WT and DKO samples did not segregate in the PCA (**Suppl. S4, C**). Of these, only 9 were non-mitochondrial proteins. By comparing both proteomics, on one hand, we observed how both tissues displayed a perturbation of the known interactors of paraplegin and AFG3L1 (AFG3L2, PHB1, PHB2, MAIP1), in line with the existing literature (**Suppl. S4, A**). In fact, in both cases there was a reduction of approximately 30% of AFG3L2 in the DKO compared to WT, which might be due to the loss of paraplegin/AFG3L1/AFG3L2 heterocomplexes. On the other hand, it can be seen that the 5 most increased proteins in spinal cord were also found highly increased in cerebellum (UQCC1, UQCC2, PARL, SLC30A9, SLC25A29), all of them mitochondrial proteins (**Fig. 4.9, A, D**). The accumulation of these proteins within both tissues upon paraplegin deficiency indicates that they could potentially play a role as common substrates of the *m*-AAA protease. However, there also are proteins which exclusively accumulated in one tissue and not the other, such as COX18 in cerebellum, suggesting a differential function of these proteases with tissue-specific substrates. Interestingly, for both tissues, many of these highly increased proteins are involved in the regulation of OXPHOS: COX18, essential for assembly and stability of complex IV, CMC1, regulator of complex IV

assembly, DNAJC30, component of the ATP synthase and UQCC1-2, assembly factors of complex III. Moreover, If any of these proteins constitute *m*-AAA protease substrates, their accumulation should also be seen at late stages of the disease. Indeed, immunoblot analysis of UQCC1 and UQCC2 performed at 48 weeks in spinal cord lysates support this idea and confirmed the proteomic results (**Fig. 4.10**).

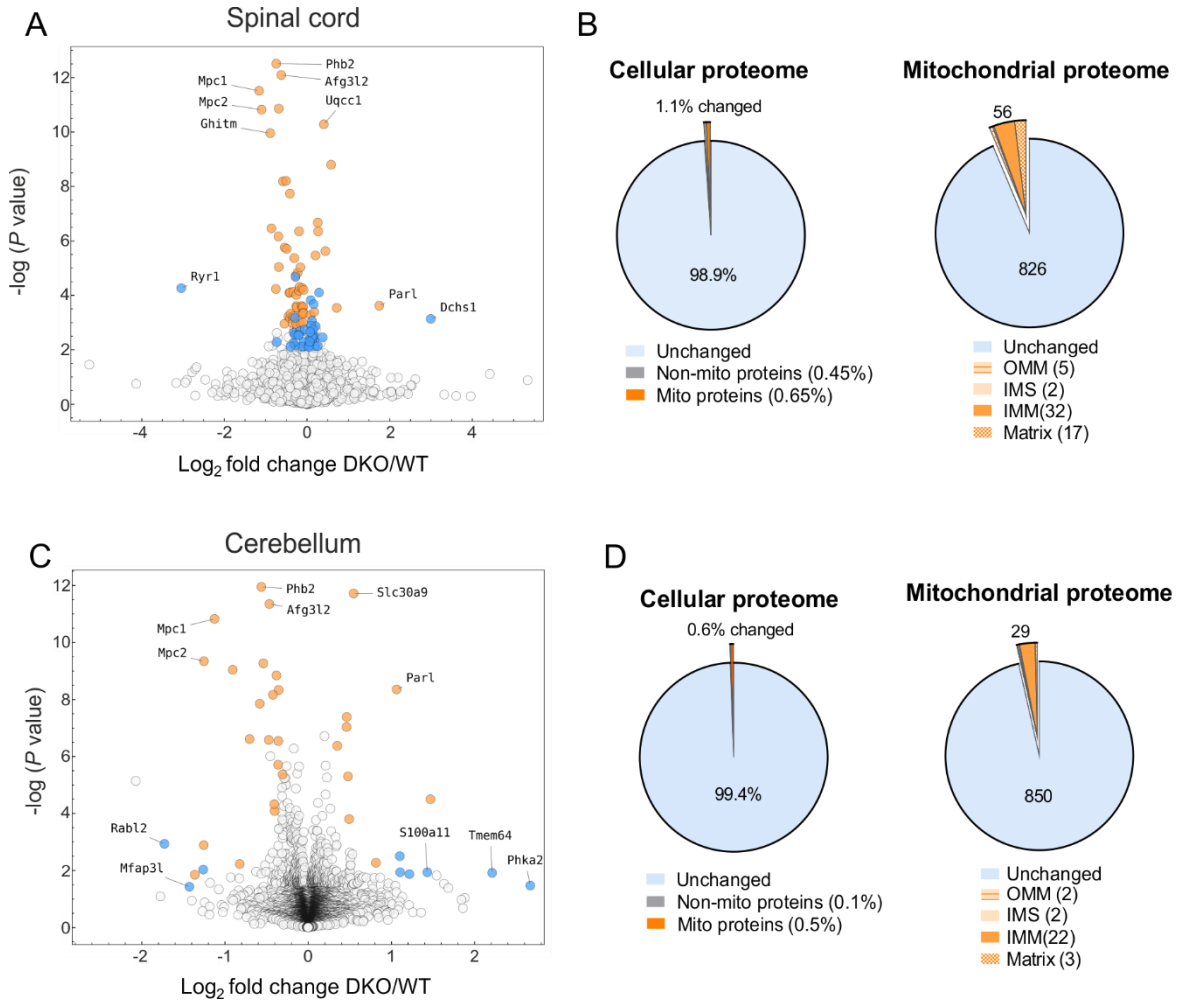

Figure 4.8. The absence of paraplegin and AFG3L1 impacts mainly but with little changes the mitochondrial proteome at 16 weeks. (A) Volcano plot of spinal cord and (C) cerebellum proteomics data with significantly changed mitochondrial proteins highlighted in orange and non-mitochondrial proteins in blue. (B) Pie charts representing the percentages of significant cellular and mitochondrial proteome changes (based on Mitocarta 3.0) in spinal cord and (D) cerebellum. q value < 0.1, n=4 per sex and genotype.

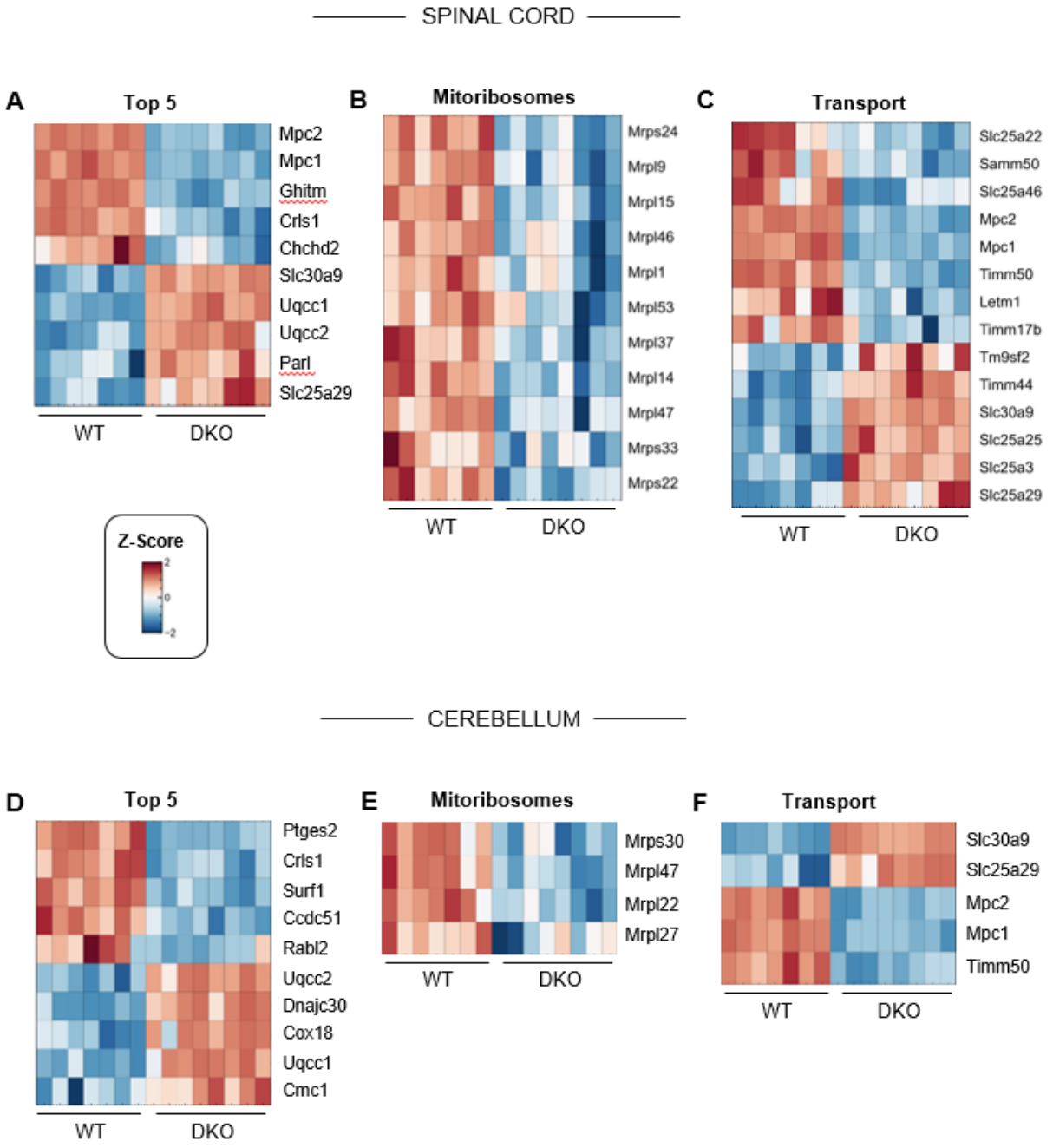

Figure 4.9. Commonalities between spinal cord and cerebellum proteomics at 16 weeks. (A-F) Heatmaps highlighting the differences between DKO and WT proteomics data with blue colours indicating significantly decreased proteins and red colours showing increased proteins. The Log_2-transformed LFQ (label-free quantification) intensities of the selected proteins were Z-Score normalized to plot the clusters in a hierarchical cluster analysis. (A, D) Heatmaps showing the top 5 most increased and decreased proteins found in the proteomics of both tissues, (B, E) all significant mitochondrial ribosomal proteins altered and (C, F) the presence of many proteins involved in protein import and transport across the organelle with dysregulated levels in the DKO compared to WT samples (q value < 0.1).

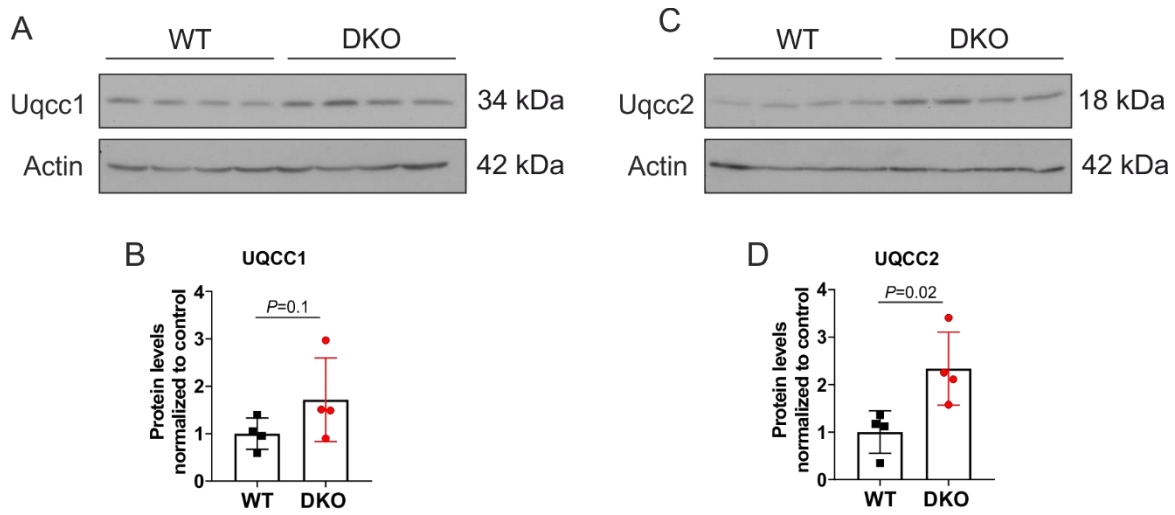

Figure 4.10. Increased levels of UQCC1 and UQCC2´proteins in DKO spinal cord at 48 weeks. (A) Immunoblot of spinal cord lysates of DKO and WT mice against UQCC1, with actin used as a loading control. (B) Quantification of immunoblots shown in A. (C) Immunoblot of spinal cord lysates probed for UQCC2. (D) Quantification of immunoblot shown in C. A total number of 4 male animals per genotype were analysed. Data represented as mean ± SD. *P* values from Student's t-test.

Additionally, in agreement with previous findings, proteomics suggested an important role for *m*-AAA proteases in mitochondrial translation, as indicated by pathway analysis (**Fig. 4.11, A-B**) and the great amount of mitochondrial ribosomal components with significantly decreased levels in spinal cord, and, to a lesser extent, in cerebellum samples (**Fig. 4.9, B, E**). Many amino acid and anion transporters were also significantly reduced or increased in DKO tissues, particularly in spinal cord (**Fig. 4.9, C, F**). Among them, MPC1 and MPC2, mitochondrial pyruvate carriers facilitating the transport of cytosolic pyruvate into the mitochondrial matrix, appeared as either the two most decreased mitochondrial proteins (spinal cord) or two of the most (cerebellum) (with approx. 57% total reduction). This implies a remodelling of the entire mitochondrial metabolism, as the main source of Acetyl CoA in mitochondria is not being efficiently uptaked. This rewiring is further support by the fact that both catabolic and anabolic processes constituted two of the most significantly enriched pathways in the DKO mice (**Fig. 4.11, A**).

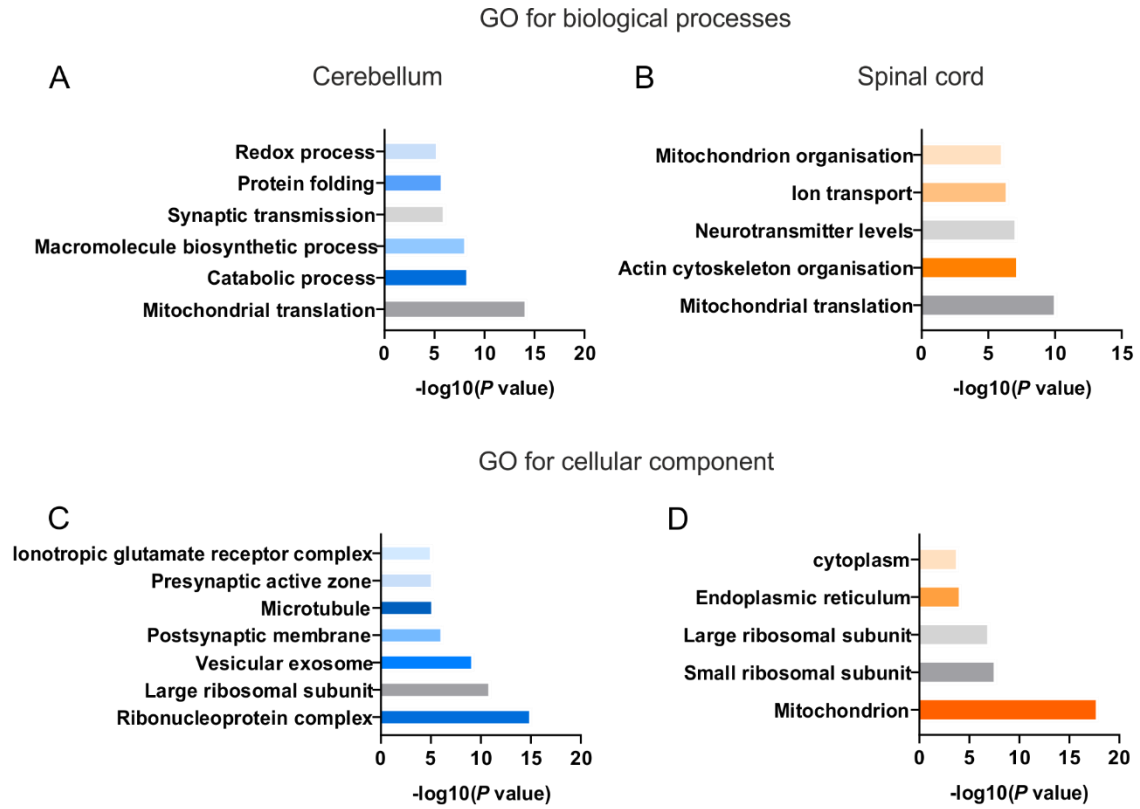

Figure 4.11. Proteomic pathway analysis indicates a dysregulation in mitochondrial translation, energy metabolism and synaptic transmission in DKO animals at 16 weeks. (A-B) Graphs highlight significantly enriched cellular processes and (C-D) components (based on the Gene Ontology (GO) database) of DKO spinal cord and cerebellar proteomics. Analysis performed by Hendrik Nolte.

Further pathway analysis, performed by Hendrik Nolte, stated as one of the most significantly enriched cellular component in the spinal cord, as predicted by the Gene Ontology (GO) database, the endoplasmic reticulum (**Fig. 4.11, D**). This, together with the fact that one of the most non-mitochondrial reduced proteins is Ryr1 (ryanodine receptor 1 -only changed in spinal cord-) (**Fig. 4.11, A**), a calcium channel mediating the release of calcium from the ER, support the EM analysis showing ER alterations and suggest that the role of *m*-AAA proteases have an impact beyond mitochondria.

Furthermore, pathway analysis also indicated a dysregulation of synaptic function in both tissues, including alterations in the post- and presynaptic membranes, the glutamate receptor complexes and the regulation of neurotransmitter levels (**Fig. 4.11, A-C**), suggesting a compromised synaptic transmission in DKO mice.

Altogether, this omic approach highlights the direct effect the loss of paraplegin have on the mitochondrial proteome, impacting not only translation but also the transport of ions and metabolites across the organelle, the import of preproteins and, in general, mitochondrial metabolism, but it also point towards an alteration the endoplasmic reticulum, supporting previous EM analysis.

4.3. Analyses of transcriptome show little to no change upon paraplegin/AFG3L1 deficiency

The fact that many proteins localizing to the inner membrane of the mitochondria were significantly accumulating in proteomics analysis suggest a potential role of the paraplegin-containing *m*-AAA proteases in their processing. To study whether their expression was matching their increased protein levels, and to further investigate the regulation of the gene expression in the DKO mice, a transcriptomic analysis was performed on mRNA of spinal cord of DKO and WT mice at 16 weeks. In general, this analysis detected very little changes in transcript levels, however, all of them very significant. The transcript that presented the highest expression in the DKO was *Vnt*, a gene encoding for vitronectin, an adhesive glycoprotein, with a FC of 1.22 and a *P* value < 0.00001 (**Table 4.2**). On the other end, *Egr3*, encoding for the early growth response protein 3 involved in mitosis, displayed the lowest expression with a FC of -1.18 and a *P* value<0.00001 (**Table 4.3**). In between, 96 transcripts appeared in the DKO spinal cord (FC > 1.12, *P* value < 0.001) whose dysregulation was not reflected at a protein level. Similarly, none of the proteins found altered in the proteomics were among the differentially expressed transcripts, supporting the idea that many of them are directly target by paraplegin.

Moreover, following Enrichr network analysis (KEGG 2021 and MSigDB databases, from genes with FC > 1.15), many of the upregulated transcripts were involved in focal adhesion, apoptosis and immune system response. Downregulated pathways, on the other side, included ligand-receptor interactions, dopaminergic synapse and the tumour necrosis factor (TNF) signaling (**Table 4.4**). Nonetheless, the genes associated with each pathway are few, reflecting that these processes are only marginally affected in DKO compared to WT samples.

Table 4.2. Top 10 upregulated transcripts found in DKO mice in transcriptomic analysis. Source: UniProt consortium 2022.

Top 10 upregulated transcripts			
Name	**Encoding proteins**	**Fold change**	***P* value**
Vtn	Vitronectin; cell adhesion protein	1.22	< 0.0001
Pdgfrb	Platelet derived growth factor receptor	1.2	
Slc7a11	Cystine/glutamate transporter	1.19	
Cfh	Complement component factor h	1.17	
Sned1	Stromal nidogen extracellular matrix protein	1.17	
Slc6a13	Sodium-dependent GABA and taurine transporter	1.16	
Ifit3	IFN-induced antiviral protein	1.16	
Atp13a5	P-type ATPases; specific to brain pericytes	1.16	
Smug1	Single-strand DNA glycosylase; DNA repair	1.15	

Table 4.3. Top 10 downregulated transcripts found in DKO mice in transcriptomic analysis. Source: UniProt consortium 2022.

Top 10 downregulated transcripts			
Name	**Encoding proteins**	**Fold change**	***P* value**
Egr3	transcription factor involved in muscle spindle development	-1.18	< 0.0001
Hbb-b1	Hemoglobin	-1.17	
Clic5	Chloride intracellular channel; hearing development	-1.17	
Galnt18	Polypeptide N-acetylgalactosaminyltransferase	-1.17	
Hoxb9	Transcription factor; body development	-1.16	
Npas1	Transcription factor; CNS development	-1.16	
Cck	Cholecystokinin; ligand-receptor interaction in brain	-1.15	
Nrgn	Neurogranin; calmodulin binding	-1.15	
Rtn4rl1	Reticulon-4 receptor-like 1; CNS development	-1.15	

Table 4.4. Significantly enriched pathways for up- and downregulated transcripts. Analysis performed with Enrichr, significance q < 0.1.

Regulation	Database	Pathway	FDR	Genes
UP	KEGG 2021	**Focal adhesion**	0.02	*Pdgfrb, Vtn, Lamc3, Col4a5, Igf1*
		Complement and coagulation cascades	0.02	*Vtn, Cfh, A2m*
	MSigDB 2020	**Interferon gamma response**	0.05	*Rnf213, Cfh, Tnfsf10, Ifit3*
		Apoptosis	0.09	*Pdgfrb, Tnfsf10, Emp1*
DOWN	KEGG 2021	**Neuroactive ligand-receptor interaction**	0.02	*Grp, F2r, Cck, Drd2, sstr3*
		Dopaminergic synapse	0.05	*Kcnj6, Camk2a, Drd2*
	MSigDB 2020	**TNF-alpha Signaling via NF-kB**	0.06	*Egr1;Egr3;Junb*

4.4. Treatment with ceftriaxone does not ameliorate DKO motor alterations nor cerebellar inflammation

Previous studies have demonstrated a role for *m*-AAA proteases in calcium buffering (Patron et al., 2018). Also, DKO proteomic analyses stated the ryanodine receptor 1, a calcium release channel, as the one of most significantly reduced protein present in the spinal cord (**Fig. 4.8, A**). Therefore, we were interested in knowing whether an overload of calcium upon glutamatergic stimulation could be a shared feature within the HSP pathology. Since this question has been already addressed in the context of spinocerebellar ataxia caused by *Afg3l2* mutations, in which heterozygous mice were successfully treated with the antibiotic ceftriaxone to ameliorate the ataxic symptomatology (Maltecca et al., 2015), we applied the same strategy in the DKO mice. Following the same protocol employed in this study, mice were treated for 5 days with either ceftriaxone (n=5) or saline (n=5) at 16 and 20 weeks of age (**Fig. 3.2**). These time-points were chosen in order to monitor the capacity of this drug to block the axonal degeneration observed in these mice. The motor phenotype was later studied at 24 weeks with the walking beam and the rotarod tests. As it can be seen in **Fig. 4.12 (A, B)**, there was no difference in the performance of either tests among saline and ceftriaxone-treated mice. Indeed, all of them showed gait problems in the same way as the DKO non-treated mice previously assessed.

To further analyse the effect of this antibiotic at a cellular level, cerebellar sections were obtained and processed by immunofluorescence to check for GFAP levels in different cerebellar areas (**Fig. 4.12, C1, C2**). Following our initial hypothesis, the treatment with ceftriaxone may ameliorate the astrogliosis previously seen in DKO mice as a result of a reduced neuronal excitotoxicity. However, the staining of GFAP of both saline **(Fig. 4.12, E1-2)** and ceftriaxone **(Fig. 4.12, F1-2)** treated mice was quite increased compared to WT samples (**Fig. 4.12, D1-2**), same as observed with the cerebellum of DKO mice (**Fig. 4.7**).

Taken all together, these results indicate a poorly effect of the antibiotic in blocking the disease as none of the parameters analysed where restored to WT conditions.

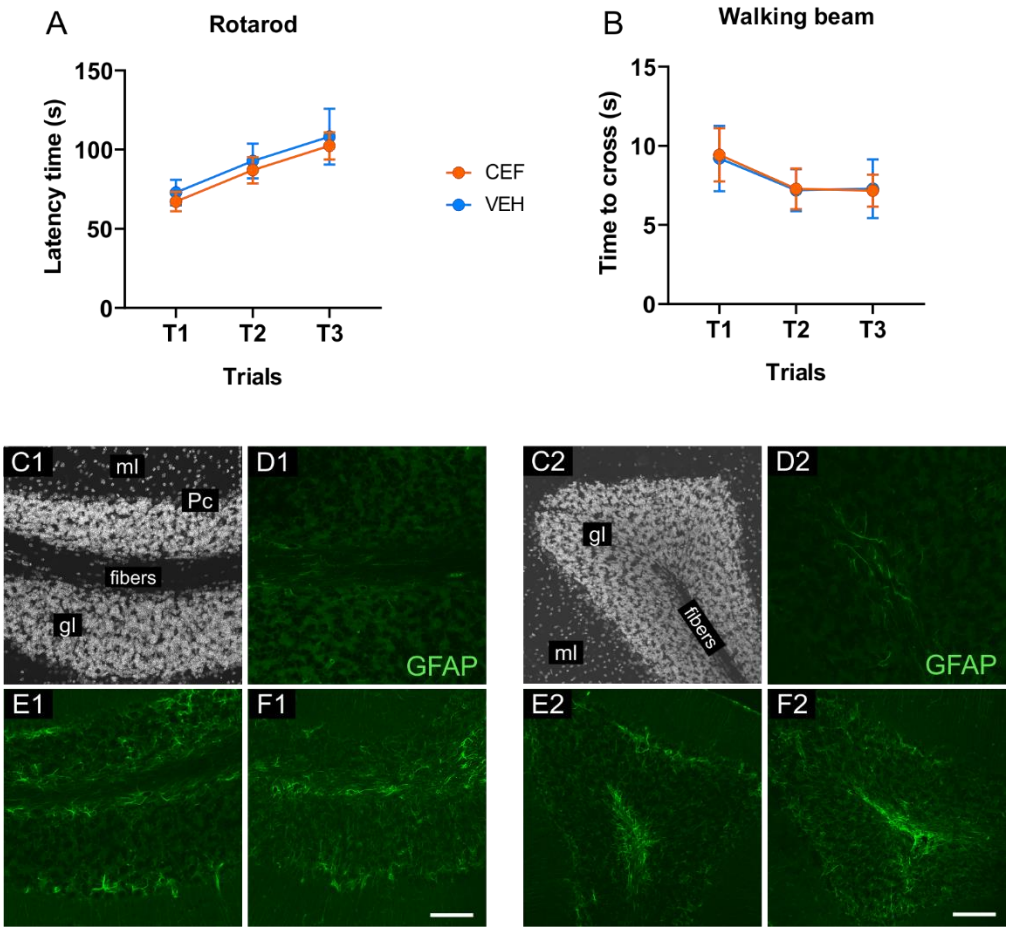

Figure 4.12. Treatment with the antibiotic ceftriaxone does not improve the phenotype of DKO mice. (A, B) Behavioural tests carried out as with DKO/WT mice, with three trials per test (T). Data represented as mean ± SD with n=5 per experimental group. (C1-2) Micrographs of two different cerebellar areas using as a layer marker DAPI. (D1-2) Immunofluorescence images showing GFAP staining of the same WT animals as employed in Fig. 4.7. (E1-2) Immunofluorescence staining of cerebellar free-floating slices against astrocytic protein GFAP of saline (vehicle) and (F1-2) ceftriaxone-treated mice. Scale bar: 20 μm. Pc: Purkinje Cell layer, gl: granule cell layer, ml: molecular cell layer.

4.5. *Sarm1* deletion partially rescues *in vivo* DKO phenotype

SARM1 constitutes a NAD^+ cleaving enzyme mediating axonal degeneration in many neurodegenerative conditions (see section 1.4.3.3). In HSP, although the function of several disease-causing genes has been identified, the mechanisms triggering axonal loss while preserving the cell bodies are still not known. Moreover, sarmoptosis has been already associated with mitochondrial dysfunction in sensory neuropathies (Summers et al., 2014) and boosting NAD^+ synthesis promotes mitochondrial function (Fang et al., 2016). Therefore, to investigate whether sarmoptosis is playing a role in SGP7-HSP, I crossed the DKO mice with a *Sarm1 knock-out* line (Sarm1KO) to obtain a triple *Sarm1*/*Spg7*/*Afg3l1 knock-out* mouse line (from now on named TKO). If this pathway is involved in the HSP pathology, deleting *Sarm1* should block the observed axonal degeneration and, therefore, lead to a rescue of the DKO phenotype. To test this hypothesis, TKO were characterised at the same time points and following the same analysis as with the DKO mice. Similarly, Sarm1KO litter mates were studied in parallel as a control, since most published studies have reported a normal lifespan with no phenotypic alterations. In fact, some have shown that Sarm1KO mice are protected from stress-induced neuronal toxicity, which is an advantage compared to aged WT mice (Kim et al., 2007; Doran et al., 2021). Because the TKO mouse line was developed at later time points than the DKO model, the weight, behavioural and ultrastructural analyses shown in this section include the results from TKO-Sarm1KO animals and the previous data from the DKO-WT mice (already shown in section 4.1).

4.5.1. Loss of SARM1 impacts mouse weight and slightly delays the onset of motor impairments observed in DKO mice

Previous weight analyses indicated a reduction of total body weight for DKO males already at the first month of age. Surprisingly, TKO animals did not display such reduction, with a weight similar to WT and Sarm1KO males (**Fig. 4.12, C**). However, although they maintained over time a weight slightly higher than DKO mice, they also presented a tendency to not gain weight, being their weight significantly different from Sarm1KO from six months on (**Fig. 4.12, A-B**). On the other hand, Sarm1KO and WT individuals replicated a standard weight pattern leaving behind TKO and DKO mice at late time points (**Fig. 4.12, A-B**).

To investigate the motor skills of both TKO and Sarm1KO mice, the rotarod and walking beam tests were performed at 16, 24 and 32 weeks of age in the same way as with the DKO mice. Interestingly, when carrying out the walking beam test, TKO mice did not display signs of motor problems up to 32 weeks old, a time point at which their performance suddenly does

not significantly differ from the DKO mice (**Fig. 4, E**). However, following ANOVA statistical test, it was neither significantly different from Sarm1KO mice, suggesting an intermediate motor phenotype of the TKO at this time point. On the contrary, the same TKO mice were unable to maintain themselves on top of the rotarod beam at any time point (**Fig. 4, F**). The difference between Sarm1KO and TKO rotarod performance became slightly bigger over time, as for the comparison between WT and DKO. The foot-base angle was also measured during the walking beam training days in males at 24 weeks. Following this gait test, TKO animals showed both an increased FBA and length of the visible sole when compared to Sarm1KO mice, but they were also statistically different from DKO mice, as if they were starting to show gait abnormalities around this time-point.

Thus, deletion of SARM1 partially improved early weight dysregulations and subtle motor deficiencies of paraplegin/AFG3L1-deficient mice.

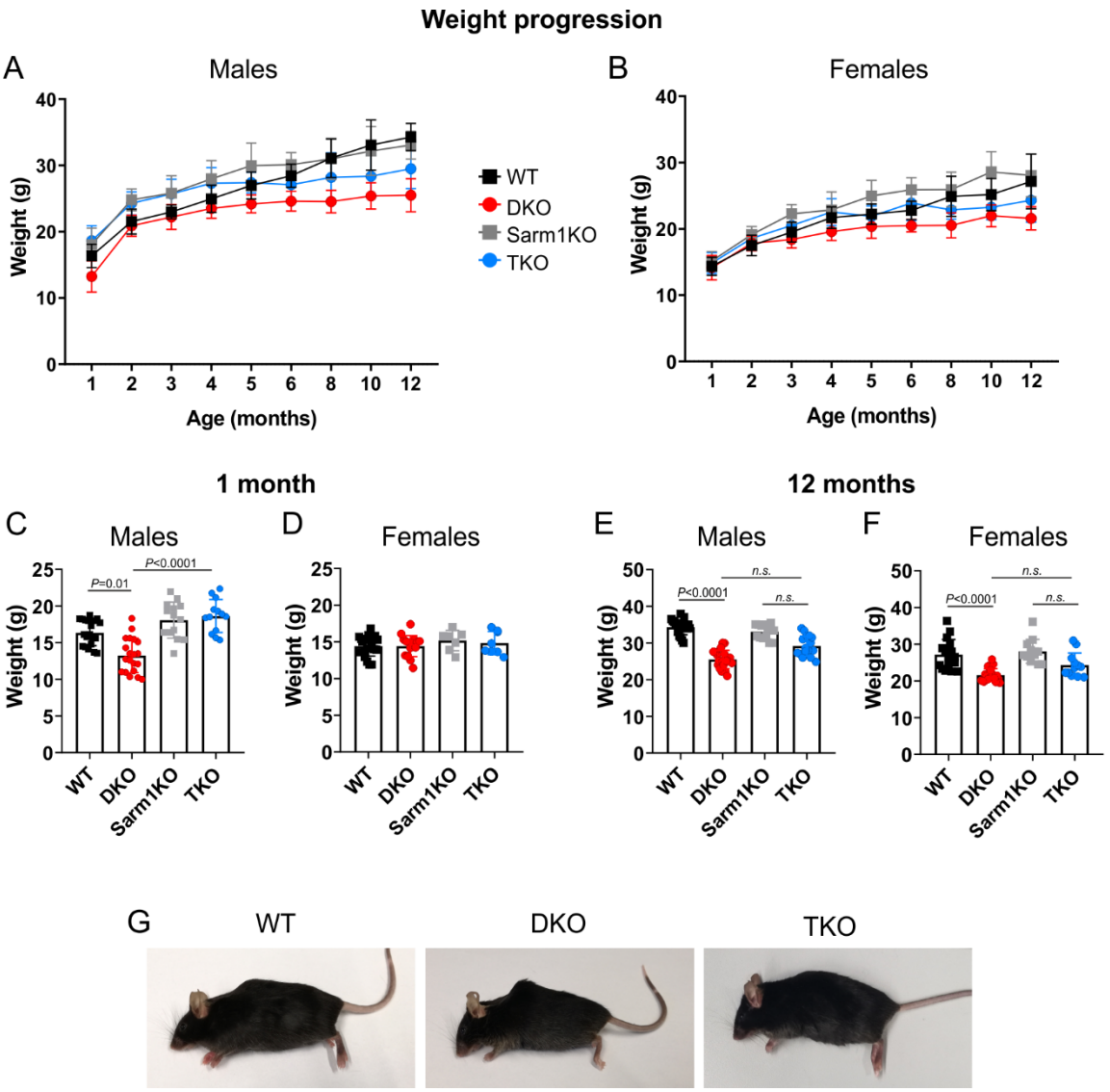

Figure 4.13. Phenotypic characterisation of the TKO mouse line compared to DKO mice. (A-B) Total body weight progression of male (n=14-20 per genotype) and female (n=8-18 per genotype) mice. Data indicated as mean±SD. (C-D) Weight evaluation at 1 month and (E-F) 12 months of age, data extracted from the main progression graphs. Data indicated as mean ± SD. Each dot represent one mouse. One-way ANOVA test with Dunn's multiple comparison test was performed for each condition. Data from DKO and WT animals are the same as represented in Fig. 4.3. (G) Images showing WT, DKO and TKO mice at 28 weeks of age.

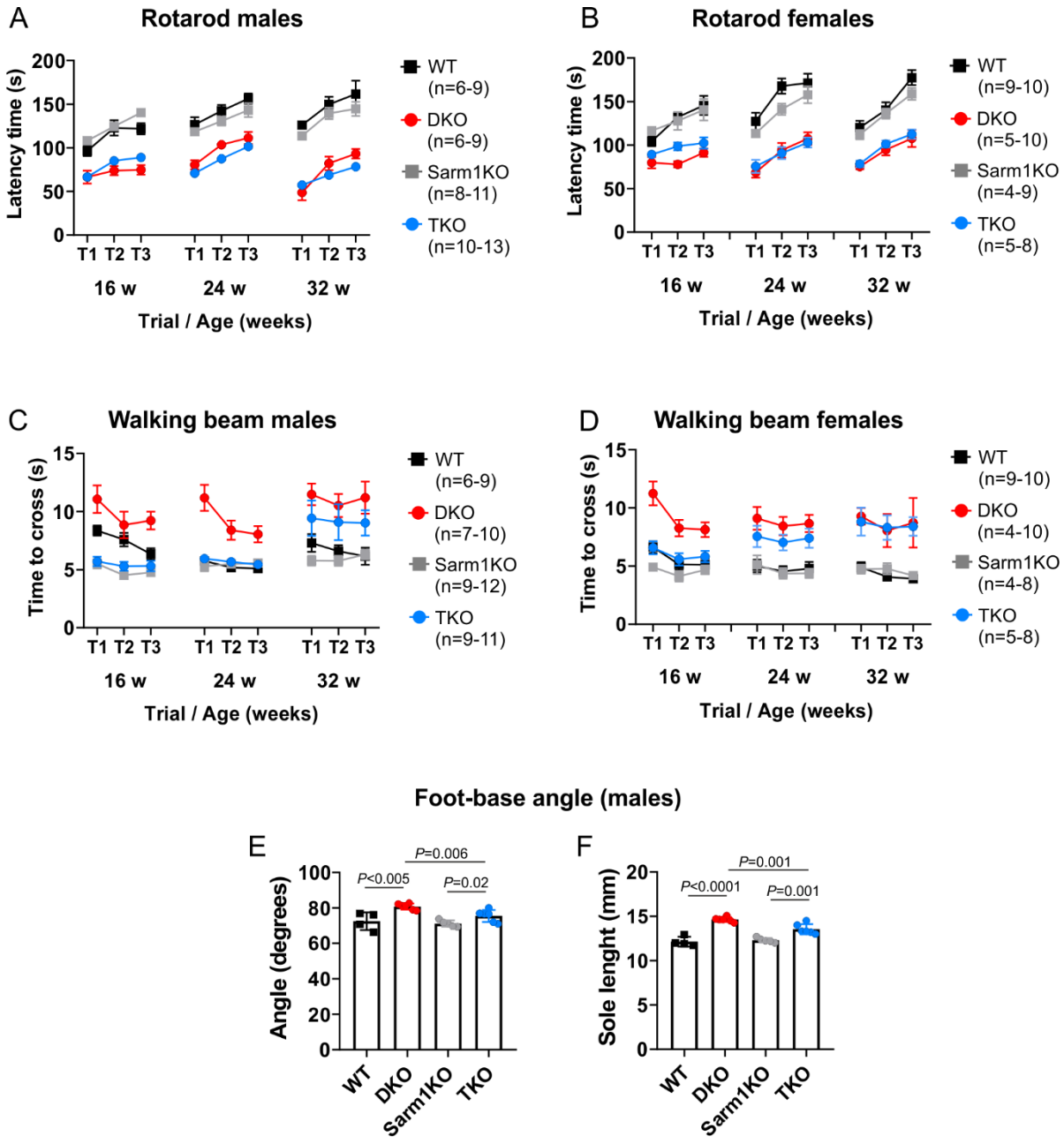

Figure 4.14. SARM1 deletion improves early DKO motor deficits assessed by the walking beam but not by other behavioural tests. (A-B) Rotarod test analysis at 16, 24 and 32 weeks with three trials (T) per time point. DKO and TKO mice behave similarly, being significantly different from Sarm1KO and WT litter mates at measured ages. (C-D) Walking beam analysis at the same time points. TKO performance differs significantly from DKO mice's at 16 (P<0.01 in T1) and 24 weeks (P<0.005 in T1), but not at 32 weeks (P=0.6 in T1), being also not statistically different from Sarm1KO nor WT mice (P=0.1 in T1). Either two-way ANOVA test or Mixed ANOVA model was performed for each time point with Tukey's multiple comparisons test. Data in A-D represent mean ± SEM. (E-F) Foot-base angle analysis in males at 28 weeks showing an intermediate phenotype of the TKO mice. Data represent mean ± SD, with each dot being one mouse. Student's t-test performed for each two-group comparison. Data from DKO and WT animals are the same as represented in Fig. 4.4.

4.5.2. Removing SARM1 in spinal cord does not affect mitochondrial abnormalities and axonal degeneration observed upon paraplegin and AFG3L1 deficiency

Loss of SARM1 prevents axonal degeneration in different mouse models of axonopathies (Gilley et al., 2017; Turkiew et al., 2017). This fact, together with the partial rescue observed in the behavioural tests, prompted me to analyse in detail the spinal cord tissue of the *Sarm1*-deficient mice to elucidate whether SARM1 is also contributing to the degeneration observed in paraplegin-deficient axons. To test this, EM analysis of TKO and Sarm1KO were carried out in this tissue. Semithin sections of distal spinal cord revealed a similar tissue structure and organisation among the different genotypes at 16 and 28 weeks of age. Nonetheless, ultrathin sections showed a similar progressive pattern of abnormal mitochondria presence in anterior axonal tracts between TKO and DKO mice, displaying similar percentages of affected axons at 16 and 28 weeks of age (**Fig. 4.15, B, E**). Although some axons were seen already degenerating at 16 weeks in both TKO and DKO spinal cord (**Fig. 4.15, C**), the axonal degeneration was remarkably prominent in these anterior areas at 28 weeks of age (**Fig. 4.15, F, G asterisks**). This degeneration became quite visible in semithin sections at 48 weeks, where degenerating axons appeared as black dots (**Fig. 4.15, H arrows**). On the contrary, the transverse ER structures observed in DKO spinal cord were only spotted sparsely in TKO samples, both at 16 not 28 weeks of age (**Fig. 4.15, A, D**).

Furthermore, Sarm1KO samples analysed at 28 weeks presented nice, electrodense mitochondria with well-organized cristae similar to WT samples (**Fig. 4.15, G**), indicating that the absence of SARM1 in a healthy background does not impact mitochondrial morphology.

To conclude, whereas SARM1 absence had no impact on neither the percentage of spinal cord tracts that displayed these mitochondria abnormalities nor the number of axons that accumulated material inside and degenerated in the DKO pathology, it did improve the ER impairments observed upon paraplegin/AFG3L1 absence in this tissue, indicating that SARM1 itself is not able to rescue mitochondrial impairments nor block or delay the degeneration process but the transverse ER alterations in spinal cord axons.

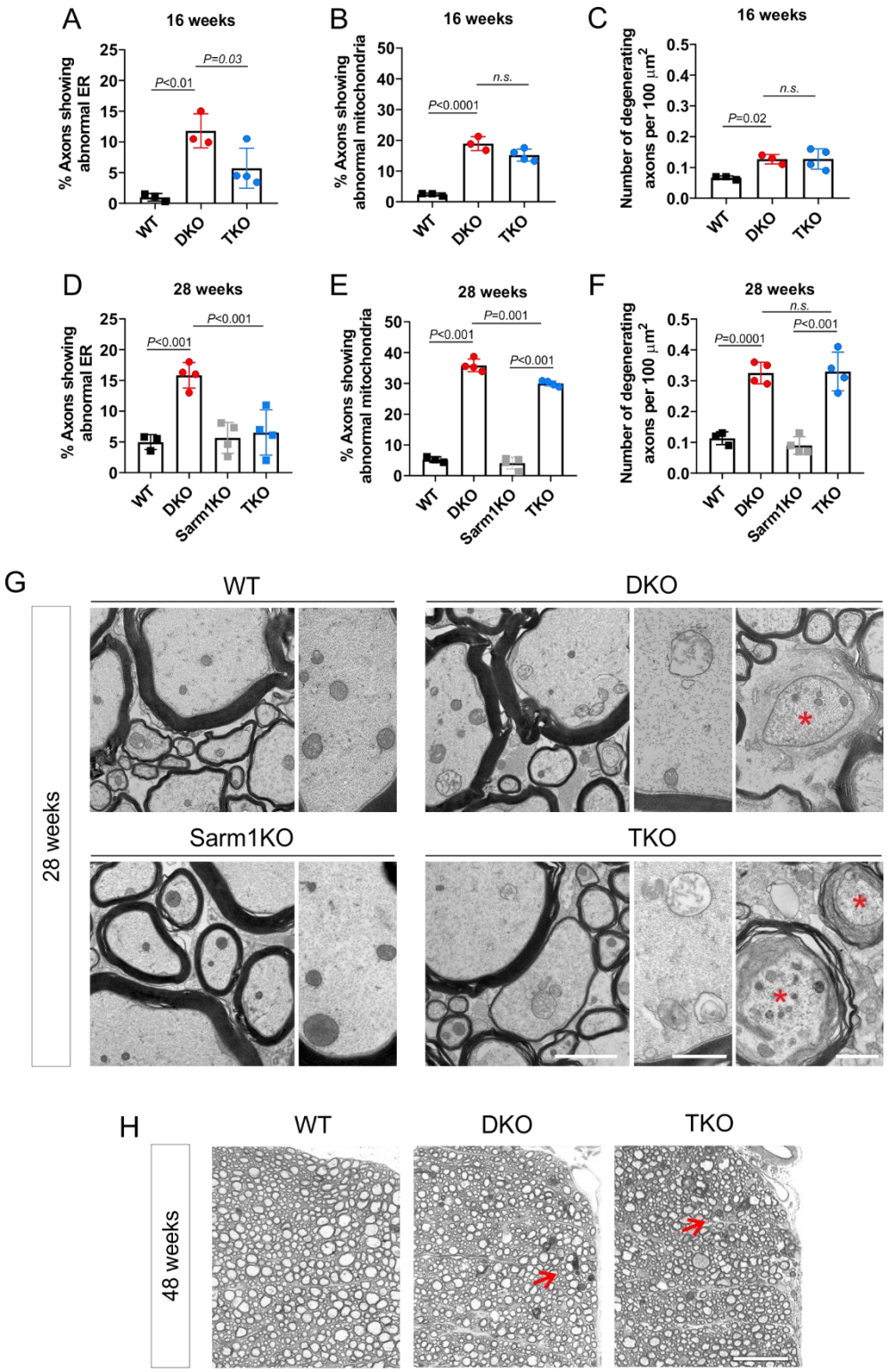

Figure 4.15. The loss of SARM1 does not improve the mitochondrial phenotype observed in DKO spinal cord. (A, D) Quantification of axons showing altered ER, (B, E) mitochondria, and (C, F) degenerating axons at 16 and 28 weeks of age. *P* values obtained with Student's t-test. Data represented as mean ± SD with n=3-4 per genotype and age. Between 200 to 400 anterior axons were counted per mouse. WT and DKO data extracted from the graphs shown in Fig. 4.5. (G) Representative EM images obtained at 28 weeks comparing the different genotypes. (H) EM semithin sections at 48 weeks. Scale bars: 2 µm in G, 1 µm enlargements in G and 40 µm in H. DKO and WT EM images obtained from the same mice used in Fig. 4.5. All analyses performed in male animals.

4.5.3. Mitochondrial impaired morphology and axonal loss of DKO granule cells are rescued in TKO samples

TKO enhanced performance in the walking beam test hinted to an improvement of cerebellum-mediated motor skills. Moreover, *in situ* hybridization analysis from the Allen Institute for Brain Science shows a high expression of *Sarm1* in cerebellar cells. However, a role of SARM1 in ataxia-like phenotypes has so far not been assessed. Therefore, to study whether SARM1 ameliorates the cerebellar phenotype observed in the DKO, 16 and 28 week old cerebellar sections were processed and observed by EM. I could not detect any differences between Sarm1KO and WT cerebellar tissues, showing both well-structured and nicely organized layers with cells containing compacted mitochondria (**Fig. 4.16, A1-2, C1-2**). Purkinje cells (PC) also appeared unaffected in all genotypes analysed (**Suppl. S5, A**). However, as described in section 4.3.1, DKO samples displayed swollen mitochondria in granule neurons (**Fig. 4.16, B1**), throughout the molecular layer (**Fig. 4.16, B2**) and in the cerebellar axonal fibers (**Suppl. S5, B**). Surprisingly, no signs of abnormalities were detected in the granule cell and molecular layer of TKO mice (**Fig. 4.16, D1-2**), where the majority of mitochondria presented a morphology that resembled those from control samples. In the white matter, however, many fibers contained altered, swollen mitochondria, indicating that afferent fibers and potentially PC axons are not rescued upon *Sarm1* deletion (**Suppl. S5, B**). This result goes in line with the previous spinal cord EM analysis showing no effect upon SARM1 absence, as many of these long afferent fibers are part of the spinocerebellar tract, which origins along the lumbar spinal cord.

To further study how the lack of paraplegin and SARM1 impact the granule cells, I stained neurites with an antibody against the phosphorylated neurofilament H, an intermediate filament protein that labels mainly axons but also some dendrites such as those from basket cells (but not PC). Indeed, many nicely-organized axons with a T shape were stained in WT cerebellar slices (**Fig. 4.16, WT 1-4)**. These so called parallel fibers are, in fact, the axons of the granule cells, which appeared then disrupted and in lower density in DKO samples (**Fig. 4.16, DKO 1-4**). Remarkably, these alterations were not present anymore in TKO tissue (**Fig. 4.16, TKO 1-4**), which displayed a staining of the parallel fibers very similar to WT samples.

Therefore, the loss of SARM1 in the cerebellum improves the aberrant mitochondrial morphology and axonal loss observed in the granular and molecular cell layers of DKO animals.

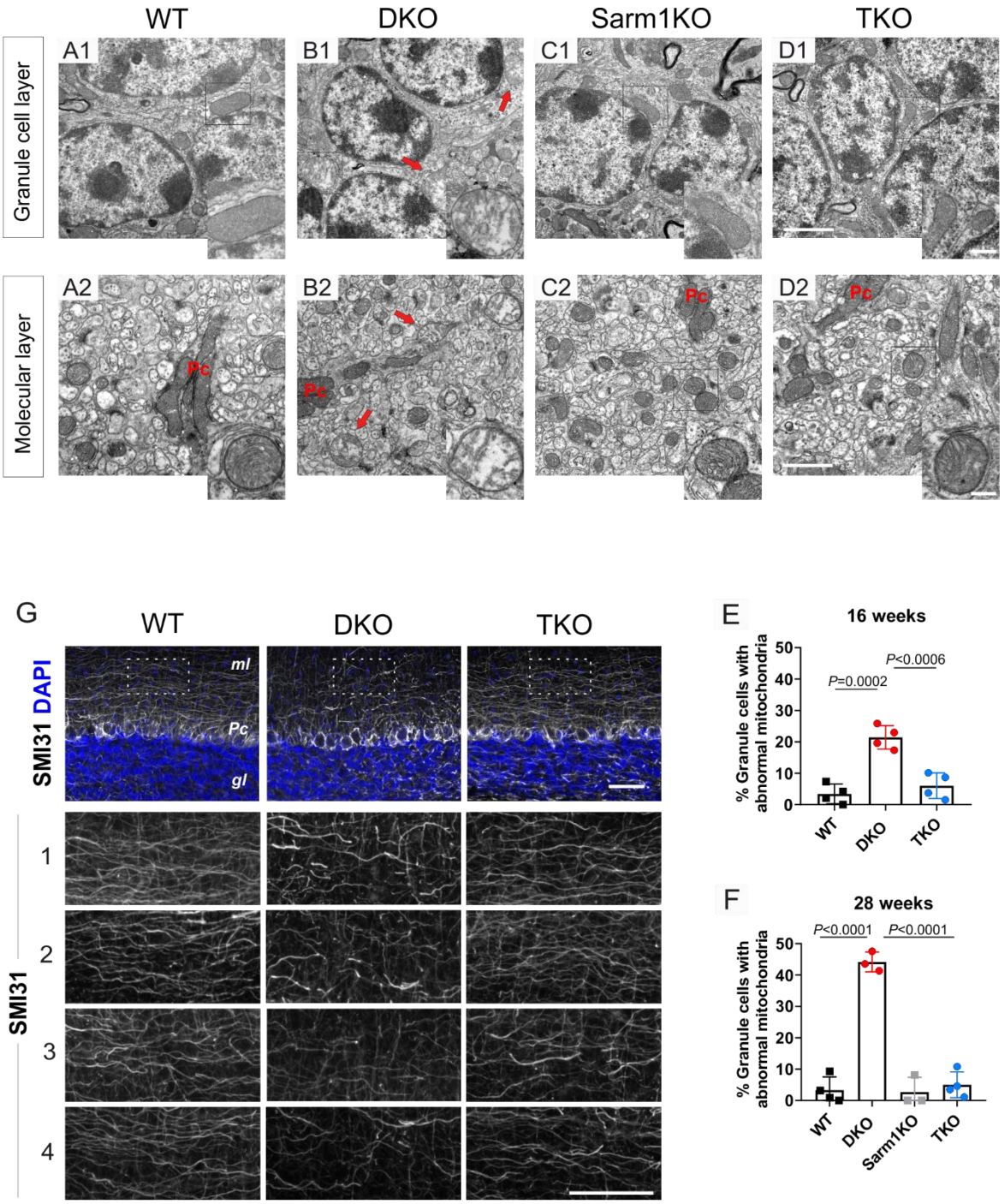

Figure 4.16. Deletion of SARM1 rescues abnormal mitochondrial morphology and axonal loss observed in the DKO cerebellum. (A-D) Electron micrographs from the granule cell layer (1) and the molecular layer (2) of the different genotypes (n=3-4 per genotype). Arrows indicate abnormal mitochondria, Pc: Purkinje cell dendrites. DKO and WT EM images obtained from the same mice used in Fig. 4.6. (E-F) Quantification of the granule cells (soma) displaying altered mitochondria at 16 and 28 weeks. Data appear as mean ± SD, with each dot being one animal. Over 100 granule cells were counted per mouse. *P* values obtained from one-way ANOVA test with Tukey's multiple comparison test. DKO and WT values are the same as displayed in Fig. 4.6. (G) Immunofluorescence staining against SMI31 with enlargements representing four different biological replicates (1-4). All analyses performed in male animals. Scale bars: 2 μm in A1-D1, 1 μm in A2-D2, 500 nm in A-D enlargements, and 40 μm in G.

4.5.4. Both spinal cord and cerebellar glial reactivity ameliorates upon Sarm1 deletion

In addition to mediate neurodegenerative processes, SARM1 can also regulate intrinsic neuronal immune responses, triggering the recruitment of immune cells to affected neuronal regions (Wang et al., 2018). In fact, deletion of SARM1 has been found to decreased inflammation after spinal cord injury (H. Liu et al., 2021) and in a model of glaucoma (Ko et al., 2020). Since DKO mice showed increased reactive astroglia and microglia in spinal cord and cerebellum, I aimed next to investigate whether the observed neuroinflammation is attenuated by removing SARM1 from these tissues. For that, I stained in parallel 28 week old free floating sections of WT, DKO and TKO with antibodies against GFAP and IBA-1.

As can be seen in **Fig. 4.17, A**, cerebellar slices from TKO individuals did not show the increased GFAP staining nor the reactive IBA-1 stained microglia observed in DKO tissue. Indeed, this was reflected in the quantification analysis showing a remarkable increase in the area of both GFAP and IBA-1 positive cells, which was significantly diminished in TKO mice (**Fig. 4.17, B, D**). Moreover, whereas the average size of $GFAP^+$ particles in DKO samples were not significantly differing from WT, they did from TKO mice, whose staining was hardly detectable (**Fig. 4.17, C**). On the other side, the mean particle of IBA1-stained glial cells was considerably higher in DKO mice, suggesting a reactive microglial morphology, which was restored to WT conditions in TKO cerebellum (**Fig. 4.17, E**).

Spinal cord free-floating sections labelled with same markers gave a comparable result for GFAP staining (**Fig. 4.18, A**), whose area occupied was the highest in DKO samples (**Fig. 4.18, B**), although the average size of $GFAP^+$ fragments were similar among the genotypes (**Fig. 4.18, C**). In this tissue, deletion of SARM1 did not entirely restore this astrogliosis, as the area occupied by GFAP positive cells in TKO spinal cord was something in between WT and DKO samples (**Fig. 4.18, B**). Furthermore, spinal cord microglial cells did not show signs of reactivity, as neither the area occupied by IBA-1+ cells nor their mean particle were changed between the different genotypes.

In conclusion, cerebellar tissue lacking SARM1 exhibits a lessening of astroglial and microglial reactivity triggered upon an alteration of the *m*-AAA protease in DKO mice, a fact also observed in anterior distal spinal cord with GFAP-positive cells, pointing towards the possibility of an improved motor performance via decreased neuroinflammation.

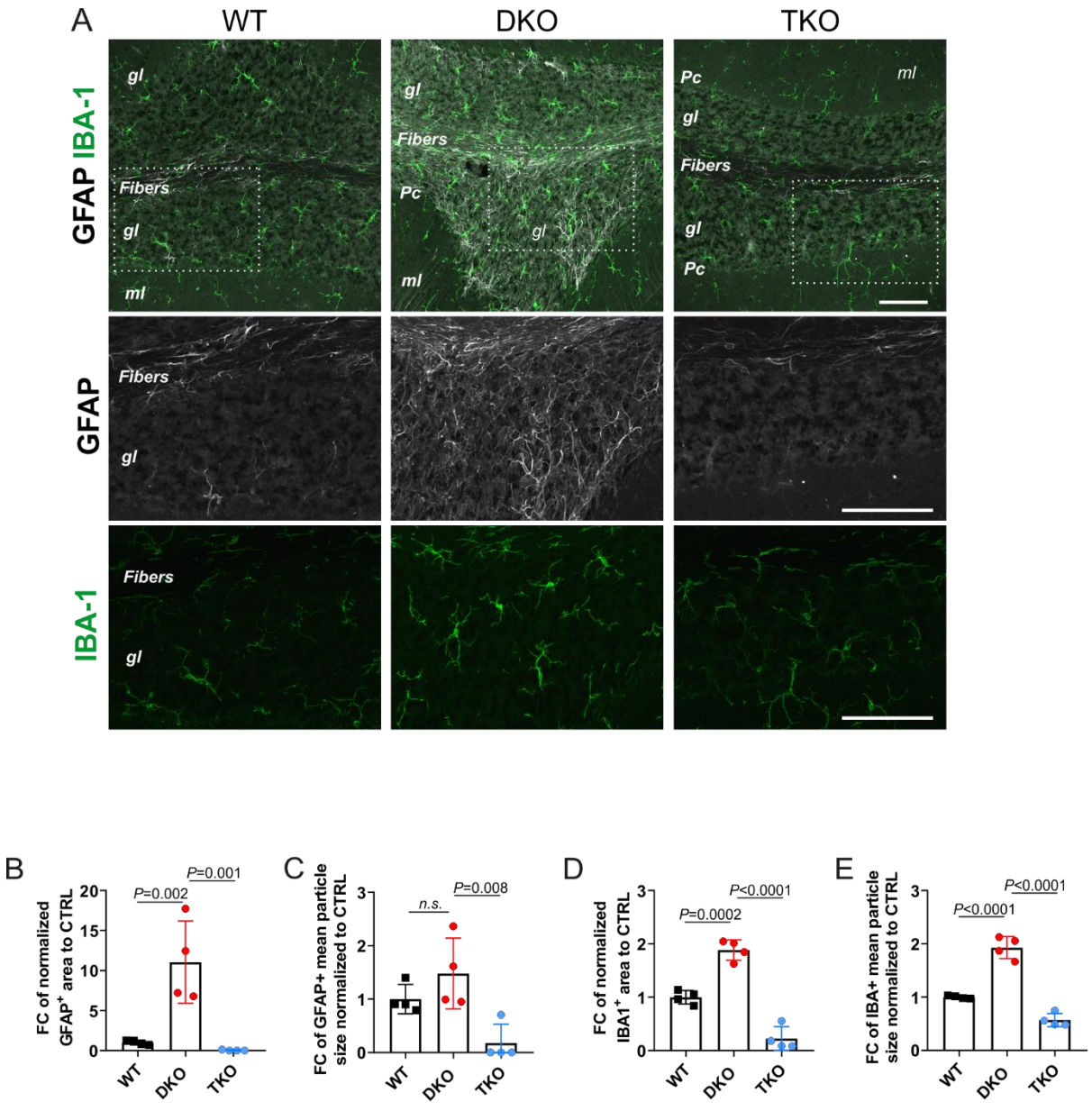

Figure 4.17. Attenuation of cerebellar inflammation upon SARM1 loss. (A) Immunofluorescence of free floating slices of the cerebellar vermis (n=4 per genotype) at 28 weeks against GFAP (astrocytes, grey) and IBA-1 (microglia, green), represented as maximal projection images. Pc: Purkinje cell layer, gl: granular cell layer, ml: molecular cell layer. Scale bars: 20 μm. (B-C) Area fraction occupied by GFAP-positive cells and the average size of total particle counts in the same area (n=3-4 lobules per mouse). (D-E) Area fraction occupied by IBA-1-positive cells and the mean size of particle count (n=3-4 lobules per mouse). Data are presented as mean ± SD. Each dot correspond to one mouse. *P* values from one-way ANOVA with Tukey's multiple comparison test. WT and DKO mice used for this analysis were the same as used for Fig. 4.7. All analyses performed in male animals.

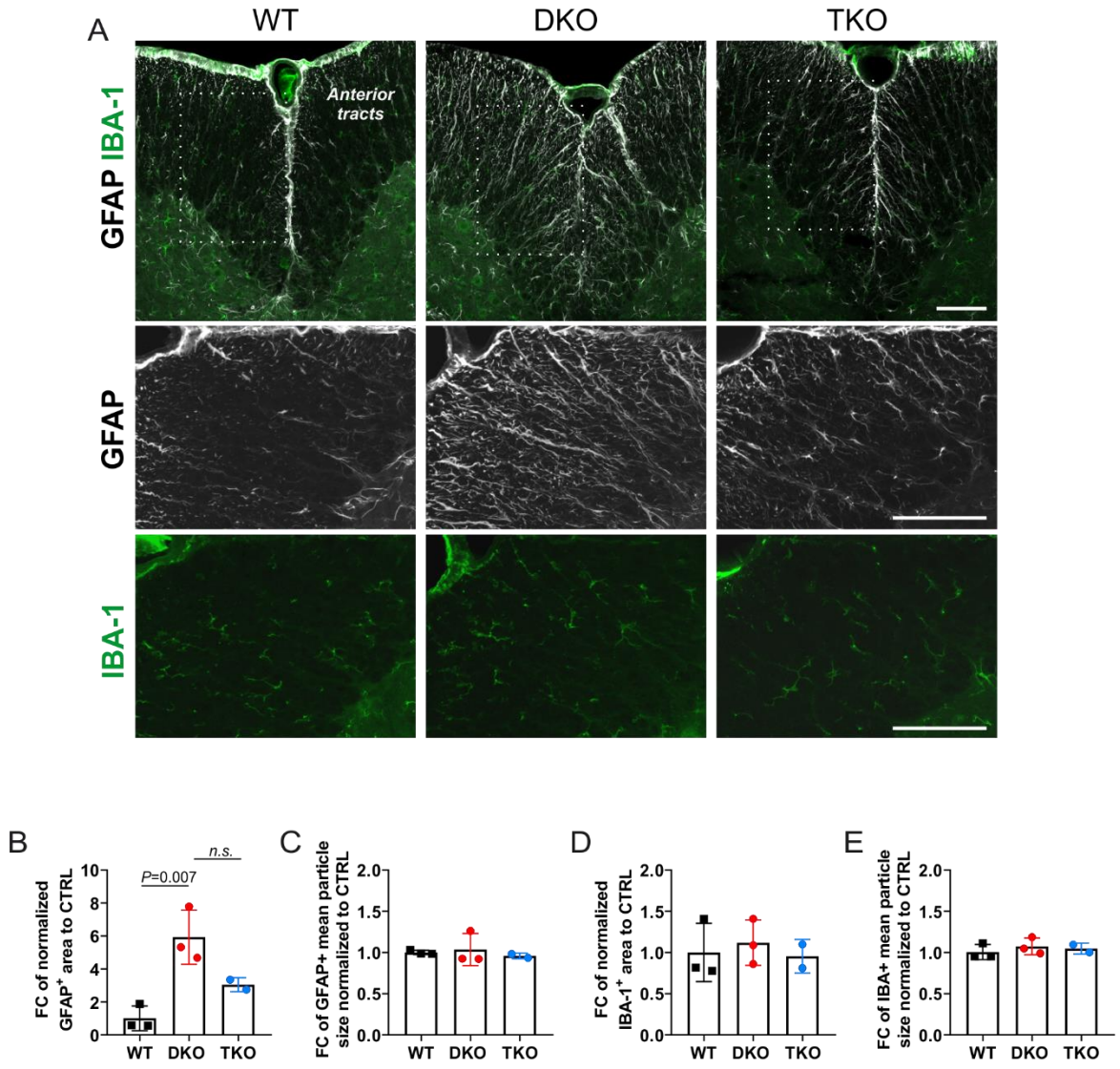

Figure 4.18. Mitigation of spinal cord inflammation upon SARM1 loss. (A) Maximal projection confocal images of lumbar spinal cord at 28 weeks against GFAP (astrocytes, grey) and IBA-1 (microglia, green). Scale bars: 20 μm. (B) Fold change (FC) of normalized GFAP positive area. (C) Normalized average size of GFAP positive particles. (D) FC of normalized IBA-1$^+$ area. (E) Normalized average size of IBA-1 positive particles. Data are presented as mean ± SD. Each dot correspond to one mouse. *P* value obtained from ordinary one-way ANOVA with Tukey's multiple comparison test. WT and DKO mice used for this analysis were the same as used for Fig. 4.7. All analyses performed in male animals.

4.6. An impairment of the *m*-AAA protease impacts NAD metabolism

So far *in vivo* analysis have hinted to an involvement of SARM1 in the HSP pathology, yet its activation has not been demonstrated in DKO tissues. Recently, cADPR has arised as a gene dosage-sensitive biomarker of SARM1 activity (Sasaki et al., 2020). In fact, Sasaki et al. found that SARM1 activity is the major source of cADPR in the brain, sciatic nerves and cultured dorsal root ganglion neurons in absence of injury. Upon cell damage, cADPR levels increase proportionally to SARM1 gene dosage, suggesting that SARM1 also constitutes the main regulator of cADPR levels under pathological conditions. To check for SARM1 activity, cADPR metabolites were measured in 16 and 28 week old spinal cord and cerebellar samples by Dr. Susanne Brodesser following same protocol as in Sasaki et al.. At 16 weeks, DKO spinal cord presented a significant increase in cADPR compared to WT samples (**Fig. 4.19, A**), whereas DKO cerebellum only showed a tendency but without being significant (**Fig. 4.19, C**). This tendency was also observed in this tissue at 28 weeks (**Fig. 4.19, D**). However, spinal cord cADPR from DKO mice did not differ from WT samples at 28 weeks (**Fig. 4.19, B**), which could be explained by the fact that at this time point several spinal cord axons have already degenerated. Moreover, both tissues, in particular spinal cord, constitute very heterogeneous samples, containing not only different neuronal types but also many glial cells, which makes difficult the detection of biochemical alterations of a small subset of affected axons and neurons. Therefore, although further analysis in pure neuronal populations are needed to confirm SARM1 activity in this model, the aforementioned results suggest a contribution of SARM1 from early on to the paraplegin-associated HSP pathology.

Furthermore, despite Sasaki et al. findings, we were able to detect cADPR similarly in both Sarm1KO and TKO mice at the same extent as in WT samples, which reflects the complexity of the tissue and indicates a contribution of other NAD^+-dependent enzymes to cADPR basal levels.

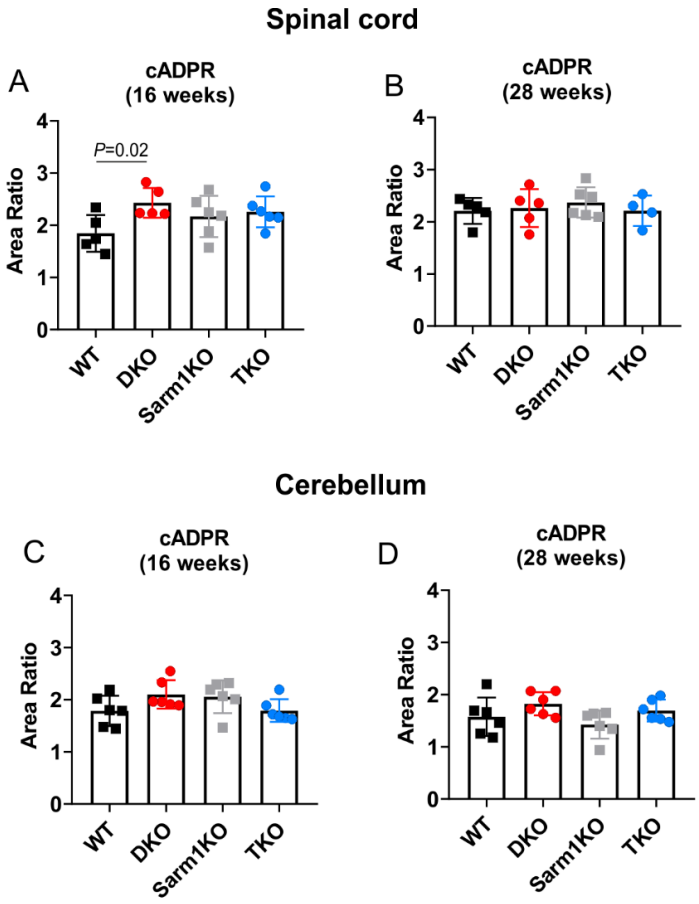

Figure 4.19. cADPR levels are increased in DKO spinal cord at 16 weeks. (A-B) Area ratio of cADPR measurements in spinal cord and (C-D) cerebellum at 16 and 28 weeks of age (n=4-6). Data presented as mean ± SD. Each dot corresponds to one mouse, all males. Student's t-test comparing WT and DKO animals. Analysis performed by Susanne Brodesser.

SARM1 can also be phosphorylated by the c-jun N-terminal kinase (JNK) under oxidative stress, which enhances its NADase activity (Murata et al., 2018). To investigate whether this is occurring in the DKO mice, I performed western blot at 28 weeks in WT and DKO spinal cord lysates to analyse the levels of JNK and pJNK proteins. This analysis revealed no appreciable difference between the two genotypes in either the normal nor the phosphorylated protein (**Suppl. S6, A-B**). Moreover, the activation of the mitogen-activated protein kinase MKK4 has been shown to promote NMNAT2 turnover in Wallerian degeneration, leading to SARM1 activation and the subsequent axonal death (Walker et al., 2017). As an estimation for SARM1 activity, immunoblot analyses of MKK4 and pMKK4 were carried out in spinal cord and cerebellar lysates at 28 weeks. Whereas the ratio pMKK4/MKK4 in cerebellum only showed an increased tendency in DKO mice (**Fig. 4.20, A, C**), in spinal cord it was significantly higher than the ratio of WT samples (**Fig. 4.20, B, D**), indicating an activation of MKK4 kinases and supporting the idea of an activated MKK4/SARM1 degenerative axis.

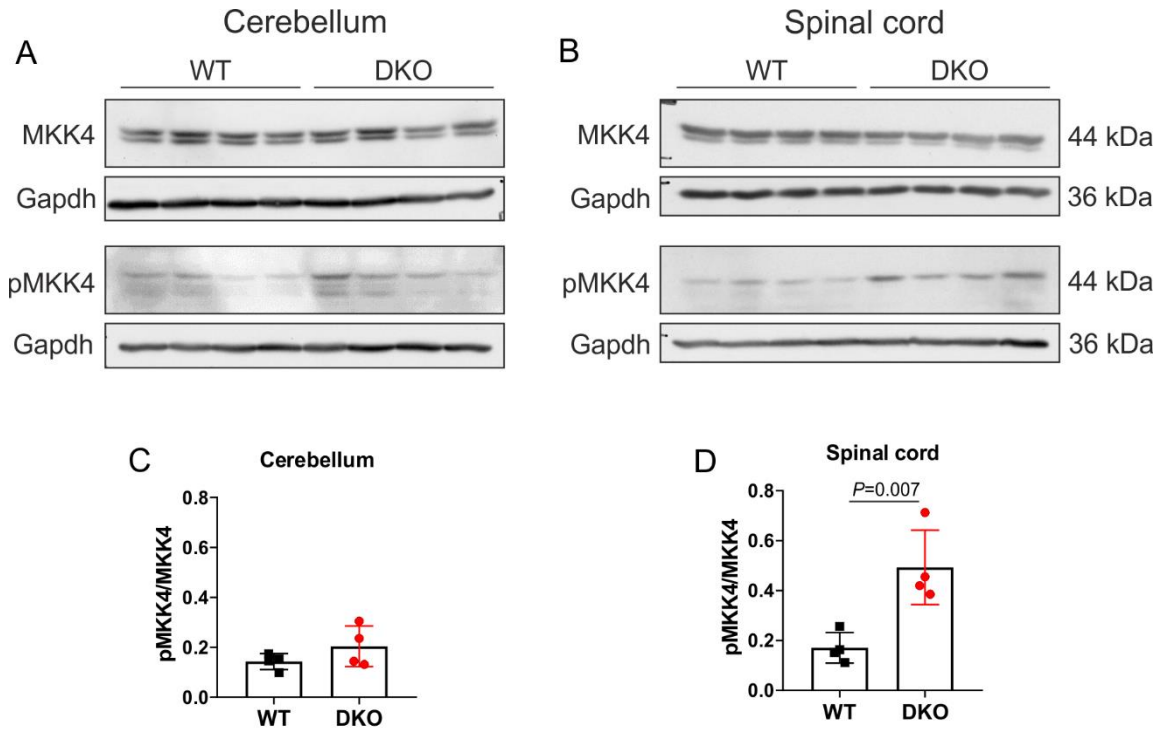

Figure 4.20. MKK4 gets highly phosphorylated in DKO spinal cord compared to WT mice. (A-B) Immunoblots of cerebellum and spinal cord lysates at 28 weeks against MKK4 and phosphorylated MKK4 (pMKK4), with GAPDH used a loading control. (C-D) Quantification of immunoblots shown in A and B, respectively. Data represented as mean ± SD, with each dot being one mouse, all males. *P* value obtained from Student's t-test.

The activity of SARM1 not only raises cADPR levels but promotes a decline in NAD^+ levels in neurons (Gerdts et al., 2015). Such reduction can also be influenced by an alteration of OXPHOS activity, particularly complex I, which regenerates NAD^+ from NADH. As stated by proteomic analysis, many proteins involved in OXPHOS presented altered levels in DKO samples, which could be impacting the NAD^+/NADH redox pair, further contributing to the activation of SARM1. To investigate whether this redox ratio is affected in paraplegin/AFG3L1-deficient mice, the same frozen spinal cord and cerebellar tissue used to measure cADPR, were also processed to detect both NAD^+ and NADH metabolites. DKO mice exhibited a tendency to a lower NAD^+/NADH ratio at 16 weeks of age (**Fig. 4.21, A, C**). This difference became significant in cerebellar tissue at 28 weeks (**Fig. 4.21, D**), whereas for 28 week old spinal cord both WT and KO had similar NAD^+/NADH ratio, not even showing the tendency observed at 16 weeks (**Fig. 4.21, B**). As with cADPR measurements, this might be explained by the prominent axonal degeneration the spinal cord presents, while cerebellar granule cells, the main neuronal type affected there, despite presenting mitochondrial alterations remain morphologically intact. Interestingly, 28 week old cerebellum from TKO mice did not show reduced NAD^+/NADH ratio compared to Sarm1KO samples (**Fig. 4.21, D**). Furthermore, we

could observed in general a big variability among all processed samples, reflecting not only the heterogeneity of the tissue but also the importance of the timing in the sample collection procedure, as this stress can quickly influence the volatile levels of both metabolites.

To conclude, these results not only point towards a dysregulated NAD^+/NADH homeostasis in DKO mice but also establish SARM1 as an important factor modulating this redox ratio in the mouse HSP-like pathology.

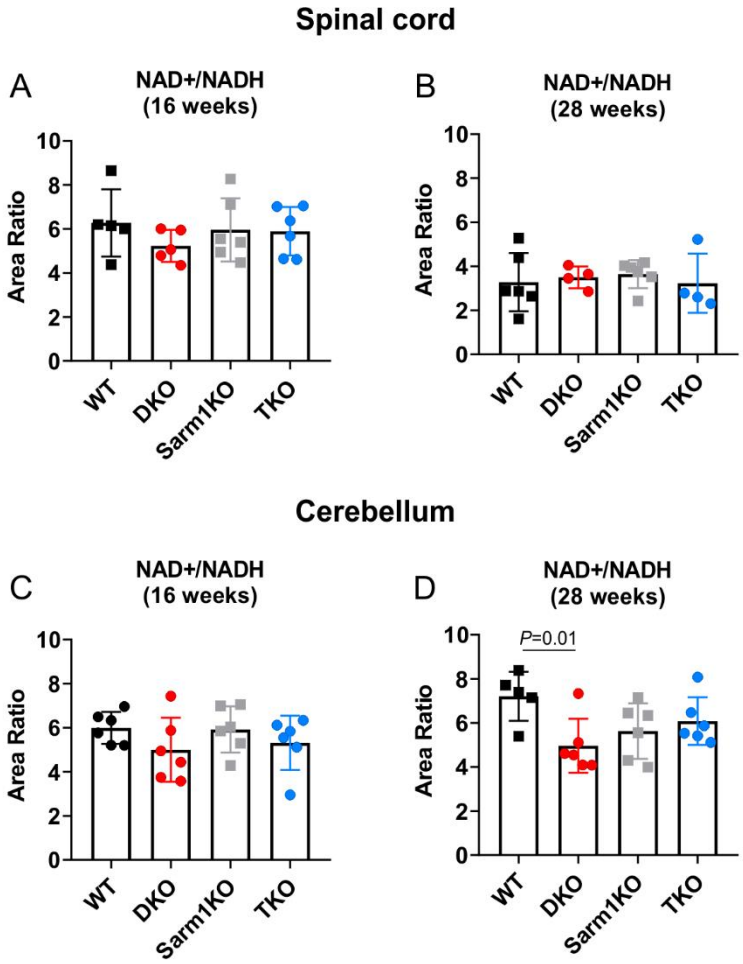

Figure 4.21. NAD^+/NADH ratio declines in DKO cerebellum at 28 weeks. (A-B) Area ratio of NAD^+/NADH measurements in spinal cord and (C-D) cerebellum at 16 and 28 weeks of age (n=4-6). Data are presented as mean ± SD. Each dot corresponds to one mouse, all males. One-way ANOVA was performed to compare all genotypes. Analysis performed by Susanne Brodesser.

4.7. Proteomics at 28 weeks reveal an alteration of a variety of cellular pathways upon absence of paraplegin and SARM1

Proteomics performed at 16 weeks in WT and DKO animals suggested, in line with previous findings, a role for paraplegin/AFG3L1 *m*-AAA proteases in ribosome biogenesis and assembly, OXPHOS activity and the transport of metabolites across mitochondria. This analysis, together with previous work on AFG3L2 (Maltecca et al., 2012, 2015), also hinted to an impaired calcium homeostasis, which may not only impact mitochondria but also other organelles, such as the ER. However, how these organelle alterations impair in a long-term scale cell function and trigger axonal loss in the HSP pathology remains unclear. The understanding of these long-term downstream effects upon paraplegin absence also allow us to decipher common underlying mechanism of the different types of HSP models, often caused by unrelated genes affecting totally different pathways (Klebe et al., 2015). Furthermore, the *in vivo* analysis with SARM1-deficient mice highlighted a contribution of sarmoptosis to the HSP-like mouse pathology. However, this contribution is tissue-dependent, as mitochondrial morphology appeared rescued in the cerebellum of TKO mice but not in the spinal cord, where several axons degenerated even in absence of SARM1. Moreover, this rescue seems rather short-term, as motor abilities of TKO mice assessed by the walking beam test appeared impaired from 32 weeks on. Therefore, sarmoptosis might be one of many factors implicated.

Hence, to understand the molecular role of SARM1 within the HSP pathology and shed light into other potential pathways involved, proteomic analysis were performed in parallel in all WT, DKO, Sarm1KO and TKO spinal cord and cerebellar samples at 28 weeks of age (n=5 per genotype). The proteomic output was then analysed by comparing separately litters mates coming from the same matings and with the same genetic background: DKO versus WT (C57BL6/N) and TKO versus Sarm1KO (88% C57BL6/N, 12% C57BL6/J). Protein changes were considered significant when q value < 0.1 and *P* value < 0.05 (no FC cut-off was applied).

In average, 7660 proteins were successfully quantified in cerebellum, out of which 1863 were significantly changed in absence of paraplegin/AFG3L1 (**Fig. 4.22, A; Suppl. Table S3**), many more than at 16 weeks of age. In fact, PCA clearly showed a segregation among the different phenotypes (**Suppl. S7, A**). Interestingly, only 3.8% of the total changed proteins were mitochondrial proteins (**Fig. 4.22, A-B**) (predicted by Mouse Mitocarta 3.0 with a total of 868 proteins detected), revealing downstream pathological pathways of the mitochondrial impairment. Moreover, the majority of these mitochondrial proteins localised either at the IMM or the matrix, in line with currently known interactors and substrates of *m*-AAA proteases. Strikingly, only 218 out of the total proteins detected were differentially expressed in the TKO samples compared to Sarm1KO mice (**Fig. 4.22, C**), 27% of which were mitochondrial

proteins. The majority of these mitochondrial proteins were similarly altered in the DKO at 28 (**Fig. 4.22, D**) and 16 week old samples, such as MPC1-1, PHB1-2, AFG3L2 and UQCC1, most likely because these proteins are directly associated with the *m*-AAA complexes which are likewise impaired in the TKO mice. Only 5 mitochondrial proteins were significantly changed in TKO cerebellum (vs Sarm1KO) but not in DKO samples (vs WT) (**Fig. 4.22, D**): SLC25A14 (mitochondrial transporter of inorganic anions, FC=1.4), PDK1 (kinase modulating cell energetics via pyruvate dehydrogenase activity, FC=-1.2), the mitochondrial ribosomal protein MRPS18 (FC=-1.2), MIPEP (mitochondrial peptidase, FC=-1.4) and FDX1 (biosynthesis of steroid hormones, FC=-1.7). The fact that these mitochondrial proteins are changed upon SARM1 absence arises the interesting possibility that SARM1 might be directly mediating changes at the level of mitochondria through its activity. Furthermore, TKO exhibited many non-mitochondria proteins changed that were not so much overlapping with the ones found altered in the DKO (**Fig. 4.22, E**). This first assessment of the proteomic analysis indicate that the lack of SARM1 in the cerebellum is able to remodel the entire cellular proteome in absence of paraplegin.

Spinal cord proteomics showed about 7534 found records, 27 of which were significantly altered in DKO mice (**Fig. 4.22, F; Suppl. Table S4**), which was incredibly less than 28 week old cerebellum and 16 week old spinal cord analysis. This is in congruence with the previous analysis of axonal degeneration shown, as the axonal loss is likely dwindling the real impact the impaired *m*-AAA protease has in this tissue. PCA showed a segregation only of the DKO mice from the rest of the genotypes (**Suppl. S7, B**). Out of these 27 proteins changed, 24 were mitochondrial proteins (**Fig. 4.22, G**), all of them already found altered at 16 weeks of age. Similarly, the TKO/Sarm1KO comparison in spinal cord gave a comparable outcome, with 23 proteins changed from which 18 were mitochondrial proteins, all of them changed comparably in DKO tissues (**Fig. 4.22, H**). Additionally, only 4 proteins were significantly changed in TKO spinal cord (vs Sarm1KO) but not in DKO tissue (vs WT): ACTG2 (actin, FC=-2.7), PDLIM7 (cytoskeleton organisation, FC=-2.5), SYT10 (synaptic transmission, FC=2) and TCP11L2 (signal transduction, FC=-5.4). Further differences within this tissue will later be studied by pathway analysis comparisons.

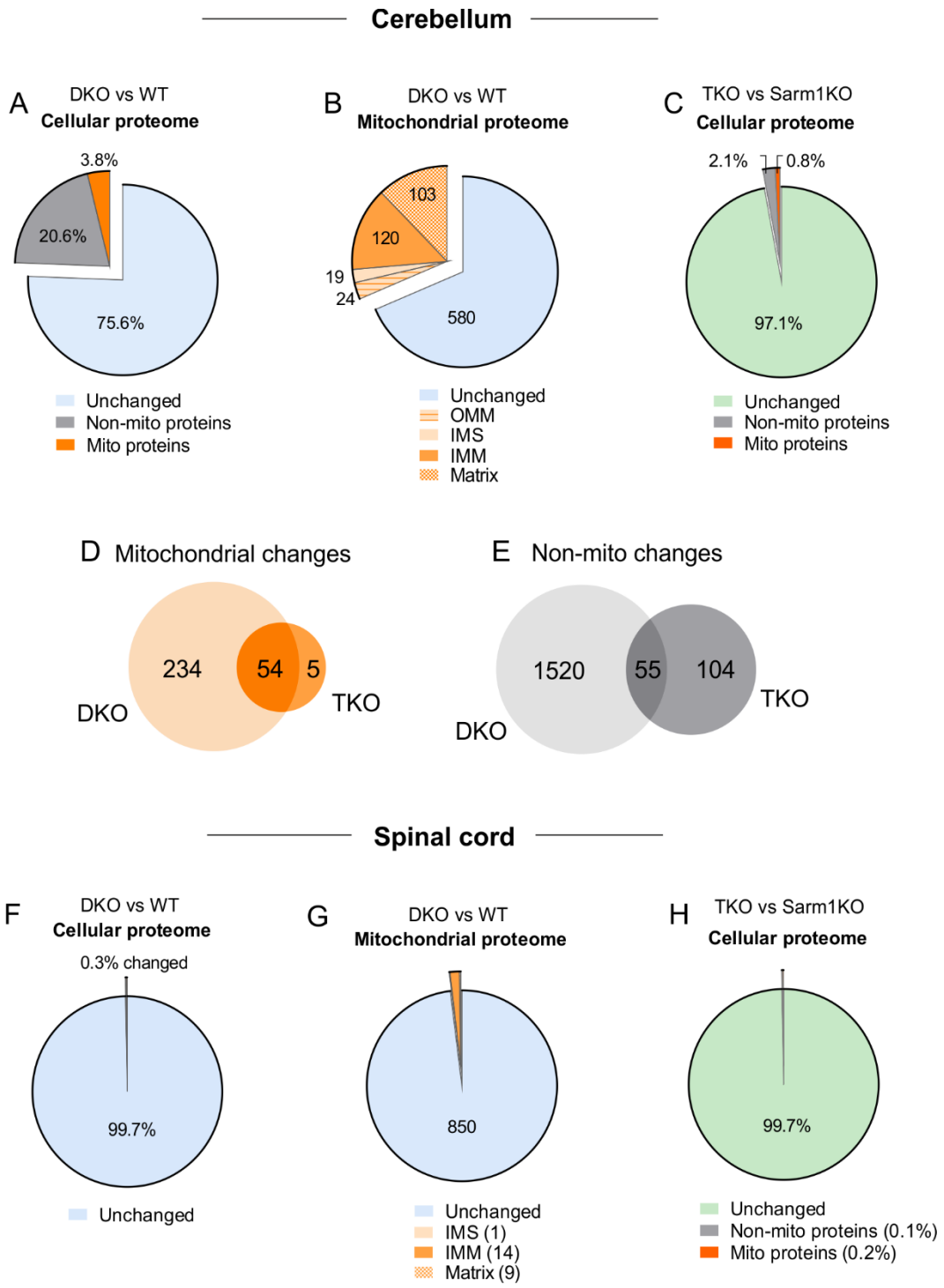

Figure 4.22. The loss of paraplegin/AFG3L1 affects predominantly the cerebellar proteome at 28 weeks. (A-B) Pie charts representing the proportion of cellular and mitochondrial proteome changes in cerebellum and (F-G) spinal cord of the DKO mice compared to WT samples. (C-H) Pie charts from TKO vs Sarm1KO proteomic analysis. (D-E) Venn diagrams of significantly changed mitochondrial and non-mitochondrial proteins in DKO cerebellum (vs WT) and in TKO samples (vs Sarm1KO). q value < 0.1, *P* value < 0.05. No FC cut-off was applied. n=5 samples per genotype.

4.7.1. The absence of paraplegin and AFG3L1 greatly influences proteins involved in cerebellar bioenergetics

One of the most affected cellular pathways of the DKO cerebellum was OXPHOS. Not only was this pathway highly enriched (**Fig. 4.25, A**) but also many proteins were found either significantly increased or decreased when compared to WT samples (66 out of 106 proteins allocated to the term OXPHOS) (**Fig. 4.23, A**). These proteins are involved in the structure and assembly of all five OXPHOS complexes, but it altered in particular complex I (CI). The majority of these CI subunits were increased (FC > 1.5 in 7 out of 23), with few subunits showing reduced levels, among them mitochondrial-encoded proteins: MT-ND4, MT-ND2 and MT-ND5 (FC < -2). Mitochondrial-encoded proteins from other complexes were also altered: MT-CO2, MT-CO3 and MT-ATP8. This support the previous described role of *m*-AAA proteases in mitochondrial translation and confirms the proteomic results obtained at 16 weeks in the DKO mice. In line with this, several mitochondrial ribosomal components were also observed decreased (39 out of 47 detected in total), with only three of them displaying more levels than the WT samples (**Table S3**). Interestingly, at this time point DKO cerebellum also showed a big amount of cytoplasmic ribosomal proteins decreased (23 out of 46 measured), indicating that an alteration of *m*-AAA proteases also impacts cytosolic translation (**Suppl. Table S3**).

Although an accumulation of OXPHOS subunits does not go in hand with a change in OXPHOS activity, a beyond-physiological ROS production can be an indicator that these complexes are not working appropriately. Different proteins involved in antioxidant functions are significantly increased in DKO cerebellum, including superoxide dismutases (SOD1 and SOD2), glutathione reductase (GSR) and peroxiredoxin family members (PRDX3, PRDX5) (**Fig. 4.23, A**). Furthermore, many proteins from the metabolism of carbohydrates were altered in the DKO cerebellum (q value < 0.1), supporting the idea of a hindered mitochondrial ATP production. Among them, MPC1 and MPC2 appeared as the most reduced proteins, with approximately a 90% reduction of MPC1 compared to WT samples. This implies that only a little portion of cytosolic pyruvate enters the mitochondria, hampering, therefore, mitochondrial metabolism. In fact, many glycolysis-associated proteins were significantly increased in DKO samples, including HK2, GDPGP1, GAPDH, PFKFB4 and PCK2, suggesting a shift in the metabolism towards anaerobic respiration. Furthermore, fatty acid metabolism, and lipid metabolism in general, also appeared affected, as many proteins were found altered in the DKO cerebellum, such as ACOT7 (thioester hydrolase), SCD1 (Acyl-CoA desaturase) and MBOAT7 (acyltransferase) (**Suppl. Table S3**).

In contrast to this, TKO cerebellum did not present OXPHOS alterations when compared to Sarm1KO samples, with the exception of three proteins: SCO2 (complex II maturation),

SURF1 (complex IV assembly) and UQCC1 (complex III assembly) (**Fig. 4.23, B**). These three proteins are similarly changed in 16 and 28 weeks DKO proteomics, most likely due to a direct effect of *m*-AAA protease absence. In congruence with this, TKO samples did not exhibit changes in antioxidant enzymes, indicating a controlled ROS homeostasis. Despite presenting also MPC1-2 transporters highly reduced, TKO cerebellum presented normal levels of the aforementioned metabolic enzymes compared to Sarm1KO samples (**Fig. 4.23, B**). In some cases, TKO even displayed proteins with totally opposite levels than the DKOs, for example the transporters SLC4A1 and SLC47A1 and the carbonic anhydrase CA1, all quite decreased in DKO samples but significantly increased in TKO samples (**Table 4.5**).

These results highlight the presence of different metabolic scenarios in DKO and TKO cerebellar tissues, with a metabolic rewiring taking place upon *m*-AAA deficiency which is then restored in absence of SARM1.

Table 4.5. **List of proteins changed in opposite directions in the different genotypes.**

Protein	Description	**TKO** (vs Sarm1KO)	**Sarm1KO, DKO** (vs WT)
BPGM	Regulates hemoglobin oxygen transport	↑	↓
CA1	Catalyses the reversible hydration of carbon dioxide	↑	↓
EPB42	Erythrocyte membrane protein band	↑	↓
MRPL50	Nuclear-encoded mitochondrial ribosome	↓	↑
SERPINA3K	Serine protease inhibitor (targets mainly trypsin)	↑	↓
SERPIN1C	Serine protease inhibitor (targets thrombin and trypsin)	↑	↓
SLC4A1	Structural glycoprotein and anion exchange transporter	↑	↓
SLC47A1	Transporter of cationic drugs that cleanses the CSF	↑	↓

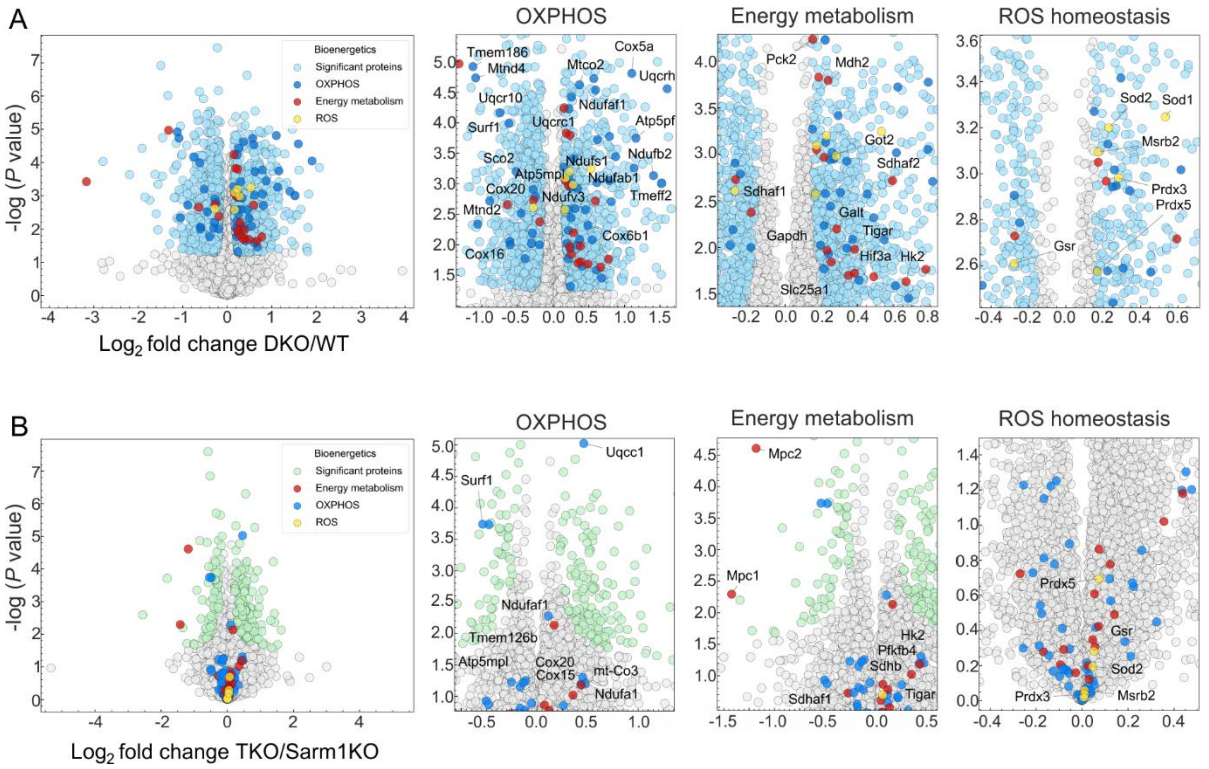

Figure 4.23. Cerebellum from DKO mice exhibit altered cellular respiration, which is restored in TKO samples. (A) Volcano plot and its corresponding close ups highlighting OXPHOS subunits (indicated in dark blue), proteins involved in energy metabolism (red) and ROS homeostasis (yellow) of DKO compared to WT cerebellum (all significant proteins changed are highlighted in light blue). (B) Volcano plot and its close ups of TKO vs Sarm1KO samples (total significantly changed proteins in green). q value < 0.1, *P* value < 0.05. n=5 per genotype.

4.7.2. NAD⁺ homeostasis alterations in DKO cerebellar tissue

NAD⁺ homeostasis is tightly linked to mitochondrial metabolism. Within mitochondria, CI activity constitutes a crucial factor contributing to its maintenance, as it regenerates NAD⁺ from NADH while transferring the electrons forward in the ETC. Indeed, mutations in CI subunits responsible for the NADH oxidation (NDUFS1, NDUFV1-2) are associated with a variety of neurological conditions in humans, such as leukoencephalopathy, schizophrenia, Alzheimer's disease and the Down syndrome (Karry et al., 2004; S. H. Kim et al., 2001; Z. Liu et al., 2022). As mentioned in the previous section, the levels of many complex I subunits appeared dysregulated in DKO cerebellum, as opposed to TKO samples, which displayed no significant differences compared to Sarm1KO samples. Moreover, mitochondrial NAD⁺ homeostasis is also ensured by other means, including the NAD⁺ Salvage pathway (see section 1.4.1). Proteomic analysis interestingly showed altered levels of the key enzymes involved in this pathway: NMNAT2 (cytosol) and NMNAT3 (mitochondria), displaying both enzymes increased levels in DKO cerebellar tissue (FC > 1.5) (**Fig. 4.24, A**). To confirm this

results, a staining using an antibody against NMNAT2 was performed in cerebellar free floating slices, where DKO tissues showed indeed increased levels of this NAD enzyme compared to both WT and TKO samples (**Fig. 4.25**).

In line with this, other proteins of the NAD^+ metabolism were also found changed: Naxe, an enzyme that prevents the accumulation of toxic NAD metabolites (NADHX and NADPHX), NADK2, an enzyme that synthesizes $NADP^+$ from NAD^+, QPRT, a rate-limiting enzyme of the kynurenine pathway and SLC25A51, the recently-discovered mitochondrial NAD^+ transporter (**Fig. 4.24, A**). Interestingly, upon SARM1 deletion, none of these proteins were significantly changed anymore (**Fig. 4.24, B**), suggesting a regulated NAD^+ homeostasis in TKO cerebellar samples.

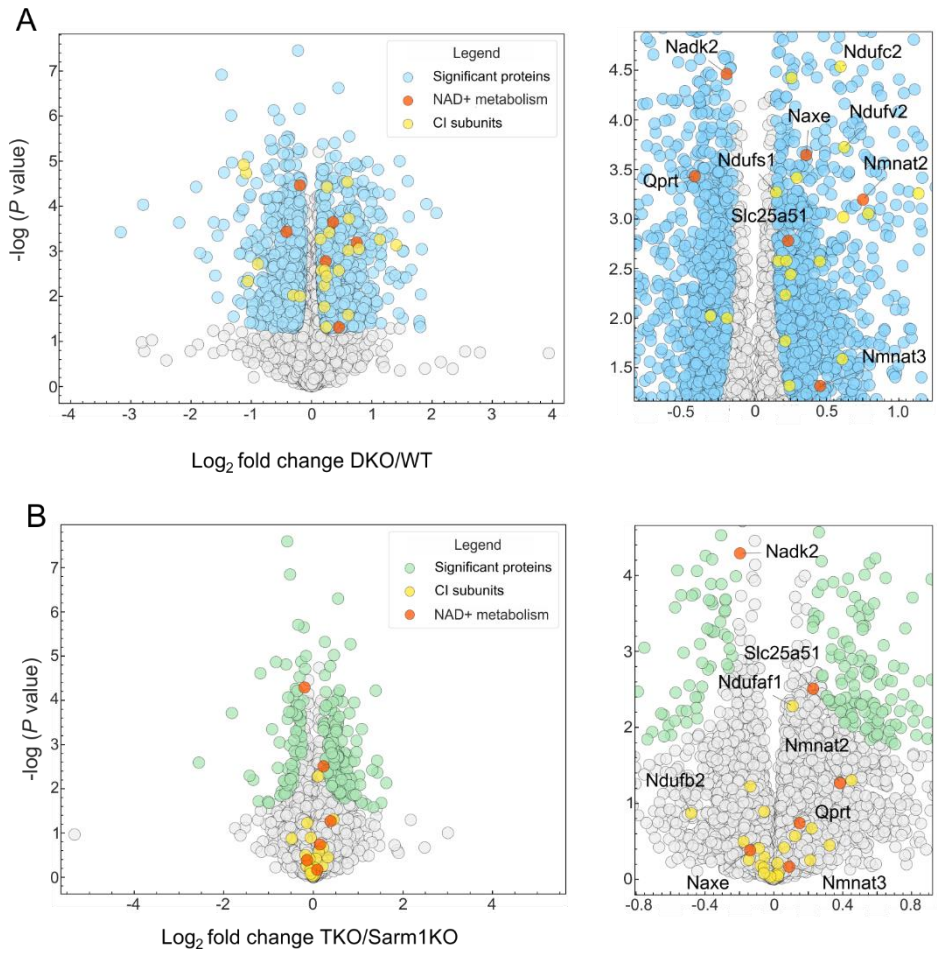

Figure 4.24. Cerebellar proteomics of DKO mice exhibits several NAD^+-related proteins altered, which are rescued to control levels in TKO cerebellum. (A) Volcano plot of DKO mice when compared to WT mates and its corresponding close up, highlighting total significantly changed proteins (blue), altered complex I subunits (yellow) and proteins involved in NAD^+ metabolism (red). (B) Similar volcano plot corresponding to the comparison between TKO and Sarm1KO cerebellum and its respective close up (total significantly changed proteins in green). q value < 0.1, *P* value < 0.05. n=5 samples per genotype.

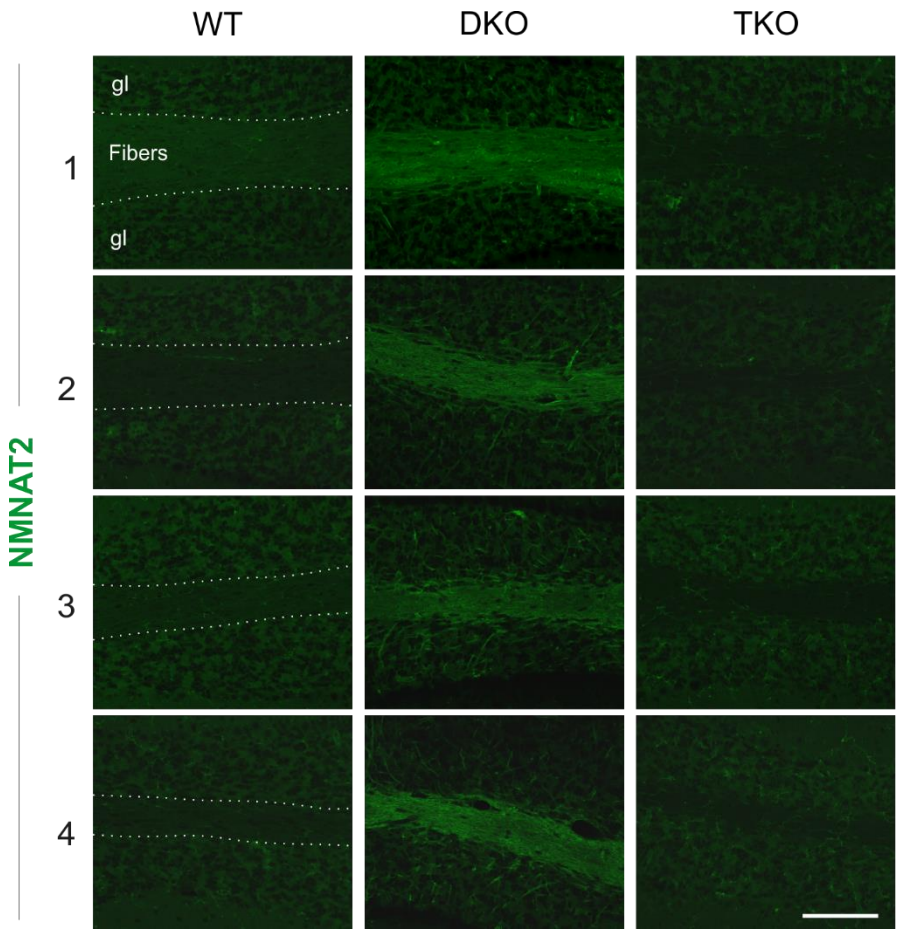

Figure 4.25. Increased staining of NMNAT2 in DKO cerebellar fibers. Immunofluorescence staining against NMNAT2 in four biological replicates (1-4) of WT, DKO and TKO genotypes. Scale bar: 40 μm. gl: granule layer.

4.7.3. Cellular pathway differences between SARM1 and paraplegin-deficient mice are tissue-dependent

Proteomics were also processed using the Gene Set Enrichment Analysis (GSEA) software, which allows the analysis of the entire proteome based on pre-ranked lists defined by a statistic value, without previous filtering. In this way, it performs enrichment analysis against different pathways to study the distribution of certain categories (for example, the GO dataset) across the ranked list of proteins (Reimand et al., 2019). As the main outcome, it gives an enrichment score normalized by the size of the proteins in the defined category (NES) and an adjusted *P* value (FDR, q value). Following this analysis, those pathways enriched at the top of the ranked list present higher NES values (positive), whereas those distributed at the bottom exhibit lower NES values (negative). For the current analysis, a test statistic was used for the ranking, which integrates the information of both *P* value and FC of the given proteins. Moreover, only resulting pathways presenting a q value < 0.2 were considered for analysis. Since this analysis considers the entire list of detected proteins, not only a comparison between the KO mice and their respective control is useful, but also between TKO and DKO mice, as it could give some hints towards broad cellular differences existing between both genotypes that are missing in the previous comparisons.

Pathway analysis of 28 weeks cerebellum using the GOBP database confirmed previous analysis at a protein level, as OXPHOS, the superoxide metabolic process, and energy derivation by oxidation of organic compounds were highly positively enriched pathways, whereas cytoplasmic translation was found negatively enriched in DKO samples (**Fig. 4.26, A**). Moreover, these broad analyses also brought up other enriched pathways in DKO cerebellum, such as the protein localization to mitochondrial membrane. In agreement with this, many TIM and TOM subunits were observed significantly changed in DKO proteomic analysis. Surprisingly, none of these pathways was found altered in TKO cerebellum with respect to Sarm1KO samples (**Fig. 4.26, B**), which was further confirmed by comparing TKO with DKO samples, being all of them negatively enriched in this last comparison (**Fig. 4.26, C**). Furthermore, one of the highest positively enriched categories in TKO cerebellum was the regulation of coagulation, which goes in line with the fact that many SERPINs (serine protease inhibitors) appeared significantly increased in proteomic analysis. Although SERPINs have been mainly studied in the context of cancer, it seems that in the brain they carry a neuroprotective role protecting neurons from apoptosis (Yepes et al., 2000). Other TKO greatly enriched categories included DNA repair, immune response and inflammatory response, maybe reflecting the way these mice cope with the consequences of a *m*-AAA protease deficiency.

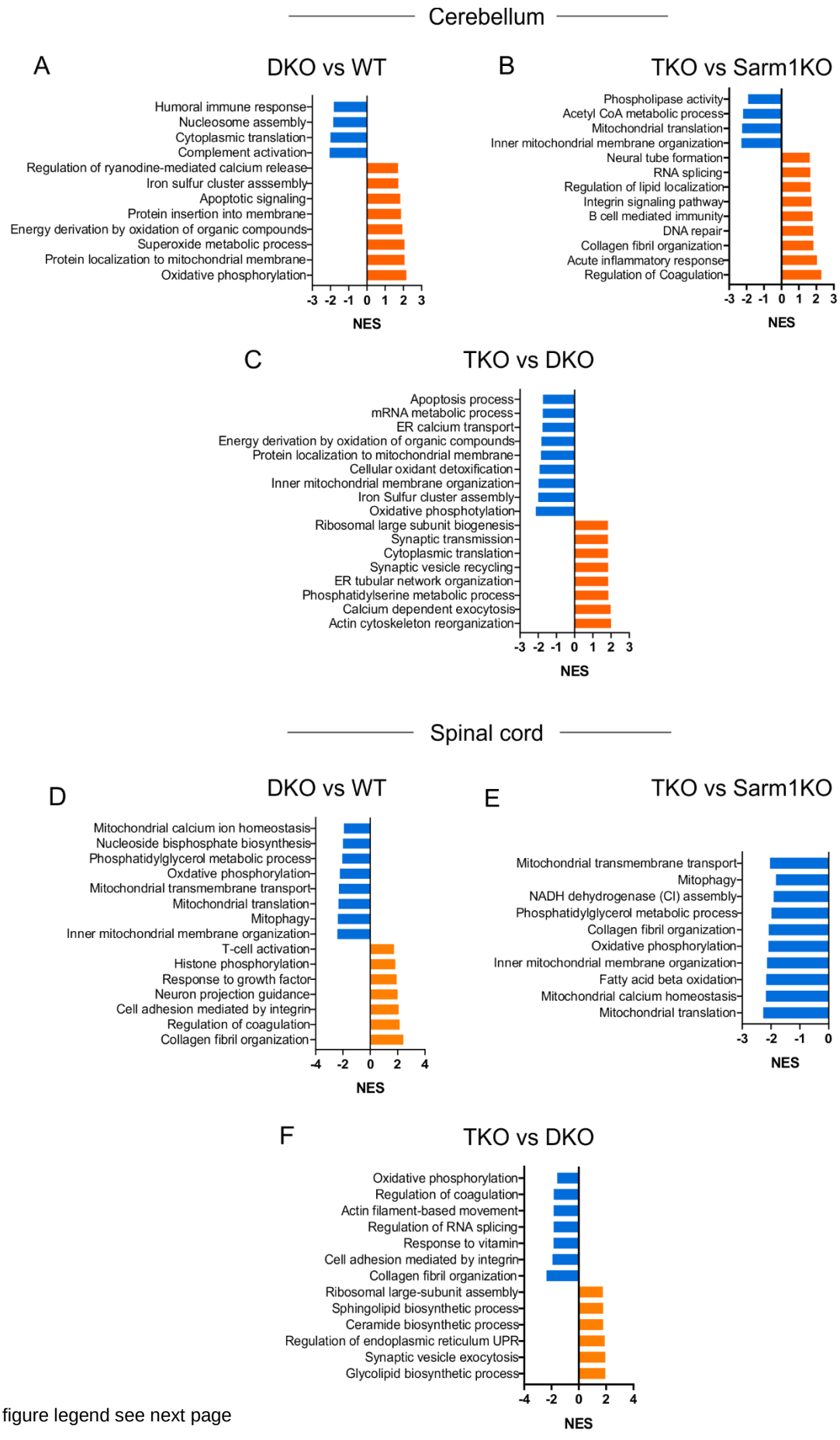

For figure legend see next page

Figure 4.26. Proteomics pathway analyses at 28 weeks reveal cellular differences between DKO and TKO mice in a tissue-specific manner. (A-F) Graphs representing GO categories for biological processes obtained by GSEA analysis of proteomics data. (A, D) Category differences between DKO and WT mice, (B, E) TKO and Sarm1KO samples and (C, F) TKO and DKO tissues. NES represents the normalized enrichment factor. q value < 0.2. A detailed description of the pathways, including the individual significance, can be found in Table S5.1-3 and S6.1-3.

28 weeks spinal cord proteomics showed little protein changes. However, pathway analysis showed a wider diversity of pathway differences between all different genotypes. First, paraplegin and AFG3L1 loss in this tissue seems to highly impact cell adhesion mediated by collagen and integrins, as this pathway not only was already enriched at 16 weeks (**Fig. 4.11, A**) but also was the most positively enriched at 28 weeks (**Fig. 4.26, D**). Moreover, many pathways showing high NES were related to neuronal development, including “neuron projection guidance”, response to growth factor an cell chemotaxis. Surprisingly, almost all mitochondrial-related categories positively enriched in DKO cerebellum were then observed negatively enriched in the spinal cord. This is the case for the organization of the inner membrane, OXPHOS and the nucleoside triphosphate biosynthesis. Many other mitochondrial pathways were also found negatively enriched, such as mitophagy and mitochondrial calcium homeostasis. Moreover, lipid metabolism seems to also be affected in the DKO, as low NES categories appeared involving phospholipase activity, the metabolism of phosphatidylglycerol, thioester and steroids. When comparing with Sarm1KO, TKO exhibited a similar outcome to DKO analysis, although this comparison only yielded negatively enriched categories (**Fig. 4.26, E**). Among these, there appeared the lipid and mitochondrial-related pathways already found in the DKO/WT comparison. Nonetheless, one of the main pathway differences observed between TKO/Sarm1KO and DKO/WT mice was cell adhesion, as TKO mice showed this pathway negatively enriched instead.

Further pathways analyses directly comparing TKO with DKO samples in both tissues pointed towards a different status of synaptic transmission, as categories such as the organization of synaptic vesicles and calcium regulated exocytosis presented higher NES in TKO tissues, and towards a differential regulation of the ER network, as TKO samples showed -ER tubular organization, ER calcium transport and the ER unfolded protein response- as significantly enriched categories when compared to DKO samples (**Fig. 4.26, F**).

4.8. The loss of Sarm1 rewires mitochondrial proteome in *wild-type* conditions

The cellular interaction network of SARM1 in a steady state has barely been in a focus of research. We know that SARM1 is able to modulate neuronal polarity by interacting with syndecan-2 (Chen et al., 2011) and it also binds PINK1 and TRAF6 to regulate mitophagy (Murata et al., 2013). However, how the loss of SARM1 broadly influences the cerebellar and spinal cord proteome in physiological conditions remains unclear. To shed light into this direction, 28 weeks proteomic analyses from Sarm1KO tissue were compared to WT mice (proteins were considered significant when q value < 0.1, *P* value < 0.05; no FC cut-off applied) and further analysed by pathways analysis using the GSEA software (q value < 0.2).

The deletion of SARM1 in spinal cord only altered the levels of 15 proteins, which were mainly involved in three cellular processes: the organization of the extracellular matrix (COL2A1, COL1A1), mitochondrial metabolism (NDUFS6, ATOX1) and the regulation of RNA splicing (ALYERF, SRSF7) (**Fig. 4.27, A; Suppl. Table S4**). Pathway analysis also included these processes as significantly enriched in Sarm1KO spinal cord, and highlighted other categories with higher NES such as sterol biosynthesis, fatty acid metabolism and positive regulation of T-cell proliferation, and with lower NES, including OXPHOS, microtubule polymerization and the negative regulation of calcium transport (**Fig. 4.30, A**).

Cerebellar proteomic analysis unravelled a higher impact of SARM1 deletion on the cerebellar proteome, as 122 proteins were significantly changed in Sarm1KO tissue compared to WT (**Fig. 4.27, B; Suppl. Table S3**). In general, two groups of proteins were observed: one formed by proteins significantly changed in Sarm1KO with respect to WT, which were not changed in the previous TKO/Sarm1KO comparison (group 1), reflecting changes that are intrinsic to SARM1 function, and another set of altered proteins (group 2) that were also dysregulated in TKO animals compared to Sarm1KO individuals, suggesting that these proteins are part of the crosstalk network between SARM1 and paraplegin.

Group 1 of proteins clustered in various pathways using String network analysis (**Fig. 4.28**), which were the same cellular processes found in spinal cord protein and pathway analysis (**Fig. 4.30, A**), although surprisingly with a totally opposite enrichment value (**Fig. 4.30, B**). Noteworthy to mention, is the substantial amount of altered proteins affecting mitochondrial function in Sarm1KO cerebellum (20 in total, FC > 1.5), 2/3 of which were OXPHOS subunits and protein import machinery components. Interestingly, within the changes observed in OXPHOS proteins, the mitochondrial-encoded ATP8 subunit (complex V) appeared significantly increased in Sarm1KO samples (FC=3), similarly as observed with DKO cerebellum (FC > 3).

Moreover, deletion of SARM1 seems to also affect glutamatergic synaptic transmission, as this category was found enriched in Sarm1KO cerebellum after GSEA analysis (**Fig. 4.30, B**).

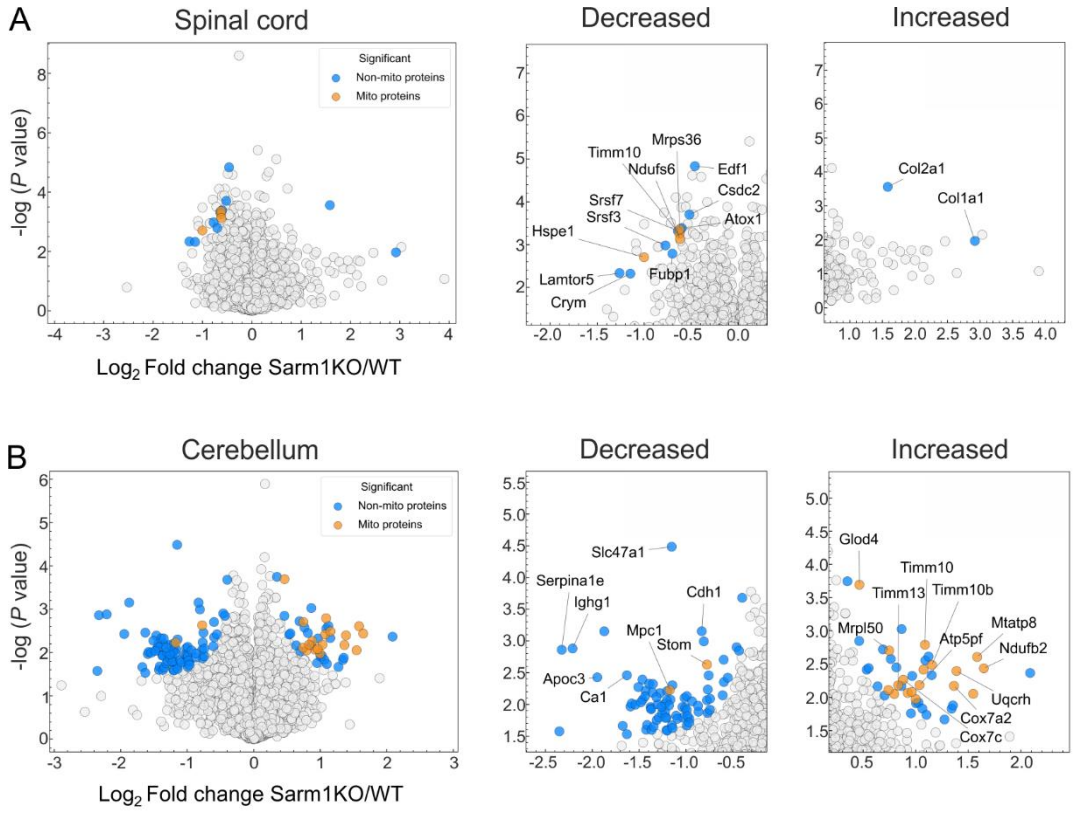

Figure 4.27. The loss of SARM1 in cerebellum remodels the cerebellar proteome in absence of damage. (A) Volcano plots from spinal cord and (B) cerebellum and their respective close ups highlighting significantly increased and decreased mitochondrial proteins (orange) and non-mitochondrial proteins (blue). q value < 0.1, *P* value < 0.05. n=5 per genotype.

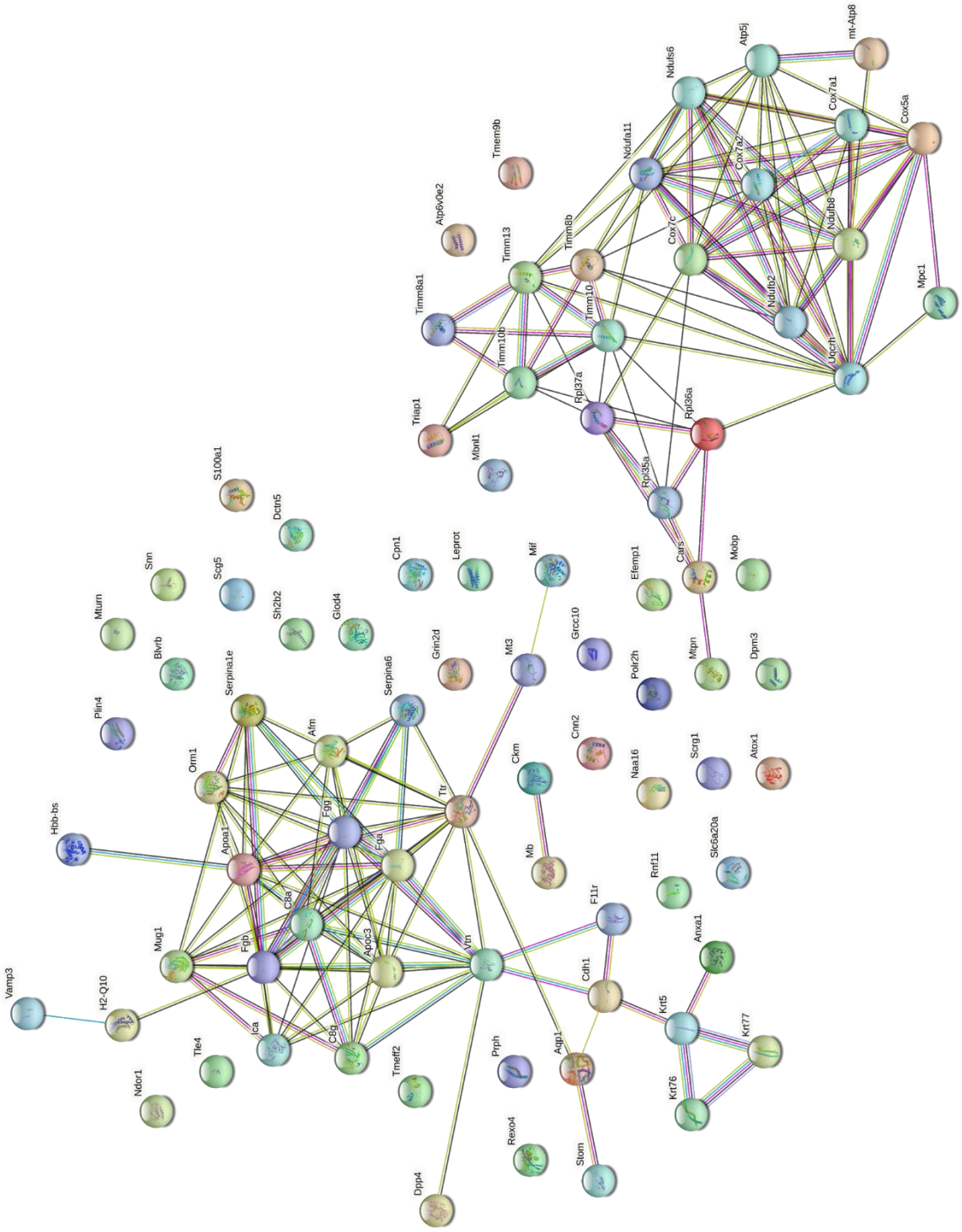

Figure 4.28. String network analysis of proteins belonging to group 1 of the Sarm1KO vs WT comparison. The represented proteins are altered in Sarm1KO individuals (vs WT), with similar protein levels in TKO mice (vs Sarm1KO), indicating that these changes are influenced by SARM1 function *per se*. (q value < 0.1)

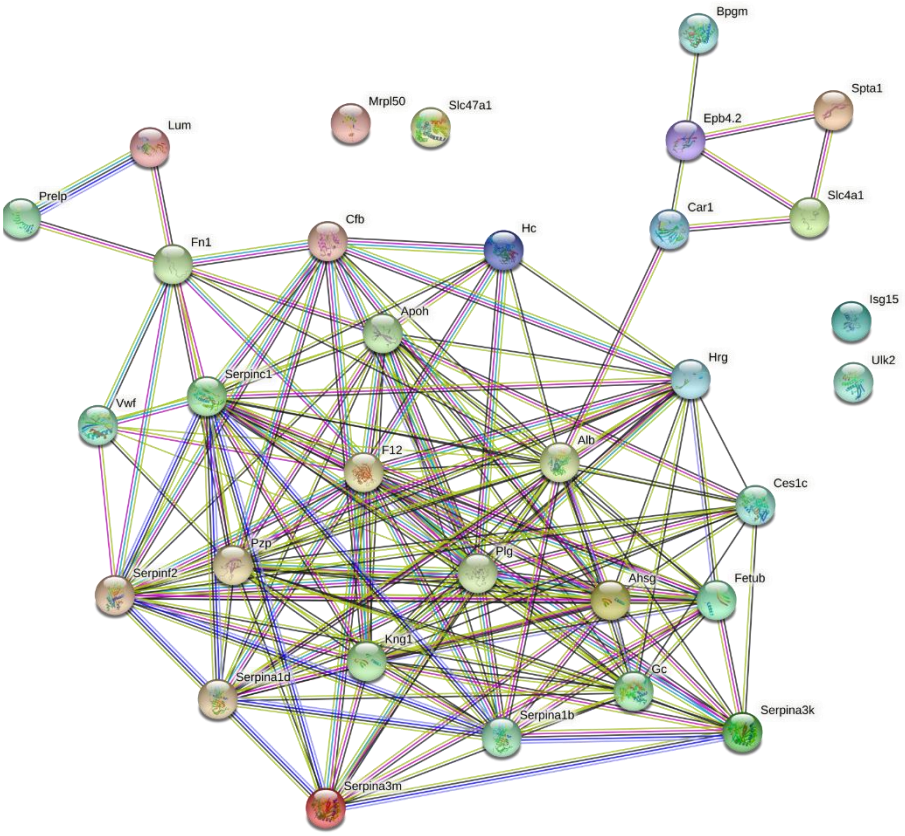

Figure 4.29. String network analysis of proteins belonging to group 2 of the Sarm1KO vs WT comparison. The represented proteins are altered in Sarm1KO individuals (vs WT) and in TKO mice (vs Sarm1KO), reflecting alterations influenced by both SARM1 and paraplegin absence. (q value < 0.1)

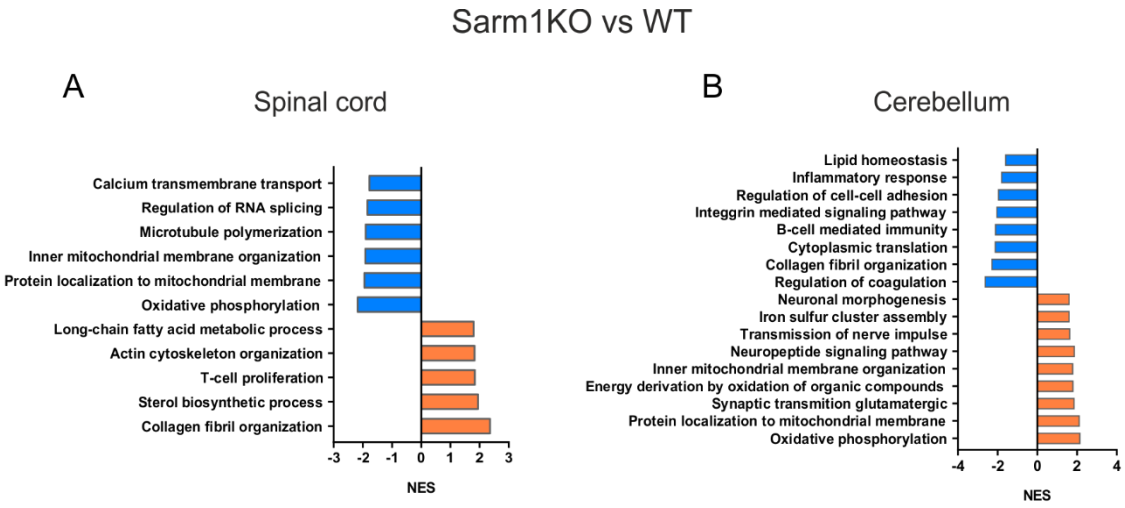

Figure 4.30. Pathway analysis reveals alterations in various cellular processes upon SARM1 absence. (A-B) Graphs representing the pathway analysis performed with GSEA of highly positively and negatively enriched cellular pathways (q value < 0.2). A detailed description of the pathways, including the individual significance, can be found in Table S5.4 and S6.4.

On the contrary, group 2, exclusive of cerebellar tissue, contained 33 proteins (27% of the total change) including mostly endopeptidase inhibitors and glycoproteins, which clustered together in the String analysis (**Fig. 4.29**). These inhibitors target various cysteine and serine proteases involved in blood coagulation such as thrombin and trypsin. Plasminogen, the precursor of plasmin (promotes fibrin breakdown and the removal of blood clots), was also found altered in Sarm1KO animals. Besides their role in thromboembolic conditions, these proteins participate in multiple brain processes, including learning and memory via modulation of synaptic transmission and plasticity (Ben Shimon et al., 2015; Briens et al., 2017). Additionally, thrombin also presents pro-inflammatory activity (Ben Shimon et al., 2015). Sarm1KO mice displayed reduced levels of protease inhibitors, glycoproteins and plasminogen compared to WT, indicating a direct role of SARM1 in inflammatory responses and glutamatergic synaptic transmission, while TKO animals, on the contrary, exhibited increased levels of these proteins compared to Sarm1KO (q value < 0.1, FC > 1.5), as if trying to shut down these processes to cope with the consequences of paraplegin loss. Furthermore, only two proteins were found increased in Sarm1KO cerebellum, one of which was the nuclear-encoded mitochondrial ribosomal protein MRPL50. Unexpectedly, this mitoribosomal component was also found increased in DKO cerebellum, but significantly decreased in TKO mice compared to their respective controls. This fact, apart from supporting the previously mentioned role of SARM1 in mitochondrial translation, places MRPL50 in the network influenced by both SARM1 and paraplegin. This mitoribosomal protein is, however, not the only protein following this pattern, as the proteins that were found oppositely regulated in DKO and TKO samples compared to their controls, described in **table 4.5** (*section 4.7.1*), were also significantly decreased in Sarm1KO compared to WT. This finding supports the idea of a common protein network between SARM1 and paraplegin whose implication has yet to be studied.

5. Discussion

5.1. The DKO mouse line as an accurate research model to study SPG7-HSP

The first aim of this thesis was to develop a mouse model that could mimic closely the human SPG7 pathology. This autosomal recessive HSP condition is caused by mutations in *Spg7*, the gene encoding for paraplegin, a subunit of the *m*-AAA protease localized to the inner membrane of the mitochondria. AFG3L2 and, only in murine, AFG3L1, assemble with paraplegin to make up the different *m*-AAA protease complexes involved in mitochondrial quality control. The role of paraplegin in the appearance of HSP was previously studied using a mouse model *knock-out* (KO) for *Spg7* (Ferreirinha et al., 2004). These mice recapitulated the main features of the human patients: spinal cord and peripheral axonopathy, optic atrophy and mild muscular impairments. However, as with many other mouse models of HSP (Blackstone, 2015; Fassier et al., 2015), the clinical manifestations are only noticeable at late ages.

Several factors could be contributing to the mouse phenotype onset, for instance the fact that the dorsal corticospinal tract (CST), whose degeneration constitute the main HSP neuropathological feature, is polysynaptic and with shorter corticospinal axons in mice compared to humans (Sengul & Watson, 2012). In fact, I demonstrated in this study that the most affected spinal cord tracts in the DKO mice are instead those located in anterior areas, corresponding to long ascending and descending axonal fibers of different motor, and to a lesser extent sensory, pathways (described in the introductory section 1.1.2) (**Fig 4.5**). One way to explain this could be the higher length these motor axons present in mice, which, similar to those of the CST in humans, would make their distal areas vulnerable to an impairment of mitochondrial functions. However, sensory tracts originate peripherally and do not concur with this hypothesis, indicating that there must exist other neuron-specific factors in play.

Moreover, the old *Spg7* KO model presents AFG3L1 and paraplegin-2. Most of the current evidence about AFG3L1 indicates that this protein might be present in mouse as a redundant mechanism to support a functional *m*-AAA protease. For instance, the brain expression of *Afg3l1* is quite low compared to its homolog *Afg3l2* and *Spg7* (Koppen et al., 2007; Martinelli et al., 2009). In addition to this, mice lacking AFG3L1 develop no clinical phenotype and show neuronal mitochondria that resembles those from WT animals (**Suppl. S2, A**). These findings indicate that the rest of the *m*-AAA protease subunits can perfectly make up for the loss of this protein. However, the recent study from Hurst et al., demonstrated a compensatory effect of AFG3L1, by rescuing the calcium impairments observed in the *SPG7* KO human cells with the mouse AFG3L1. Besides this, *Afg3l1* constitutes a pseudogene in humans (Kremmidiotis et

al., 2001). Therefore, to accurately reproduce the human HSP disease and rule out a compensatory effect of AFG3L1, a mouse model lacking both paraplegin and AFG3L1 proteins was needed (DKO model). In this thesis, I showed how this new mouse model displays indeed a worsening of the phenotype, exhibiting weight alterations and axonal degeneration earlier than reported in the previous *Spg7* KO model (**Fig. 4.2-4.3**). These results support a cooperative role between paraplegin and AFG3L1 mediated by the formation of *m*-AAA protease heterocomplexes, which are likely carrying out complex-specific functions. Moreover, the pathological phenotype observed in the DKO mice is halfway to the one observed in mice without paraplegin and haploinsufficient for *Afg3l2* (Martinelli et al., 2009), which agrees with the low expression of *Afg3l1* detected in the brain compared to the high expression of *Afg3l2*.

Nevertheless, the worsening of the phenotype should not be attributed exclusively to AFG3L1, as DKO mice also lack paraplegin-2. This isoform of paraplegin does not contain a mitochondria targeted sequence and localizes instead to the endoplasmic reticulum (ER) (Mancuso et al., 2012). Although the levels of paraplegin-2 appeared lower than those of the mitochondrial paraplegin and its function is so far unknown, the protein structure is conserved between both isoforms, suggesting that paraplegin-2 might be carrying out quality control functions in the ER. Supporting this idea, I showed in this study long, swollen ER structures in the spinal cord anterior axons that were never observed in the previous (mitochondrial isoform-specific) *Spg7* KO model. These alterations were first seen at 16 weeks and the axons displaying them progressively increased over time (**Fig, 4.5, G**), similarly as for the mitochondrial phenotype observed (**Fig, 4.5, H**). Remarkably, AFG3L1 lacking axons did not show these ER structures at 28 weeks (**Suppl. S2, E**), suggesting that this phenotype is exclusively due to the absence of paraplegin-2. Interestingly, this ER phenomenon was recently described in a mouse model of HSP lacking REEP1 and ATL1, two proteins involved in tubular ER morphogenesis (Zhu et al., 2022). In this report, they demonstrated the presence of transverse expansions of the ER in myelinated CST axons. Although the affected axons of the DKO mice are those located anteriorly, the ER structures observed are quite similar, indicating that a comparable phenomenon is occurring in SPG7-HSP. Within the cerebellum, granule cells (GCs) arose as the most affected cell type in DKO mice, displaying big atrophic mitochondria (**Fig. 4.6**). ER alterations were observed only in few GCs. These alterations should, however, not be ruled out in this cell type, as their cytoplasm only constitute a tiny surrounding area, making the detection of organelles challenging. Why a protein, potentially involved in ER quality control, would determine the morphological arrangements of the ER organelle is intriguing and requires further investigation. Additionally, proteomic analysis performed at 16 weeks also hinted towards an impairment of ER function, particularly in calcium handling, as the most reduced protein in the DKO spinal cord was RYR1 (Ryanodine

receptor 1: calcium release from ER) and in the cerebellum TMEM64 (Transmembrane protein 64: SERCA2-dependent calcium signaling) (**Fig. 4.8**). Pathways analysis performed at the same age using the GO database with proteomic data highlighted an enrichment in the DKO spinal cord of the ER cellular component (**Fig. 4.11**). At 28 weeks, this analysis also displayed as an enriched category the “regulation of ryanodine-mediated calcium released” (**Fig. 4.26**), further supporting the previous findings. Given the importance the tubular ER present in neuronal maintenance, it is conceivable that its impairment is actively contributing to the pathogenic phenotype observed in DKO mice. This idea is highly appealing as around half of HSP cases are caused by mutations in ER-shaping proteins (Sonda et al., 2021). Although further studies are required, the discovery of an ER involvement in the DKO mice pathology not only opens up the way towards new research directions within SPG7-HSP but also arises as potential common mechanism linking the pathology of this HSP subtype to other HSP forms.

5.2. The role of NAD metabolism in the SPG7-HSP pathology

NAD^+, an essential coenzyme key to metabolism, has gained relevance as a therapeutic strategy in different models of aging and mitochondrial diseases (C. F. Lee et al., 2019; Srivastava, 2016), bringing up an impaired NAD homeostasis as an important factor underlying the mitochondrial pathology. In this context, deletion of SARM1, a crucial NADase enzyme cleaving NAD^+ into cADPR, ADPR and NAM, has also been proven beneficial in delaying the axonal degeneration of many axonopathies, including these mediated by mitochondrial dysfunction (Gilley et al., 2017; Summers et al., 2014; Turkiew et al., 2017). Thus, in this study I sought to untangle whether a similar NAD^+-related mechanism is involved in SPG7-HSP. Indeed, DKO animals presented a dysregulation of the NAD^+/NADH ratio, as they showed a significant reduction of this ratio in cerebellum at 28 weeks of age, with a modest trend to lower levels in spinal cord and cerebellum at 16 weeks, compared to WT samples (**Fig. 4.21**). Moreover, the levels of cADPR, a biomarker of SARM1 activation (Sasaki et al., 2020), were significantly increased in spinal cord at 16 weeks, with an upwards trend in cerebellum at 16 and 28 weeks of age (**Fig. 4.19**). This increase appears to be SARM1-specific, as deletion of this protein in DKO mice does not impact cADPR levels when compared with Sarm1KO controls (**Fig. 4.19**). The activation of MKK4 kinases (*via* their phosphorylation) has also been associated with SARM1 activity *via* increased turnover of NMNAT2, a cytosolic enzyme responsible for NAD+ biosynthesis (Walker et al., 2017). At 28 weeks, DKO mice displayed an increased pMKK4/MKK4 ratio in spinal cord lysates, with a slight trend to higher levels in the cerebellum, indicating an activation of this MAPK pathway upon paraplegin and AFG3L1 absence (**Fig. 4.20**). Despite this increase, the levels of the NAD^+/NADH ratio and cADPR

were unchanged in this tissue at 28 weeks. One possibility could be that this kinase activation is not coming from neuronal tissue but from glial cells instead. Although little is known about the activation of this specific MKK4 pathway in glia, the glial MAPK signalling has been shown to mediate inflammation *via* an increased cytokine production (Kaminska et al., 2009). Because DKO mice displayed a high number of reactive astroglial and microglial cells, an activation of the glial pMKK4 pathway in the DKO model should not be excluded. Moreover, not only does the spinal cord constitute a high heterogenous tissue, with many different cell types and axonal tracts, but it was also prominently affected at this stage, presenting many anterior axons that had already degenerated (**Fig. 4.5, I**). Therefore, neither the tissue heterogenicity nor the degeneration favours the detection *in vivo* of the metabolic alterations that are restricted to a subset of affected motor axons, as analysis will mainly detect the rest of the non-affected cells. This fact is also reflected in the proteomics performed in this tissue. At 16 weeks, around 1,1% of the entire tissue proteome detected was significantly changed (**Fig. 4.8, B**), whereas at 28 weeks the percentage went down to only 0.3% (**Fig. 4.22, F**). Cerebellar tissue did not experience such axonal degeneration, but it still shows mitochondrial impairments, which could potentially be the reason behind such a dramatical difference in the total of proteome changes between both tissues at 28 weeks (**Fig. 4.8, A; Fig. 4.22, A**).

Among these cerebellar changes, many proteins related to NAD metabolism appeared altered in DKO animals (**Fig. 4.24**). Most of them were OXPHOS subunits from complex I, including those involved in the oxidation of NADH, but also enzymes from the salvage pathway: NMNAT2 (cytosol) and NMNAT3 (mitochondria) and the NAD^+ mitochondrial transporter SLC25A51. This finding arises the question of how an impairment in a mitochondrial quality control protease disrupts cytosolic NAD pathways. One hypothesis is that this process begins with an impaired CI activity derived either by an altered mitochondrial translation or because paraplegin/AFG3L1 complexes specifically process some CI subunits, as has been seen in yeast (Arlt et al., 1996; Guélin et al., 1996). Supporting this, SPG7 fibroblast were shown to present CI activity deficiency *in vitro* (Atorino et al., 2003). This activity decline greatly impacts the NAD^+ mitochondrial pool, as it hampers its regeneration from NADH. Because this metabolite is essential for mitochondrial function and the different subcellular NAD^+ pools are interconnected, NAD^+ might be shuttled from cytosol to mitochondria to ensure proper mitochondrial activity, while its biosynthesis is endorsed in both compartments by upregulating both NMNAT2 and NMNAT3. Indeed, the levels of both enzymes and the NAD^+ transporter were increased in DKO cerebellum, supporting this hypothesis. Moreover, since the DKO mitochondrial impairments constitute a chronic, progressive event, it is reasonable to think that eventually the levels of NAD^+ in the cytosol drop sufficiently to affect the NMN/NAD^+ ratio known to activate SARM1, thereby consuming the remaining NAD^+ available and triggering

the ultimate axonal fragmentation (Ko et al., 2021). Moreover, despite having higher levels of NMNAT2/3 than WT samples, DKO mice still present a deficient NAD^+/NADH ratio (**Fig. 21, D**), further highlighting the great impact the loss of paraplegin/AFG3L1 have on the NAD^+ metabolism.

Nonetheless, this hypothesis does not concur with the multiple evidence demonstrating an activation of SARM1 upon a decline in the levels of NMNAT2. Because NMNAT2 is such a short-live protein, it must be continuously transported from the soma to distal axonal regions to ensure there proper NAD^+ homeostasis. Axonal transport impairments, mitochondrial dysfunction or increased MKK4 activation (Gilley & Coleman, 2010; Walker et al., 2017) enhance NMNAT2 turnover and lead to its decline. The subsequent NAD^+ drop increases the NMN/NAD^+ ratio and activates SARM1, triggering the degeneration. This currently accepted model led me to first hypothesize that a similar situation could be happening upon paraplegin/AFG3L1 loss. Nonetheless, my results indicate that an absence of paraplegin/AFG3L1 leads to a reduction of NAD^+, likely activating SARM1-mediated degeneration but instead in an NMNAT2 independent manner, as opposed to what has been demonstrated up to date.

To further understand the role of NAD^+ metabolism and SARM1 contribution to the SPG7 pathology, mice carrying mutations in all three genes, *Spg7*, *Afg3l1* and *Sarm1*, were generated (namely TKO). Since blocking SARM1-mediated degeneration improves the phenotype of many mouse models of neurodegeneration, I first postulated that deleting SARM1 would ameliorate the motor deficits observed in the DKO mice by delaying the spinal cord axonal degeneration. Surprisingly, TKO performance varied depending on the type of behavioural test applied. In the rotarod, both males and females exhibited an inability to maintain themselves on top of the rod for longer than a minute at any of the time points measured (**Fig. 4.14, A-B**), whereas in the walking beam, they behaved similarly to WT and Sarm1KO controls with no signs of motor deficits up to 24 weeks in the case of females and 32 weeks in males (**Fig. 4.14, C-D**). One way to understand this different outcome could be by highlighting what these tests measure. Although both tests assess general body balance, the walking beam test is frequently used to detect gait and fine movement impairments, processes driven primarily by the cerebellum (Sherrard, 2011), whereas the rotarod test requires strength and proper coordination, something that actively involves spinal cord activity (Ahmed, 2014). Based on that, these behavioural studies suggested that SARM1 contribution was tissue-dependent, with a potential involvement in cerebellar function. Indeed, and as opposed to most current evidence, SARM1 deletion did not improve spinal cord mitochondrial morphology nor axonal degeneration (**Fig. 4.15**) but it did improve the cerebellar mitochondrial phenotype and recued the loss of parallel fibers observed in DKO mice (**Fig. 4.16**). Nonetheless, the ER

structures observed in DKO spinal cord were absent in TKO tissue (**Fig. 4.15, A, D**), indicating that SARM1 activity is also impacting ER-related processes. In line with this, at 28 weeks, different pathways concerning ER function were enriched in TKO compared to DKO animals, such as the regulation of the ER unfolded protein response (UPR), ER morphology and calcium transport (**Fig. 4.26**). These data, together with the EM and proteomics at 16 weeks, point out a problem in the DKO in ER metabolism, particularly in calcium handing. Although the role of SARM1 in calcium signalling under healthy conditions remains unclear, its enzymatic activity gives rise to cADPR and NAADP, second messengers promoting calcium mobilization form the ER and the endosomes, respectively (Higashida et al., 2007; H. C. Lee & Zhao, 2019). The role of these metabolites have been studied more in depth with CD38, another NAD^+ cleaving enzyme whose activity has been compared with that of SARM1 in the brain (H. C. Lee & Zhao, 2019). CD38 participates in the pathogenesis of numerous diseases, including neurodegenerative conditions (Guerreiro et al., 2020), *via* modulation of calcium signaling (Higashida et al., 2007). Therefore, it seems logical to think that SARM1 is also affecting calcium dynamics in the brain through its cADPR/NAADP-producing activity and, given the rescued observed in ER dynamics, that abrogation of this activity counteracts the negative effect paraplegin-2 absence trigger in the ER. The possibility of an ER modulation via calcium signaling by both SARM1 and paraplegin is intriguing and should be further investigate in the future.

TKO mice experienced the same level of spinal cord axonal degeneration as DKO mice (**Fig. 4.15, F, C**), indicating firstly that mitochondrial phenotype, and not the ER alteration, is the main trigger of the degeneration, and secondly, that the molecular pathways driving the spinal cord axonal loss in SPG7-HSP are either SARM1-independent or involve another cell death pathway that acts in a redundancy with SARM1. On the contrary, loss of SARM1 in the cerebellum rescued both the mitochondrial alterations in GCs and the loss and straight organisation of the parallel fibers (**Fig. 4.16**). This finding is rather striking, as it has always been assumed that the abnormalities in mitochondrial morphology are a direct cause of an impaired *m*-AAA protease function within this organelle. Thus, these results establish SARM1 as a factor mediating the cerebellar mitochondrial pathology in this specific cell type. Mitochondrial swellings have been proposed to be a consequence of mPTP opening due to high calcium concentrations (Jang et al., 2021; Kwong & Molkentin, 2015). Because it is known that the *m*-AAA protease regulates the turnover of EMRE (MCU regulator subunit) (König et al., 2016), it is plausible to think that mitochondria acquire this swollen phenotype in the DKO due to an increased calcium uptake with the subsequent opening of the mPTP. Following this, mitochondria might benefit from not having SARM1 around, as SARM1 activity constitutes the main source of cellular cADPR in the brain (Sasaki et al., 2020). Reduced levels of cADPR, as

a result of SARM1 absence, could lead to lower levels of calcium via reduced stimulation of the ER calcium channels, mitigating mitochondrial burden. Although the levels of cADPR measured at 28 weeks in TKO and Sarm1KO cerebellum were similar to WT samples (**Fig. 4.19**), no difference was detected between these genotypes, unlike DKO mice compared to WT, supporting this theory. Why this mechanism emerges in the cerebellum and not in the spinal cord is a mystery. A possible explanation resides in the presence of mitochondria with different metabolic profiles between tissues (Pagliarini et al., 2008) and among cell types (Fecher et al., 2019). For instance, cerebellar GCs efficiently buffer calcium *via* MCU transporters in contrast to mitochondria from Purkinje cells (Fecher et al., 2019). The expression of the different *m*-AAA subunits is also tissue-specific (Koppen et al., 2007; Martinelli et al., 2009). Moreover, not only SARM1 is mainly express in neurons but also its function has seen to vary depending on the cellular environment, showing both detrimental (Krauss et al., 2020) and protective (Ding et al., 2022) roles in axonal survival. Therefore, the cellular environment and the differential expression of the different proteins might ultimately determine their specific functions and might explain the DKO tissue-specific rescue. In any case, the partial rescued observed upon SARM1 deletion appears to be rather short-term, as TKO males start displaying motor impairments in the walking beam at 32 weeks of age. Further EM analysis in TKO animals at later time points will be helpful to uncover whether these behavioural deficiencies correlate with mitochondrial impairments.

Additionally, deletion of SARM1 is likely to be improving the NAD^+ metabolic impairments of the DKO animals due to a reduction of its consumption. Indeed, proteomics at 28 weeks revealed no difference in the levels of NMNAT2, NMNAT3 nor the NAD^+ transporter in TKO cerebellum compared to Sarm1KO controls (**Fig. 4.24, B**). Moreover, no alterations were seen in complex I subunits. Therefore, these results support an activation of SARM1 in DKO cerebellum which disrupts NAD^+ homeostasis not only in the cytosol but also in the mitochondria, likely affecting complex I activity. Moreover, because SARM1 has also been involved in mitophagy (Murata et al., 2013), it could be participating in the SPG7 pathology *via* other molecular pathways beyond the consumption of NAD^+.

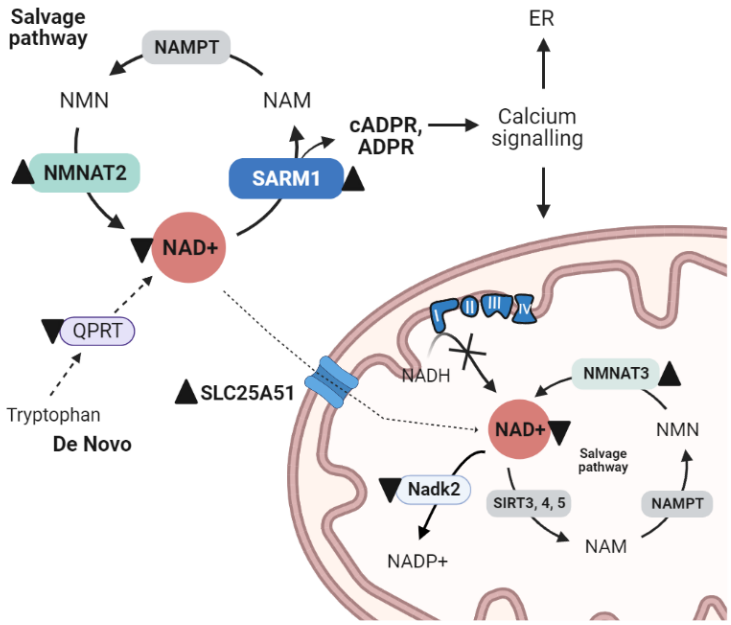

Figure 5.1. Model of the NAD⁺ dysregulation upon paraplegin/AFG3L1 deficiency. The absence of these *m*-AAA complexes may lead to an OXPHOS impairment, particularly of complex I, which hampers the regeneration of NAD⁺ from NADH. Eventually, mitochondrial NAD⁺ levels decline. Given the importance of mitochondria in neurons, the cell might ensure mitochondrial NAD⁺ homeostasis by favouring the import of this metabolite from the cytosol into the mitochondrial matrix and upregulating both the NAD⁺ biosynthetic enzymes NMNAT2-3. Nonetheless, a long-term mitochondrial impairment may ultimately lead to a NAD⁺ decline in both compartments, affecting the NMN/NAD⁺ ratio known to activate SARM1. A triangle was placed next to those proteins found significantly altered in 28 weeks proteomics (increased or decreased). Image created with BioRender 2022.

5.3. Uncovering the functions of paraplegin and its interplay with SARM1

Mitochondrial metabolism

Numerous studies have shed light into the diverse functions of the *m*-AAA protease. However, many of them come from studying their yeast homologous. In mammals, although some of its regulatory substrates have already been elucidated, most of the times they either rely on the presence of AFG3L2 or have not been investigated in the CNS. Moreover, the fact that mutations in *AFG3L2* and *SPG7* result in different clinical phenotypes reinforce the idea of *m*-AAA protease complex-specific functions across the different tissues. Therefore, I aimed to identify potential novel substrates and molecular pathways altered upon paraplegin absence and explore their role in the axonal degeneration observed in SPG7-HSP. Proteomic analysis on spinal cord and cerebellar tissue of WT and DKO mice at 16 weeks attribute the paraplegin/AFG3L1 heterocomplexes a clear role in mitochondrial translation, as many mitochondrial ribosomal proteins were significantly decreased (**Fig. 4.9**) and this category was the most enriched in pathway analysis (**Fig. 4.11**). This role was previously demonstrated in

Spg7 KO liver (Nolden et al., 2005) and upon AFG3L2 loss (Almajan et al., 2012). Indeed, one of the best described substrates of the *m*-AAA protease is MRPL32 (Bonn et al., 2011; Nolden et al., 2005). An impairment of the *m*-AAA protease leads to an accumulation of this ribosomal protein in yeast, but, intriguingly, it leads to reduced levels in mammals. The fact that the mammalian *m*-AAA protease can process MRPL32 in yeast and can compensate for the loss of the yeast *m*-AAA protease (Nolden et al., 2005) not only indicates that this ribosomal component is a putative substrate of the murine *m*-AAA protease, but also that there must be another peptidase degrading this protein when paraplegin is absent. Apart from MRPL32, many other ribosomal components appeared decreased in DKO at both 16 and 28 weeks proteomics (**Fig. 4.9, E; Suppl. Table S3**), a phenomenon also observed in the TKO/Sarm1KO comparison (**Suppl. Table S3**), suggesting that some of these ribosomal particles may also be putative substrates of the mouse paraplegin.

Thus, the control of ribosome assembly and the consequent mitochondrial translation appears to be a housekeeping function of the *m*-AAA protease, guaranteed ubiquitously by all its complexes. Surprisingly, cytoplasmic translation was likewise affected at 28 weeks in DKO cerebellum, indicating that the long-term loss of these *m*-AAA protease complexes also leads to an impairment of cytosolic translation.

Furthermore, if mitochondrial translation is altered, it is likely to affect the oxidative phosphorylation (OXPHOS) mainly via impaired synthesis of its mitochondrial-encoded subunits. Although at 16 weeks only few nuclear-encoded OXPHOS subunits appeared significantly changed (**Fig. 4.9**), at 28 weeks many of them, both nuclear and mitochondrial encoded, were altered in DKO cerebellum (**Fig. 4.23, A**). Interestingly, while the mitochondrial-encoded subunits presented reduced levels, the nuclear-encoded OXPHOS proteins (from CI to CV) were mostly accumulating, particularly those of complex I. Likewise, pathway analysis at this age also hinted towards a dysregulation of the respiratory chain activity and ATP production (**Fig. 4.26**). An impaired mitochondrial respiration due to an *m*-AAA protease dysfunction has been reported in yeast and mammals, including fibroblasts from SPG7-HSP patients (Atorino et al., 2003). Moreover, this process, together with an increased production of ROS, seems to constitute one of the pathogenic mechanisms contributing to degeneration mediated by AFG3L2 loss (Almajan et al., 2012; Maltecca et al., 2009, 2012). In the pathogenesis of SPG7-HSP, however, it does not seem to be a primary defect, as several OXPHOS subunits appeared altered in proteomics at 28 weeks but not at 16 weeks, when already a substantial percentage of GCs and cerebellar axons show abnormal mitochondria. Moreover, the previous *Spg7* KO model only showed ATP deficits at very late stages (Ferreirinha et al., 2004). Therefore, an impairment of mitochondrial respiration rather appears as a consequence of accumulative mitochondrial damage due to the loss of paraplegin over

time. Nonetheless, already at 16 weeks the two transporters shuttling pyruvate from the cytosol to the mitochondria (MPC1, MPC2) were dramatically reduced, and even more at 28 weeks. This reduction appears to be only at a protein level, as transcriptomic analysis at 16 weeks did not reveal changes at the levels of gene expression. This points towards a compromised mitochondrial activity already at an early age, with a shift in the glucose metabolism to promote glycolysis and shut down mitochondria to prevent them from further damage. This self-defence mechanism could explain why proteomics at 16 weeks revealed so little changes compared to 28 weeks. Nevertheless, it is striking that in the cerebellar tissue most of the OXPHOS subunits detected were accumulating, unless this was a result of a time-dependent accumulation of proteins which cannot be degraded due to a general quality control impairment. Future transcriptomic analysis at this later age would be useful to understand whether the gene expression of these proteins is upregulated as a compensatory mechanism, to cope with a mitochondrial deficiency, or if they accumulate over time as a result of mitochondrial damage. In line with this, only at 28 weeks, many protein related to ROS homeostasis and glycolytic enzymes were increased, including HK2 and GAPDH. The fact that HK2 is significantly increased (FC > 1.5) is quite interesting, as an upregulation of this enzyme has been recently showed to promote apoptosis of dopaminergic neurons in Parkinson's disease (Li et al., 2022) and it is in general related to a reprograming of the metabolism to an enhancement of glycolysis under pathological conditions (Gimenez-Cassina et al., 2009; Wolf et al., 2011). Taken all together, these results indicate that, as in many other mitochondria-related conditions, DKO cerebellar cells try to compensate the mitochondrial dysfunction by enhancing glycolytic ATP production.

Spinal cord proteomics, as stated previously, detected little protein changes. However, pathway analysis of the whole proteome measurement revealed a negative enrichment of OXPHOS in DKO spinal cord (**Fig. 4.26, D**), the complete opposite of cerebellar tissue. The mitochondrial pyruvate transporters were similarly decreased, supporting the idea of a lessen mitochondrial ATP production also in this tissue but without bringing up the compensatory mechanisms observed in cerebellum.

Interestingly, deletion of SARM1 in cerebellum dropped substantially the amount of proteins detected upon paraplegin/AFG3L1 loss (**Fig. 4.22, C**), further highlighting its involvement in the SPG7-HSP pathology. Different studies have previously attributed SARM1 a role as an inhibitor of mitochondrial respiration via reduction of NAD^+ levels (Murata et al., 2018). For example, in prion infected mice, SARM1 absence led to an increased mitochondrial oxygen consumption (OCR) compared to infected WT mice, although no change in the protein levels of the complexes were observed (Ward et al., 2022). In my study, TKO mice did not display changes in the levels of OXPHOS proteins compared to Sarm1KO mice, with the exception of

UQCC1, SCO2 and SURF1 (**Fig. 4.23, B**), which are likewise altered in DKO animals. On the one hand, this consistent accumulation of mitochondrial IMM/matrix proteins regardless of Sarm1KO presence indicates a direct role of the *m*-AAA protease in their processing, and therefore they arise as potential novel candidates to be substrates of paraplegin/AFG3L1 complexes. On the other hand, several mitochondrial ribosomal components were also decreased in TKO cerebellum and mitochondrial translation was a category negatively enriched compared to Sarm1KO individuals, further supporting this conserved function of the *m*-AAA protease. Moreover, MPC1 and MPC2 were likewise diminished in TKO mice. In spite of this, almost all OXPHOS proteins measured, including the mitochondria-encoded subunits, were not affected and neither was the cytoplasmic translation. Indeed, the OXPHOS category was found oppositely enriched in TKO compared to DKO animals (**Table 5.1**). The metabolic enzymes and the ROS-related proteins observed altered in DKO tissue were also not altered upon deletion of SARM1. Nevertheless, in order to ultimately determine an impairment of the mitochondrial respiration, further biochemical measurements, such as the OCR, should be performed in the future with the different genotypes.

These results suggest that, despite the mitochondrial translation difficulties, SARM1 deletion was beneficial to prevent the accumulation of such mitochondrial damage over time in a way that delays the metabolic reprograming taking place upon mitochondrial dysfunction due to paraplegin/AFG3L1 loss. This improved metabolic scenario in TKO cerebellum might allow mitochondria to efficiently handle calcium, which could be another possibility why mitochondrial phenotype is rescued in GCs.

Synaptic transmission

Although synaptic activity has never been assessed *per se* in paraplegin-deficient mice, abnormal mitochondria were seen accumulated in synaptic terminals from an early age (Ferreirinha et al., 2004). Recently, the study from Sambri et al., revealed an impaired release of neurotransmitters to the synaptic cleft due to a dysregulation of the mPTP opening upon paraplegin loss, affecting synaptic transmission. In agreement with these findings, many pathways from proteomic analysis related to synaptic activity were consistently enriched at both 16 and 28 weeks in DKO animals (**Fig. 4.11; 4.26**), including the exocytosis of synaptic vesicles and the ionotropic glutamate receptors. Similarly, several synapsis-associated proteins were significantly altered in 28 weeks DKO/WT proteomics, such as NMDA receptors, SNARE proteins and the calmodulin-dependent proteins CaMKII, CamKK1 and CamKmt. In particular, CaMKII is well-known for its role in synaptic plasticity, being essential for memory formation (Bayer & Schulman, 2019). In this context, SARM1 has been shown to also modulate

synaptic plasticity via interaction with syndecan-2 (syn-2), a synaptic heparan sulfate proteoglycan (Chen et al., 2011) and, in *C. elegans*, with UNC-34 (CaMKII) (Chuang & Bargmann, 2005). In hippocampal neurons, SARM1 absence inhibited mGlut-associated long-term depression whereas it enhanced NMNDAR-dependent long-term potentiation (Lin et al., 2014). Remarkably, TKO cerebellum did not exhibit changes in the levels of any of above-mentioned proteins compared to Sarm1KO and WT controls (**Suppl. Table S3**). Additionally, categories such as “synaptic vesicle exocytosis” were positively enriched in TKO compared to DKO samples. These outcomes point to an alteration of synaptic transmission upon paraplegin/AFG3L1 loss that is restored upon SARM1 deletion.

F-actin cytoskeleton and cell adhesion

An unexpected finding of both transcriptomic and proteomic analyses was the consistent upregulation of cell adhesion and cytoskeleton organization pathways upon paraplegin/AFG3L1 absence. On one side, SPG7 pathogenesis seems to involve actin processes as the “actin cytoskeleton organization” and “actin filament-based process” categories were highly enriched at both 16 and 28 weeks in spinal cord (**Fig. 4.11; Fig. 4.26**). These alterations may be happening due to the mitochondrial dysfunction *per se*, as actin filaments regulate mitochondrial dynamics, trafficking, mitophagy and metabolism (Illescas et al., 2021). Remarkably, not only TKO animals did not show these differences compared to Sarm1KO controls but they also displayed a totally opposite enrichment of these pathways compared to both DKO tissues (**Fig. 4.26**). These results agree with the current evidence stating SARM1 as a negative regulator of axonal F-actin cytoskeleton (Chen et al., 2011; Ketschek et al., 2022).

On the other side, spinal cord transcriptomics analysis already hinted to a cell adhesion alteration at 16 weeks, with vitronectin as the most upregulated transcript in DKO samples (**Table 4.2**). At 28 weeks, proteomics in this tissue showed collagen proteins drastically increased in DKO samples (FC > 8) consistently with the pathway analysis outcome; where the categories “Collagen fibril organization” and “cell adhesion mediated by integrin” were positively enriched (**Fig. 4.26**). This is consistent with a problem in the cytoskeleton, as cell adhesion processes require cytoskeletal dynamics and vice versa. For example, cell migration strongly relies on focal adhesions interactions with F-actin filaments, which is also greatly influenced by mitochondrial dynamics and metabolism (Madan et al., 2022). In fact, lowering mitochondrial ATP production or calcium buffering inhibits cell motility (Cunniff et al., 2016; Prudent et al., 2016). Because these mitochondrial processes are likely to be impaired in the DKO model, it makes sense to think that these dysfunctional mitochondria are affecting the focal adhesion and cytoskeletal dynamics. Intriguingly, while in cerebellum only the ”actin

cytoskeleton reorganization" category was significantly increased in TKO versus DKO mice (no adhesion pathways), in spinal cord deleting SARM1 restored the levels of the collagen-related proteins and changed the pathway analysis outcome, as the GOBP adhesion and cytoskeletal-related categories were negatively regulated in TKO versus DKO. These results not only imply a great impact of the *m*-AAA impairments in spinal cord F-actin filaments and focal adhesion but also a tissue-specific involvement of SARM1 in these processes.

5.4. The contribution of neuroinflammation to the SPG7-HSP condition

Often neuronal injury triggers the pro-inflammatory activation of glial cells, particularly microglia and astroglia, which chronically leads to severe tissue damage, a compromise of the blood-brain barrier and neuronal death (Skaper et al., 2018). Moreover, this neuroinflammatory process is tightly linked to the immune system, with immune cell infiltration in affected areas (Ising & Heneka, 2018). The characterisation I carried out in the newly generated DKO model demonstrated the presence and proliferation of reactive microglia and astroglia in cerebellum, and, to a lesser extent, spinal cord, at 16 and 28 weeks of age. This observation is in concordance with the ultrastructural analysis results, as the cerebellar GC layer and axonal fibers, together with the anterior tracts of the spinal cord, were displaying gliosis the most (**Fig. 4.6**). Sustained pro-inflammatory activation of these glial cells is likely impairing its involvement in synapsis and cognitive processes and contributing to the SPG7 pathology, as seen in other neurodegenerative conditions (Chitnis & Weiner, 2017). This phenomenon may, in fact, be a reason why the treatment with ceftriaxone did not result in an improvement of the SPG7 phenotype, as treatment was initiated at 16 weeks, when astrocytes appeared already reactive. This beta-lactam antibiotic accelerates the uptake of glutamate from the synaptic cleft *via* upregulation of the glutamate transporter EAAT2 (S. G. Lee et al., 2008), a strategy that resulted beneficial to improve SCA28 pathology caused by *Afg3l2* mutations (Maltecca et al., 2015). In the DKO model, however, pro-inflammatory astrocytes are likely to be both not responding to this manipulation and already altering their neuronal interactions. An alternative strategy would be to treat the mice before the onset of the symptoms, for instance at 2-3 months, and closely monitor them to assess whether a treatment with this drug at early time points is able to ameliorate the motor deficits.

Furthermore, 28-weeks pathway analysis of proteomics also revealed an involvement of the immune system in a tissue-specific fashion, with GOBP categories such as "complement activation" and "humoral immune response" negatively enriched in cerebellum and "T-cell activation", on the contrary, positively enriched in spinal cord (**Fig. 4.26**). The fact that cerebellum is downregulating these innate and adaptative immune pathways may indicate an

attempt to mitigate the inflammation already present and reduce tissue damage, a mechanism that appears to not be occurring in spinal cord. Instead, the adaptative immune upregulation seen in spinal cord might be due to the mere infiltration of T-cells, a common response observed upon neuronal injury (Hammond et al., 2019).

Additionally, the *m*-AAA protease also plays an important role within glial cells. Specific deletion of *Afg3l2* in adult oligodendrocytes leads to late-onset myelin impairments and axonal degeneration, whereas the complete abolishment of m-AAA complexes triggers rapid oligodendrocyte death (S. Wang et al., 2016). Similar effects are seen in astrocytes, where mutations in *Afg3l2* are associated not only with abnormal mitochondria, but also with metabolic stress and an altered reactive morphology (Murru et al., 2019). Because paraplegin forms heterocomplexes with both AFG3L2 and AFG3L1, I cannot exclude that an intrinsic impairment of glial cells in DKO mice is contributing to the SPG7 pathology and, therefore, to the results I present in this thesis, such as the omics analysis. This limitation can be overcome in the future by targeting paraplegin exclusively in glial or neuronal cells and performing the omics analysis in pure cell populations either *in vitro* or *in vivo* previous fluorescence-activated cell sorting (FACS).

Interestingly, in absence of SARM1, paraplegin/AFG3L1 loss did not trigger neuroinflammation in either tissue (**Fig. 4.17**; **Fig. 4.18**). Additionally, while the enrichment of the immune pathways showed similar results between the DKO/WT and TKO/Sarm1KO comparisons in spinal cord, in cerebellum TKO presented a positive enrichment of the B-cell mediated immunity compared to Sarm1KO samples (**Fig 4.26**), suggesting an active involvement of SARM1 in immune processes. These results are in agreement with the evidence demonstrating a negative role of SARM1 in regulating TLR signaling (Carty et al., 2006; Peng et al., 2010). This inhibitory effect of SARM1 in cerebellum may explain the downregulation of immune pathways observed in DKO samples and the consequent upregulation upon its deletion. SARM1 was also shown to promote the production of Ccl3, Ccl4, and Ccl5 cytokines in macrophages. This effect was later attributed not to SARM1 activity but to the close location of these cytokine locus to the Sarm1 loci on the mouse chromosome 11 (Uccellini et al., 2020). Because this specific Sarm1KO line was the same employed to generate the TKO animals, it is likely that this production is interfering with the global effect seen upon Sarm1 deletion. Nonetheless, a study using a different model showed that SARM1 is required for the expression of other cytokines upon traumatic axonal injury, suggesting that SARM1 is indeed involved in cytokine production (Q. Wang et al., 2018). Furthermore, SARM1 activation has been shown to be both a downstream mediator of neuroinflammatory and necroptotic signaling (Ko et al., 2020) and a promoter of neuroinflammation via NF-kB signaling (Bloom et al., 2022; Liu et al., 2021). The results from my study support the latter idea, as

deletion of SARM1 attenuated both astroglia and microglia reactivity in both tissues. Nevertheless, because SARM1 is also expressed in astrocytes (Liu et al., 2021), a modulation of astroglial activity in a cell-autonomous manner cannot be ruled out.

5.5. SARM1 absence remodels cellular proteome

The fact that SARM1 is capable of restoring mitochondrial morphology in cerebellum and ER structures in the spinal cord arose the question whether SARM1 itself is able to alter the cellular proteome in normal conditions and not in a degenerative context. Moreover, there exist studies attributing SARM1 a physiological role in neuronal morphogenesis. For example, in hipocampal neurons *in vitro*, removing SARM1 caused a lowering of dendritic spines number and complexity and shorter axons (Chen et al., 2011), whereas in sensory neurons both *in vitro* and *in vivo* its deletion led to increase axon branching via promotion of actin cytoskeleton dynamics and filopodia formation (Ketschek et al., 2022). The results from my thesis showed no alteration of the general spinal cord and cerebellar tissue structure upon SARM1 loss. Mitochondrial morphology and general organelle and filament axonal content of Sarm1KO mice also resemble WT samples in both tissues (**Fig. 4.16; Fig. 4.17**). Nonetheless, because other brain areas were not the main target of the SPG7 pathology, the morphological implications of SARM1 loss in other tissues were not assessed and cannot be ruled out.

Despite no evident structural tissue alterations, the proteome of Sarm1KO mice did differ from WT samples at 28 weeks of age, particularly in the cerebellum (**Fig. 4.27, B**). In fact, many of these altered proteins were involved in actin cytoskeleton, cell adhesion and neuronal morphogenesis, in agreement with current literature evidence, indicating that indeed Sarm1KO is also involved in these processes in spinal cord and cerebellum (**Fig. 4.30**). Moreover, and consistent with previously described potential roles of SARM1 in calcium handling and synaptic transmission, different categories such as “transmission of nerve impulse”, “synaptic transmission glutamatergic” and “calcium transmembrane transport” appeared differentially regulated in Sarm1KO animals (**Fig. 4.30**). Furthermore, it was no surprise to observe proteins and pathways related to inflammatory response and the adaptative immune system decreased in Sarm1KO cerebellum. These immune pathways were, however, not changed in spinal cord, pointing towards a differential role of SARM1 in immunity within these tissues. Intriguingly, other pathways appeared differentially regulated between spinal cord and cerebellum, such as those related to cell adhesion and mitochondrial pathways, further supporting cell-autonomous roles of SARM1. In fact, in cerebellum many mitochondrial proteins appeared increased, which mainly involved mitochondrial respiration and protein import (**Fig. 4.25**). Because the loss of SARM1 implies more NAD^+ available, and a boosting of this metabolite is known to enhance mitochondrial biogenesis via the SIRT1-PGC-1α pathway (Koh & Kim, 2021), one can argue

that Sarm1KO mice might present an accumulation of mitochondrial proteins as a result of having more mitochondria. However, PCA from 28 weeks proteomics did not show a general shift of the Sarm1KO mitochondrial mass compared to WT cerebellum (**Suppl. S7, C**), indicating that they present similar amounts of mitochondria.

The link between SARM1 activity and mitochondria respiration has been mostly studied in the context of neurotoxicity, for example upon treatment with rotenone or CCCP (Hughes et al., 2021; Summers et al., 2014), which places mitochondrial dysfunction upstream of SARM1 activation. Whether SARM1 in its "inactive" or "locked" steady state affects *per se* mitochondrial respiration is still under debate. A recent study from Ward et al., found a significant increase in the protein levels of CII and CIV in Sarm1KO brain, which, however, seemed to not impact the oxygen consumption rate, as both Sarm1KO and WT samples displayed a similar value. In my thesis, I showed an increased expression of CI, CIII, CIV and CV subunits (all FC > 1.5), including the mitochondrial-encoded MT-ATP8 protein, in Sarm1KO cerebellum compared to WT controls (**Fig. 4.27, B**), supporting a predisposition of these mice to a dysregulation of mitochondrial respiration. If we compare the pathway and proteomics analyses among the different genotypes, we see how both Sarm1KO and DKO mice (which are WT for *Sarm1*) presented several increased OXPHOS subunits and a higher enrichment of this GOBP category in cerebellum, which is an entirely opposite outcome compared to spinal cord analyses (T**able 5.1**). Surprisingly, this enrichment is attenuated in TKO mice, which instead show this pathway negatively enriched compared to DKO mice. One way of interpreting this would be that, because TKO versus Sarm1KO did not exhibit any OXPHOS differences, TKO animals also upregulate this pathway but to a lesser extent that DKO mice. Due to the cerebellar rescue observed upon SARM1 loss, the reduction of OXPHOS subunits expression seems beneficial for mitochondria lacking paraplegin/AFG3L1, which may also be influenced by the presence of higher NAD^+ levels. In spinal cord, neither Sarm1 nor DKO mice displayed such changes in OXPHOS, showing instead a lower enrichment of this pathway (**Table 5.1**). Thus, these results point to a negative effect of SARM1 in mitochondrial respiration which could be exacerbated upon an *m*-AAA protease impairment.

Table 5.1. Scheme representing the pathway analysis enrichments observed for the oxidative phosphorylation in the different proteomic comparisons. Blue arrows indicate a positive NES, red arrows a negative NES and equal symbol represent no change.

	DKO (vs WT)	TKO (vs Sarm1KO)	TKO (vs DKO)	Sarm1KO (vs WT)
Cerebellum	↑	=	↓	↑
Spinal cord	↓	↓	↓	↓

Interestingly, many subunits of the TIM import machinery were also accumulating upon SARM1 loss, particularly from TIM8-13 and TIM10 complexes (**Suppl. Table S3**), but none from other translocation machineries, indicating that SARM1 is specifically regulating the levels of these proteins. A possibility would be that they constitute interactors. Whereas most evidence argue a location of SARM1 either in the cytosol or associated to the mitochondrial outer membrane, one individual study showed that SARM1 interacts with PINK1 in the mitochondrial intermembrane space (Murata et al., 2013). Thus, cerebellar SARM1 may similarly bind to certain TIM subunits and modulate mitochondrial protein import.

Furthermore, it was striking to see a set of proteins whose levels were changed similarly between Sarm1KO and DKO animals compared to the same WT controls, but decreased in TKO versus Sarm1KO samples. Function wise, these proteins, listed in **Table 4.5**, seem to belong to different cellular pathways, localizing even to different subcompartments. A particular example is the mitochondrial ribosomal protein MRPL50, whose levels increase upon SARM1 loss in WT conditions. If, besides SARM1, paraplegin/AFG3L1 complexes are also missing, MRPL50 levels go down instead (TKO/Sarm1KO comparison). This not only implies a common regulation of this protein by SARM1 and the *m*-AAA protease but, in line with the rest of the proteomic analysis, it suggest an effect of SARM1 activity on the mitochondrial proteome. The rest of the proteins found follow the same trend but in a opposite manner (**Table 4.5**), favouring the interesting idea of a common network influenced by both SARM1 and paraplegin/AFG3L1 complexes. Nonetheless, because these considerations come from descriptive proteomics analysis, further investigations are needed to assess its biological implication within the cell.

5.6. Conclusion

The findings presented in this study highlight an involvement of paraplegin/AFG3L1 complexes in a variety of mitochondrial activities, such as ribosome biogenesis and the transport of ions and metabolites across the organelle. The loss of both proteases in mice leads to an earlier onset of the SPG7-HSP phenotype compared to the previous *Spg7* KO model (Ferreirinha et al., 2004), with a considerable accumulation, already at 16 weeks, of abnormal mitochondria in anterior spinal cord axonal tracts and in fibers and granule cells of the cerebellum. Moreover, this study constitutes the first that shows transverse ER structures in spinal cord fibers upon paraplegin/AFG3L1 absence. I have also proved an impairment of the NAD^+ homeostasis in the DKO mice. In fact, this study demonstrates for the first time a contribution of SARM1 to the SPG7-HSP pathology, mediating the mitochondrial impairments and the loss of parallel fibers in the cerebellum. In the spinal cord, SARM1 deletion rescued the ER alterations but not the mitochondrial phenotype or the axonal degeneration observed in the DKO mice. Furthermore, this study reveals tissue-specific differences in the function of both paraplegin/AFG3L1 complexes and SARM1 within the CNS. Additionally, the loss of SARM1 in a non-pathological environment remodels the cellular proteome, particularly in the cerebellum. Further investigations should be performed to confirm the paraplegin/AFG3L1 putative substrates proposed in this study as well as understand the mechanism behind the SARM1 *in vivo* rescue, for example by studying the paraplegin-SARM1 interplay in calcium signalling and mitochondrial respiration. The assessment of these mechanisms in different tissues will also help understanding why mutations in paraplegin are associated with such specific neuronal phenotype. Moreover, additional studies are needed to determine the localization/s of SARM1 and its function in a healthy context within and beyond the scope of mitochondria.

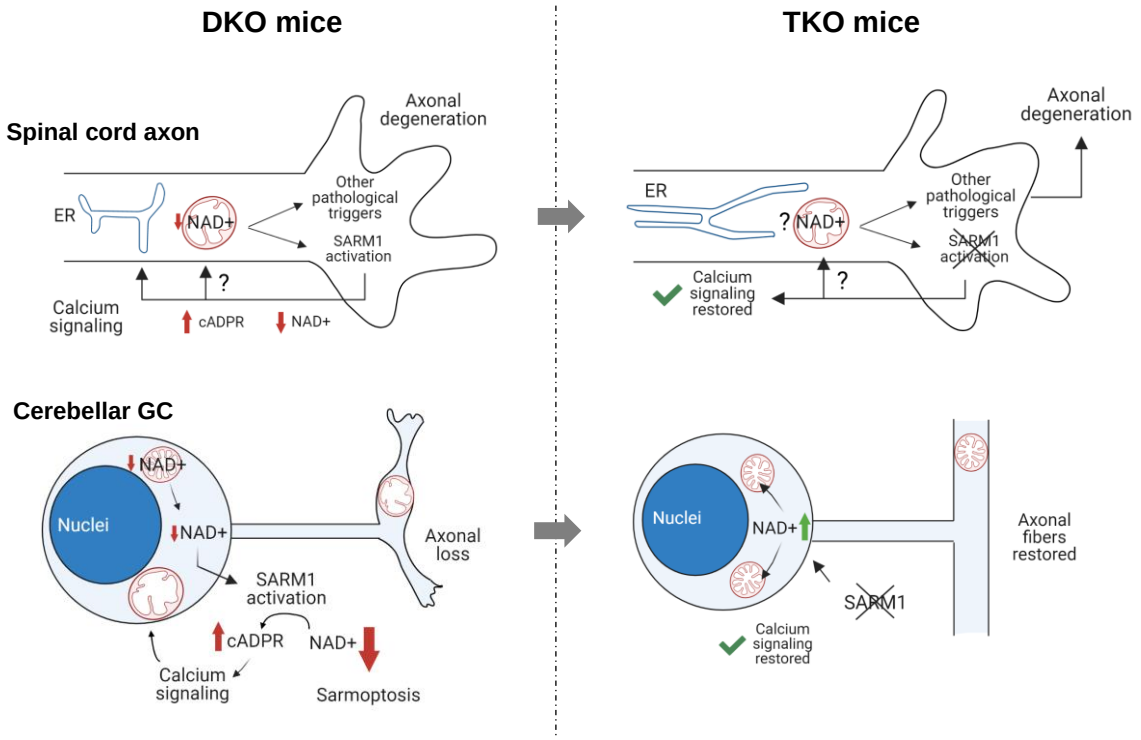

Figure 5.2. Model of the SARM1 tissue-specific contribution upon paraplegin/AFG3L1 deficiency. As explain in Fig. 5.1, the long-term loss of paraplegin/AFG3L1 complexes leads to a dysregulated mitochondrial and cellular NAD^+ homeostasis and the consequent SARM1 activation. In DKO cerebellar granule cells (GC), the resulting rise in cADPR levels leads to swollen abnormal mitochondria, whereas in spinal cord axons they affect ER morphogenesis, in both cases *via* activation of calcium-dependent channels, affecting calcium signalling. The link between SARM1-mediated cADPR production and the swollen mitochondrial morphology in spinal cord is not clear, as TKO mice still present these mitochondrial abnormalities. Moreover, the increased consumption of NAD^+ by SARM1 triggers the downstream degeneration cascade leading to axonal loss in cerebellum. As such, the removal of SARM1 in tissue prevents parallel fiber loss and rescues the mitochondrial morphology. In spinal cord, however, SARM1 is not the only factor contributing to the axonal degeneration, as its absence does not prevent the spinal cord axonal death. Image created with BioRender 2022.

6. References

Ahmed, Z. (2014). Trans-Spinal Direct Current Stimulation Alters Muscle Tone in Mice with and without Spinal Cord Injury with Spasticity. *Journal of Neuroscience*, *34*(5), 1701–1709. https://doi.org/10.1523/JNEUROSCI.4445-13.2014

Allen, N. J., & Lyons, D. A. (2018). Glia as architects of central nervous system formation and function. *Science*, *362*(6411), 181–185. https://doi.org/10.1126/science.aat0473

Almajan, E. R., Richter, R., Paeger, L., Martinelli, P., Barth, E., Decker, T., Larsson, N.-G., Kloppenburg, P., Langer, T., & Rugarli, E. I. (2012). AFG3L2 supports mitochondrial protein synthesis and Purkinje cell survival. *Journal of Clinical Investigation*, *122*(11), 4048–4058. https://doi.org/10.1172/JCI64604

Anderson, S., Bankier, A. T., Barrell, B. G., de Bruijn, M. H. L., Coulson, A. R., Drouin, J., Eperon, I. C., Nierlich, D. P., Roe, B. A., Sanger, F., Schreier, P. H., Smith, A. J. H., Staden, R., & Young, I. G. (1981). Sequence and organization of the human mitochondrial genome. In *Greenberg. R. As'r. 1* (Vol. 290, Issue 6).

Angeletti, C., Amici, A., Gilley, J., Loreto, A., Trapanotto, A. G., Antoniou, C., Merlini, E., Coleman, M. P., & Orsomando, G. (2022). SARM1 is a multi-functional NAD(P)ase with prominent base exchange activity, all regulated bymultiple physiologically relevant NAD metabolites. *IScience*, *25*(2), 103812. https://doi.org/10.1016/j.isci.2022.103812

Apps, R., & Garwicz, M. (2005). Anatomical and physiological foundations of cerebellar information processing. In *Nature Reviews Neuroscience* (Vol. 6, Issue 4, pp. 297–311). https://doi.org/10.1038/nrn1646

Arlt, H., Tauer, R., Feldmann, H., Neupert, W., & Langer, T. (1996). The YTA10–12 Complex, an AAA Protease with Chaperone-like Activity in the Inner Membrane of Mitochondria. *Cell*, *85*(6), 875–885. https://doi.org/10.1016/S0092-8674(00)81271-4

Ashrafi, G., de Juan-Sanz, J., Farrell, R. J., & Ryan, T. A. (2020). Molecular Tuning of the Axonal Mitochondrial Ca2+ Uniporter Ensures Metabolic Flexibility of Neurotransmission. *Neuron*, *105*(4), 678-687.e5. https://doi.org/10.1016/j.neuron.2019.11.020

Atorino, L., Silvestri, L., Koppen, M., Cassina, L., Ballabio, A., Marconi, R., Langer, T., & Casari, G. (2003). Loss of m-AAA protease in mitochondria causes complex I deficiency and increased sensitivity to oxidative stress in hereditary spastic paraplegia. *Journal of Cell Biology*, *163*(4), 777–787. https://doi.org/10.1083/jcb.200304112

Augusto-Oliveira, M., Arrifano, G. P., Lopes-Araújo, A., Santos-Sacramento, L., Takeda, P. Y., Anthony, D. C., Malva, J. O., & Crespo-Lopez, M. E. (2019). What Do Microglia Really Do in Healthy Adult Brain? *Cells*, *8*(10), 1293. https://doi.org/10.3390/cells8101293

Baker, T. A., & Sauer, R. T. (2012). ClpXP, an ATP-powered unfolding and protein-degradation machine. *Biochimica et Biophysica Acta (BBA) - Molecular Cell Research*, *1823*(1), 15–28. https://doi.org/10.1016/j.bbamcr.2011.06.007

Barnham, K. J., Masters, C. L., & Bush, A. I. (2004). Neurodegenerative diseases and oxidative stress. *Nature Reviews Drug Discovery*, *3*(3), 205–214. https://doi.org/10.1038/nrd1330

Bas-Orth, C., Tan, Y. W., Lau, D., & Bading, H. (2017). Synaptic activity drives a genomic program that promotes a neuronal warburg effect. *Journal of Biological Chemistry*, *292*(13), 5183–5194. https://doi.org/10.1074/jbc.M116.761106

Bayer, K. U., & Schulman, H. (2019). CaM Kinase: Still Inspiring at 40. *Neuron*, *103*(3), 380–394. https://doi.org/10.1016/j.neuron.2019.05.033

Beetz, C., Koch, N., Khundadze, M., Zimmer, G., Nietzsche, S., Hertel, N., Huebner, A.-K., Mumtaz, R., Schweizer, M., Dirren, E., Karle, K. N., Irintchev, A., Alvarez, V., Redies, C., Westermann, M., Kurth, I., Deufel, T., Kessels, M. M., Qualmann, B., & Hübner, C. A. (2013). A spastic paraplegia mouse model reveals REEP1-dependent ER shaping. *Journal of Clinical Investigation*, *123*(10), 4273–4282. https://doi.org/10.1172/JCI65665

Beirowski, B., Babetto, E., Gilley, J., Mazzola, F., Conforti, L., Janeckova, L., Magni, G., Ribchester, R. R., & Coleman, M. P. (2009). Non-Nuclear WldS Determines Its Neuroprotective Efficacy for Axons and Synapses In Vivo. *Journal of Neuroscience*, *29*(3), 653–668. https://doi.org/10.1523/JNEUROSCI.3814-08.2009

Ben Shimon, M., Lenz, M., Ikenberg, B., Becker, D., Shavit Stein, E., Chapman, J., Tanne, D., Pick, C. G., Blatt, I., Neufeld, M., Vlachos, A., & Maggio, N. (2015). Thrombin regulation of synaptic transmission and plasticity: implications for health and disease. *Frontiers in Cellular Neuroscience*, *9*. https://doi.org/10.3389/fncel.2015.00151

Benarroch, E. (2022). What Is the Role of Mitochondrial Dysfunction in Programmed Axon Death? *Neurology*, *98*, 836–840. https://doi.org/10.1212/WNL.0000000000200691

Berger, F., Lau, C., Dahlmann, M., & Ziegler, M. (2005). Subcellular Compartmentation and Differential Catalytic Properties of the Three Human Nicotinamide Mononucleotide Adenylyltransferase Isoforms. *Journal of Biological Chemistry*, *280*(43), 36334–36341. https://doi.org/10.1074/jbc.M508660200

Bernardi, P., & Forte, M. (2015). Commentary: SPG7 is an essential and conserved component of the mitochondrial permeability transition pore. *Frontiers in Physiology*, *6*. https://doi.org/10.3389/fphys.2015.00320

Blackstone, C. (2015). Murine Models of Autosomal Recessive Hereditary Spastic Paraplegia. In *Movement Disorders* (pp. 1087–1093). Elsevier. https://doi.org/10.1016/B978-0-12-405195-9.00071-8

Blackstone, C. (2018). *Hereditary spastic paraplegia* (pp. 633–652). https://doi.org/10.1016/B978-0-444-64076-5.00041-7

Blackstone, C. (2020). Early-onset hereditary spastic paraplegia: the possibility of a genetic diagnosis. *Developmental Medicine & Child Neurology*, *62*(9), 1011–1011. https://doi.org/10.1111/dmcn.14564

Blackstone, C., O'Kane, C. J., & Reid, E. (2011). Hereditary spastic paraplegias: membrane traffic and the motor pathway. *Nature Reviews Neuroscience*, *12*(1), 31–42. https://doi.org/10.1038/nrn2946

Bloom, A. J., Mao, X., Strickland, A., Sasaki, Y., Milbrandt, J., & DiAntonio, A. (2022). Constitutively active SARM1 variants that induce neuropathy are enriched in ALS patients. *Molecular Neurodegeneration*, *17*(1), 1. https://doi.org/10.1186/s13024-021-00511-x

Bonn, F., Tatsuta, T., Petrungaro, C., Riemer, J., & Langer, T. (2011). Presequence-dependent folding ensures MrpL32 processing by the m-AAA protease in mitochondria. *The EMBO Journal*, *30*(13), 2545–2556. https://doi.org/10.1038/emboj.2011.169

Bratkowski, M., Xie, T., Thayer, D. A., Lad, S., Mathur, P., Yang, Y.-S., Danko, G., Burdett, T. C., Danao, J., Cantor, A., Kozak, J. A., Brown, S. P., Bai, X., & Sambashivan, S. (2020). Structural and Mechanistic Regulation of the Pro-degenerative NAD Hydrolase SARM1. *Cell Reports*, *32*(5), 107999. https://doi.org/10.1016/j.celrep.2020.107999

Briens, A., Bardou, I., Lebas, H., Miles, L. A., Parmer, R. J., Vivien, D., & Docagne, F. (2017). Astrocytes regulate the balance between plasminogen activation and plasmin clearance via cell-surface actin. *Cell Discovery*, *3*(1), 17001. https://doi.org/10.1038/celldisc.2017.1

Bross, P., Naundrup, S., Hansen, J., Nielsen, M. N., Christensen, J. H., Kruhøffer, M., Palmfeldt, J., Corydon, T. J., Gregersen, N., Ang, D., Georgopoulos, C., & Nielsen, K. L. (2008). The Hsp60-(p.V98I) Mutation Associated with Hereditary Spastic Paraplegia SPG13 Compromises Chaperonin Function Both in Vitro and in Vivo. *Journal of Biological Chemistry*, *283*(23), 15694–15700. https://doi.org/10.1074/jbc.M800548200

Burté, F., Carelli, V., Chinnery, P. F., & Yu-Wai-Man, P. (2015). Disturbed mitochondrial dynamics and neurodegenerative disorders. *Nature Reviews Neurology*, *11*(1), 11–24. https://doi.org/10.1038/nrneurol.2014.228

Cagnoli, C., Mariotti, C., Taroni, F., Seri, M., Brussino, A., Michielotto, C., Grisoli, M., di Bella, D., Migone, N., Gellera, C., di Donato, S., & Brusco, A. (2006). SCA28, a novel form of autosomal dominant cerebellar ataxia on chromosome 18p11.22–q11.2. *Brain*, *129*(1), 235–242. https://doi.org/10.1093/brain/awh651

Cagnoli, C., Stevanin, G., Brussino, A., Barberis, M., Mancini, C., Margolis, R. L., Holmes, S. E., Nobili, M., Forlani, S., Padovan, S., Pappi, P., Zaros, C., Leber, I., Ribai, P., Pugliese, L., Assalto, C., Brice, A., Migone, N., Dürr, A., & Brusco, A. (2010). Missense mutations in the AFG3L2 proteolytic domain account for ∼1.5% of European autosomal dominant cerebellar ataxias. *Human Mutation*, *31*(10), 1117–1124. https://doi.org/10.1002/humu.21342

Calvo, S. E., & Mootha, V. K. (2010). The Mitochondrial Proteome and Human Disease. *Annual Review of Genomics and Human Genetics*, *11*(1), 25–44. https://doi.org/10.1146/annurev-genom-082509-141720

Camacho-Pereira, J., Tarragó, M. G., Chini, C. C. S., Nin, V., Escande, C., Warner, G. M., Puranik, A. S., Schoon, R. A., Reid, J. M., Galina, A., & Chini, E. N. (2016). CD38 Dictates Age-Related NAD Decline and Mitochondrial Dysfunction through an SIRT3-Dependent Mechanism. *Cell Metabolism*, *23*(6), 1127–1139. https://doi.org/10.1016/j.cmet.2016.05.006

Cambronne, X. A., Stewart, M. L., Kim, D., Jones-Brunette, A. M., Morgan, R. K., Farrens, D. L., Cohen, M. S., & Goodman, R. H. (2016). Biosensor reveals multiple sources for mitochondrial NAD+. *Science*, *352*(6292), 1474–1477. https://doi.org/10.1126/science.aad5168

Cantó, C., Menzies, K. J., & Auwerx, J. (2015). NAD+ Metabolism and the Control of Energy Homeostasis: A Balancing Act between Mitochondria and the Nucleus. In *Cell Metabolism* (Vol. 22, Issue 1, pp. 31–53). Cell Press. https://doi.org/10.1016/j.cmet.2015.05.023

Carty, M., Goodbody, R., Schröder, M., Stack, J., Moynagh, P. N., & Bowie, A. G. (2006). The human adaptor SARM negatively regulates adaptor protein TRIF–dependent Toll-like receptor signaling. *Nature Immunology*, *7*(10), 1074–1081. https://doi.org/10.1038/ni1382

Casari, G., de Fusco, M., Ciarmatori, S., Zeviani, M., Mora, M., Fernandez, P., de Michele, G., Filla, A., Cocozza, S., Marconi, R., Dürr, A., Fontaine, B., & Ballabio, A. (1998). Spastic Paraplegia and OXPHOS Impairment Caused by Mutations in Paraplegin, a Nuclear-Encoded Mitochondrial Metalloprotease. *Cell*, *93*(6), 973–983. https://doi.org/10.1016/S0092-8674(00)81203-9

Chen, C.-Y., Lin, C.-W., Chang, C.-Y., Jiang, S.-T., & Hsueh, Y.-P. (2011). Sarm1, a negative regulator of innate immunity, interacts with syndecan-2 and regulates neuronal morphology. *Journal of Cell Biology*, *193*(4), 769–784. https://doi.org/10.1083/jcb.201008050

Chen, E. Y., Tan, C. M., Kou, Y., Duan, Q., Wang, Z., Meirelles, G. V., Clark, N. R., & Ma'ayan, A. (2013). Enrichr: interactive and collaborative HTML5 gene list enrichment analysis tool. *BMC Bioinformatics*, *14*(1), 128. https://doi.org/10.1186/1471-2105-14-128

Cheng, A., Yang, Y., Zhou, Y., Maharana, C., Lu, D., Peng, W., Liu, Y., Wan, R., Marosi, K., Misiak, M., Bohr, V. A., & Mattson, M. P. (2016). Mitochondrial SIRT3 Mediates Adaptive Responses of Neurons to Exercise and Metabolic and Excitatory Challenges. *Cell Metabolism*, *23*(1), 128–142. https://doi.org/10.1016/j.cmet.2015.10.013

Chitnis, T., & Weiner, H. L. (2017). CNS inflammation and neurodegeneration. *Journal of Clinical Investigation*, *127*(10), 3577–3587. https://doi.org/10.1172/JCI90609

Chuang, C.-F., & Bargmann, C. I. (2005). A Toll-interleukin 1 repeat protein at the synapse specifies asymmetric odorant receptor expression via ASK1 MAPKKK signaling. *Genes & Development*, *19*(2), 270–281. https://doi.org/10.1101/gad.1276505

Coleman, M. P., & Freeman, M. R. (2010). Wallerian Degeneration, WldS, and Nmnat. *Annual Review of Neuroscience*, *33*(1), 245–267. https://doi.org/10.1146/annurev-neuro-060909-153248

Conforti, L., Tarlton, A., Mack, T. G. A., Mi, W., Buckmaster, E. A., Wagner, D., Perry, V. H., & Coleman, M. P. (2000). A Ufd2/D4Cole1e chimeric protein and overexpression of Rbp7 in the slow Wallerian degeneration (WldS) mouse. *Proceedings of the National Academy of Sciences*, *97*(21), 11377–11382. https://doi.org/10.1073/pnas.97.21.11377

Conforti, L., Wilbrey, A., Morreale, G., Janeckova, L., Beirowski, B., Adalbert, R., Mazzola, F., di Stefano, M., Hartley, R., Babetto, E., Smith, T., Gilley, J., Billington, R. A., Genazzani, A. A., Ribchester, R. R., Magni, G., & Coleman, M. (2009). WldS protein requires Nmnat activity and a short N-terminal sequence to protect axons in mice. *Journal of Cell Biology*, *184*(4), 491–500. https://doi.org/10.1083/jcb.200807175

Consalez, G. G., Goldowitz, D., Casoni, F., & Hawkes, R. (2021). Origins, Development, and Compartmentation of the Granule Cells of the Cerebellum. In *Frontiers in Neural Circuits* (Vol. 14). Frontiers Media S.A. https://doi.org/10.3389/fncir.2020.611841

Covarrubias, A. J., Perrone, R., Grozio, A., & Verdin, E. (2021). NAD+ metabolism and its roles in cellular processes during ageing. *Nature Reviews Molecular Cell Biology*, *22*(2), 119–141. https://doi.org/10.1038/s41580-020-00313-x

Crawford, C. L., Antoniou, C., Komarek, L., Schultz, V., Donald, C. L., Montague, P., Barnett, S. C., Linington, C., Willison, H. J., Kohl, A., Coleman, M. P., & Edgar, J. M. (2022). SARM1 Depletion Slows Axon Degeneration in a CNS Model of Neurotropic Viral Infection. *Frontiers in Molecular Neuroscience*, *15*. https://doi.org/10.3389/fnmol.2022.860410

Cunniff, B., McKenzie, A. J., Heintz, N. H., & Howe, A. K. (2016). AMPK activity regulates trafficking of mitochondria to the leading edge during cell migration and matrix invasion. *Molecular Biology of the Cell*, *27*(17), 2662–2674. https://doi.org/10.1091/mbc.e16-05-0286

Demichev, V., Messner, C. B., Vernardis, S. I., Lilley, K. S., & Ralser, M. (2020). DIA-NN: neural networks and interference correction enable deep proteome coverage in high throughput. *Nature Methods*, *17*(1), 41–44. https://doi.org/10.1038/s41592-019-0638-x

Deshwal, S., Fiedler, K. U., & Langer, T. (2020). Mitochondrial Proteases: Multifaceted Regulators of Mitochondrial Plasticity. *Annual Review of Biochemistry*, *89*(1), 501–528. https://doi.org/10.1146/annurev-biochem-062917-012739

Devine, M. J., & Kittler, J. T. (2018). Mitochondria at the neuronal presynapse in health and disease. In *Nature Reviews Neuroscience* (Vol. 19, Issue 2, pp. 63–80). Nature Publishing Group. https://doi.org/10.1038/nrn.2017.170

di Bella, D., Lazzaro, F., Brusco, A., Plumari, M., Battaglia, G., Pastore, A., Finardi, A., Cagnoli, C., Tempia, F., Frontali, M., Veneziano, L., Sacco, T., Boda, E., Brussino, A., Bonn, F., Castellotti, B., Baratta, S., Mariotti, C., Gellera, C., … Taroni, F. (2010). Mutations in the mitochondrial protease gene AFG3L2 cause dominant hereditary ataxia SCA28. *Nature Genetics*, *42*(4), 313–321. https://doi.org/10.1038/ng.544

di Stefano, M., Loreto, A., Orsomando, G., Mori, V., Zamporlini, F., Hulse, R. P., Webster, J., Donaldson, L. F., Gering, M., Raffaelli, N., Coleman, M. P., Gilley, J., & Conforti, L. (2017). NMN Deamidase Delays Wallerian Degeneration and Rescues Axonal Defects Caused by NMNAT2 Deficiency In Vivo. *Current Biology*, *27*(6), 784–794. https://doi.org/10.1016/j.cub.2017.01.070

di Stefano, M., Nascimento-Ferreira, I., Orsomando, G., Mori, V., Gilley, J., Brown, R., Janeckova, L., Vargas, M. E., Worrell, L. A., Loreto, A., Tickle, J., Patrick, J., Webster, J. R. M., Marangoni, M., Carpi, F. M., Pucciarelli, S., Rossi, F., Meng, W., Sagasti, A., … Conforti, L. (2015). A rise in NAD precursor nicotinamide mononucleotide (NMN) after injury promotes axon degeneration. *Cell Death & Differentiation*, *22*(5), 731–742. https://doi.org/10.1038/cdd.2014.164

DiAntonio, A., Milbrandt, J., & Figley, M. D. (2021). The SARM1 TIR NADase: Mechanistic Similarities to Bacterial Phage Defense and Toxin-Antitoxin Systems. *Frontiers in Immunology*, *12*. https://doi.org/10.3389/fimmu.2021.752898

Ding, C., Wu, Y., Dabas, H., & Hammarlund, M. (2022). Activation of the CaMKII-Sarm1-ASK1-p38 MAP kinase pathway protects against axon degeneration caused by loss of mitochondria. *ELife*, *11*. https://doi.org/10.7554/eLife.73557

Doran, C. G., Sugisawa, R., Carty, M., Roche, F., Fergus, C., Hokamp, K., Kelly, V. P., & Bowie, A. G. (2021). CRISPR/Cas9-mediated SARM1 knockout and epitope-tagged mice reveal that SARM1 does not regulate nuclear transcription, but is expressed in macrophages. *Journal of Biological Chemistry*, *297*(6), 101417. https://doi.org/10.1016/j.jbc.2021.101417

Doxaki, C., & Palikaras, K. (2021). Neuronal Mitophagy: Friend or Foe? In *Frontiers in Cell and Developmental Biology* (Vol. 8). Frontiers Media S.A. https://doi.org/10.3389/fcell.2020.611938

Ebert, D., Haller, R. G., & Walton, M. E. (2003). Energy Contribution of Octanoate to Intact Rat Brain Metabolism Measured by 13C Nuclear Magnetic Resonance Spectroscopy. *The Journal of Neuroscience*, *23*(13), 5928–5935. https://doi.org/10.1523/JNEUROSCI.23-13-05928.2003

Essuman, K., Summers, D. W., Sasaki, Y., Mao, X., DiAntonio, A., & Milbrandt, J. (2017). The SARM1 Toll/Interleukin-1 Receptor Domain Possesses Intrinsic NAD + Cleavage Activity that Promotes Pathological Axonal Degeneration. *Neuron*, *93*(6), 1334-1343.e5. https://doi.org/10.1016/j.neuron.2017.02.022

Fan, M., Zhang, J., Tsai, C.-W., Orlando, B. J., Rodriguez, M., Xu, Y., Liao, M., Tsai, M.-F., & Feng, L. (2020). Structure and mechanism of the mitochondrial Ca2+ uniporter holocomplex. *Nature*, *582*(7810), 129–133. https://doi.org/10.1038/s41586-020-2309-6

Fang, E. F., Hou, Y., Palikaras, K., Adriaanse, B. A., Kerr, J. S., Yang, B., Lautrup, S., Hasan-Olive, M. M., Caponio, D., Dan, X., Rocktäschel, P., Croteau, D. L., Akbari, M., Greig, N. H., Fladby, T., Nilsen, H., Cader, M. Z., Mattson, M. P., Tavernarakis, N., & Bohr, V. A. (2019). Mitophagy inhibits amyloid-β and tau pathology and reverses cognitive deficits in models of Alzheimer's disease. *Nature Neuroscience*, *22*(3), 401–412. https://doi.org/10.1038/s41593-018-0332-9

Fang, E. F., Kassahun, H., Croteau, D. L., Scheibye-Knudsen, M., Marosi, K., Lu, H., Shamanna, R. A., Kalyanasundaram, S., Bollineni, R. C., Wilson, M. A., Iser, W. B., Wollman, B. N., Morevati, M., Li, J., Kerr, J. S., Lu, Q., Waltz, T. B., Tian, J., Sinclair, D. A., … Bohr, V. A. (2016). NAD + Replenishment Improves Lifespan and Healthspan in Ataxia Telangiectasia Models via Mitophagy and DNA Repair. *Cell Metabolism*, *24*(4), 566–581. https://doi.org/10.1016/j.cmet.2016.09.004

Fassier, C., Hazan, J., & Melki, J. (2015). Mouse Models of Autosomal Dominant Spastic Paraplegia. In *Movement Disorders* (pp. 1073–1086). Elsevier. https://doi.org/10.1016/B978-0-12-405195-9.00070-6

Fecher, C., Trovò, L., Müller, S. A., Snaidero, N., Wettmarshausen, J., Heink, S., Ortiz, O., Wagner, I., Kühn, R., Hartmann, J., Karl, R. M., Konnerth, A., Korn, T., Wurst, W., Merkler, D., Lichtenthaler, S. F., Perocchi, F., & Misgeld, T. (2019). Cell-type-specific profiling of brain mitochondria reveals functional and molecular diversity. *Nature Neuroscience*, *22*(10), 1731–1742. https://doi.org/10.1038/s41593-019-0479-z

Ferreirinha, F., Quattrini, A., Pirozzi, M., Valsecchi, V., Dina, G., Broccoli, V., Auricchio, A., Piemonte, F., Tozzi, G., Gaeta, L., Casari, G., Ballabio, A., & Rugarli, E. I. (2004). Axonal degeneration in paraplegin-deficient mice is associated with abnormal mitochondria and impairment of axonal transport. *Journal of Clinical Investigation*, *113*(2), 231–242. https://doi.org/10.1172/JCI20138

Fey, A., Schachner, M., & Irintchev, A. (2010). A Novel Motion Analysis Approach Reveals Late Recovery in C57BL/6 Mice and Deficits in NCAM-Deficient Mice after Sciatic Nerve Crush. *Journal of Neurotrauma*, *27*(5), 815–828. https://doi.org/10.1089/neu.2009.1217

Fields, R. D., & Dutta, D. J. (2019). Treadmilling Model for Plasticity of the Myelin Sheath. *Trends in Neurosciences*, *42*(7), 443–447. https://doi.org/10.1016/j.tins.2019.04.002

Figley, M. D., Gu, W., Nanson, J. D., Shi, Y., Sasaki, Y., Cunnea, K., Malde, A. K., Jia, X., Luo, Z., Saikot, F. K., Mosaiab, T., Masic, V., Holt, S., Hartley-Tassell, L., McGuinness, H. Y., Manik, M. K., Bosanac, T., Landsberg, M. J., Kerry, P. S., … Ve, T. (2021). SARM1 is a metabolic sensor activated by an increased NMN/NAD+ ratio to trigger axon degeneration. *Neuron*, *109*(7), 1118-1136.e11. https://doi.org/10.1016/j.neuron.2021.02.009

Finnegan, L. K., Chadderton, N., Kenna, P. F., Palfi, A., Carty, M., Bowie, A. G., Millington-Ward, S., & Farrar, G. J. (2022). SARM1 Ablation Is Protective and Preserves Spatial Vision in an In Vivo Mouse Model of Retinal Ganglion Cell Degeneration. *International Journal of Molecular Sciences*, *23*(3), 1606. https://doi.org/10.3390/ijms23031606

Fischer, L. R., Culver, D. G., Davis, A. A., Tennant, P., Wang, M., Coleman, M., Asress, S., Adalbert, R., Alexander, G. M., & Glass, J. D. (2005). The WldS gene modestly prolongs survival in the SOD1G93A fALS mouse. *Neurobiology of Disease*, *19*(1–2), 293–300. https://doi.org/10.1016/j.nbd.2005.01.008

Fivenson, E. M., Lautrup, S., Sun, N., Scheibye-Knudsen, M., Stevnsner, T., Nilsen, H., Bohr, V. A., & Fang, E. F. (2017). Mitophagy in neurodegeneration and aging. *Neurochemistry International*, *109*, 202–209. https://doi.org/10.1016/j.neuint.2017.02.007

Gerdts, J., Brace, E. J., Sasaki, Y., DiAntonio, A., & Milbrandt, J. (2015). SARM1 activation triggers axon degeneration locally via NAD+ destruction. *Science*, *348*(6233), 453–457. https://doi.org/10.1126/science.1258366

Gerdts, J., Summers, D. W., Milbrandt, J., & DiAntonio, A. (2016). Axon Self-Destruction: New Links among SARM1, MAPKs, and NAD+ Metabolism. *Neuron*, *89*(3), 449–460. https://doi.org/10.1016/j.neuron.2015.12.023

Gerdts, J., Summers, D. W., Sasaki, Y., DiAntonio, A., & Milbrandt, J. (2013). Sarm1-Mediated Axon Degeneration Requires Both SAM and TIR Interactions. *Journal of Neuroscience*, *33*(33), 13569–13580. https://doi.org/10.1523/JNEUROSCI.1197-13.2013

Gilley, J., & Coleman, M. P. (2010). Endogenous Nmnat2 Is an Essential Survival Factor for Maintenance of Healthy Axons. *PLoS Biology*, *8*(1), e1000300. https://doi.org/10.1371/journal.pbio.1000300

Gilley, J., Orsomando, G., Nascimento-Ferreira, I., & Coleman, M. P. (2015). Absence of SARM1 Rescues Development and Survival of NMNAT2-Deficient Axons. *Cell Reports*, *10*(12), 1974–1981. https://doi.org/10.1016/j.celrep.2015.02.060

Gilley, J., Ribchester, R. R., & Coleman, M. P. (2017). Sarm1 Deletion, but Not Wld S , Confers Lifelong Rescue in a Mouse Model of Severe Axonopathy. *Cell Reports*, *21*(1), 10–16. https://doi.org/10.1016/j.celrep.2017.09.027

Gimenez-Cassina, A., Lim, F., Cerrato, T., Palomo, G. M., & Diaz-Nido, J. (2009). Mitochondrial Hexokinase II Promotes Neuronal Survival and Acts Downstream of Glycogen Synthase Kinase-3. *Journal of Biological Chemistry*, *284*(5), 3001–3011. https://doi.org/10.1074/jbc.M808698200

Ginhoux, F., Greter, M., Leboeuf, M., Nandi, S., See, P., Gokhan, S., Mehler, M. F., Conway, S. J., Ng, L. G., Stanley, E. R., Samokhvalov, I. M., & Merad, M. (2010). Fate Mapping Analysis Reveals That Adult Microglia Derive from Primitive Macrophages. *Science*, *330*(6005), 841–845. https://doi.org/10.1126/science.1194637

Giorgi, C., Danese, A., Missiroli, S., Patergnani, S., & Pinton, P. (2018). Calcium Dynamics as a Machine for Decoding Signals. *Trends in Cell Biology*, *28*(4), 258–273. https://doi.org/10.1016/j.tcb.2018.01.002

Giorgi, C., Marchi, S., & Pinton, P. (2018). The machineries, regulation and cellular functions of mitochondrial calcium. *Nature Reviews Molecular Cell Biology*, *19*(11), 713–730. https://doi.org/10.1038/s41580-018-0052-8

Giovannoni, F., & Quintana, F. J. (2020). The Role of Astrocytes in CNS Inflammation. *Trends in Immunology*, *41*(9), 805–819. https://doi.org/10.1016/j.it.2020.07.007

Gladkova, C., Maslen, S. L., Skehel, J. M., & Komander, D. (2018). Mechanism of parkin activation by PINK1. *Nature*, *559*(7714), 410–414. https://doi.org/10.1038/s41586-018-0224-x

Glynn, S. E. (2017). Multifunctional Mitochondrial AAA Proteases. *Frontiers in Molecular Biosciences*, *4*. https://doi.org/10.3389/fmolb.2017.00034

Gomes, A. P., Price, N. L., Ling, A. J. Y., Moslehi, J. J., Montgomery, M. K., Rajman, L., White, J. P., Teodoro, J. S., Wrann, C. D., Hubbard, B. P., Mercken, E. M., Palmeira, C. M., de Cabo, R., Rolo, A. P., Turner, N., Bell, E. L., & Sinclair, D. A. (2013). Declining NAD+ Induces a Pseudohypoxic State Disrupting Nuclear-Mitochondrial Communication during Aging. *Cell*, *155*(7), 1624–1638. https://doi.org/10.1016/j.cell.2013.11.037

Guélin, E., Rep, M., & Grivell, L. A. (1996). Afg3p, a mitochondrial ATP-dependent metalloprotease, is involved in degradation of mitochondrially-encoded Cox1, Cox3, Cob, Su6, Su8 and Su9 subunits of the inner membrane complexes III, IV and V. *FEBS Letters*, *381*(1–2), 42–46. https://doi.org/10.1016/0014-5793(96)00074-9

Guerreiro, S., Privat, A.-L., Bressac, L., & Toulorge, D. (2020). CD38 in Neurodegeneration and Neuroinflammation. *Cells*, *9*(2), 471. https://doi.org/10.3390/cells9020471

Hallows, W. C., Lee, S., & Denu, J. M. (2006). Sirtuins deacetylate and activate mammalian acetyl-CoA synthetases. *Proceedings of the National Academy of Sciences*, *103*(27), 10230–10235. https://doi.org/10.1073/pnas.0604392103

Hammond, T. R., Marsh, S. E., & Stevens, B. (2019). Immune Signaling in Neurodegeneration. *Immunity*, *50*(4), 955–974. https://doi.org/10.1016/j.immuni.2019.03.016

Hasbani, D., & Omalley, K. (2006). WldS mice are protected against the Parkinsonian mimetic MPTP. *Experimental Neurology*, *202*(1), 93–99. https://doi.org/10.1016/j.expneurol.2006.05.017

Hewamadduma, C. A., Hoggard, N., O'Malley, R., Robinson, M. K., Beauchamp, N. J., Segamogaite, R., Martindale, J., Rodgers, T., Rao, G., Sarrigiannis, P., Shanmugarajah, P., Zis, P., Sharrack, B., McDermott, C. J., Shaw, P. J., & Hadjivassiliou, M. (2018). Novel genotype-phenotype and MRI correlations in a large cohort of patients with SPG7 mutations. *Neurology: Genetics*, *4*(6). https://doi.org/10.1212/NXG.0000000000000279

Hicks, A. N., Lorenzetti, D., Gilley, J., Lu, B., Andersson, K.-E., Miligan, C., Overbeek, P. A., Oppenheim, R., & Bishop, C. E. (2012). Nicotinamide Mononucleotide Adenylyltransferase 2 (Nmnat2) Regulates Axon Integrity in the Mouse Embryo. *PLoS ONE*, *7*(10), e47869. https://doi.org/10.1371/journal.pone.0047869

Higashida, H., Salmina, A. B., Olovyannikova, R. Y., Hashii, M., Yokoyama, S., Koizumi, K., Jin, D., Liu, H.-X., Lopatina, O., Amina, S., Islam, M. S., Huang, J.-J., & Noda, M. (2007).

Cyclic ADP-ribose as a universal calcium signal molecule in the nervous system. *Neurochemistry International*, *51*(2–4), 192–199. https://doi.org/10.1016/j.neuint.2007.06.023

Hirabayashi, Y., Kwon, S.-K., Paek, H., Pernice, W. M., Paul, M. A., Lee, J., Erfani, P., Raczkowski, A., Petrey, D. S., Pon, L. A., & Polleux, F. (2017). *ER-mitochondria tethering by PDZD8 regulates Ca 2+ dynamics in mammalian neurons*. https://www.science.org

Hirschey, M. D., Shimazu, T., Goetzman, E., Jing, E., Schwer, B., Lombard, D. B., Grueter, C. A., Harris, C., Biddinger, S., Ilkayeva, O. R., Stevens, R. D., Li, Y., Saha, A. K., Ruderman, N. B., Bain, J. R., Newgard, C. B., Farese Jr, R. v., Alt, F. W., Kahn, C. R., & Verdin, E. (2010). SIRT3 regulates mitochondrial fatty-acid oxidation by reversible enzyme deacetylation. *Nature*, *464*(7285), 121–125. https://doi.org/10.1038/nature08778

Hornig-Do, H.-T., Tatsuta, T., Buckermann, A., Bust, M., Kollberg, G., Rötig, A., Hellmich, M., Nijtmans, L., & Wiesner, R. J. (2012). Nonsense mutations in the COX1 subunit impair the stability of respiratory chain complexes rather than their assembly. *The EMBO Journal*, *31*(5), 1293–1307. https://doi.org/10.1038/emboj.2011.477

Horsefield, S., Burdett, H., Zhang, X., Manik, M. K., Shi, Y., Chen, J., Qi, T., Gilley, J., Lai, J.-S., Rank, M. X., Casey, L. W., Gu, W., Ericsson, D. J., Foley, G., Hughes, R. O., Bosanac, T., von Itzstein, M., Rathjen, J. P., Nanson, J. D., … Kobe, B. (2019). NAD+ cleavage activity by animal and plant TIR domains in cell death pathways. *Science*, *365*(6455), 793–799. https://doi.org/10.1126/science.aax1911

Hoxha, E., Gabriele, R. M. C., Balbo, I., Ravera, F., Masante, L., Zambelli, V., Albergo, C., Mitro, N., Caruso, D., di Gregorio, E., Brusco, A., Borroni, B., & Tempia, F. (2017). Motor Deficits and Cerebellar Atrophy in Elovl5 Knock Out Mice. *Frontiers in Cellular Neuroscience*, *11*. https://doi.org/10.3389/fncel.2017.00343

Hughes, C. S., Foehr, S., Garfield, D. A., Furlong, E. E., Steinmetz, L. M., & Krijgsveld, J. (2014). Ultrasensitive proteome analysis using paramagnetic bead technology. *Molecular Systems Biology*, *10*(10), 757. https://doi.org/10.15252/msb.20145625

Hughes, R. O., Bosanac, T., Mao, X., Engber, T. M., DiAntonio, A., Milbrandt, J., Devraj, R., & Krauss, R. (2021). Small Molecule SARM1 Inhibitors Recapitulate the SARM1−/− Phenotype and Allow Recovery of a Metastable Pool of Axons Fated to Degenerate. *Cell Reports*, *34*(1), 108588. https://doi.org/10.1016/j.celrep.2020.108588

Hurst, S., Baggett, A., Csordas, G., & Sheu, S.-S. (2019). SPG7 targets the m-AAA protease complex to process MCU for uniporter assembly, Ca2+ influx, and regulation of mitochondrial permeability transition pore opening. *Journal of Biological Chemistry*, *294*(28), 10807–10818. https://doi.org/10.1074/jbc.RA118.006443

Illescas, M., Peñas, A., Arenas, J., Martín, M. A., & Ugalde, C. (2021). Regulation of Mitochondrial Function by the Actin Cytoskeleton. *Frontiers in Cell and Developmental Biology*, *9*. https://doi.org/10.3389/fcell.2021.795838

Imai, S., & Guarente, L. (2016). It takes two to tango: NAD+ and sirtuins in aging/longevity control. *Npj Aging and Mechanisms of Disease*, *2*(1), 16017. https://doi.org/10.1038/npjamd.2016.17

Ip, C. W., Kroner, A., Bendszus, M., Leder, C., Kobsar, I., Fischer, S., Wiendl, H., Nave, K.-A., & Martini, R. (2006). Immune Cells Contribute to Myelin Degeneration and Axonopathic

Changes in Mice Overexpressing Proteolipid Protein in Oligodendrocytes. *Journal of Neuroscience*, *26*(31), 8206–8216. https://doi.org/10.1523/JNEUROSCI.1921-06.2006

Irintchev, A., Simova, O., Eberhardt, K. A., Morellini, F., & Schachner, M. (2005). Impacts of lesion severity and tyrosine kinase receptor B deficiency on functional outcome of femoral nerve injury assessed by a novel single-frame motion analysis in mice. *European Journal of Neuroscience*, *22*(4), 802–808. https://doi.org/10.1111/j.1460-9568.2005.04274.x

Ising, C., & Heneka, M. T. (2018). Functional and structural damage of neurons by innate immune mechanisms during neurodegeneration. *Cell Death & Disease*, *9*(2), 120. https://doi.org/10.1038/s41419-017-0153-x

Jang, S., Chapa-Dubocq, X. R., Fossati, S., & Javadov, S. (2021). Analysis of Mitochondrial Calcium Retention Capacity in Cultured Cells: Permeabilized Cells Versus Isolated Mitochondria. *Frontiers in Physiology*, *12*. https://doi.org/10.3389/fphys.2021.773839

Jebara, F., Weiss, C., & Azem, A. (2017). Hsp60 and Hsp70 Chaperones: Guardians of Mitochondrial Proteostasis. In *eLS* (pp. 1–9). John Wiley & Sons, Ltd. https://doi.org/10.1002/9780470015902.a0027152

Jiang, Y., Liu, T., Lee, C.-H., Chang, Q., Yang, J., & Zhang, Z. (2020). The NAD+-mediated self-inhibition mechanism of pro-neurodegenerative SARM1. *Nature*, *588*(7839), 658–663. https://doi.org/10.1038/s41586-020-2862-z

Jurga, A. M., Paleczna, M., & Kuter, K. Z. (2020). Overview of General and Discriminating Markers of Differential Microglia Phenotypes. *Frontiers in Cellular Neuroscience*, *14*. https://doi.org/10.3389/fncel.2020.00198

Kaminska, B., Gozdz, A., Zawadzka, M., Ellert-Miklaszewska, A., & Lipko, M. (2009). MAPK Signal Transduction Underlying Brain Inflammation and Gliosis as Therapeutic Target. *The Anatomical Record: Advances in Integrative Anatomy and Evolutionary Biology*, *292*(12), 1902–1913. https://doi.org/10.1002/ar.21047

Karry, R., Klein, E., & ben Shachar, D. (2004). Mitochondrial complex i subunits expression is altered in schizophrenia: a postmortem study. *Biological Psychiatry*, *55*(7), 676–684. https://doi.org/10.1016/j.biopsych.2003.12.012

Kelliher, M. T., Saunders, H. A., & Wildonger, J. (2019). Microtubule control of functional architecture in neurons. In *Current Opinion in Neurobiology* (Vol. 57, pp. 39–45). Elsevier Ltd. https://doi.org/10.1016/j.conb.2019.01.003

Ketschek, A., Holland, S. M., & Gallo, G. (2022a). SARM1 Suppresses Axon Branching Through Attenuation of Axonal Cytoskeletal Dynamics. *Frontiers in Molecular Neuroscience*, *15*. https://doi.org/10.3389/fnmol.2022.726962

Ketschek, A., Holland, S. M., & Gallo, G. (2022b). SARM1 Suppresses Axon Branching Through Attenuation of Axonal Cytoskeletal Dynamics. *Frontiers in Molecular Neuroscience*, *15*. https://doi.org/10.3389/fnmol.2022.726962

Khundadze, M., Kollmann, K., Koch, N., Biskup, C., Nietzsche, S., Zimmer, G., Hennings, J. C., Huebner, A. K., Symmank, J., Jahic, A., Ilina, E. I., Karle, K., Schöls, L., Kessels, M., Braulke, T., Qualmann, B., Kurth, I., Beetz, C., & Hübner, C. A. (2013). A Hereditary Spastic Paraplegia Mouse Model Supports a Role of ZFYVE26/SPASTIZIN for the Endolysosomal System. *PLoS Genetics*, *9*(12), e1003988. https://doi.org/10.1371/journal.pgen.1003988

Killackey, S. A., Rahman, M. A., Soares, F., Zhang, A. B., Abdel-Nour, M., Philpott, D. J., & Girardin, S. E. (2019). The mitochondrial Nod-like receptor NLRX1 modifies apoptosis through SARM1. *Molecular and Cellular Biochemistry*, *453*(1–2), 187–196. https://doi.org/10.1007/s11010-018-3444-3

Kim, S. H., Vlkolinsky, R., Cairns, N., Fountoulakis, M., & Lubec, G. (2001). The reduction of NADH ubiquinone oxidoreductase 24- and 75-kDa subunits in brains of patients with Down syndrome and Alzheimer's disease. *Life Sciences*, *68*(24), 2741–2750. https://doi.org/10.1016/S0024-3205(01)01074-8

Kim, Y., Zhou, P., Qian, L., Chuang, J.-Z., Lee, J., Li, C., Iadecola, C., Nathan, C., & Ding, A. (2007). MyD88-5 links mitochondria, microtubules, and JNK3 in neurons and regulates neuronal survival. *Journal of Experimental Medicine*, *204*(9), 2063–2074. https://doi.org/10.1084/jem.20070868

Kitay, B. M., McCormack, R., Wang, Y., Tsoulfas, P., & Zhai, R. G. (2013). Mislocalization of neuronal mitochondria reveals regulation of Wallerian degeneration and NMNAT/WLDS-mediated axon protection independent of axonal mitochondria. *Human Molecular Genetics*, *22*(8), 1601–1614. https://doi.org/10.1093/hmg/ddt009

Klebe, S., Depienne, C., Gerber, S., Challe, G., Anheim, M., Charles, P., Fedirko, E., Lejeune, E., Cottineau, J., Brusco, A., Dollfus, H., Chinnery, P. F., Mancini, C., Ferrer, X., Sole, G., Destée, A., Mayer, J.-M., Fontaine, B., Seze, J. de, … Durr, A. (2012). Spastic paraplegia gene 7 in patients with spasticity and/or optic neuropathy. *Brain*, *135*(10), 2980–2993. https://doi.org/10.1093/brain/aws240

Klebe, S., Stevanin, G., & Depienne, C. (2015). Clinical and genetic heterogeneity in hereditary spastic paraplegias: From SPG1 to SPG72 and still counting. *Revue Neurologique*, *171*(6–7), 505–530. https://doi.org/10.1016/j.neurol.2015.02.017

Klutho, P. J., Dashek, R. J., Song, L., & Baines, C. P. (2020). Genetic manipulation of SPG7 or NipSnap2 does not affect mitochondrial permeability transition. *Cell Death Discovery*, *6*(1), 5. https://doi.org/10.1038/s41420-020-0239-6

Ko, K. W., Devault, L., Sasaki, Y., Milbrandt, J., & DiAntonio, A. (2021). Live imaging reveals the cellular events downstream of SARM1 activation. *ELife*, *10*. https://doi.org/10.7554/eLife.71148

Ko, K. W., Milbrandt, J., & DiAntonio, A. (2020). SARM1 acts downstream of neuroinflammatory and necroptotic signaling to induce axon degeneration. *Journal of Cell Biology*, *219*(8). https://doi.org/10.1083/jcb.201912047

Koh, J.-H., & Kim, J.-Y. (2021). Role of PGC-1α in the Mitochondrial NAD+ Pool in Metabolic Diseases. *International Journal of Molecular Sciences*, *22*(9), 4558. https://doi.org/10.3390/ijms22094558

König, T., Tröder, S. E., Bakka, K., Korwitz, A., Richter-Dennerlein, R., Lampe, P. A., Patron, M., Mühlmeister, M., Guerrero-Castillo, S., Brandt, U., Decker, T., Lauria, I., Paggio, A., Rizzuto, R., Rugarli, E. I., De Stefani, D., & Langer, T. (2016). The m -AAA Protease Associated with Neurodegeneration Limits MCU Activity in Mitochondria. *Molecular Cell*, *64*(1), 148–162. https://doi.org/10.1016/j.molcel.2016.08.020

Koopman, W. J. H., Distelmaier, F., Smeitink, J. A. M., & Willems, P. H. G. M. (2013). OXPHOS mutations and neurodegeneration. In *EMBO Journal* (Vol. 32, Issue 1, pp. 9–29). https://doi.org/10.1038/emboj.2012.300

Koppen, M., Bonn, F., Ehses, S., & Langer, T. (2009). Autocatalytic Processing of m-AAA Protease Subunits in Mitochondria. *Molecular Biology of the Cell*, *20*(19), 4216–4224. https://doi.org/10.1091/mbc.e09-03-0218

Koppen, M., Metodiev, M. D., Casari, G., Rugarli, E. I., & Langer, T. (2007). Variable and Tissue-Specific Subunit Composition of Mitochondrial m-AAA Protease Complexes Linked to Hereditary Spastic Paraplegia. *Molecular and Cellular Biology*, *27*(2), 758–767. https://doi.org/10.1128/MCB.01470-06

Korbel, D., Wurth, S., Käser, M., & Langer, T. (2004). Membrane protein turnover by the m-AAA protease in mitochondria depends on the transmembrane domains of its subunits. *EMBO Reports*, *5*(7), 698–703. https://doi.org/10.1038/sj.embor.7400186

Kory, N., uit de Bos, J., van der Rijt, S., Jankovic, N., Güra, M., Arp, N., Pena, I. A., Prakash, G., Chan, S. H., Kunchok, T., Lewis, C. A., & Sabatini, D. M. (2020). MCART1/SLC25A51 is required for mitochondrial NAD transport. *Science Advances*, *6*(43). https://doi.org/10.1126/sciadv.abe5310

Krauss, R., Bosanac, T., Devraj, R., Engber, T., & Hughes, R. O. (2020). Axons Matter: The Promise of Treating Neurodegenerative Disorders by Targeting SARM1-Mediated Axonal Degeneration. *Trends in Pharmacological Sciences*, *41*(4), 281–293. https://doi.org/10.1016/j.tips.2020.01.006

Kremmidiotis, G., Gardner, A. E., Settasatian, C., Savoia, A., Sutherland, G. R., & Callen, D. F. (2001). Molecular and Functional Analyses of the Human and Mouse Genes Encoding AFG3L1, a Mitochondrial Metalloprotease Homologous to the Human Spastic Paraplegia Protein. *Genomics*, *76*(1–3), 58–65. https://doi.org/10.1006/geno.2001.6560

Kuleshov, M. v., Jones, M. R., Rouillard, A. D., Fernandez, N. F., Duan, Q., Wang, Z., Koplev, S., Jenkins, S. L., Jagodnik, K. M., Lachmann, A., McDermott, M. G., Monteiro, C. D., Gundersen, G. W., & Ma'ayan, A. (2016). Enrichr: a comprehensive gene set enrichment analysis web server 2016 update. *Nucleic Acids Research*, *44*(W1), W90–W97. https://doi.org/10.1093/nar/gkw377

Kwong, J. Q., & Molkentin, J. D. (2015). Physiological and Pathological Roles of the Mitochondrial Permeability Transition Pore in the Heart. *Cell Metabolism*, *21*(2), 206–214. https://doi.org/10.1016/j.cmet.2014.12.001

Lai, M.-Y., Li, J., Zhang, X.-X., Wu, W., Li, Z.-P., Sun, Z.-X., Zhao, M.-Y., Yang, D.-M., Wang, D.-D., Li, W., Zhao, D.-M., Zhou, X.-M., & Yang, L.-F. (2022). SARM1 participates in axonal degeneration and mitochondrial dysfunction in prion disease. *Neural Regeneration Research*, *17*(10), 2293. https://doi.org/10.4103/1673-5374.337051

Lautrup, S., Sinclair, D. A., Mattson, M. P., & Fang, E. F. (2019). NAD+ in Brain Aging and Neurodegenerative Disorders. *Cell Metabolism*, *30*(4), 630–655. https://doi.org/10.1016/j.cmet.2019.09.001

Lee, C. F., Caudal, A., Abell, L., Nagana Gowda, G. A., & Tian, R. (2019). Targeting NAD+ Metabolism as Interventions for Mitochondrial Disease. *Scientific Reports*, *9*(1), 3073. https://doi.org/10.1038/s41598-019-39419-4

Lee, H. C., & Zhao, Y. J. (2019). Resolving the topological enigma in Ca2+ signaling by cyclic ADP-ribose and NAADP. *Journal of Biological Chemistry*, *294*(52), 19831–19843. https://doi.org/10.1074/jbc.REV119.009635

Lee, S., Augustin, S., Tatsuta, T., Gerdes, F., Langer, T., & Tsai, F. T. F. (2011). Electron Cryomicroscopy Structure of a Membrane-anchored Mitochondrial AAA Protease. *Journal of Biological Chemistry*, *286*(6), 4404–4411. https://doi.org/10.1074/jbc.M110.158741

Lee, S.-G., Su, Z.-Z., Emdad, L., Gupta, P., Sarkar, D., Borjabad, A., Volsky, D. J., & Fisher, P. B. (2008). Mechanism of Ceftriaxone Induction of Excitatory Amino Acid Transporter-2 Expression and Glutamate Uptake in Primary Human Astrocytes. *Journal of Biological Chemistry*, *283*(19), 13116–13123. https://doi.org/10.1074/jbc.M707697200

Lemon, R. N. (2008). Descending pathways in motor control. In *Annual Review of Neuroscience* (Vol. 31, pp. 195–218). https://doi.org/10.1146/annurev.neuro.31.060407.125547

Li, J., Chen, L., Qin, Q., Wang, D., Zhao, J., Gao, H., Yuan, X., Zhang, J., Zou, Y., Mao, Z., Xiong, Y., Min, Z., Yan, M., Wang, C., & Xue, Z. (2022). Upregulated hexokinase 2 expression induces the apoptosis of dopaminergic neurons by promoting lactate production in Parkinson's disease. *Neurobiology of Disease*, *163*, 105605. https://doi.org/10.1016/j.nbd.2021.105605

Li, Y., Pazyra-Murphy, M. F., Avizonis, D., de Sá Tavares Russo, M., Tang, S., Chen, C.-Y., Hsueh, Y.-P., Bergholz, J. S., Jiang, T., Zhao, J. J., Zhu, J., Ko, K. W., Milbrandt, J., DiAntonio, A., & Segal, R. A. (2022). Sarm1 activation produces cADPR to increase intra-axonal Ca++ and promote axon degeneration in PIPN. *Journal of Cell Biology*, *221*(2). https://doi.org/10.1083/jcb.202106080

Liberati, N. T., Fitzgerald, K. A., Kim, D. H., Feinbaum, R., Golenbock, D. T., & Ausubel, F. M. (2004). Requirement for a conserved Toll/interleukin-1 resistance domain protein in the Caenorhabditis elegans immune response. *Proceedings of the National Academy of Sciences*, *101*(17), 6593–6598. https://doi.org/10.1073/pnas.0308625101

Lin, C.-W., Chen, C.-Y., Cheng, S.-J., Hu, H.-T., & Hsueh, Y.-P. (2014). Sarm1 deficiency impairs synaptic function and leads to behavioral deficits, which can be ameliorated by an mGluR allosteric modulator. *Frontiers in Cellular Neuroscience*, *8*. https://doi.org/10.3389/fncel.2014.00087

Lin, C.-W., Liu, H.-Y., Chen, C.-Y., & Hsueh, Y.-P. (2014). Neuronally-expressed Sarm1 regulates expression of inflammatory and antiviral cytokines in brains. *Innate Immunity*, *20*(2), 161–172. https://doi.org/10.1177/1753425913485877

Linnerbauer, M., Wheeler, M. A., & Quintana, F. J. (2020). Astrocyte Crosstalk in CNS Inflammation. *Neuron*, *108*(4), 608–622. https://doi.org/10.1016/j.neuron.2020.08.012

Liu, H., Zhang, J., Xu, X., Lu, S., Yang, D., Xie, C., Jia, M., Zhang, W., Jin, L., Wang, X., Shen, X., Li, F., Wang, W., Bao, X., Li, S., Zhu, M., Wang, W., Wang, Y., Huang, Z., & Teng, H. (2021a). SARM1 promotes neuroinflammation and inhibits neural regeneration after spinal cord injury through NF-κB signaling. *Theranostics*, *11*(9), 4187–4206. https://doi.org/10.7150/thno.49054

Liu, H., Zhang, J., Xu, X., Lu, S., Yang, D., Xie, C., Jia, M., Zhang, W., Jin, L., Wang, X., Shen, X., Li, F., Wang, W., Bao, X., Li, S., Zhu, M., Wang, W., Wang, Y., Huang, Z., & Teng, H. (2021b). SARM1 promotes neuroinflammation and inhibits neural regeneration after spinal cord injury through NF-κB signaling. *Theranostics*, *11*(9), 4187–4206. https://doi.org/10.7150/thno.49054

Liu, L., Su, X., Quinn, W. J., Hui, S., Krukenberg, K., Frederick, D. W., Redpath, P., Zhan, L., Chellappa, K., White, E., Migaud, M., Mitchison, T. J., Baur, J. A., & Rabinowitz, J. D. (2018). Quantitative Analysis of NAD Synthesis-Breakdown Fluxes. *Cell Metabolism*, *27*(5), 1067-1080.e5. https://doi.org/10.1016/j.cmet.2018.03.018

Liu, Y., Cheng, A., Li, Y.-J., Yang, Y., Kishimoto, Y., Zhang, S., Wang, Y., Wan, R., Raefsky, S. M., Lu, D., Saito, T., Saido, T., Zhu, J., Wu, L.-J., & Mattson, M. P. (2019). SIRT3 mediates hippocampal synaptic adaptations to intermittent fasting and ameliorates deficits in APP mutant mice. *Nature Communications*, *10*(1), 1886. https://doi.org/10.1038/s41467-019-09897-1

Liu, Z., Zhang, L., Ren, C., Xu, M., Li, S., Ban, R., Wu, Y., Chen, L., Sun, S., Elstner, M., Shimura, M., Ogawa-Tominaga, M., Murayama, K., Shi, T., Prokisch, H., & Fang, F. (2022). Whole genome and exome sequencing identify NDUFV2 mutations as a new cause of progressive cavitating leukoencephalopathy. *Journal of Medical Genetics*, *59*(4), 351–357. https://doi.org/10.1136/jmedgenet-2020-107383

Loreto, A., Hill, C. S., Hewitt, V. L., Orsomando, G., Angeletti, C., Gilley, J., Lucci, C., Sanchez-Martinez, A., Whitworth, A. J., Conforti, L., Dajas-Bailador, F., & Coleman, M. P. (2020). Mitochondrial impairment activates the Wallerian pathway through depletion of NMNAT2 leading to SARM1-dependent axon degeneration. *Neurobiology of Disease*, *134*. https://doi.org/10.1016/j.nbd.2019.104678

Loring, H. S., Czech, V. L., Icso, J. D., O'Connor, L., Parelkar, S. S., Byrne, A. B., & Thompson, P. R. (2021). A phase transition enhances the catalytic activity of SARM1, an NAD+ glycohydrolase involved in neurodegeneration. *ELife*, *10*. https://doi.org/10.7554/eLife.66694

Loring, H. S., & Thompson, P. R. (2020). Emergence of SARM1 as a Potential Therapeutic Target for Wallerian-type Diseases. *Cell Chemical Biology*, *27*(1), 1–13. https://doi.org/10.1016/j.chembiol.2019.11.002

Lüders, K. A., Patzig, J., Simons, M., Nave, K.-A., & Werner, H. B. (2017). Genetic dissection of oligodendroglial and neuronal Plp1 function in a novel mouse model of spastic paraplegia type 2. *Glia*, *65*(11), 1762–1776. https://doi.org/10.1002/glia.23193

Luong, T. N., Carlisle, H. J., Southwell, A., & Patterson, P. H. (2011). Assessment of Motor Balance and Coordination in Mice using the Balance Beam. *Journal of Visualized Experiments*, *49*. https://doi.org/10.3791/2376

Luongo, T. S., Eller, J. M., Lu, M.-J., Niere, M., Raith, F., Perry, C., Bornstein, M. R., Oliphint, P., Wang, L., McReynolds, M. R., Migaud, M. E., Rabinowitz, J. D., Johnson, F. B., Johnsson, K., Ziegler, M., Cambronne, X. A., & Baur, J. A. (2020). SLC25A51 is a mammalian mitochondrial NAD+ transporter. *Nature*, *588*(7836), 174–179. https://doi.org/10.1038/s41586-020-2741-7

Lupoli, F., Vannocci, T., Longo, G., Niccolai, N., & Pastore, A. (2018). The role of oxidative stress in Friedreich's ataxia. *FEBS Letters*, *592*(5), 718–727. https://doi.org/10.1002/1873-3468.12928

Mack, T. G. A., Reiner, M., Beirowski, B., Mi, W., Emanuelli, M., Wagner, D., Thomson, D., Gillingwater, T., Court, F., Conforti, L., Fernando, F. S., Tarlton, A., Andressen, C., Addicks, K., Magni, G., Ribchester, R. R., Perry, V. H., & Coleman, M. P. (2001). Wallerian degeneration of injured axons and synapses is delayed by a Ube4b/Nmnat chimeric gene. *Nature Neuroscience*, *4*(12), 1199–1206. https://doi.org/10.1038/nn770

Madan, S., Uttekar, B., Chowdhary, S., & Rikhy, R. (2022). Mitochondria Lead the Way: Mitochondrial Dynamics and Function in Cellular Movements in Development and Disease. *Frontiers in Cell and Developmental Biology*, *9*. https://doi.org/10.3389/fcell.2021.781933

Magistretti, P. J. (2014). Synaptic Plasticity and the Warburg Effect. *Cell Metabolism*, *19*(1), 4–5. https://doi.org/10.1016/j.cmet.2013.12.012

Mahmoud, S., Gharagozloo, M., Simard, C., & Gris, D. (2019). Astrocytes Maintain Glutamate Homeostasis in the CNS by Controlling the Balance between Glutamate Uptake and Release. *Cells*, *8*(2), 184. https://doi.org/10.3390/cells8020184

Maltecca, F., Aghaie, A., Schroeder, D. G., Cassina, L., Taylor, B. A., Phillips, S. J., Malaguti, M., Previtali, S., Guenet, J.-L., Quattrini, A., Cox, G. A., & Casari, G. (2008). The Mitochondrial Protease AFG3L2 Is Essential for Axonal Development. *Journal of Neuroscience*, *28*(11), 2827–2836. https://doi.org/10.1523/JNEUROSCI.4677-07.2008

Maltecca, F., Baseggio, E., Consolato, F., Mazza, D., Podini, P., Young, S. M., Drago, I., Bahr, B. A., Puliti, A., Codazzi, F., Quattrini, A., & Casari, G. (2015). Purkinje neuron Ca2+ influx reduction rescues ataxia in SCA28 model. *Journal of Clinical Investigation*, *125*(1), 263–274. https://doi.org/10.1172/JCI74770

Maltecca, F., de Stefani, D., Cassina, L., Consolato, F., Wasilewski, M., Scorrano, L., Rizzuto, R., & Casari, G. (2012). Respiratory dysfunction by AFG3L2 deficiency causes decreased mitochondrial calcium uptake via organellar network fragmentation. *Human Molecular Genetics*, *21*(17), 3858–3870. https://doi.org/10.1093/hmg/dds214

Maltecca, F., Magnoni, R., Cerri, F., Cox, G. A., Quattrini, A., & Casari, G. (2009). Haploinsufficiency of AFG3L2, the Gene Responsible for Spinocerebellar Ataxia Type 28, Causes Mitochondria-Mediated Purkinje Cell Dark Degeneration. *Journal of Neuroscience*, *29*(29), 9244–9254. https://doi.org/10.1523/JNEUROSCI.1532-09.2009

Mancini, C., Hoxha, E., Iommarini, L., Brussino, A., Richter, U., Montarolo, F., Cagnoli, C., Parolisi, R., Gondor Morosini, D. I., Nicolò, V., Maltecca, F., Muratori, L., Ronchi, G., Geuna, S., Arnaboldi, F., Donetti, E., Giorgio, E., Cavalieri, S., di Gregorio, E., … Tempia, F. (2019). Mice harbouring a SCA28 patient mutation in AFG3L2 develop late-onset ataxia associated with enhanced mitochondrial proteotoxicity. *Neurobiology of Disease*, *124*, 14–28. https://doi.org/10.1016/j.nbd.2018.10.018

Mancuso, G., Barth, E., Crivello, P., & Rugarli, E. I. (2012). Alternative Splicing of Spg7, a Gene Involved in Hereditary Spastic Paraplegia, Encodes a Variant of Paraplegin Targeted to the Endoplasmic Reticulum. *PLoS ONE*, *7*(5), e36337. https://doi.org/10.1371/journal.pone.0036337

Martin, S. M., O'Brien, G. S., Portera-Cailliau, C., & Sagasti, A. (2010). Wallerian degeneration of zebrafish trigeminal axons in the skin is required for regeneration and developmental pruning. *Development*, *137*(23), 3985–3994. https://doi.org/10.1242/dev.053611

Martinelli, P., la Mattina, V., Bernacchia, A., Magnoni, R., Cerri, F., Cox, G., Quattrini, A., Casari, G., & Rugarli, E. I. (2009). Genetic interaction between the m-AAA protease isoenzymes reveals novel roles in cerebellar degeneration. *Human Molecular Genetics*, *18*(11), 2001–2013. https://doi.org/10.1093/hmg/ddp124

Martínez-Reyes, I., & Chandel, N. S. (2020). Mitochondrial TCA cycle metabolites control physiology and disease. In *Nature Communications* (Vol. 11, Issue 1). Nature Research. https://doi.org/10.1038/s41467-019-13668-3

Maureen J, van Etten, R. A., Wright, C. T., Walberg, M. W., & Clayton, D. A. (1981). Sequence and Gene Organization of Mouse Mitochondrial DNA. In *Cell* (Vol. 26).

Maynard, M. E., Redell, J. B., Zhao, J., Hood, K. N., Vita, S. M., Kobori, N., & Dash, P. K. (2020). Sarm1 loss reduces axonal damage and improves cognitive outcome after repetitive mild closed head injury. *Experimental Neurology*, *327*. https://doi.org/10.1016/j.expneurol.2020.113207

Mink, M., Fogelgren, B., Olszewski, K., Maroy, P., & Csiszar, K. (2001). A novel human gene (SARM) at chromosome 17q11 encodes a protein with a SAM motif and structural similarity to Armadillo/β-catenin that is conserved in mouse, Drosophila, and Caenorhabditis elegans. *Genomics*, *74*(2), 234–244. https://doi.org/10.1006/geno.2001.6548

Misgeld, T., & Schwarz, T. L. (2017). Mitostasis in Neurons: Maintaining Mitochondria in an Extended Cellular Architecture. In *Neuron* (Vol. 96, Issue 3, pp. 651–666). Cell Press. https://doi.org/10.1016/j.neuron.2017.09.055

Mootha, V. K., Lindgren, C. M., Eriksson, K.-F., Subramanian, A., Sihag, S., Lehar, J., Puigserver, P., Carlsson, E., Ridderstråle, M., Laurila, E., Houstis, N., Daly, M. J., Patterson, N., Mesirov, J. P., Golub, T. R., Tamayo, P., Spiegelman, B., Lander, E. S., Hirschhorn, J. N., … Groop, L. C. (2003). PGC-1α-responsive genes involved in oxidative phosphorylation are coordinately downregulated in human diabetes. *Nature Genetics*, *34*(3), 267–273. https://doi.org/10.1038/ng1180

Mukherjee, P., Winkler, C. W., Taylor, K. G., Woods, T. A., Nair, V., Khan, B. A., & Peterson, K. E. (2015). SARM1, Not MyD88, Mediates TLR7/TLR9-Induced Apoptosis in Neurons. *The Journal of Immunology*, *195*(10), 4913–4921. https://doi.org/10.4049/jimmunol.1500953

Murata, H., Khine, C. C., Nishikawa, A., Yamamoto, K. ichi, Kinoshita, R., & Sakaguchi, M. (2018). C-Jun N-terminal kinase (JNK)-mediated phosphorylation of SARM1 regulates NAD cleavage activity to inhibit mitochondrial respiration. *Journal of Biological Chemistry*, *293*(49), 18933–18943. https://doi.org/10.1074/jbc.RA118.004578

Murata, H., Sakaguchi, M., Kataoka, K., & Huh, N. (2013). SARM1 and TRAF6 bind to and stabilize PINK1 on depolarized mitochondria. *Molecular Biology of the Cell*, *24*(18), 2772–2784. https://doi.org/10.1091/mbc.e13-01-0016

Murru, S., Hess, S., Barth, E., Almajan, E. R., Schatton, D., Hermans, S., Brodesser, S., Langer, T., Kloppenburg, P., & Rugarli, E. I. (2019). Astrocyte-specific deletion of the mitochondrial m-AAA protease reveals glial contribution to neurodegeneration. *Glia*, *67*(8), 1526–1541. https://doi.org/10.1002/glia.23626

Nargund, A. M., Fiorese, C. J., Pellegrino, M. W., Deng, P., & Haynes, C. M. (2015). Mitochondrial and Nuclear Accumulation of the Transcription Factor ATFS-1 Promotes OXPHOS Recovery during the UPRmt. *Molecular Cell*, *58*(1), 123–133. https://doi.org/10.1016/j.molcel.2015.02.008

Nolden, M., Ehses, S., Koppen, M., Bernacchia, A., Rugarli, E. I., & Langer, T. (2005). The m-AAA Protease Defective in Hereditary Spastic Paraplegia Controls Ribosome Assembly in Mitochondria. *Cell*, *123*(2), 277–289. https://doi.org/10.1016/j.cell.2005.08.003

Okabe, K., Yaku, K., Tobe, K., & Nakagawa, T. (2019). Implications of altered NAD metabolism in metabolic disorders. *Journal of Biomedical Science*, *26*(1), 34. https://doi.org/10.1186/s12929-019-0527-8

Osterloh, J. M., Yang, J., Rooney, T. M., Fox, A. N., Adalbert, R., Powell, E. H., Sheehan, A. E., Avery, M. A., Hackett, R., Logan, M. A., MacDonald, J. M., Ziegenfuss, J. S., Milde, S., Hou, Y.-J., Nathan, C., Ding, A., Brown, R. H., Conforti, L., Coleman, M., … Freeman, M. R. (2012). dSarm/Sarm1 Is Required for Activation of an Injury-Induced Axon Death Pathway. *Science*, *337*(6093), 481–484. https://doi.org/10.1126/science.1223899

Pagliarini, D. J., Calvo, S. E., Chang, B., Sheth, S. A., Vafai, S. B., Ong, S.-E., Walford, G. A., Sugiana, C., Boneh, A., Chen, W. K., Hill, D. E., Vidal, M., Evans, J. G., Thorburn, D. R., Carr, S. A., & Mootha, V. K. (2008). A Mitochondrial Protein Compendium Elucidates Complex I Disease Biology. *Cell*, *134*(1), 112–123. https://doi.org/10.1016/j.cell.2008.06.016

Pan, Z.-G., & An, X.-S. (2018). SARM1 deletion restrains NAFLD induced by high fat diet (HFD) through reducing inflammation, oxidative stress and lipid accumulation. *Biochemical and Biophysical Research Communications*, *498*(3), 416–423. https://doi.org/10.1016/j.bbrc.2018.02.115

Panneerselvam, P., Singh, L. P., Ho, B., Chen, J., & Ding, J. L. (2012). Targeting of pro-apoptotic TLR adaptor SARM to mitochondria: definition of the critical region and residues in the signal sequence. *Biochemical Journal*, *442*(2), 263–271. https://doi.org/10.1042/BJ20111653

Panneerselvam, P., Singh, L. P., Selvarajan, V., Chng, W. J., Ng, S. B., Tan, N. S., Ho, B., Chen, J., & Ding, J. L. (2013). T-cell death following immune activation is mediated by mitochondria-localized SARM. *Cell Death & Differentiation*, *20*(3), 478–489. https://doi.org/10.1038/cdd.2012.144

Papa, L., & Germain, D. (2014). SirT3 Regulates the Mitochondrial Unfolded Protein Response. *Molecular and Cellular Biology*, *34*(4), 699–710. https://doi.org/10.1128/MCB.01337-13

Papa, S., Martino, P. L., Capitanio, G., Gaballo, A., de Rasmo, D., Signorile, A., & Petruzzella, V. (2012). *The Oxidative Phosphorylation System in Mammalian Mitochondria* (pp. 3–37). https://doi.org/10.1007/978-94-007-2869-1_1

Pareek, G., & Pallanck, L. J. (2020). Inactivation of the mitochondrial protease Afg3l2 results in severely diminished respiratory chain activity and widespread defects in mitochondrial gene expression. *PLOS Genetics*, *16*(10), e1009118. https://doi.org/10.1371/journal.pgen.1009118

Patron, M., Sprenger, H.-G., & Langer, T. (2018). m-AAA proteases, mitochondrial calcium homeostasis and neurodegeneration. *Cell Research*, *28*(3), 296–306. https://doi.org/10.1038/cr.2018.17

Peng, J., Yuan, Q., Lin, B., Panneerselvam, P., Wang, X., Luan, X. L., Lim, S. K., Leung, B. P., Ho, B., & Ding, J. L. (2010). SARM inhibits both TRIF- and MyD88-mediated AP-1

activation. *European Journal of Immunology*, *40*(6), 1738–1747. https://doi.org/10.1002/eji.200940034

Perea, G., Navarrete, M., & Araque, A. (2009). Tripartite synapses: astrocytes process and control synaptic information. *Trends in Neurosciences*, *32*(8), 421–431. https://doi.org/10.1016/j.tins.2009.05.001

Pfeffer, G., Gorman, G. S., Griffin, H., Kurzawa-Akanbi, M., Blakely, E. L., Wilson, I., Sitarz, K., Moore, D., Murphy, J. L., Alston, C. L., Pyle, A., Coxhead, J., Payne, B., Gorrie, G. H., Longman, C., Hadjivassiliou, M., McConville, J., Dick, D., Imam, I., … Chinnery, P. F. (2014). Mutations in the SPG7 gene cause chronic progressive external ophthalmoplegia through disordered mitochondrial DNA maintenance. *Brain*, *137*(5), 1323–1336. https://doi.org/10.1093/brain/awu060

Pierson, T. M., Adams, D., Bonn, F., Martinelli, P., Cherukuri, P. F., Teer, J. K., Hansen, N. F., Cruz, P., Mullikin for the NISC Comparative Sequencing Program, J. C., Blakesley, R. W., Golas, G., Kwan, J., Sandler, A., Fuentes Fajardo, K., Markello, T., Tifft, C., Blackstone, C., Rugarli, E. I., Langer, T., … Toro, C. (2011). Whole-Exome Sequencing Identifies Homozygous AFG3L2 Mutations in a Spastic Ataxia-Neuropathy Syndrome Linked to Mitochondrial m-AAA Proteases. *PLoS Genetics*, *7*(10), e1002325. https://doi.org/10.1371/journal.pgen.1002325

Pinti, M., Gibellini, L., Liu, Y., Xu, S., Lu, B., & Cossarizza, A. (2015). Mitochondrial Lon protease at the crossroads of oxidative stress, ageing and cancer. *Cellular and Molecular Life Sciences*, *72*(24), 4807–4824. https://doi.org/10.1007/s00018-015-2039-3

Poitelon, Y., Kopec, A. M., & Belin, S. (2020). Myelin Fat Facts: An Overview of Lipids and Fatty Acid Metabolism. *Cells*, *9*(4), 812. https://doi.org/10.3390/cells9040812

Press, C., & Milbrandt, J. (2008). Nmnat Delays Axonal Degeneration Caused by Mitochondrial and Oxidative Stress. *Journal of Neuroscience*, *28*(19), 4861–4871. https://doi.org/10.1523/JNEUROSCI.0525-08.2008

Prudent, J., Popgeorgiev, N., Gadet, R., Deygas, M., Rimokh, R., & Gillet, G. (2016). Mitochondrial Ca2+ uptake controls actin cytoskeleton dynamics during cell migration. *Scientific Reports*, *6*(1), 36570. https://doi.org/10.1038/srep36570

Pudla, M., Limposuwan, K., & Utaisincharoen, P. (2011). Burkholderia pseudomallei-Induced Expression of a Negative Regulator, Sterile-α and Armadillo Motif-Containing Protein, in Mouse Macrophages: a Possible Mechanism for Suppression of the MyD88-Independent Pathway. *Infection and Immunity*, *79*(7), 2921–2927. https://doi.org/10.1128/IAI.01254-10

Raffaello, A., Mammucari, C., Gherardi, G., & Rizzuto, R. (2016). Calcium at the Center of Cell Signaling: Interplay between Endoplasmic Reticulum, Mitochondria, and Lysosomes. *Trends in Biochemical Sciences*, *41*(12), 1035–1049. https://doi.org/10.1016/j.tibs.2016.09.001

Reimand, J., Isserlin, R., Voisin, V., Kucera, M., Tannus-Lopes, C., Rostamianfar, A., Wadi, L., Meyer, M., Wong, J., Xu, C., Merico, D., & Bader, G. D. (2019). Pathway enrichment analysis and visualization of omics data using g:Profiler, GSEA, Cytoscape and EnrichmentMap. *Nature Protocols*, *14*(2), 482–517. https://doi.org/10.1038/s41596-018-0103-9

Richter, U., Lahtinen, T., Marttinen, P., Suomi, F., & Battersby, B. J. (2015). Quality control of mitochondrial protein synthesis is required for membrane integrity and cell fitness. *Journal of Cell Biology*, *211*(2), 373–389. https://doi.org/10.1083/jcb.201504062

Richter, U., Ng, K. Y., Suomi, F., Marttinen, P., Turunen, T., Jackson, C., Suomalainen, A., Vihinen, H., Jokitalo, E., Nyman, T. A., Isokallio, M. A., Stewart, J. B., Mancini, C., Brusco, A., Seneca, S., Lombès, A., Taylor, R. W., & Battersby, B. J. (2019). Mitochondrial stress response triggered by defects in protein synthesis quality control. *Life Science Alliance*, *2*(1), e201800219. https://doi.org/10.26508/lsa.201800219

Sacco, T., Boda, E., Hoxha, E., Pizzo, R., Cagnoli, C., Brusco, A., & Tempia, F. (2010). Mouse brain expression patterns of Spg7, Afg3l1, and Afg3l2 transcripts, encoding for the mitochondrial m-AAA protease. In *BMC Neuroscience* (Vol. 11). http://www.biomedcentral.com/1471-2202/11/55

Sambri, I., Massa, F., Gullo, F., Meneghini, S., Cassina, L., Carraro, M., Dina, G., Quattrini, A., Patanella, L., Carissimo, A., Iuliano, A., Santorelli, F., Codazzi, F., Grohovaz, F., Bernardi, P., Becchetti, A., & Casari, G. (2020). Impaired flickering of the permeability transition pore causes SPG7 spastic paraplegia. *EBioMedicine*, *61*. https://doi.org/10.1016/j.ebiom.2020.103050

Sasaki, Y., Engber, T. M., Hughes, R. O., Figley, M. D., Wu, T., Bosanac, T., Devraj, R., Milbrandt, J., Krauss, R., & DiAntonio, A. (2020). cADPR is a gene dosage-sensitive biomarker of SARM1 activity in healthy, compromised, and degenerating axons. *Experimental Neurology*, *329*, 113252. https://doi.org/10.1016/j.expneurol.2020.113252

Schmidt, O., Pfanner, N., & Meisinger, C. (2010). Mitochondrial protein import: From proteomics to functional mechanisms. In *Nature Reviews Molecular Cell Biology* (Vol. 11, Issue 9, pp. 655–667). https://doi.org/10.1038/nrm2959

Sen, S., Lagas, S., Roy, A., & Kumar, H. (2022). Cytoskeleton saga: Its regulation in normal physiology and modulation in neurodegenerative disorders. *European Journal of Pharmacology*, *925*, 175001. https://doi.org/10.1016/j.ejphar.2022.175001

Sengul, G., & Watson, C. (2012). Spinal Cord. In *The Mouse Nervous System* (pp. 424–458). Elsevier Inc. https://doi.org/10.1016/B978-0-12-369497-3.10013-5

Shanmughapriya, S., Rajan, S., Hoffman, N. E., Higgins, A. M., Tomar, D., Nemani, N., Hines, K. J., Smith, D. J., Eguchi, A., Vallem, S., Shaikh, F., Cheung, M., Leonard, N. J., Stolakis, R. S., Wolfers, M. P., Ibetti, J., Chuprun, J. K., Jog, N. R., Houser, S. R., … Madesh, M. (2015). SPG7 Is an Essential and Conserved Component of the Mitochondrial Permeability Transition Pore. *Molecular Cell*, *60*(1), 47–62. https://doi.org/10.1016/j.molcel.2015.08.009

Sherrard, R. M. (2011). *Cerebellar Control of Fine Motor Function* (pp. 263–279). https://doi.org/10.1007/978-1-61779-301-1_14

Shi, Y., Kerry, P. S., Nanson, J. D., Bosanac, T., Sasaki, Y., Krauss, R., Saikot, F. K., Adams, S. E., Mosaiab, T., Masic, V., Mao, X., Rose, F., Vasquez, E., Furrer, M., Cunnea, K., Brearley, A., Gu, W., Luo, Z., Brillault, L., … Ve, T. (2022). Structural basis of SARM1 activation, substrate recognition, and inhibition by small molecules. *Molecular Cell*, *82*(9), 1643-1659.e10. https://doi.org/10.1016/j.molcel.2022.03.007

Sillitoe, R. v., Fu, Y. H., & Watson, C. (2012). Cerebellum. In *The Mouse Nervous System* (pp. 360–397). Elsevier Inc. https://doi.org/10.1016/B978-0-12-369497-3.10011-1

Simons, M., & Nave, K.-A. (2016). Oligodendrocytes: Myelination and Axonal Support. *Cold Spring Harbor Perspectives in Biology*, *8*(1), a020479. https://doi.org/10.1101/cshperspect.a020479

Skaper, S. D., Facci, L., Zusso, M., & Giusti, P. (2018). An Inflammation-Centric View of Neurological Disease: Beyond the Neuron. *Frontiers in Cellular Neuroscience*, *12*. https://doi.org/10.3389/fncel.2018.00072

Sonda, S., Pendin, D., & Daga, A. (2021). ER Morphology in the Pathogenesis of Hereditary Spastic Paraplegia. *Cells*, *10*(11), 2870. https://doi.org/10.3390/cells10112870

Song, J., Herrmann, J. M., & Becker, T. (2021). Quality control of the mitochondrial proteome. *Nature Reviews Molecular Cell Biology*, *22*(1), 54–70. https://doi.org/10.1038/s41580-020-00300-2

Sporny, M., Guez-Haddad, J., Khazma, T., Yaron, A., Dessau, M., Shkolnisky, Y., Mim, C., Isupov, M. N., Zalk, R., Hons, M., & Opatowsky, Y. (2020). Structural basis for SARM1 inhibition and activation under energetic stress. *ELife*, *9*. https://doi.org/10.7554/eLife.62021

Sporny, M., Guez-Haddad, J., Lebendiker, M., Ulisse, V., Volf, A., Mim, C., Isupov, M. N., & Opatowsky, Y. (2019). Structural Evidence for an Octameric Ring Arrangement of SARM1. *Journal of Molecular Biology*, *431*(19), 3591–3605. https://doi.org/10.1016/j.jmb.2019.06.030

Srivastava, S. (2016). Emerging therapeutic roles for NAD+ metabolism in mitochondrial and age-related disorders. *Clinical and Translational Medicine*, *5*(1). https://doi.org/10.1186/s40169-016-0104-7

Stanley, J. L., Lincoln, R. J., Brown, T. A., McDonald, L. M., Dawson, G. R., & Reynolds, D. S. (2005). The mouse beam walking assay offers improved sensitivity over the mouse rotarod in determining motor coordination deficits induced by benzodiazepines. *Journal of Psychopharmacology*, *19*(3), 221–227. https://doi.org/10.1177/0269881105051524

Steglich, G., Neupert, W., & Langer, T. (1999). Prohibitins Regulate Membrane Protein Degradation by the *m* -AAA Protease in Mitochondria. *Molecular and Cellular Biology*, *19*(5), 3435–3442. https://doi.org/10.1128/MCB.19.5.3435

Stevenson, R., Samokhina, E., Rossetti, I., Morley, J. W., & Buskila, Y. (2020). Neuromodulation of Glial Function During Neurodegeneration. *Frontiers in Cellular Neuroscience*, *14*. https://doi.org/10.3389/fncel.2020.00278

Subramanian, A., Tamayo, P., Mootha, V. K., Mukherjee, S., Ebert, B. L., Gillette, M. A., Paulovich, A., Pomeroy, S. L., Golub, T. R., Lander, E. S., & Mesirov, J. P. (2005). Gene set enrichment analysis: A knowledge-based approach for interpreting genome-wide expression profiles. *Proceedings of the National Academy of Sciences*, *102*(43), 15545–15550. https://doi.org/10.1073/pnas.0506580102

Summers, D. W., DiAntonio, A., & Milbrandt, J. (2014). Mitochondrial Dysfunction Induces Sarm1-Dependent Cell Death in Sensory Neurons. *Journal of Neuroscience*, *34*(28), 9338–9350. https://doi.org/10.1523/JNEUROSCI.0877-14.2014

Suzuki, A., Stern, S. A., Bozdagi, O., Huntley, G. W., Walker, R. H., Magistretti, P. J., & Alberini, C. M. (2011). Astrocyte-Neuron Lactate Transport Is Required for Long-Term Memory Formation. *Cell*, *144*(5), 810–823. https://doi.org/10.1016/j.cell.2011.02.018

Synofzik, M., & Schüle, R. (2017). Overcoming the divide between ataxias and spastic paraplegias: Shared phenotypes, genes, and pathways. *Movement Disorders*, *32*(3), 332–345. https://doi.org/10.1002/mds.26944

Szklarczyk, D., Gable, A. L., Nastou, K. C., Lyon, D., Kirsch, R., Pyysalo, S., Doncheva, N. T., Legeay, M., Fang, T., Bork, P., Jensen, L. J., & von Mering, C. (2021). The STRING database in 2021: customizable protein–protein networks, and functional characterization of user-uploaded gene/measurement sets. *Nucleic Acids Research*, *49*(D1), D605–D612. https://doi.org/10.1093/nar/gkaa1074

Szretter, K. J., Samuel, M. A., Gilfillan, S., Fuchs, A., Colonna, M., & Diamond, M. S. (2009). The Immune Adaptor Molecule SARM Modulates Tumor Necrosis Factor Alpha Production and Microglia Activation in the Brainstem and Restricts West Nile Virus Pathogenesis. *Journal of Virology*, *83*(18), 9329–9338. https://doi.org/10.1128/JVI.00836-09

Tatsuta, T., Augustin, S., Nolden, M., Friedrichs, B., & Langer, T. (2007). m-AAA protease-driven membrane dislocation allows intramembrane cleavage by rhomboid in mitochondria. *The EMBO Journal*, *26*(2), 325–335. https://doi.org/10.1038/sj.emboj.7601514

Thal, D., Züchner, S., Gierer, S., Schulte, C., Schöls, L., Schüle, R., & Synofzik, M. (2015). Abnormal Paraplegin Expression in Swollen Neurites, τ- and α-Synuclein Pathology in a Case of Hereditary Spastic Paraplegia SPG7 with an Ala510Val Mutation. *International Journal of Molecular Sciences*, *16*(10), 25050–25066. https://doi.org/10.3390/ijms161025050

Tracey, T. J., Steyn, F. J., Wolvetang, E. J., & Ngo, S. T. (2018). Neuronal lipid metabolism: Multiple pathways driving functional outcomes in health and disease. In *Frontiers in Molecular Neuroscience* (Vol. 11). Frontiers Media S.A. https://doi.org/10.3389/fnmol.2018.00010

Truscott, K. N., Lowth, B. R., Strack, P. R., & Dougan, D. A. (2010). Diverse functions of mitochondrial AAA+ proteins: protein activation, disaggregation, and degradationThis paper is one of a selection of papers published in this special issue entitled 8th International Conference on AAA Proteins and has undergone the Journal's usual peer review process. *Biochemistry and Cell Biology*, *88*(1), 97–108. https://doi.org/10.1139/O09-167

Tulli, S., del Bondio, A., Baderna, V., Mazza, D., Codazzi, F., Pierson, T. M., Ambrosi, A., Nolte, D., Goizet, C., Toro, C., Baets, J., Deconinck, T., DeJonghe, P., Mandich, P., Casari, G., & Maltecca, F. (2019). Pathogenic variants in the AFG3L2 proteolytic domain cause SCA28 through haploinsufficiency and proteostatic stress-driven OMA1 activation. *Journal of Medical Genetics*, *56*(8), 499–511. https://doi.org/10.1136/jmedgenet-2018-105766

Turkiew, E., Falconer, D., Reed, N., & Höke, A. (2017). Deletion of Sarm1 gene is neuroprotective in two models of peripheral neuropathy. *Journal of the Peripheral Nervous System*, *22*(3), 162–171. https://doi.org/10.1111/jns.12219

Tyanova, S., Temu, T., Sinitcyn, P., Carlson, A., Hein, M. Y., Geiger, T., Mann, M., & Cox, J. (2016). The Perseus computational platform for comprehensive analysis of (prote)omics data. *Nature Methods*, *13*(9), 731–740. https://doi.org/10.1038/nmeth.3901

Uccellini, M. B., Bardina, S. v., Sánchez-Aparicio, M. T., White, K. M., Hou, Y.-J., Lim, J. K., & García-Sastre, A. (2020). Passenger Mutations Confound Phenotypes of SARM1-Deficient Mice. *Cell Reports*, *31*(1), 107498. https://doi.org/10.1016/j.celrep.2020.03.062

van Gassen, K. L. I., van der Heijden, C. D. C. C., de Bot, S. T., den Dunnen, W. F. A., van den Berg, L. H., Verschuuren-Bemelmans, C. C., Kremer, H. P. H., Veldink, J. H., Kamsteeg, E.-J., Scheffer, H., & van de Warrenburg, B. P. (2012). Genotype–phenotype correlations in spastic paraplegia type 7: a study in a large Dutch cohort. *Brain*, *135*(10), 2994–3004. https://doi.org/10.1093/brain/aws224

Vargas, M. E., Yamagishi, Y., Tessier-Lavigne, M., & Sagasti, A. (2015). Live Imaging of Calcium Dynamics during Axon Degeneration Reveals Two Functionally Distinct Phases of Calcium Influx. *Journal of Neuroscience*, *35*(45), 15026–15038. https://doi.org/10.1523/JNEUROSCI.2484-15.2015

Viar, K., Njoku, D., Secor McVoy, J., & Oh, U. (2020). Sarm1 knockout protects against early but not late axonal degeneration in experimental allergic encephalomyelitis. *PLOS ONE*, *15*(6), e0235110. https://doi.org/10.1371/journal.pone.0235110

Villegas, R., Martinez, N. W., Lillo, J., Pihan, P., Hernandez, D., Twiss, J. L., & Court, F. A. (2014). Calcium Release from Intra-Axonal Endoplasmic Reticulum Leads to Axon Degeneration through Mitochondrial Dysfunction. *Journal of Neuroscience*, *34*(21), 7179–7189. https://doi.org/10.1523/JNEUROSCI.4784-13.2014

Wagle, P., Nikolić, M., & Frommolt, P. (2015). QuickNGS elevates Next-Generation Sequencing data analysis to a new level of automation. *BMC Genomics*, *16*(1), 487. https://doi.org/10.1186/s12864-015-1695-x

Walker, L. J., Summers, D. W., Sasaki, Y., Brace, E., Milbrandt, J., & DiAntonio, A. (2017). MAPK signaling promotes axonal degeneration by speeding the turnover of the axonal maintenance factor NMNAT2. *ELife*, *6*. https://doi.org/10.7554/eLife.22540

Waller, A. V. (1850). Experiments on the section of the glossopharyngeal and hypoglossal nerves of the frog, and observations of the alterations produced thereby in the structure of their primitive fibres. *Philosophical Transactions of the Royal Society of London*, *140*, 423–429. https://doi.org/10.1098/rstl.1850.0021

Wallin, I. E. (1927). *Symbionticism and the origin of species / by Ivan E. Wallin.* Williams & Wilkins Company,. https://doi.org/10.5962/bhl.title.11429

Wang, Q., Zhang, S., Liu, T., Wang, H., Liu, K., Wang, Q., & Zeng, W. (2018). Sarm1/Myd88-5 Regulates Neuronal Intrinsic Immune Response to Traumatic Axonal Injuries. *Cell Reports*, *23*(3), 716–724. https://doi.org/10.1016/j.celrep.2018.03.071

Wang, S., Jacquemyn, J., Murru, S., Martinelli, P., Barth, E., Langer, T., Niessen, C. M., & Rugarli, E. I. (2016). The Mitochondrial m-AAA Protease Prevents Demyelination and Hair Greying. *PLOS Genetics*, *12*(12), e1006463. https://doi.org/10.1371/journal.pgen.1006463

Ward, A., Jessop, F., Faris, R., Shoup, D., Bosio, C. M., Peterson, K. E., & Priola, S. A. (2022). Lack of the immune adaptor molecule SARM1 accelerates disease in prion infected mice and is associated with increased mitochondrial respiration and decreased expression of NRF2. *PLOS ONE*, *17*(5), e0267720. https://doi.org/10.1371/journal.pone.0267720

Welniarz, Q., Dusart, I., & Roze, E. (2017). The corticospinal tract: Evolution, development, and human disorders. In *Developmental Neurobiology* (Vol. 77, Issue 7, pp. 810–829). John Wiley and Sons Inc. https://doi.org/10.1002/dneu.22455

White, M. A., Lin, Z., Kim, E., Henstridge, C. M., Pena Altamira, E., Hunt, C. K., Burchill, E., Callaghan, I., Loreto, A., Brown-Wright, H., Mead, R., Simmons, C., Cash, D., Coleman, M. P., & Sreedharan, J. (2019). Sarm1 deletion suppresses TDP-43-linked motor neuron degeneration and cortical spine loss. *Acta Neuropathologica Communications*, *7*(1), 166. https://doi.org/10.1186/s40478-019-0800-9

Wilkinson, P. A. , Crosby, A. H. , Turner, C. , Bradley, L. J. , Ginsberg, L. , Wood, N. W. , Schapira, A. H. , & Warner, T. T. (2004). A clinical, genetic and biochemical study of SPG7 mutations in hereditary spastic paraplegia. *Brain*, *127*(5), 973–980. https://doi.org/10.1093/brain/awh125

Wolf, A., Agnihotri, S., Micallef, J., Mukherjee, J., Sabha, N., Cairns, R., Hawkins, C., & Guha, A. (2011). Hexokinase 2 is a key mediator of aerobic glycolysis and promotes tumor growth in human glioblastoma multiforme. *Journal of Experimental Medicine*, *208*(2), 313–326. https://doi.org/10.1084/jem.20101470

Xiao, W., Wang, R.-S., Handy, D. E., & Loscalzo, J. (2018). NAD(H) and NADP(H) Redox Couples and Cellular Energy Metabolism. *Antioxidants & Redox Signaling*, *28*(3), 251–272. https://doi.org/10.1089/ars.2017.7216

Xie, N., Zhang, L., Gao, W., Huang, C., Huber, P. E., Zhou, X., Li, C., Shen, G., & Zou, B. (2020). NAD+ metabolism: pathophysiologic mechanisms and therapeutic potential. *Signal Transduction and Targeted Therapy*, *5*(1), 227. https://doi.org/10.1038/s41392-020-00311-7

Xie, Z., Bailey, A., Kuleshov, M. v., Clarke, D. J. B., Evangelista, J. E., Jenkins, S. L., Lachmann, A., Wojciechowicz, M. L., Kropiwnicki, E., Jagodnik, K. M., Jeon, M., & Ma'ayan, A. (2021). Gene Set Knowledge Discovery with Enrichr. *Current Protocols*, *1*(3). https://doi.org/10.1002/cpz1.90

Yepes, M., Sandkvist, M., Wong, M. K. K., Coleman, T. A., Smith, E., Cohan, S. L., & Lawrence, D. A. (2000). Neuroserpin reduces cerebral infarct volume and protects neurons from ischemia-induced apoptosis. *Blood*, *96*(2), 569–576. https://doi.org/10.1182/blood.V96.2.569

Zhu, P.-P., Hung, H.-F., Batchenkova, N., Nixon-Abell, J., Henderson, J., Zheng, P., Renvoisé, B., Pang, S., Xu, C. S., Saalfeld, S., Funke, J., Xie, Y., Svara, F., Hess, H. F., & Blackstone, C. (2022). Transverse endoplasmic reticulum expansion in hereditary spastic paraplegia corticospinal axons. *Human Molecular Genetics*. https://doi.org/10.1093/hmg/ddac072

Zühlke, C., Mikat, B., Timmann, D., Wieczorek, D., Gillessen-Kaesbach, G., & Bürk, K. (2015). Spinocerebellar ataxia 28: a novel AFG3L2 mutation in a German family with young onset, slow progression and saccadic slowing. *Cerebellum & Ataxias*, *2*(1), 19. https://doi.org/10.1186/s40673-015-0038-7

Zurita Rendon, O., & Shoubridge, E. A. (2012). Early complex I assembly defects result in rapid turnover of the ND1 subunit. *Human Molecular Genetics*, *21*(17), 3815–3824. https://doi.org/10.1093/hmg/dds209

Appendix

Supplementary Figures

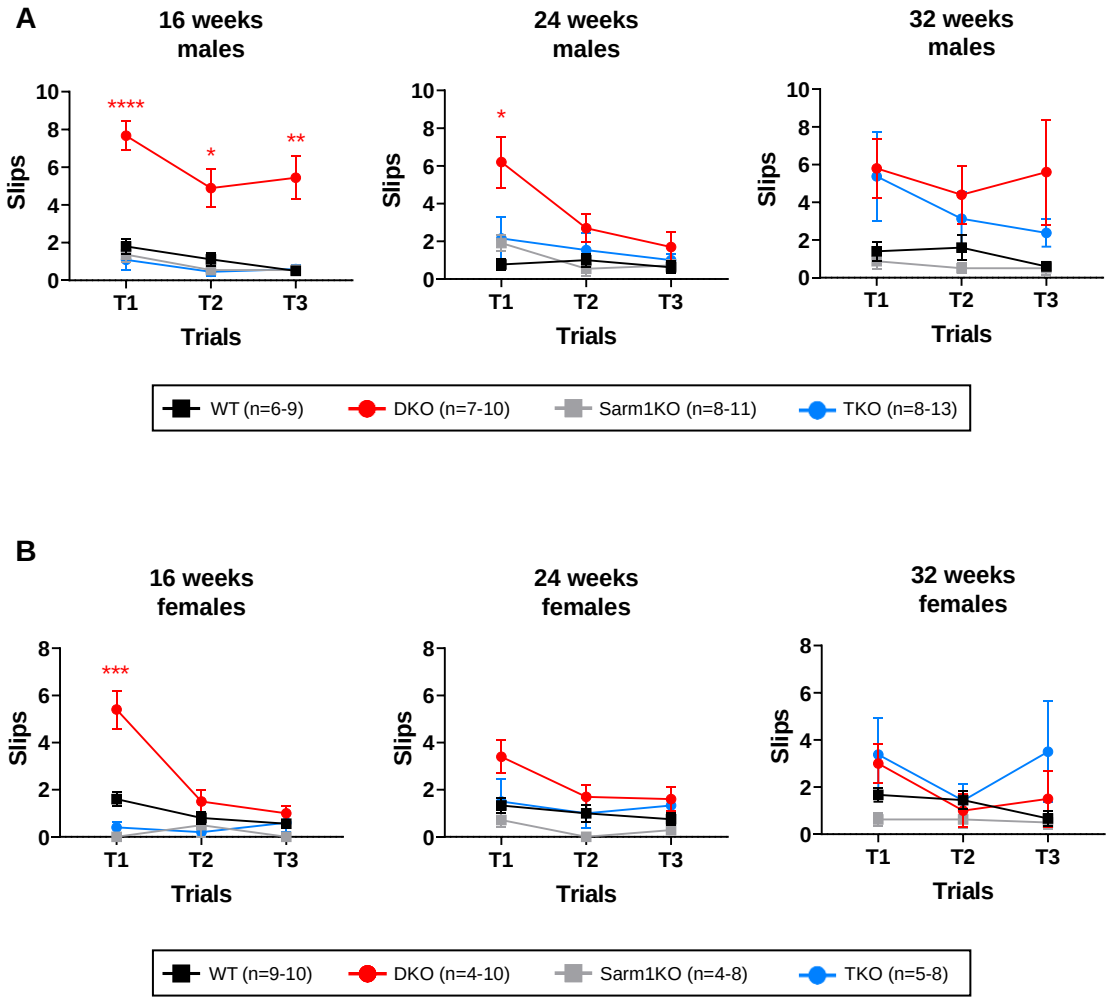

Supplementary figure S1. Number of foot slip errors during the walking beam test. The slips reflect the DKO motor deficits at early ages but is not reliable at later time points. (A) Time progression of the number of foot slips in males and (B) in females. Data represented by the mean ± SEM. The number of animals for each genotype is specified in the legend beneath the graphs. A mixed model test was used for each time point with a Tukey's multiple comparisons test; * *P* value < 0.05, ** *P* value < 0.01, *** *P* value < 0.001, **** *P* value < 0.0001.

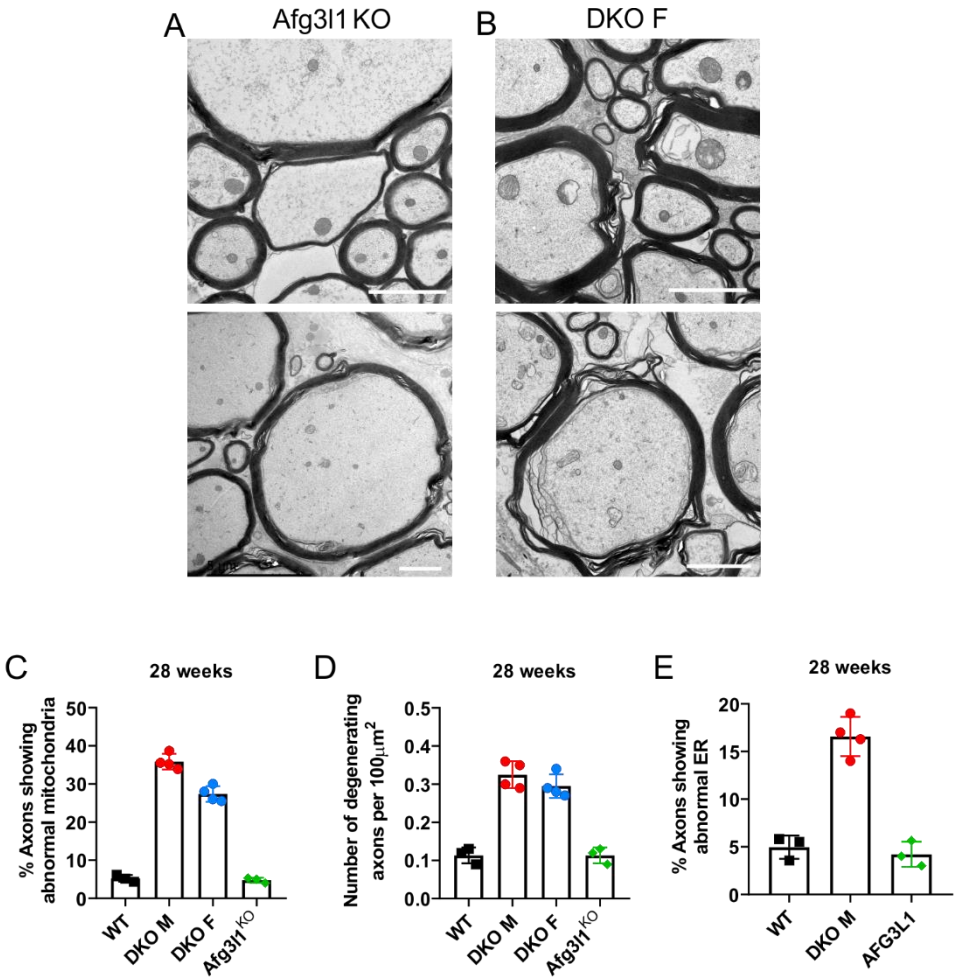

Supplementary figure S2. Ultrastructural analyses of DKO females and AFG3L1 males at 28 weeks. (A) Two representative electron micrographs of AFG3L1 KO and (B) DKO females from anterior spinal cord areas. Scale bar: 2 μm. (C) Quantification of the number of axons showing abnormal mitochondria in the different genotypes. (D) Number of axons degenerating in anterior spinal cord per 100 μm^2. (E) Percentage of axons showing abnormal ER. WT and DKO M (males) data are the same as shown in Fig. 4.5. Data represent mean ± SD, with each dot being one mouse.

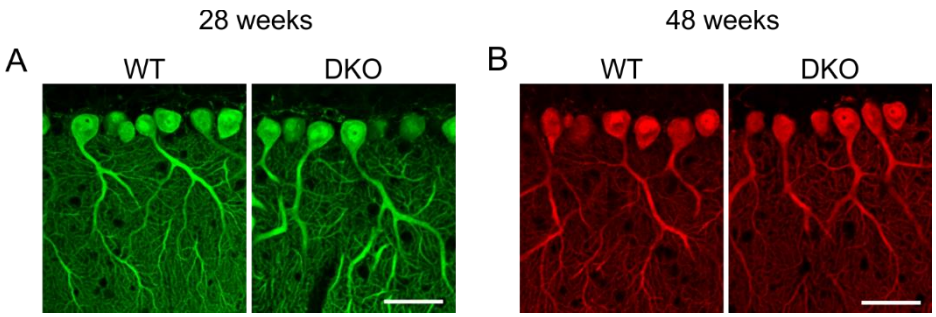

Supplementary figure S3. Immunofluorescence analysis in the cerebellum of DKO and WT mice. (A) Purkinje cells marked with Calbindin at 28 weeks and (B) 48 weeks. The soma and dendritic processes appear in the DKO very similar to their age-matched controls. Scale bar: 40 μm.

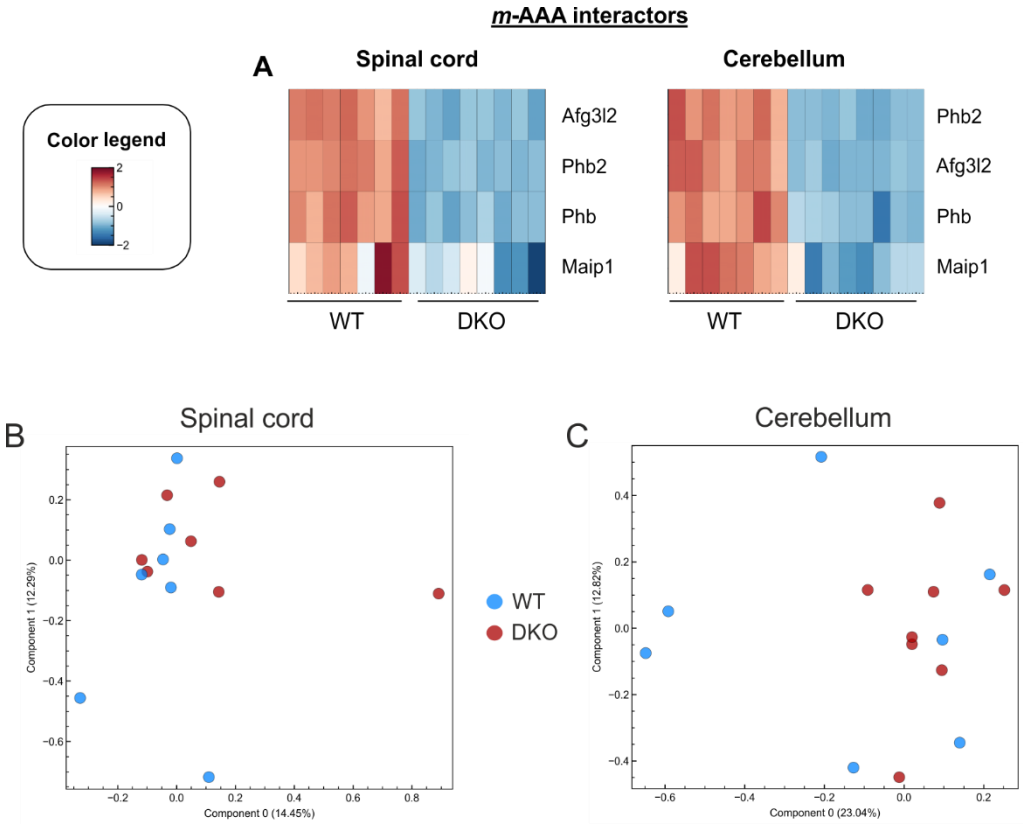

Supplementary figure S4. Proteomic analysis at 16 weeks in DKO and WT animals. (A) Heatmap highlighting the *m*-AAA protease interactors in both spinal cord and cerebellar tissue. (B) PCA results in spinal cord and (C) in cerebellum. Data subjected to row normalisation transformations (quantile) prior to PCA plotting.

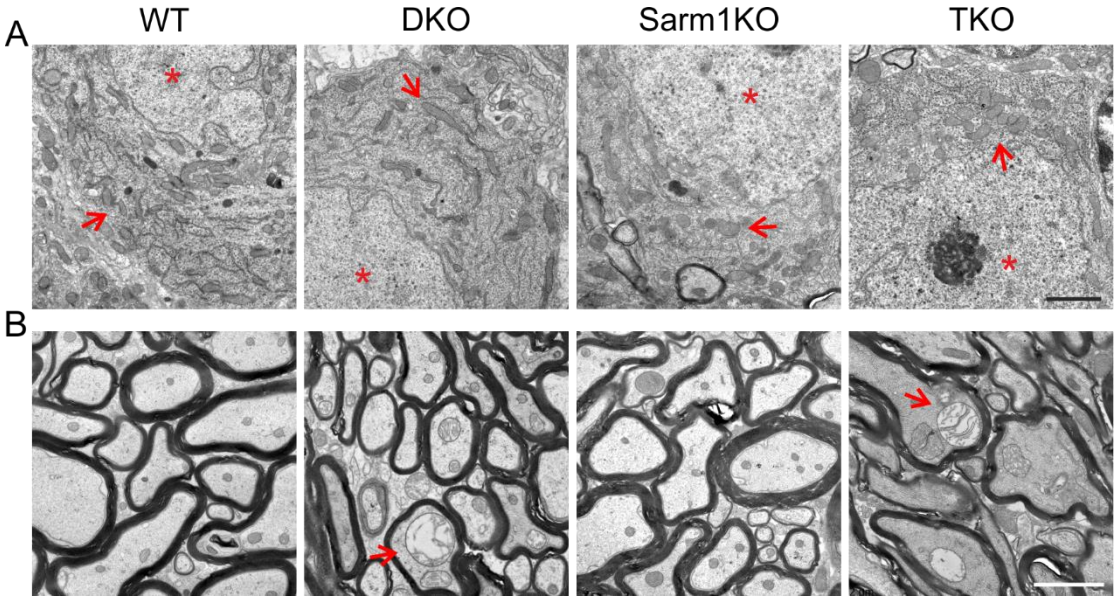

Supplementary figure S5. Ultrastructural analyses of Purkinje cells (PC) and cerebellar fibers at 28 weeks. (A) Electron micrographs of PC and (B) axonal fibers of the WT, DKO, Sarm1KO and TKO cerebellum. Arrows highlighting mitochondria, asterisks denote PC nuclei. n=3-4 per genotype. Images from the same animals as shown in Fig. 4.16. Scale bars: 2 μm.

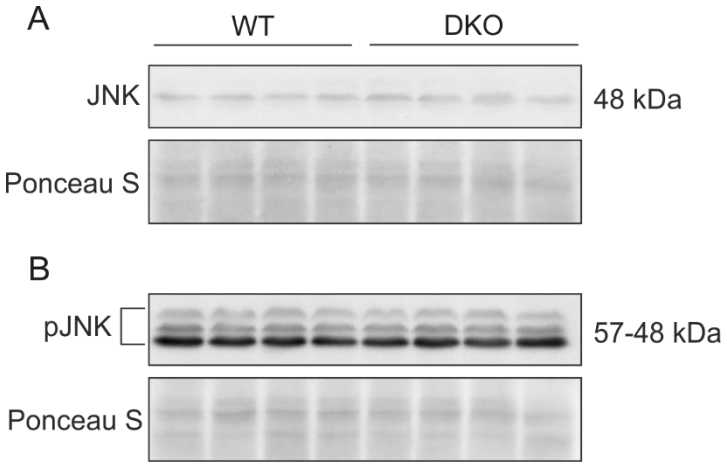

Supplementary figure S6. Immunoblot against JNK and pJNK at 28 weeks. (A) Immunoblot of spinal cord tissue probed for JNK and (B) phosphorylated JNK (pJNK) in WT and DKO mice. n=4 per genotype.

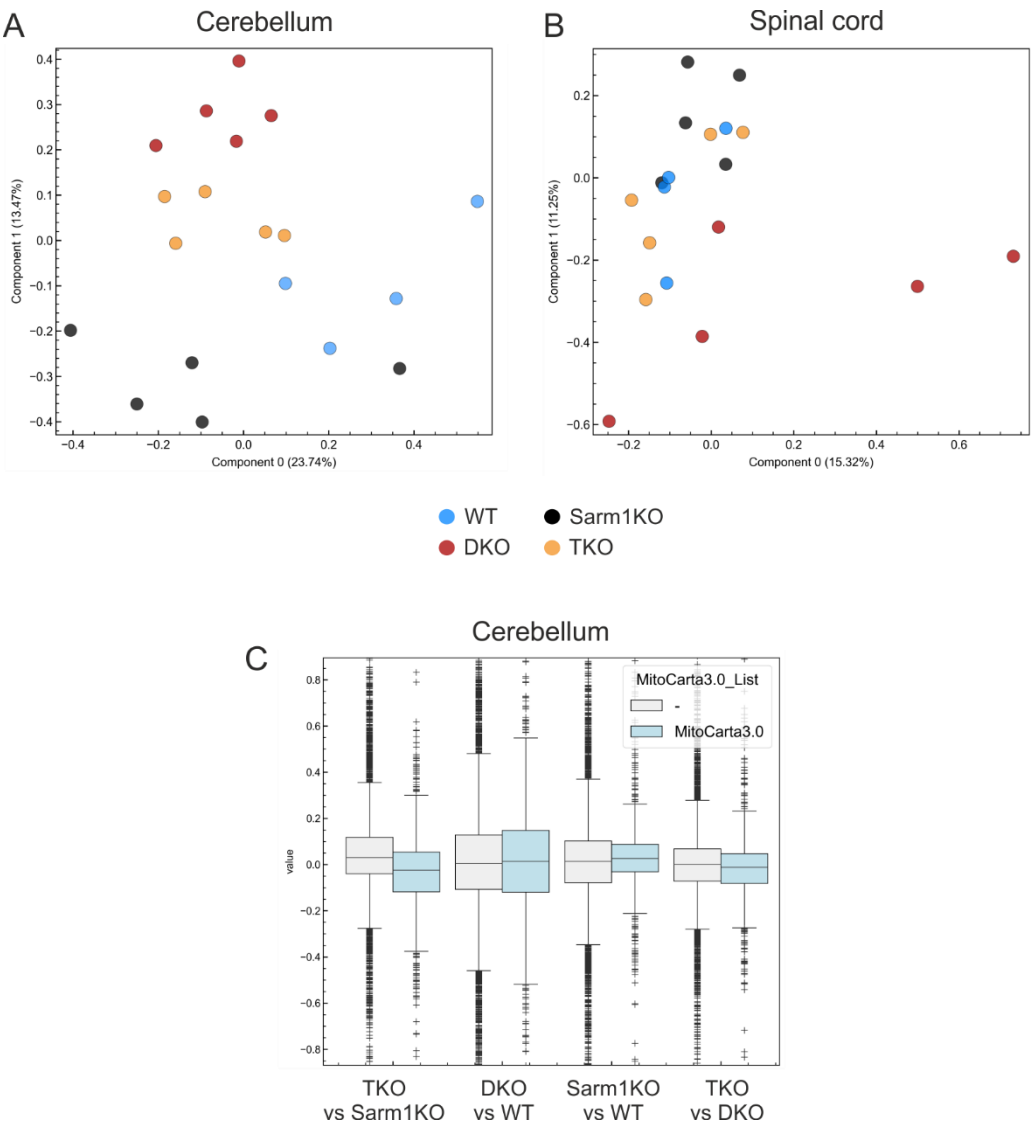

Supplementary figure S7. Proteomic analysis at 28 weeks in WT, DKO, Sarm1KO and TKO animals. (A) PCA analysis of the proteomic data from cerebellar tissue and (B) spinal cord. Data subjected to row normalisation transformations (quantile) prior to PCA plotting. (C) Graph showing the log2 fold changes (FC) of all proteins (grey) and MitoCarta 3.0 proteins (blue) in the different comparisons.

Supplementary Tables

Table S1: Cerebellar proteins significantly increased or decreased in DKO mice compared to WT animals at 16 weeks of age (q value < 0.1; p value < 0.05). Table sorted by log2FC.

Gene name	Log2FC DKO/WT	q value	-log p value	MitoCarta
Tmem64	2.21	0.04	1.92	
Cox18	1.47	0.00	4.50	+
S100a11	1.43	0.05	1.93	
Mest	1.22	0.07	1.87	
Ezh1	1.11	0.07	1.94	
Ldlr	1.10	0.02	2.50	
Parl	1.06	0.00	8.35	+
Mtatp6	0.81	0.06	2.27	+
Slc30a9	0.55	0.00	11.72	+
Cmc1	0.49	0.04	3.80	+
Slc25a29	0.48	0.01	5.30	+
Dnajc30	0.46	0.01	7.38	+
Uqcc2	0.46	0.01	7.03	+
Uqcc1	0.35	0.04	6.37	+
Maip1	-0.31	0.10	5.37	+
Fam162a	-0.36	0.02	8.33	+
Ccdc51	-0.36	0.03	6.54	+
Mrpl47	-0.36	0.05	5.71	+
Ptges2	-0.38	0.01	8.84	+
Mrps30	-0.40	0.07	4.08	+
Sco2	-0.41	0.06	4.33	+
Timm50	-0.42	0.01	8.16	+
Afg3l2	-0.47	0.00	11.35	+
Crls1	-0.47	0.01	6.58	+
Phb	-0.54	0.00	9.27	+
Phb2	-0.56	0.00	11.95	+
Surf1	-0.58	0.00	7.85	+
Ghitm	-0.70	0.00	6.61	+

Mrpl27	-0.82	0.06	2.22	+
Chchd2	-0.91	0.00	9.04	+
Mpc1	-1.12	0.00	10.83	+
Mpc2	-1.25	0.00	9.34	+
Plgrkt	-1.26	0.01	2.89	+
Hist1h1d	-1.26	0.05	2.03	
Bak1	-1.36	0.06	1.85	+
Rabl2	-1.73	0.01	2.93	

Table S2: Spinal cord proteins significantly increased or decreased in DKO mice compared to WT animals at 16 weeks of age (q value < 0.1; p value < 0.05). Table sorted by log2FC.

Gene name	Log2FC DKO/WT	q value	-log p value	MitoCarta
Dchs1	3.00	0.07	3.13	
Parl	1.75	0.03	3.62	+
Slc25a29	0.72	0.04	3.54	+
Slc30a9	0.58	0.00	8.80	+
Uqcc2	0.45	0.00	5.62	+
Uqcc1	0.41	0.00	10.28	+
Rin1	0.29	0.02	4.10	
Slc25a25	0.27	0.00	6.35	+
Slc25a3	0.26	0.00	6.67	+
Timm44	0.21	0.00	5.46	+
Sqrdl	0.17	0.05	3.38	+
Tm9sf2	0.16	0.03	3.67	
Fech	0.12	0.08	3.07	
Rab14	0.09	0.02	3.82	
Acot13	0.09	0.05	3.27	+
Samm50	-0.08	0.01	4.20	+
Immt	-0.08	0.05	3.33	+
Vwa8	-0.09	0.05	3.36	+
Gpd2	-0.09	0.03	3.58	+

Fdxr	-0.10	0.09	2.99	+
Mfn2	-0.12	0.03	3.53	+
Dnm1l	-0.12	0.01	4.27	+
Slc25a22	-0.13	0.03	3.60	+
Mres1	-0.13	0.05	3.29	+
Coq6	-0.15	0.09	2.94	+
Nadk2	-0.16	0.00	5.03	+
Letm1	-0.18	0.01	4.30	+
Opa1	-0.19	0.00	6.35	+
Aifm1	-0.19	0.01	4.17	+
Mrps22	-0.23	0.01	4.83	+
Endog	-0.25	0.03	3.56	+
Mrps33	-0.26	0.09	2.95	+
Slc25a46	-0.26	0.03	3.60	+
Pptc7	-0.26	0.02	4.01	+
Htra2	-0.28	0.01	4.72	+
Pnkd	-0.28	0.01	4.68	
Gpr56	-0.29	0.06	3.17	
Mrps24	-0.31	0.00	5.36	+
Timm17b	-0.32	0.06	3.23	+
Ptcd3	-0.33	0.02	4.13	+
Mrpl1	-0.35	0.09	2.98	+
Mrpl46	-0.35	0.07	3.14	+
Ccdc51	-0.40	0.05	3.32	+
Mrpl37	-0.41	0.02	4.11	+
Mrpl47	-0.41	0.07	3.16	+
Fam162a	-0.41	0.00	7.73	+
Mrpl9	-0.43	0.02	4.09	+
Maip1	-0.45	0.06	3.22	+
Mrpl15	-0.49	0.00	5.70	+
Timm50	-0.51	0.00	8.20	+
Mrpl14	-0.54	0.00	5.76	+
Mrpl53	-0.54	0.09	2.95	+
Ptges2	-0.58	0.00	8.19	+

Afg3l2	-0.62	0.00	12.09	+
Plgrkt	-0.68	0.00	5.04	+
Phb	-0.68	0.00	10.86	+
Surf1	-0.69	0.00	6.16	+
Phb2	-0.74	0.00	12.51	+
Chchd2	-0.75	0.01	4.23	+
Crls1	-0.86	0.00	6.46	+
Ghitm	-0.89	0.00	9.96	+
Mpc2	-1.10	0.00	10.82	+
Mpc1	-1.16	0.00	11.51	+
Ryr1	-3.04	0.01	4.26	

Table S3. List of proteins found significatively altered in 28 weeks cerebellar proteomics. The comparisons among the different genotypes are highlighted by colors. q value < 0.1, p value < 0.05, a FC cut-off was applied for the printed version (0.4). Table alphabetically sorted by gene name.

		DKO/WT				TKO/Sarm1KO				TKO/DKO				Sarm1KO/WT			
Gene name	**MitoCarta**	**Log2FC**	**q value**	**-log p value**	**Sig**	**Log2FC**	**q value**	**-log p value**	**Sig**	**Log2FC**	**q value**	**-log p value**	**Sig**	**Log2FC**	**q value**	**-log p value**	**Sig**
Abtb2		0.42	0.02	2.52	+	-0.23	0.35	1.03		-0.28	0.27	1.79		0.36	0.24	1.61	
Acta1		0.61	0.02	1.95	+	0.34	0.24	1.23		-0.13	0.73	0.30		-0.05	0.99	0.09	
Actr8		0.51	0.02	1.98	+	0.66	0.25	0.99		-0.14	0.56	0.66		-0.28	0.90	0.29	
Adam15		-0.46	0.01	3.50	+	-0.30	0.25	1.22		0.17	0.55	0.63		0.06	0.97	0.27	
Adra2a		0.64	0.02	1.62	+	0.40	0.36	0.81		0.19	0.64	0.40		0.31	0.73	0.55	
Adrbk2		0.40	0.04	1.59	+	0.16	0.72	0.30		0.01	0.97	0.04		0.17	0.93	0.30	
Afg3l2	+	-0.39	0.01	5.14	+	-0.52	0.01	6.85	+	-0.02	0.84	0.52		0.11	0.74	1.85	
Afm		-0.08	0.77	0.08		0.38	0.10	2.07		-0.33	0.49	0.63		-1.09	0.08	1.77	+
Ahsg		-0.13	0.59	0.16		0.81	0.03	3.71	+	-0.19	0.58	0.51		-1.46	0.06	2.07	+
Aifm2	+	0.53	0.04	1.27		0.47	0.06	2.46	+	0.04	0.86	0.20		0.11	0.96	0.21	
Akt1s1		0.51	0.01	2.66	+	0.25	0.50	0.60		-0.18	0.44	0.99		0.10	0.96	0.20	
Alb		-0.04	0.84	0.05		0.51	0.04	2.94	+	-0.44	0.27	1.41		-1.28	0.06	2.18	+
Alg10b		-0.68	0.01	2.89	+	0.15	0.76	0.24		0.38	0.29	1.40		-0.44	0.37	1.06	
Alg3		-0.50	0.02	1.86	+	-0.23	0.75	0.24		-0.07	0.88	0.12		-0.26	0.90	0.29	
Amer3		0.71	0.03	1.44	+	0.97	0.03	3.09	+	0.06	0.88	0.12		-0.19	0.92	0.31	
Amz2		-0.13	0.61	0.15		-0.61	0.08	2.02	+	-0.40	0.59	0.42		0.13	0.85	0.65	
Ankrd34b		0.60	0.01	2.24	+	0.07	0.81	0.24		0.04	0.85	0.22		0.38	0.54	0.79	
Ankrd46		0.66	0.03	1.51	+	0.08	0.80	0.25		-0.54	0.28	1.30		0.02	1.00	0.08	
Antkmt	+	0.54	0.02	1.81	+	-0.04	0.90	0.11		-0.24	0.38	1.10		0.29	0.59	0.82	
Anxa1		-0.33	0.12	0.84		0.29	0.21	1.44		0.12	0.73	0.30		-0.59	0.09	2.35	+
Ap3d1		-0.46	0.02	2.00	+	0.11	0.78	0.24		0.39	0.29	1.37		-0.12	0.94	0.33	
Ap5z1		0.50	0.02	2.22	+	0.27	0.59	0.44		-0.42	0.32	1.18		-0.16	0.92	0.32	
Aph1a		-0.45	0.02	2.08	+	-0.37	0.34	0.87		-0.08	0.85	0.15		-0.10	0.94	0.36	
Apoa1		-0.68	0.07	0.87		0.55	0.15	1.43		-0.02	0.98	0.02		-1.58	0.05	2.01	+
Apoc1		-0.76	0.03	1.37	+	0.22	0.54	0.56		0.15	0.69	0.34		-1.29	0.13	1.37	
Apoc3		-1.37	0.02	1.27		0.02	0.98	0.03		-0.37	0.53	0.52		-1.95	0.05	2.43	+
Apod		0.45	0.04	1.54	+	0.27	0.46	0.66		0.09	0.70	0.43		0.20	0.88	0.38	
Apoh		-0.03	0.89	0.04		0.65	0.06	2.24	+	-0.21	0.57	0.52		-1.21	0.07	1.79	+
Aptx		-0.87	0.02	1.43	+	-1.05	0.16	1.20		-0.32	0.64	0.36		0.49	0.86	0.31	
Aqp1		-0.64	0.04	1.22		0.47	0.29	0.95		0.07	0.89	0.11		-1.14	0.06	2.30	+
Arl4c		0.34	0.49	0.18		-0.44	0.07	2.40	+	-0.29	0.74	0.24		0.57	0.15	1.68	
Arl5a		-0.60	0.01	2.94	+	0.12	0.76	0.27		0.16	0.60	0.52		-0.49	0.18	1.62	
Arl6ip4		-0.77	0.00	3.41	+	-0.16	0.71	0.32		0.36	0.35	1.06		-0.08	0.98	0.14	

Ashwin		-0.48	0.04	1.41	+	-0.24	0.37	0.94		-0.05	0.89	0.11		-0.08	0.98	0.11	
Asic1		0.43	0.01	3.87	+	0.11	0.70	0.40		0.01	0.98	0.04		0.24	0.65	0.83	
Astn1		0.45	0.02	2.65	+	0.06	0.85	0.18		0.05	0.82	0.22		0.29	0.65	0.73	
Atf2		-0.66	0.01	2.83	+	-0.29	0.49	0.59		-0.02	0.97	0.03		-0.09	0.98	0.10	
Atg9a		-0.42	0.04	1.50	+	0.03	0.94	0.07		0.30	0.43	0.84		-0.16	0.63	1.51	
Atox1		0.84	0.00	3.48	+	-0.10	0.81	0.20		-0.27	0.27	1.87		0.70	0.09	2.03	+
Atp1a4		0.49	0.01	3.68	+	-0.28	0.46	0.67		-0.45	0.29	1.36		0.27	0.44	1.29	
Atp5me	+	-0.61	0.02	2.05	+	0.00	1.00	0.00		0.22	0.60	0.45		-0.40	0.12	2.55	
Atp5pf	+	1.16	0.00	3.75	+	-0.19	0.70	0.31		-0.41	0.28	2.02		1.04	0.06	2.18	+
Atp6v0e2		1.20	0.18	0.43		-0.96	0.42	0.60		-0.13	0.96	0.04		2.09	0.05	2.37	+
Atp7a		0.03	0.74	0.19		0.46	0.09	2.01	+	0.07	0.80	0.24		-0.41	0.13	2.33	
Atrn		0.45	0.03	1.94	+	0.32	0.23	1.30		-0.05	0.85	0.17		0.12	0.93	0.34	
B3gntl1		-1.56	0.01	1.97	+	-0.26	0.58	0.46		1.14	0.30	1.06		0.09	0.98	0.12	
Baalc		-0.47	0.04	1.54	+	-0.21	0.54	0.56		0.25	0.46	0.75		-0.17	0.92	0.31	
Baiap3		0.90	0.01	1.89	+	0.09	0.89	0.11		0.23	0.55	0.56		0.64	0.60	0.59	
Banf1		0.58	0.00	4.34	+	-0.02	0.94	0.07		-0.22	0.32	1.60		0.61	0.19	1.40	
Bbs9		-0.27	0.30	0.38		-0.71	0.08	1.94	+	-0.24	0.62	0.40		0.24	0.81	0.50	
Bcl10		0.57	0.02	2.01	+	0.15	0.66	0.40		-0.29	0.37	1.02		0.13	0.94	0.29	
Bend7		-0.77	0.00	4.16	+	0.13	0.78	0.23		0.52	0.25	1.56		-0.46	0.20	1.59	
Bloc1s1	+	0.42	0.02	2.27	+	0.11	0.74	0.32		-0.09	0.66	0.51		0.17	0.86	0.46	
Blvrb		-0.47	0.05	1.27		0.14	0.27	1.98		-0.05	0.84	0.21		-0.76	0.06	2.46	+
Bmpr1a		-0.60	0.01	2.35	+	-0.21	0.46	0.72		0.18	0.63	0.43		-0.13	0.85	0.64	
Bnip2		0.78	0.03	1.41	+	0.11	0.61	0.57		-0.23	0.46	0.77		0.69	0.27	1.05	
Bpgm		-0.50	0.08	0.89		0.26	0.07	3.46	+	-0.08	0.77	0.27		-1.01	0.06	2.10	+
Brf1		-0.98	0.01	1.77	+	0.19	0.64	0.41		0.77	0.26	1.36		-0.31	0.42	1.18	
Bub3		-0.52	0.01	2.84	+	0.09	0.81	0.21		0.25	0.36	1.18		-0.19	0.88	0.38	
C11orf98 homolog		-0.41	0.03	2.06	+	-0.16	0.76	0.25		0.01	0.98	0.02		0.01	1.00	0.01	
C1orf21 homolog		0.02	0.89	0.05		0.63	0.06	2.20	+	0.03	0.93	0.08		-0.41	0.42	1.00	
C1qb		-0.91	0.00	4.51	+	0.36	0.49	0.55		0.67	0.26	1.48		-0.75	0.10	1.87	
C3		-0.20	0.38	0.31		0.45	0.08	2.28	+	-0.07	0.87	0.14		-1.04	0.11	1.58	
C5		-0.05	0.83	0.06		0.84	0.04	2.61	+	0.07	0.89	0.10		-1.15	0.09	1.67	+
C8a		-0.72	0.05	1.04		0.38	0.45	0.62		0.11	0.86	0.13		-1.25	0.07	1.86	+
C8g		-0.24	0.22	0.58		0.51	0.50	0.51		-0.34	0.57	0.46		-1.31	0.08	1.75	+
Ca1		-0.67	0.09	0.78		0.56	0.03	4.16	+	-0.19	0.61	0.46		-1.63	0.05	2.46	+
Ca3		0.11	0.81	0.06		0.77	0.23	1.02		-0.27	0.81	0.16		-1.20	0.10	1.59	+
Ca4		-0.30	0.08	1.29	+	0.00	0.99	0.01		-0.65	0.04	4.71	+	-0.43	0.84	0.35	
Cachd1		0.19	0.23	0.64		0.57	0.06	2.32	+	0.12	0.68	0.38		-0.33	0.40	1.23	
Cacnb1		0.46	0.01	2.68	+	-0.13	0.70	0.35		-0.01	0.97	0.04		0.36	0.61	0.70	

Calcrl		0.91	0.01	2.83	+	0.48	0.14	1.57		-0.10	0.77	0.25		0.33	0.54	0.87	
Camkmt		-1.92	0.00	4.43	+	-1.82	0.01	3.71	+	0.23	0.43	0.90		0.05	0.99	0.13	
Casc3		0.39	0.11	0.79		1.42	0.03	2.63	+	0.16	0.63	0.45		-0.88	0.20	1.16	
Cbll1		-0.72	0.03	1.40	+	0.00	1.00	NaN		-0.27	0.61	0.42		0.00	1.00	NaN	
Cbln3		-0.42	0.04	1.52	+	-0.09	0.85	0.16		-0.14	0.50	0.90		0.41	0.95	0.18	
Ccdc32		0.71	0.01	2.18	+	0.47	0.33	0.85		-0.03	0.95	0.06		0.32	0.73	0.55	
Ccdc85a		0.50	0.02	2.08	+	0.25	0.46	0.67		0.05	0.89	0.11		0.11	0.96	0.19	
Cd44		-0.48	0.02	2.29	+	0.23	0.53	0.55		0.04	0.89	0.13		-0.53	0.24	1.29	
Cd47		-0.42	0.04	1.65	+	0.05	0.90	0.12		0.26	0.44	0.84		-0.15	0.84	0.58	
Cd63		0.22	0.14	1.03		0.56	0.04	2.88	+	0.11	0.58	0.69		-0.32	0.43	1.15	
Cd99		0.40	0.02	2.91	+	0.26	0.29	1.16		-0.10	0.53	1.05		0.00	1.00	0.00	
Cdh1		-0.36	0.18	0.58		0.39	0.37	0.79		-0.11	0.87	0.12		-0.83	0.05	3.15	+
Cdk7		0.54	0.03	1.57	+	-0.01	0.97	0.03		-0.19	0.37	1.24		0.53	0.32	1.06	
Celf4		0.54	0.01	2.34	+	0.15	0.52	0.68		-0.09	0.62	0.67		0.27	0.56	0.97	
Celf6		0.00	1.00	NaN		-1.34	0.04	2.20	+	-0.62	0.29	1.22		0.00	1.00	NaN	
Cenpi		0.45	0.02	2.26	+	0.20	0.46	0.75		-0.14	0.63	0.46		0.11	0.89	0.59	
Cep41		0.55	0.03	1.47	+	-0.12	0.72	0.33		-0.27	0.40	0.95		0.20	0.91	0.31	
Ces1c		-0.30	0.23	0.49		0.47	0.03	3.71	+	-0.17	0.60	0.50		-1.20	0.06	2.21	+
Cfb		-0.23	0.33	0.36		0.58	0.05	2.73	+	0.06	0.89	0.10		-1.03	0.09	1.79	+
Cfh		-0.17	0.44	0.26		0.50	0.03	3.60	+	0.06	0.85	0.16		-0.92	0.14	1.42	
Cfi		-0.27	0.32	0.33		0.54	0.06	2.41	+	0.13	0.78	0.21		-1.01	0.13	1.44	
Chac2		-0.59	0.02	2.14	+	0.13	0.77	0.24		0.22	0.59	0.47		-0.48	0.17	1.80	
Chchd2	+	-0.88	0.00	3.34	+	-0.92	0.03	3.35	+	0.01	0.97	0.03		0.13	0.91	0.42	
Chchd4	+	0.49	0.03	1.57	+	-0.04	0.82	0.33		-0.16	0.36	1.60		0.53	0.22	1.38	
Chd6		0.43	0.03	1.87	+	0.30	0.61	0.41		-0.36	0.56	0.47		-0.13	0.95	0.26	
Chpt1	+	-0.77	0.01	2.39	+	-0.57	0.19	1.24		0.11	0.83	0.16		0.01	1.00	0.03	
Ciao2a		0.43	0.01	4.43	+	0.12	0.70	0.36		-0.23	0.26	2.15		0.05	0.98	0.15	
Ciao2b		1.00	0.00	4.41	+	0.06	0.92	0.08		-0.42	0.32	1.18		0.57	0.20	1.41	
Ckm		0.03	0.96	0.01		0.65	0.42	0.63		-0.48	0.73	0.23		-1.22	0.06	2.01	+
Clasrp		1.52	0.02	1.51	+	0.00	1.00	NaN		-1.26	0.27	1.21		0.00	1.00	NaN	
Clmp		-0.86	0.01	1.90	+	-0.48	0.23	1.11		0.29	0.58	0.46		-0.05	0.99	0.11	
Clns1a		-0.57	0.01	3.02	+	0.06	0.88	0.14		0.32	0.32	1.27		-0.29	0.38	1.44	
Clta		0.69	0.00	3.82	+	-0.07	0.88	0.12		-0.30	0.26	1.82		0.48	0.23	1.36	
Cltb		0.54	0.02	1.88	+	0.00	1.00	0.00		-0.23	0.44	0.86		0.39	0.44	0.98	
Cnbp		0.75	0.00	4.50	+	0.07	0.89	0.11		-0.26	0.41	0.95		0.48	0.24	1.33	
Cnih2		-0.47	0.07	1.03		-1.01	0.09	1.71	+	-0.44	0.51	0.54		0.10	0.95	0.32	
Cnn2		-0.09	0.72	0.10		0.77	0.42	0.61		0.00	0.99	0.00		-1.04	0.07	1.96	+
Cntn3		0.60	0.03	1.56	+	0.16	0.72	0.31		0.05	0.90	0.10		0.24	0.90	0.31	

Col7a1		0.65	0.01	3.46	+	-0.04	0.86	0.19		-0.38	0.23	2.59		0.23	0.64	0.90	
Commd8		0.54	0.01	2.67	+	-0.15	0.72	0.30		-0.50	0.23	3.06		0.30	0.70	0.60	
Cox16	+	-0.60	0.02	2.00	+	-0.50	0.29	0.93		-0.23	0.55	0.55		-0.33	0.72	0.56	
Cox17	+	0.88	0.00	3.44	+	0.05	0.92	0.09		-0.16	0.51	0.74		0.77	0.10	1.82	
Cox18	+	0.00	1.00	NaN		1.08	0.08	1.73		-0.05	0.81	0.25		0.00	1.00	NaN	
Cox5a	+	1.10	0.00	4.81	+	-0.10	0.86	0.14		-0.37	0.27	1.53		0.92	0.07	2.07	+
Cox5b		0.85	0.00	4.33	+	-0.06	0.90	0.11		-0.29	0.27	1.71		0.65	0.11	1.94	
Cox6b1	+	0.49	0.02	2.32	+	-0.18	0.56	0.54		-0.19	0.37	1.25		0.52	0.16	1.74	
Cox7a1	+	0.82	0.01	2.71	+	-0.09	0.84	0.18		-0.22	0.44	0.86		0.80	0.08	2.05	+
Cox7a2	+	1.52	0.00	3.01	+	0.19	0.69	0.34		-0.14	0.47	1.01		1.36	0.06	2.17	+
Cox7c	+	-0.81	0.03	1.25		-0.81	0.12	1.47		0.75	0.32	1.01		0.88	0.06	2.26	+
Cpn1		0.06	0.83	0.05		0.47	0.30	0.91		-0.51	0.46	0.62		-1.22	0.08	1.79	+
Creg2		1.03	0.01	1.75	+	0.09	0.91	0.09		0.05	0.93	0.07		0.71	0.49	0.71	
Crls1	+	-0.87	0.01	1.96	+	-0.50	0.20	1.21		0.14	0.75	0.26		-0.16	0.93	0.29	
Cryzl2	+	-0.51	0.01	3.47	+	-0.02	0.94	0.08		0.18	0.43	1.03		-0.24	0.45	1.44	
Csdc2		0.41	0.02	2.78	+	0.33	0.15	1.74		-0.21	0.29	1.92		-0.02	1.00	0.03	
Csnk1g2		0.07	0.62	0.19		0.70	0.04	2.81	+	0.00	0.99	0.01		-0.39	0.64	0.63	
Csrp3		0.93	0.00	3.01	+	0.27	0.65	0.36		-0.06	0.79	0.27		0.50	0.67	0.55	
Ctc1		1.16	0.00	2.88	+	0.36	0.41	0.72		-0.71	0.27	1.81		0.17	0.93	0.30	
Ctdspl2		-0.44	0.02	2.60	+	-0.10	0.78	0.25		0.00	0.99	0.00		0.16	0.98	0.12	
Ctsl		0.43	0.01	3.75	+	0.00	1.00	0.00		-0.11	0.60	0.63		0.26	0.66	0.75	
Ctss		-0.55	0.02	1.85	+	-0.11	0.66	0.47		0.27	0.34	1.27		-0.32	0.58	0.81	
Cuta		0.71	0.00	3.99	+	-0.01	0.99	0.01		-0.37	0.32	1.20		0.54	0.30	1.09	
Cyb561d2		-0.84	0.01	2.04	+	-0.49	0.27	0.98		0.11	0.79	0.21		-0.24	0.85	0.41	
Cyc1		0.45	0.00	6.62	+	-0.01	0.98	0.03		-0.19	0.32	1.71		0.25	0.44	1.37	
Cycs	+	0.68	0.03	1.45	+	-0.17	0.46	0.81		-0.18	0.43	1.08		0.81	0.11	1.73	
Dbndd2		-0.41	0.05	1.46	+	-0.35	0.18	1.49		-0.17	0.56	0.60		-0.13	0.92	0.35	
Dcp2		0.52	0.03	1.58	+	0.31	0.41	0.75		-0.07	0.82	0.19		0.14	0.95	0.25	
Dctn5		-0.60	0.01	3.78	+	0.20	0.42	0.84		0.38	0.27	2.00		-0.43	0.09	2.85	+
Dcun1d3		0.42	0.04	1.53	+	0.66	0.05	2.62	+	-0.05	0.86	0.15		-0.20	0.83	0.50	
Ddrgk1		-0.52	0.01	2.72	+	-0.07	0.91	0.10		0.41	0.31	1.24		-0.10	0.96	0.19	
Ddx21		-0.78	0.01	2.28	+	0.28	0.64	0.38		0.46	0.36	0.96		-0.35	0.79	0.45	
Ddx39a		-0.44	0.05	1.38	+	0.01	0.99	0.01		0.22	0.42	0.97		-0.23	0.85	0.41	
Ddx51		0.85	0.01	2.47	+	0.42	0.55	0.46		-0.48	0.43	0.72		-0.11	0.98	0.13	
Derpc		1.07	0.01	1.89	+	-0.05	0.94	0.06		-0.30	0.39	0.97		0.82	0.25	1.04	
Dgat1		-0.81	0.01	2.78	+	-0.05	0.86	0.16		0.36	0.30	1.38		-0.41	0.18	1.95	
Dgka		0.51	0.03	1.55	+	0.15	0.57	0.58		-0.04	0.86	0.19		0.24	0.76	0.60	
Dhcr7		-0.41	0.01	4.89	+	0.05	0.85	0.18		0.15	0.45	1.05		-0.40	0.19	1.85	

Dhfr		0.42	0.01	2.99	+	0.34	0.14	1.78		-0.06	0.83	0.21		-0.04	0.99	0.15	
Diablo	+	0.73	0.01	2.37	+	0.34	0.24	1.20		-0.34	0.26	2.08		0.09	0.97	0.17	
Diras2		-0.55	0.00	4.17	+	-0.14	0.60	0.52		0.23	0.31	1.70		-0.10	0.95	0.31	
Dlgap2		0.59	0.02	1.75	+	-0.06	0.89	0.12		-0.08	0.78	0.24		0.43	0.43	0.95	
Dnajb5		0.28	0.13	0.90		0.65	0.03	3.97	+	-0.05	0.89	0.12		-0.42	0.12	2.44	
Dnajc30	+	0.62	0.02	1.98	+	0.62	0.04	2.57	+	-0.09	0.76	0.29		-0.11	0.95	0.26	
Dnmt3a		-0.48	0.02	1.97	+	0.18	0.64	0.41		0.18	0.62	0.44		-0.48	0.17	1.75	
Dok7		0.52	0.03	1.71	+	0.66	0.18	1.23		0.06	0.92	0.08		-0.24	0.85	0.41	
Dolk		-0.66	0.01	2.04	+	0.26	0.67	0.33		0.29	0.56	0.49		-0.71	0.14	1.59	
Dop1b		0.49	0.02	2.00	+	0.04	0.82	0.31		-0.17	0.46	0.96		0.26	0.42	1.44	
Dph6		0.80	0.01	3.03	+	0.17	0.63	0.45		-0.49	0.28	1.85		0.18	0.81	0.62	
Dpm3		1.29	0.00	4.26	+	-0.08	0.89	0.11		-0.42	0.28	1.40		0.96	0.09	1.76	+
Dpp4		-0.28	0.08	1.33	+	0.38	0.12	1.89		0.13	0.52	0.82		-0.55	0.09	2.42	+
Dpy19l3		0.27	0.25	0.46		0.89	0.06	2.06	+	0.15	0.72	0.30		-0.42	0.57	0.72	
Dstyk		1.03	0.01	2.08	+	1.63	0.04	2.13	+	-0.12	0.76	0.26		-0.88	0.28	0.97	
Dusp23		-0.50	0.03	1.72	+	-0.51	0.23	1.11		0.08	0.86	0.14		0.00	1.00	0.00	
Dusp28		0.43	0.03	2.06	+	0.13	0.53	0.73		-0.17	0.46	0.90		-0.06	0.98	0.12	
Ebag9		-0.51	0.01	3.06	+	-0.15	0.63	0.47		0.23	0.44	0.84		-0.10	0.91	0.54	
Ebna1bp2		0.56	0.06	1.07		0.68	0.07	2.03	+	-0.02	0.95	0.06		-0.14	0.97	0.16	
Ebpl		0.98	0.02	1.44	+	-0.67	0.56	0.42		-0.73	0.49	0.56		0.92	0.22	1.09	
Ece1		0.42	0.05	1.32	+	0.35	0.16	1.63		-0.06	0.86	0.15		0.10	0.95	0.26	
Eed		0.56	0.03	1.44	+	0.69	0.09	1.81	+	-0.05	0.89	0.11		-0.17	0.94	0.25	
Eef1b		0.43	0.01	3.46	+	-0.06	0.86	0.16		-0.28	0.26	2.89		0.22	0.68	0.80	
Efemp1		0.00	1.00	NaN		1.87	0.40	0.61		0.00	1.00	NaN		-2.35	0.08	1.57	+
Efhd1	+	0.50	0.03	1.82	+	0.21	0.72	0.29		-0.27	0.45	0.78		-0.07	0.99	0.08	
Eif1ad		0.49	0.01	3.79	+	0.18	0.67	0.37		-0.32	0.41	0.87		-0.01	1.00	0.02	
Eif5b		-0.68	0.00	3.87	+	0.10	0.84	0.16		0.46	0.29	1.33		-0.25	0.69	0.70	
Emilin2		-0.06	0.70	0.13		-0.64	0.06	2.16	+	-0.68	0.28	1.69		-0.30	0.68	0.65	
Endod1		-0.78	0.01	3.05	+	0.32	0.53	0.51		0.59	0.26	1.53		-0.62	0.19	1.40	
Enpp4		0.77	0.01	2.29	+	0.06	0.92	0.08		-0.38	0.46	0.68		0.10	0.98	0.13	
Entpd2		0.56	0.03	1.44	+	0.07	0.80	0.26		0.06	0.67	0.66		0.33	0.76	0.51	
Eny2		0.54	0.01	2.68	+	0.22	0.27	1.34		0.01	0.97	0.06		0.32	0.35	1.41	
Epb42		-0.74	0.05	1.07		0.47	0.07	2.33	+	-0.03	0.95	0.06		-1.46	0.05	2.39	+
Epc2		0.06	0.61	0.22		0.57	0.07	2.18	+	0.02	0.94	0.08		-0.49	0.22	1.44	
Ergic2		-0.82	0.01	2.07	+	-1.01	0.10	1.55		0.26	0.33	1.31		0.31	0.89	0.30	
Erh		0.85	0.00	4.30	+	0.16	0.64	0.44		-0.25	0.32	1.46		0.72	0.20	1.25	
Erich6		0.24	0.17	0.74		0.45	0.03	3.53	+	-0.03	0.91	0.11		-0.03	1.00	0.04	
Ess2		-0.12	0.54	0.20		0.58	0.09	1.88	+	0.31	0.46	0.72		-0.28	0.65	0.73	

Exosc1		-0.85	0.02	1.43	+	-0.30	0.38	0.83		0.71	0.26	1.37		0.23	0.79	0.55	
Exosc7		-0.42	0.02	2.55	+	0.01	0.98	0.02		0.20	0.30	1.92		-0.17	0.78	0.71	
Exosc8		-0.55	0.02	1.93	+	0.29	0.30	1.06		0.25	0.44	0.87		-0.53	0.12	2.03	
Exosc9		-0.88	0.03	1.38	+	0.00	1.00	NaN		0.29	0.64	0.35		0.00	1.00	NaN	
F11r		-0.58	0.01	3.65	+	0.01	0.97	0.03		0.18	0.56	0.56		-0.46	0.08	2.90	+
F12		-0.14	0.59	0.15		0.80	0.05	2.28	+	-0.27	0.49	0.66		-1.54	0.06	2.00	+
F2		0.20	0.35	0.34		0.42	0.08	2.25	+	-0.21	0.57	0.53		-0.69	0.22	1.21	
Fabp5		0.54	0.01	2.77	+	-0.08	0.88	0.13		-0.10	0.71	0.37		0.38	0.61	0.68	
Fam118a		0.16	0.25	0.67		0.47	0.07	2.34	+	0.00	0.99	0.01		-0.32	0.26	1.74	
Fam136a	+	0.71	0.01	2.74	+	0.06	0.88	0.13		-0.06	0.58	1.74		0.62	0.14	1.69	
Fam160b2		0.59	0.04	1.33	+	0.59	0.12	1.65		-0.18	0.63	0.42		-0.21	0.85	0.42	
Fam174a		-1.56	0.00	3.34	+	0.54	0.63	0.36		1.02	0.27	2.23		-1.12	0.22	1.04	
Fam177a1		0.46	0.01	2.63	+	0.15	0.68	0.37		-0.02	0.93	0.11		0.18	0.89	0.37	
Fam193b		-1.60	0.00	2.46	+	-0.21	0.75	0.25		1.12	0.26	1.46		-0.28	0.76	0.56	
Fam207a		-0.37	0.12	0.76		0.75	0.04	2.43	+	0.53	0.26	1.60		-0.59	0.20	1.39	
Fam32a		-0.46	0.03	1.78	+	0.12	0.75	0.28		0.01	0.97	0.04		-0.57	0.18	1.54	
Fan1		0.87	0.01	1.81	+	1.43	0.04	2.36	+	-0.33	0.25	1.87		-0.42	0.89	0.28	
Fau		-0.45	0.01	3.33	+	-0.04	0.91	0.10		0.18	0.49	0.77		-0.17	0.83	0.59	
Fbln1		0.49	0.04	1.48	+	0.55	0.05	2.76	+	0.05	0.90	0.10		-0.15	0.88	0.46	
Fbxl17		0.10	0.60	0.17		0.61	0.08	1.99	+	0.44	0.29	1.34		-0.15	0.93	0.30	
Fchsd1		0.41	0.05	1.32	+	0.24	0.38	0.90		-0.08	0.72	0.37		0.09	0.97	0.20	
Fdft1		0.90	0.00	3.57	+	-0.11	0.82	0.18		-0.03	0.95	0.06		0.71	0.20	1.26	
Fdx1	+	0.23	0.40	0.27		-0.73	0.09	1.84	+	-0.33	0.52	0.56		0.62	0.17	1.51	
Fdx2	+	0.42	0.02	2.75	+	0.10	0.80	0.22		-0.21	0.37	1.24		0.15	0.92	0.34	
Fetub		-0.32	0.19	0.56		0.55	0.07	2.13	+	-0.05	0.90	0.10		-1.16	0.06	2.07	+
Fga		-0.62	0.07	0.90		0.63	0.30	0.86		0.26	0.70	0.29		-1.34	0.09	1.65	+
Fgb		-0.61	0.08	0.87		0.67	0.25	0.97		0.23	0.72	0.27		-1.41	0.08	1.67	+
Fgg		-0.53	0.11	0.73		0.65	0.28	0.92		0.18	0.78	0.20		-1.37	0.09	1.60	+
Fggy		0.33	0.16	0.64		0.60	0.08	2.05	+	-0.05	0.91	0.09		-0.34	0.48	0.97	
Fhdc1		0.82	0.01	2.61	+	0.65	0.33	0.80		-0.15	0.68	0.36		0.12	0.98	0.10	
Fhod1		-0.77	0.01	2.35	+	0.24	0.67	0.34		0.55	0.26	1.41		-0.51	0.36	0.99	
Fkbp10	+	0.69	0.01	2.62	+	0.58	0.06	2.31	+	-0.25	0.39	1.06		0.00	1.00	0.01	
Flg2		-0.09	0.41	0.46		-0.42	0.07	2.53	+	0.06	0.78	0.29		0.30	0.36	1.45	
Fmc1	+	0.41	0.04	1.65	+	-0.13	0.83	0.17		-0.36	0.44	0.72		-0.08	0.99	0.09	
Fmn1		0.70	0.03	1.49	+	0.24	0.60	0.44		-0.36	0.41	0.83		-0.05	1.00	0.07	
Fn1		-0.38	0.11	0.85		0.34	0.09	2.34	+	0.03	0.93	0.08		-0.96	0.09	1.78	+
Fndc3a		-0.53	0.01	3.75	+	-0.05	0.80	0.34		0.32	0.27	2.53		-0.16	0.51	2.27	
Foxo1		0.43	0.02	2.35	+	0.07	0.89	0.12		-0.16	0.66	0.38		0.37	0.49	0.90	

Frk		-0.85	0.03	1.35	+	0.33	0.57	0.45		0.27	0.70	0.29		-1.46	0.12	1.40	
Fsip2		0.44	0.03	1.65	+	0.45	0.28	0.97		-0.17	0.50	0.76		-0.28	0.81	0.47	
Fstl1		0.55	0.02	2.17	+	0.05	0.96	0.04		-0.59	0.44	0.67		-0.10	0.98	0.14	
Fth1	+	0.53	0.01	3.98	+	0.06	0.89	0.13		-0.14	0.47	1.00		0.28	0.61	0.82	
Fundc1	+	-0.68	0.00	3.70	+	-0.27	0.41	0.77		0.21	0.53	0.61		-0.21	0.57	1.18	
Fundc2	+	-0.62	0.00	5.28	+	-0.18	0.49	0.69		0.18	0.37	1.32		-0.19	0.78	0.68	
Fxn	+	0.97	0.02	1.67	+	-0.25	0.55	0.51		-0.43	0.37	0.91		0.69	0.20	1.30	
Fxyd1		-1.03	0.00	4.20	+	-0.15	0.81	0.19		0.30	0.44	0.81		-0.40	0.65	0.62	
Fxyd6		-0.49	0.01	3.60	+	-0.04	0.93	0.08		0.55	0.22	2.35		0.09	0.95	0.26	
Gabpa		-0.02	0.88	0.05		0.41	0.04	3.12	+	0.14	0.50	0.87		0.10	0.99	0.09	
Gabrd		-0.40	0.03	1.98	+	0.11	0.77	0.25		-0.02	0.93	0.09		-0.54	0.20	1.45	
Gadl1		-0.73	0.01	2.83	+	-0.41	0.60	0.40		0.36	0.45	0.70		0.16	0.97	0.15	
Gbp2		0.63	0.11	0.67		1.05	0.05	2.09	+	0.16	0.75	0.24		-0.30	0.89	0.30	
Gc		-0.44	0.12	0.70		0.45	0.09	2.15	+	-0.11	0.77	0.25		-1.30	0.06	2.00	+
Gca		0.75	0.02	1.60	+	-0.37	0.70	0.28		-0.52	0.54	0.48		0.63	0.30	1.03	
Gfra2		0.48	0.02	2.25	+	-0.10	0.80	0.22		0.07	0.82	0.19		0.43	0.51	0.80	
Ggact		0.59	0.00	4.84	+	0.13	0.76	0.26		-0.16	0.43	1.15		0.41	0.45	0.93	
Ghitm	+	-1.46	0.00	3.59	+	-0.39	0.48	0.57		0.56	0.30	1.19		-0.44	0.51	0.79	
Glod4	+	0.07	0.39	1.03		0.02	0.90	0.16		0.46	0.03	6.80	+	0.46	0.06	3.69	+
Glrx		0.71	0.00	4.01	+	-0.12	0.77	0.25		-0.16	0.45	1.00		0.59	0.14	1.71	
Glrx5	+	0.58	0.01	3.48	+	0.05	0.88	0.14		-0.22	0.31	1.67		0.33	0.39	1.25	
Gm5629		-0.18	0.65	0.11		0.77	0.21	1.07		-0.54	0.40	0.78		-1.67	0.08	1.66	+
Gnb1		0.47	0.01	3.53	+	-0.05	0.88	0.14		-0.22	0.39	1.09		0.27	0.40	1.43	
Gng10		-0.42	0.04	1.65	+	0.09	0.91	0.08		0.16	0.75	0.25		-0.35	0.69	0.59	
Gng13		0.64	0.01	3.13	+	0.14	0.52	0.74		-0.30	0.27	2.27		0.49	0.46	0.84	
Gng2		0.87	0.00	3.10	+	0.15	0.61	0.49		-0.10	0.59	0.73		0.63	0.10	2.03	
Gng4		0.97	0.01	2.22	+	0.00	1.00	0.00		0.04	0.90	0.11		0.73	0.41	0.82	
Gng5		0.48	0.00	4.85	+	0.18	0.25	1.65		-0.18	0.29	2.22		0.32	0.60	0.75	
Gon4l		-0.59	0.03	1.45	+	-0.29	0.46	0.65		0.30	0.50	0.63		-0.16	0.94	0.27	
Gpatch8		-0.67	0.01	2.37	+	0.01	0.99	0.01		0.21	0.58	0.51		-0.29	0.83	0.43	
Gpx3		0.17	0.55	0.17		0.71	0.07	2.04	+	-0.03	0.97	0.04		-0.82	0.18	1.27	
Gramd2b		0.69	0.02	1.85	+	0.04	0.96	0.05		-0.12	0.77	0.24		0.54	0.28	1.14	
Grasp		-0.57	0.02	2.21	+	-0.46	0.19	1.29		0.10	0.82	0.17		0.16	0.90	0.37	
Grb14		-0.66	0.01	2.33	+	-0.79	0.05	2.47	+	0.13	0.71	0.32		0.14	0.93	0.29	
Grcc10		0.80	0.00	3.30	+	-0.08	0.87	0.14		-0.11	0.75	0.28		0.82	0.06	2.45	+
Grid1		0.41	0.04	1.63	+	0.19	0.41	0.93		-0.01	0.95	0.09		0.14	0.91	0.38	
Grin2b		0.76	0.01	1.96	+	0.15	0.69	0.35		0.08	0.78	0.25		0.43	0.63	0.61	
Grin2d		0.22	0.10	1.41	+	-0.20	0.43	0.81		0.03	0.90	0.11		0.46	0.09	2.85	+

Grm7		0.50	0.02	2.19	+	-0.03	0.93	0.08		0.03	0.91	0.10		0.37	0.57	0.76	
Grm8		0.55	0.01	2.42	+	0.06	0.85	0.18		0.08	0.71	0.43		0.44	0.31	1.20	
Gtf2h2		0.45	0.10	0.80		0.83	0.08	1.90	+	0.03	0.95	0.05		-0.32	0.70	0.59	
H1-0		-0.81	0.01	2.42	+	0.39	0.43	0.67		0.34	0.43	0.78		-0.49	0.69	0.52	
H1-1		-0.46	0.03	1.75	+	0.32	0.33	0.95		0.24	0.44	0.85		0.01	1.00	0.01	
H1-4		-0.97	0.02	1.46	+	0.18	0.83	0.16		0.57	0.42	0.73		-0.35	0.85	0.36	
H1-5		-0.72	0.02	1.83	+	0.23	0.65	0.37		0.32	0.45	0.74		0.01	1.00	0.00	
H2-Q10		-0.71	0.06	0.98		0.45	0.16	1.44		0.10	0.84	0.15		-1.38	0.06	1.96	+
H6pd		0.74	0.01	2.03	+	0.72	0.13	1.48		-0.25	0.67	0.32		-0.10	0.96	0.22	
Hap1		0.73	0.02	1.55	+	-0.11	0.79	0.23		0.13	0.65	0.42		0.63	0.47	0.75	
Hbb-b1		0.05	0.83	0.06		0.41	0.14	1.66		-0.34	0.44	0.75		-0.97	0.10	1.71	+
Hikeshi		0.75	0.00	4.90	+	-0.16	0.71	0.32		-0.47	0.27	1.97		0.51	0.18	1.61	
Hint1	+	0.49	0.01	3.90	+	-0.13	0.72	0.32		-0.22	0.38	1.12		0.43	0.20	1.63	
Hivep2		0.40	0.04	1.55	+	0.29	0.16	1.73		-0.17	0.46	0.93		0.14	0.95	0.24	
Hk2		0.67	0.02	1.63	+	0.44	0.22	1.18		-0.54	0.31	1.14		-0.14	0.93	0.29	
Hmga1		-0.54	0.02	1.85	+	0.18	0.71	0.30		0.19	0.62	0.44		-0.27	0.86	0.36	
Hmgn2		-1.74	0.00	2.87	+	0.34	0.78	0.20		0.92	0.34	0.91		-0.89	0.40	0.79	
Hmgn3		-1.13	0.01	2.32	+	0.14	0.82	0.17		0.70	0.26	1.36		-0.31	0.86	0.35	
Hrg		-0.08	0.73	0.10		0.55	0.03	3.48	+	-0.11	0.74	0.30		-0.99	0.10	1.67	+
Hspb2		-2.79	0.00	4.03	+	-2.56	0.03	2.59	+	0.37	0.46	0.67		0.10	0.98	0.13	
Hspb8		0.64	0.03	1.34	+	-0.03	0.97	0.03		-0.37	0.45	0.72		0.28	0.83	0.41	
Ica		-0.35	0.12	0.82		0.33	0.32	0.97		-0.05	0.90	0.11		-0.98	0.09	1.81	+
Ica1l		0.50	0.02	2.16	+	0.37	0.21	1.31		-0.03	0.92	0.11		0.06	0.99	0.11	
Iffo1		0.00	1.00	NaN		-0.75	0.03	3.05	+	0.12	0.61	0.57		0.00	1.00	NaN	
Ift122		-0.02	0.90	0.04		0.46	0.04	2.90	+	0.63	0.22	2.28		0.14	0.90	0.42	
Ift22		0.67	0.00	4.33	+	-0.17	0.70	0.33		-0.31	0.30	1.45		0.53	0.19	1.56	
Ig gamma-3		-0.05	0.90	0.03		0.03	0.96	0.04		-1.07	0.27	1.25		-1.37	0.06	1.92	+
Igh-3		-0.15	0.65	0.12		0.50	0.26	0.99		-0.56	0.33	1.01		-1.37	0.06	1.93	+
Ighg1		-0.60	0.16	0.54		1.03	0.04	2.29	+	-0.23	0.76	0.21		-2.21	0.03	2.88	+
Igkc		-0.44	0.30	0.32		0.60	0.16	1.38		-0.24	0.64	0.37		-1.42	0.09	1.60	+
Ikbkg		-0.44	0.04	1.64	+	-0.29	0.10	2.47		0.04	0.89	0.13		-0.04	0.99	0.13	
Ilrun		0.94	0.01	2.82	+	0.59	0.16	1.38		-0.29	0.55	0.52		0.08	0.96	0.24	
Impact		0.56	0.02	2.15	+	0.11	0.74	0.32		0.12	0.60	0.59		0.42	0.42	0.98	
Ing4		0.96	0.02	1.46	+	0.57	0.80	0.17		-0.45	0.70	0.27		-0.06	1.00	0.02	
Inpp5k		0.43	0.03	1.84	+	0.50	0.07	2.31	+	0.00	0.99	0.01		0.02	1.00	0.05	
Ints11		-2.20	0.00	3.63	+	0.00	1.00	NaN		1.17	0.26	1.62		0.00	1.00	NaN	
Iqgap2		0.59	0.02	1.91	+	1.08	0.03	3.35	+	0.21	0.53	0.61		-0.37	0.44	1.00	
Isg15		-0.23	0.30	0.40		0.39	0.09	2.24	+	-0.01	0.98	0.02		-0.77	0.10	1.86	+

Isy1		-0.47	0.01	3.43	+	-0.37	0.16	1.59		-0.03	0.91	0.10		0.03	1.00	0.06	
Itfg2		0.41	0.04	1.67	+	0.52	0.17	1.33		-0.08	0.86	0.14		-0.08	0.97	0.17	
Itih2		-0.16	0.43	0.27		0.50	0.03	3.44	+	-0.04	0.91	0.10		-0.97	0.10	1.68	
Jagn1		-0.59	0.01	2.33	+	-0.09	0.63	0.62		0.36	0.26	1.88		-0.18	0.68	0.97	
Jpt1		0.55	0.03	1.71	+	0.15	0.70	0.33		-0.11	0.55	0.81		0.22	0.86	0.40	
Jtb		0.54	0.02	1.77	+	0.03	0.96	0.05		-0.01	0.98	0.02		0.67	0.12	1.78	
Kcnc2		0.71	0.02	1.80	+	0.04	0.95	0.05		-0.19	0.57	0.53		0.26	0.89	0.32	
Kcnc4		0.65	0.01	2.57	+	-0.59	0.35	0.77		-0.48	0.44	0.70		0.70	0.12	1.76	
Kcnh1		0.86	0.12	0.60		0.73	0.06	2.21	+	-0.13	0.63	0.48		0.20	0.98	0.12	
Kcnk13		0.32	0.06	1.41	+	0.61	0.07	2.09	+	-0.18	0.59	0.51		-0.46	0.17	1.81	
Kcnq3		0.50	0.02	1.99	+	0.64	0.11	1.69		-0.02	0.95	0.07		-0.19	0.90	0.35	
Kctd4		0.60	0.02	1.99	+	-0.22	0.69	0.32		-0.16	0.76	0.24		0.38	0.71	0.54	
Kdelr2		0.90	0.02	1.70	+	-0.26	0.88	0.11		-0.94	0.39	0.74		0.23	0.95	0.17	
Kdm6a		0.42	0.03	1.73	+	0.63	0.10	1.76		0.00	0.99	0.02		-0.20	0.88	0.37	
Khdrbs3		0.42	0.03	1.72	+	-0.14	0.53	0.72		-0.10	0.53	0.98		0.25	0.82	0.46	
Klhdc7a		0.61	0.02	1.84	+	0.89	0.17	1.22		-0.05	0.96	0.04		-0.42	0.40	1.03	
Klhl3		-0.81	0.02	1.81	+	0.81	0.32	0.79		0.12	0.73	0.30		-1.17	0.27	0.92	
Kng1		-0.27	0.33	0.33		0.55	0.03	3.56	+	-0.13	0.72	0.31		-1.22	0.07	1.89	+
Krt5		1.81	0.02	1.32	+	-0.44	0.59	0.41		-1.12	0.39	0.73		1.00	0.08	1.91	+
Krt76		1.16	0.07	0.79		-0.25	0.71	0.28		-0.37	0.76	0.21		1.09	0.05	2.55	+
Krt77		0.00	1.00	NaN		0.00	1.00	NaN		0.00	1.00	NaN		-1.21	0.09	1.59	+
L3hypdh		1.45	0.01	2.29	+	0.00	1.00	NaN		-0.11	0.84	0.15		0.00	1.00	NaN	
Lamp5		0.57	0.04	1.39	+	0.00	0.99	0.01		-0.08	0.76	0.29		0.28	0.85	0.38	
Lamtor4		0.66	0.03	1.56	+	0.51	0.18	1.29		0.12	0.51	0.94		0.14	0.95	0.20	
Lamtor5		1.03	0.01	2.53	+	0.16	0.71	0.31		-0.21	0.40	1.05		0.77	0.16	1.44	
Lancl3		-0.59	0.03	1.62	+	0.06	0.86	0.17		0.34	0.40	0.88		-0.19	0.82	0.55	
Lbp		0.80	0.02	1.57	+	0.76	0.03	3.30	+	-0.12	0.66	0.41		-0.04	0.99	0.10	
Leprot		0.02	0.94	0.02		0.71	0.23	1.05		-0.22	0.65	0.36		-1.14	0.10	1.63	+
Lgals1		0.53	0.01	3.05	+	0.08	0.85	0.17		-0.19	0.45	0.91		0.34	0.46	1.01	
Lgals3bp		-0.45	0.04	1.60	+	-0.33	0.48	0.59		0.14	0.78	0.21		-0.07	0.98	0.16	
Lhfpl4		0.60	0.01	2.14	+	0.00	1.00	NaN		0.25	0.31	1.56		0.00	1.00	NaN	
Lhfpl5		-0.55	0.02	1.82	+	-0.11	0.77	0.26		0.27	0.41	0.91		-0.11	0.95	0.26	
Lipt2	+	0.35	0.09	1.07		0.42	0.07	2.39	+	-0.09	0.64	0.60		-0.06	0.99	0.12	
Lmbrd1		-0.71	0.01	2.80	+	-0.60	0.09	1.90	+	0.10	0.81	0.18		-0.02	1.00	0.11	
Lmln		1.82	0.01	2.04	+	0.58	0.35	0.78		-0.38	0.51	0.57		0.41	0.90	0.28	
Lpin1		0.46	0.04	1.54	+	-0.05	0.90	0.11		-0.17	0.52	0.71		0.19	0.92	0.31	
Lrrc4c		1.03	0.01	2.16	+	0.11	0.80	0.21		0.12	0.78	0.22		0.83	0.14	1.49	
Lrrtm1		1.52	0.00	2.42	+	-0.07	0.92	0.08		0.01	0.98	0.02		1.23	0.15	1.28	

Lsm11		-0.59	0.02	1.80	+	0.10	0.89	0.11		0.18	0.76	0.23		-0.51	0.24	1.30	
Luc7l3		-0.42	0.01	2.87	+	0.17	0.60	0.49		0.17	0.46	0.91		-0.20	0.90	0.34	
Lum		0.21	0.48	0.20		0.70	0.09	1.78	+	-0.30	0.69	0.29		-0.81	0.05	2.99	+
Ly6h		0.62	0.03	1.45	+	-0.07	0.90	0.10		0.24	0.51	0.65		0.55	0.66	0.54	
Lypla1	+	0.62	0.01	2.82	+	-0.39	0.33	0.89		-0.46	0.25	1.59		0.55	0.16	1.70	
Lypla2		0.72	0.00	4.95	+	-0.26	0.60	0.44		-0.48	0.25	1.55		0.54	0.20	1.44	
Lyrm9	+	0.64	0.01	3.43	+	0.37	0.23	1.22		-0.18	0.36	1.43		0.18	0.88	0.40	
Mageh1		-0.65	0.01	2.15	+	0.12	0.84	0.16		0.16	0.73	0.28		-0.35	0.79	0.45	
Map1lc3b		0.33	0.04	1.81	+	0.44	0.06	2.66	+	0.07	0.77	0.31		-0.13	0.89	0.47	
Map2k5		0.27	0.23	0.50		0.92	0.02	3.95	+	-0.07	0.81	0.23		-0.72	0.10	1.90	
Map3k11		0.45	0.02	2.34	+	0.24	0.25	1.36		-0.04	0.82	0.30		0.23	0.65	0.85	
Map3k12		-0.44	0.02	2.07	+	-0.12	0.77	0.24		0.26	0.55	0.52		0.06	0.98	0.19	
Map3k9		0.15	0.29	0.59		0.59	0.06	2.26	+	0.10	0.65	0.49		-0.26	0.66	0.75	
Mapk15		1.15	0.00	2.95	+	0.00	1.00	NaN		0.00	1.00	NaN		0.00	1.00	NaN	
Mapkap1		-0.57	0.01	2.26	+	-0.26	0.60	0.43		-0.02	0.97	0.02		-0.29	0.68	0.67	
Mapkapk5		0.70	0.03	1.48	+	0.55	0.54	0.46		-0.33	0.62	0.39		0.03	1.00	0.02	
Marcksl1		-0.49	0.01	2.59	+	0.06	0.88	0.13		0.14	0.64	0.43		-0.30	0.59	0.81	
Matk		0.48	0.02	2.03	+	-0.02	0.97	0.04		0.02	0.94	0.09		0.30	0.77	0.51	
Mavs	+	-0.44	0.01	4.55	+	0.10	0.73	0.33		0.18	0.37	1.35		-0.30	0.40	1.28	
Mb		-0.04	0.95	0.01		0.49	0.53	0.48		-0.61	0.66	0.30		-1.29	0.07	1.79	+
Mbnl1		1.00	0.02	1.52	+	-0.35	0.52	0.52		-0.24	0.62	0.42		1.15	0.06	2.33	+
Mbnl2		0.76	0.02	1.73	+	1.40	0.12	1.37		0.36	0.34	1.11		-0.28	0.95	0.20	
Mboat7		-0.72	0.00	4.79	+	0.28	0.47	0.63		0.59	0.23	2.52		-0.46	0.23	1.43	
Mcm3ap		0.75	0.01	2.25	+	0.68	0.05	2.36	+	-0.34	0.41	0.85		-0.44	0.30	1.22	
Mcm6		-0.89	0.01	1.80	+	0.32	0.54	0.49		0.77	0.25	1.55		-0.45	0.46	0.88	
Mcmbp		-0.47	0.03	1.77	+	-0.21	0.31	1.19		0.14	0.63	0.45		-0.03	1.00	0.10	
Mdp1		1.03	0.00	3.74	+	-0.05	0.92	0.08		-0.51	0.26	1.74		0.58	0.18	1.54	
Meaf6		0.40	0.03	2.01	+	0.46	0.15	1.50		-0.11	0.57	0.70		-0.03	1.00	0.04	
Meak7		-0.54	0.01	3.73	+	-0.05	0.89	0.14		0.19	0.46	0.85		-0.27	0.35	1.67	
Med12		-0.91	0.01	1.88	+	-0.02	0.97	0.03		0.60	0.27	1.35		-0.39	0.49	0.87	
Med20		0.60	0.16	0.53		-1.22	0.08	1.71	+	-1.10	0.31	1.04		1.06	0.20	1.13	
Med24		-0.83	0.02	1.59	+	-0.83	0.10	1.64		-0.06	0.95	0.05		-0.05	0.99	0.12	
Meis1		0.51	0.04	1.30	+	-0.06	0.87	0.15		-0.17	0.63	0.44		0.39	0.46	0.93	
Metap2		-0.42	0.02	2.23	+	0.05	0.91	0.10		0.23	0.46	0.78		-0.23	0.68	0.76	
Mettl26		0.63	0.00	3.92	+	-0.16	0.67	0.38		-0.34	0.25	1.79		0.43	0.22	1.57	
Mettl5	+	1.45	0.01	1.62	+	1.10	0.50	0.48		-0.21	0.93	0.06		0.14	0.98	0.13	
Mfap3l		0.48	0.04	1.51	+	0.89	0.10	1.62		-0.44	0.32	1.16		-0.85	0.14	1.47	
Mfsd10		-0.98	0.02	1.40	+	0.23	0.62	0.42		0.81	0.27	1.24		-0.38	0.43	1.01	

Mfsd6		0.48	0.01	3.06	+	-0.09	0.67	0.49		0.00	0.99	0.01		0.44	0.22	1.53	
Micos10	+	-0.77	0.01	1.89	+	-0.30	0.54	0.51		0.13	0.71	0.32		-0.39	0.64	0.64	
Mid1ip1		0.79	0.01	1.99	+	0.25	0.49	0.61		-0.08	0.71	0.40		0.37	0.62	0.67	
Mif		1.46	0.00	5.00	+	0.02	0.98	0.02		-0.39	0.26	1.79		1.12	0.05	2.61	+
Mipep	+	0.02	0.86	0.07		-0.46	0.03	3.76	+	-0.12	0.60	0.59		0.37	0.12	2.66	
Mkrn3		-0.60	0.01	2.29	+	-0.18	0.61	0.46		0.26	0.29	1.71		-0.17	0.90	0.37	
Mobp		-1.15	0.00	4.57	+	0.32	0.60	0.42		0.69	0.26	1.39		-0.99	0.08	1.91	+
Mocs2		0.65	0.00	3.87	+	0.58	0.42	0.63		-0.10	0.46	1.62		0.08	0.99	0.06	
Morc2a		-0.41	0.03	1.95	+	-0.28	0.29	1.12		0.00	0.99	0.00		0.12	0.97	0.17	
Mpc1	+	-3.17	0.00	3.42	+	-1.42	0.04	2.29	+	0.55	0.51	0.54		-1.17	0.06	2.23	+
Mpc2	+	-1.32	0.00	4.97	+	-1.18	0.01	4.61	+	0.01	0.97	0.04		-0.18	0.82	0.58	
Mpv17l	+	-1.04	0.01	2.41	+	-0.21	0.79	0.21		0.58	0.36	0.89		-0.15	0.96	0.19	
Mrpl14	+	-0.75	0.00	4.83	+	-0.39	0.04	3.30	+	0.30	0.27	2.46		-0.07	0.95	0.57	
Mrpl20	+	-0.81	0.01	2.32	+	-0.43	0.04	3.10	+	0.37	0.33	1.15		0.07	0.96	0.27	
Mrpl21	+	-0.56	0.01	3.46	+	-0.26	0.31	1.07		0.22	0.46	0.81		-0.08	0.92	0.69	
Mrpl32	+	-0.49	0.04	1.39	+	-0.53	0.07	2.22	+	0.11	0.79	0.21		0.11	0.90	0.51	
Mrpl33	+	-0.58	0.01	3.30	+	-0.28	0.18	1.64		0.30	0.25	1.97		0.00	1.00	0.01	
Mrpl38	+	-0.40	0.05	1.36	+	-0.45	0.07	2.40	+	0.14	0.55	0.68		0.16	0.87	0.47	
Mrpl45	+	-0.16	0.10	2.49	+	-0.45	0.03	4.06	+	-0.10	0.55	0.92		0.19	0.36	2.79	
Mrpl50	+	0.39	0.06	1.30	+	-0.57	0.05	2.46	+	-0.23	0.39	1.07		0.75	0.06	2.70	+
Mrpl53	+	-0.20	0.18	0.79		-0.44	0.09	2.12	+	-0.01	0.98	0.03		0.22	0.68	0.80	
Mrpl54	+	-0.47	0.06	1.11		-0.51	0.09	2.06	+	0.15	0.64	0.43		0.10	0.97	0.18	
Mrps11		-0.67	0.01	2.81	+	0.19	0.44	0.83		0.41	0.27	2.01		-0.45	0.12	2.36	
Mrps24	+	0.52	0.01	3.37	+	0.33	0.19	1.50		-0.28	0.31	1.41		0.01	1.00	0.03	
Mrps33	+	-1.02	0.00	2.88	+	-0.57	0.08	2.09	+	0.41	0.36	0.95		0.01	1.00	0.04	
Mt2		1.32	0.00	2.54	+	0.15	0.88	0.11		-0.50	0.48	0.60		0.67	0.70	0.47	
Mt3		2.07	0.00	3.85	+	-0.07	0.95	0.05		-0.77	0.29	1.17		1.35	0.06	1.88	+
Mtatp8	+	1.91	0.00	4.05	+	0.04	0.96	0.04		-0.45	0.29	1.30		1.58	0.05	2.61	+
mt-Co3	+	0.79	0.00	3.78	+	0.43	0.22	1.20		-0.20	0.43	0.96		0.31	0.70	0.61	
Mtnd2	+	-1.06	0.01	2.34	+	0.21	0.75	0.25		0.59	0.26	1.55		-0.84	0.20	1.20	
Mtnd4	+	-1.09	0.00	4.73	+	0.32	0.57	0.45		0.68	0.26	1.84		-0.87	0.11	1.70	
Mtpn		0.86	0.00	4.56	+	0.20	0.48	0.70		-0.12	0.52	0.92		0.64	0.09	2.16	+
Mturn		0.58	0.20	0.44		0.38	0.49	0.56		0.83	0.49	0.56		1.03	0.07	1.92	+
Mug1		-0.37	0.19	0.54		0.44	0.11	1.89		-0.13	0.76	0.25		-1.20	0.06	2.06	+
Mul1	+	0.54	0.01	2.59	+	0.40	0.11	1.90		-0.14	0.58	0.60		0.03	0.99	0.10	
Myadm		-0.49	0.01	2.68	+	0.19	0.47	0.73		0.39	0.24	3.06		-0.39	0.32	1.27	
Mycbp		0.42	0.04	1.71	+	0.31	0.25	1.21		-0.19	0.44	0.94		0.10	0.97	0.17	
Mydgf		-0.44	0.01	4.91	+	0.08	0.80	0.24		0.31	0.26	2.03		-0.19	0.68	0.93	

Myl6		0.47	0.02	2.58	+	0.10	0.65	0.51		-0.27	0.26	2.40		0.13	0.89	0.51	
Myo9b		-0.48	0.03	1.86	+	-0.32	0.19	1.48		-0.03	0.87	0.21		-0.13	0.93	0.30	
Myof		-0.43	0.01	3.34	+	0.07	0.82	0.21		0.29	0.27	1.82		-0.21	0.66	0.91	
Naa16		0.56	0.01	3.71	+	-0.27	0.32	1.04		-0.30	0.26	1.78		0.53	0.09	2.41	+
Nacc1		-0.41	0.02	2.17	+	-0.12	0.64	0.51		0.10	0.66	0.47		-0.04	0.99	0.09	
Ndor1		0.18	0.58	0.15		0.00	1.00	NaN		0.00	1.00	NaN		1.06	0.07	1.83	+
Ndufa1	+	0.61	0.03	1.59	+	0.45	0.19	1.30		-0.17	0.53	0.67		0.08	0.98	0.12	
Ndufa11	+	-0.78	0.01	2.23	+	-0.23	0.41	0.82		-0.08	0.77	0.29		-0.74	0.10	1.91	+
Ndufa4	+	0.57	0.00	4.72	+	0.00	0.99	0.01		-0.16	0.31	2.25		0.44	0.17	1.90	
Ndufab1	+	0.62	0.01	3.02	+	0.02	0.96	0.05		-0.19	0.46	0.86		0.50	0.21	1.46	
Ndufb1	+	0.67	0.01	3.11	+	0.03	0.93	0.09		-0.13	0.47	1.07		0.56	0.11	2.10	
Ndufb2	+	1.41	0.00	3.13	+	-0.48	0.32	0.87		-0.47	0.26	1.65		1.65	0.04	2.44	+
Ndufb8	+	1.14	0.00	3.26	+	-0.02	0.97	0.03		-0.17	0.37	1.45		1.07	0.06	2.42	+
Ndufc2	+	0.60	0.00	4.54	+	-0.08	0.84	0.18		-0.23	0.30	1.77		0.44	0.21	1.60	
Ndufs6	+	0.79	0.01	3.05	+	-0.06	0.87	0.16		-0.20	0.25	3.14		0.74	0.08	2.11	+
Ndufv2	+	0.62	0.00	3.72	+	-0.14	0.76	0.26		-0.41	0.26	1.77		0.38	0.44	0.99	
Ndufv3	+	0.45	0.02	2.57	+	-0.18	0.60	0.50		-0.16	0.44	1.04		0.47	0.18	1.66	
Nell2		0.63	0.01	2.15	+	0.28	0.43	0.73		0.04	0.89	0.12		0.45	0.31	1.17	
Nenf		0.56	0.03	1.65	+	0.00	0.99	0.01		-0.37	0.26	1.80		0.23	0.76	0.62	
Nfu1	+	0.45	0.02	2.52	+	0.03	0.93	0.08		-0.29	0.26	2.22		0.16	0.87	0.45	
Nfyc		0.31	0.37	0.27		1.52	0.08	1.68	+	0.82	0.31	1.03		-0.39	0.83	0.38	
Nmnat2		0.75	0.01	3.19	+	0.39	0.21	1.27		-0.34	0.35	1.10		0.03	1.00	0.09	
Nmnat3	+	0.46	0.05	1.32	+	0.09	0.84	0.17		-0.10	0.82	0.18		0.10	0.97	0.16	
Nol3		0.49	0.01	2.53	+	-0.26	0.53	0.54		-0.13	0.53	0.80		0.56	0.21	1.37	
Nol6		0.59	0.02	1.79	+	0.29	0.30	1.06		-0.14	0.65	0.41		0.33	0.63	0.71	
Nol9		1.09	0.01	1.80	+	0.20	0.84	0.14		-0.63	0.48	0.58		0.32	0.81	0.45	
Nop14		-0.62	0.01	2.10	+	-0.45	0.21	1.19		0.22	0.63	0.41		0.13	0.88	0.53	
Nop58		-0.43	0.01	3.45	+	0.02	0.96	0.06		0.26	0.32	1.46		-0.16	0.84	0.56	
Nos3		0.06	0.67	0.16		0.47	0.09	2.07	+	0.27	0.36	1.10		-0.17	0.80	0.66	
Npc2		0.68	0.00	3.97	+	0.25	0.29	1.15		-0.21	0.36	1.33		0.20	0.69	0.88	
Nrip2		0.47	0.01	3.55	+	-0.24	0.55	0.52		-0.20	0.46	0.86		0.33	0.68	0.61	
Ntng1		0.41	0.03	1.89	+	0.13	0.74	0.29		-0.11	0.77	0.25		0.07	0.97	0.19	
Nubp1		-0.55	0.01	2.42	+	-0.33	0.32	0.96		0.13	0.66	0.41		-0.08	0.97	0.18	
Nutf2		0.80	0.00	3.59	+	-0.05	0.92	0.09		-0.20	0.40	1.12		0.63	0.12	1.79	
Olfml3		0.00	1.00	NaN		1.40	0.01	4.22	+	-0.24	0.55	0.53		-0.44	0.58	0.68	
Olig2		1.79	0.02	1.40	+	0.99	0.23	1.00		-0.08	0.88	0.12		0.73	0.86	0.30	
Oprm1		0.96	0.02	1.43	+	0.30	0.64	0.38		0.24	0.61	0.42		0.59	0.62	0.57	
Orc4		-0.65	0.02	1.65	+	0.36	0.35	0.87		0.18	0.64	0.40		-0.73	0.11	1.83	

Orm1		0.04	0.91	0.03		1.03	0.13	1.39		-0.22	0.66	0.35		-1.63	0.09	1.53	+
Oxld1	+	1.29	0.01	2.39	+	0.58	0.23	1.07		-0.42	0.46	0.65		0.29	0.73	0.57	
Pak1ip1		-0.99	0.00	3.46	+	0.10	0.87	0.13		0.74	0.26	1.53		-0.08	0.99	0.09	
Parl	+	0.81	0.00	4.89	+	0.83	0.02	5.27	+	0.02	0.93	0.09		0.02	1.00	0.12	
Pawr		-0.50	0.04	1.33	+	0.23	0.45	0.72		0.46	0.31	1.22		-0.31	0.37	1.35	
Pcbd1		0.47	0.02	2.02	+	0.08	0.86	0.15		0.00	0.99	0.00		0.18	0.93	0.27	
Pcdhb6		0.55	0.01	2.76	+	0.83	0.05	2.22	+	-0.09	0.82	0.18		-0.08	0.99	0.08	
Pcsk1		0.59	0.03	1.62	+	-0.01	0.98	0.03		0.14	0.57	0.61		0.49	0.53	0.73	
Pcsk1n		1.07	0.00	3.12	+	-0.24	0.69	0.31		-0.16	0.53	0.72		0.92	0.19	1.21	
Pcyt1b		0.70	0.02	1.74	+	0.65	0.18	1.24		-0.05	0.90	0.10		-0.14	0.97	0.14	
Pde6d		-0.50	0.02	2.29	+	-0.32	0.14	1.88		0.13	0.64	0.45		-0.06	0.95	0.49	
Pds5b		-0.41	0.04	1.54	+	0.21	0.50	0.64		0.20	0.52	0.65		-0.15	0.95	0.20	
Penk		0.72	0.02	1.77	+	0.09	0.79	0.25		-0.17	0.47	0.86		0.58	0.23	1.27	
Pet100	+	0.55	0.02	2.08	+	0.48	0.21	1.20		-0.06	0.90	0.10		0.05	0.99	0.13	
Pet117	+	-0.45	0.02	2.52	+	-0.12	0.53	0.78		0.15	0.53	0.71		-0.14	0.69	1.43	
Pfdn5		0.65	0.00	3.69	+	-0.02	0.96	0.04		-0.37	0.26	2.36		0.26	0.70	0.67	
Pfkfb4		0.78	0.02	1.76	+	0.36	0.29	1.02		-0.33	0.26	1.93		0.08	0.98	0.11	
Pfn3		-1.62	0.00	3.64	+	-0.37	0.72	0.27		0.69	0.46	0.61		-0.50	0.58	0.66	
Phb	+	-0.63	0.00	6.13	+	-0.61	0.01	4.81	+	-0.11	0.52	0.97		-0.14	0.65	1.97	
Phb2	+	-0.54	0.00	5.92	+	-0.58	0.03	7.59	+	-0.04	0.77	0.59		0.02	0.99	0.31	
Phf20l1		-0.55	0.02	2.15	+	-0.09	0.80	0.22		0.23	0.46	0.81		-0.37	0.47	0.94	
Phf8		0.66	0.02	1.94	+	0.53	0.09	1.96	+	-0.21	0.39	1.17		0.30	0.90	0.29	
Pid1		0.47	0.03	1.88	+	0.35	0.16	1.60		0.10	0.70	0.39		0.10	0.96	0.22	
Pigo		-1.07	0.00	3.07	+	-0.04	0.95	0.06		0.42	0.37	0.90		-0.49	0.24	1.34	
Pik3ip1		0.53	0.02	2.20	+	0.12	0.69	0.38		-0.05	0.86	0.16		0.63	0.25	1.15	
Pkd2		0.02	0.83	0.10		0.55	0.04	2.72	+	-0.05	0.84	0.19		-0.45	0.20	1.59	
Plekhf1		-0.58	0.01	3.53	+	-0.01	0.98	0.02		0.32	0.31	1.35		-0.30	0.25	2.00	
Plekhg3		-0.59	0.03	1.53	+	-0.48	0.33	0.83		0.16	0.79	0.19		-0.06	0.98	0.16	
Plekhh3		-0.42	0.03	1.95	+	-0.01	0.98	0.02		0.19	0.55	0.59		0.14	0.97	0.13	
Plg		-0.29	0.26	0.43		0.49	0.04	2.87	+	-0.02	0.97	0.04		-1.10	0.08	1.82	+
Plgrkt	+	-1.13	0.00	3.93	+	-0.83	0.01	4.86	+	0.24	0.41	0.97		-0.02	1.00	0.08	
Plin4		-1.20	0.00	3.78	+	0.12	0.86	0.13		0.65	0.31	1.11		-0.77	0.08	2.07	+
Plk1		0.81	0.00	3.48	+	0.28	0.52	0.54		-0.19	0.55	0.59		0.25	0.82	0.48	
Plxnc1		0.44	0.04	1.48	+	-0.09	0.79	0.25		-0.32	0.35	1.13		0.11	0.95	0.26	
Pmch		1.39	0.00	2.46	+	-0.66	0.29	0.88		-0.61	0.25	1.49		1.12	0.19	1.18	
Pmfbp1		-0.98	0.01	1.85	+	-0.31	0.29	1.07		0.53	0.33	1.03		-0.17	0.83	0.57	
Pnck		0.63	0.01	2.22	+	0.22	0.36	1.00		-0.18	0.56	0.57		0.03	1.00	0.04	
Pnisr		0.29	0.06	1.56	+	0.43	0.05	3.13	+	-0.20	0.37	1.25		0.09	0.99	0.08	
Pnp		-0.41	0.02	2.21	+	0.08	0.70	0.49		0.15	0.41	1.31		-0.44	0.18	1.82	

Pnpla7		0.50	0.02	2.06	+	-0.08	0.92	0.08		-0.24	0.53	0.59		0.35	0.69	0.59	
Pold1		-0.68	0.01	2.30	+	-0.12	0.84	0.16		0.57	0.32	1.07		-0.06	0.98	0.13	
Polr2d		-0.55	0.04	1.41	+	-0.02	0.98	0.02		0.07	0.91	0.09		-0.34	0.45	1.04	
Polr2g		-0.45	0.04	1.44	+	-0.04	0.93	0.08		0.16	0.72	0.28		-0.04	1.00	0.07	
Polr2i		1.16	0.02	1.40	+	-0.04	0.96	0.03		-0.50	0.34	1.01		0.70	0.75	0.42	
Pot1		0.08	0.54	0.26		0.81	0.06	2.08	+	0.26	0.40	0.99		-0.35	0.62	0.69	
Ppdpf		0.00	1.00	NaN		1.18	0.09	1.65	+	0.44	0.32	1.17		0.00	1.00	NaN	
Ppip5k2		0.43	0.03	1.91	+	0.15	0.68	0.36		0.05	0.88	0.14		0.15	0.94	0.26	
Ppp1r3f		0.40	0.01	5.12	+	-0.09	0.66	0.55		-0.12	0.48	1.14		0.32	0.17	2.55	
Ppp2cb		0.53	0.00	4.56	+	0.07	0.85	0.17		-0.05	0.77	0.35		0.38	0.28	1.43	
Ppp2r1b		-0.67	0.03	1.49	+	-0.21	0.63	0.42		0.02	0.97	0.03		-0.25	0.89	0.33	
Ppp3r1		0.42	0.03	2.12	+	-0.04	0.93	0.08		-0.24	0.39	1.06		0.30	0.57	0.86	
Ppwd1		0.19	0.24	0.57		0.59	0.03	4.22	+	-0.11	0.62	0.56		-0.31	0.68	0.64	
Prelp		-0.34	0.11	0.87		0.41	0.10	2.08	+	0.18	0.59	0.50		-0.60	0.06	2.70	+
Prkaa2		-0.43	0.05	1.34	+	-0.42	0.05	2.85	+	0.11	0.72	0.33		0.10	0.93	0.46	
Prkab1		-0.42	0.01	3.32	+	-0.17	0.28	1.61		0.15	0.44	1.16		-0.09	0.90	0.83	
Prkci		-1.03	0.01	2.05	+	0.57	0.42	0.64		0.56	0.36	0.88		-0.86	0.20	1.17	
Prkcz		-0.45	0.01	2.66	+	-0.21	0.52	0.60		-0.02	0.97	0.04		-0.22	0.58	1.10	
Prpf18		-0.43	0.03	1.96	+	-0.19	0.64	0.41		-0.02	0.97	0.03		0.08	0.99	0.08	
Prpf38b		-0.68	0.01	2.67	+	0.08	0.87	0.14		0.23	0.48	0.73		-0.15	0.97	0.14	
Prpf4b		-0.40	0.04	1.66	+	0.16	0.60	0.50		0.19	0.54	0.62		-0.21	0.84	0.45	
Prph		-0.32	0.14	0.75		0.14	0.85	0.15		-0.27	0.66	0.32		-0.77	0.07	2.23	+
Prr12		0.41	0.01	3.20	+	0.04	0.86	0.19		-0.38	0.20	3.00		0.14	0.92	0.35	
Psap		0.83	0.01	2.93	+	-0.08	0.84	0.17		-0.31	0.26	1.99		0.67	0.12	1.80	
Psmb8		0.04	0.79	0.10		0.45	0.08	2.17	+	0.33	0.30	1.42		-0.21	0.78	0.62	
Ptgis		0.55	0.03	1.46	+	0.51	0.17	1.34		-0.01	0.98	0.02		-0.23	0.92	0.28	
Ptpn6		-1.85	0.00	2.96	+	-0.16	0.68	0.36		2.03	0.07	3.33	+	0.44	0.24	1.41	
Ptrhd1		0.66	0.01	3.47	+	-0.14	0.76	0.26		-0.39	0.25	1.92		0.47	0.31	1.16	
Pts		-0.92	0.00	3.22	+	-0.11	0.83	0.18		0.31	0.49	0.64		-0.55	0.12	1.91	
Pvalb		0.53	0.02	1.83	+	0.10	0.74	0.32		-0.34	0.35	1.08		0.30	0.71	0.61	
Pwp1		1.27	0.01	1.95	+	0.53	0.57	0.42		-0.20	0.74	0.25		0.58	0.71	0.48	
Pwwp3a		0.42	0.03	1.75	+	0.15	0.72	0.31		-0.15	0.70	0.32		0.12	0.93	0.32	
Pzp		-0.19	0.46	0.23		0.53	0.03	3.33	+	-0.25	0.47	0.73		-1.26	0.06	1.96	+
Qpct		1.66	0.00	2.59	+	0.11	0.83	0.17		0.03	0.95	0.05		0.75	0.62	0.55	
Qpctl		-0.68	0.02	1.98	+	-0.32	0.56	0.48		-0.02	0.97	0.03		-0.44	0.44	0.91	
Qprt		-0.41	0.01	3.43	+	0.15	0.50	0.74		0.14	0.33	2.15		-0.42	0.13	2.29	
Rab27b		0.43	0.04	1.54	+	0.02	0.96	0.05		0.07	0.76	0.31		0.22	0.92	0.29	

Rab36		1.16	0.00	3.42	+	0.33	0.47	0.60		-0.01	0.95	0.07		1.05	0.11	1.59	
Rab3a		-0.40	0.01	5.54	+	0.08	0.73	0.39		0.17	0.35	1.62		-0.31	0.18	2.45	
Rabl6		-0.42	0.02	2.47	+	0.03	0.95	0.06		0.24	0.44	0.86		-0.18	0.76	0.74	
Ralgapa2		-0.84	0.01	2.98	+	-0.13	0.75	0.28		0.36	0.40	0.87		-0.13	0.95	0.21	
Ralgps1		0.63	0.00	4.16	+	0.50	0.12	1.67		-0.11	0.60	0.65		-0.09	0.97	0.17	
Ramac		0.92	0.00	2.90	+	0.57	0.08	2.06	+	-0.38	0.26	1.82		-0.04	1.00	0.07	
Rasgrp2		0.40	0.04	1.62	+	-0.08	0.76	0.30		0.10	0.65	0.48		0.30	0.82	0.43	
Rassf8		0.64	0.02	1.89	+	0.65	0.09	1.86	+	-0.05	0.91	0.09		-0.11	0.95	0.26	
Rbm28		0.56	0.00	4.50	+	0.35	0.10	2.20		-0.10	0.64	0.52		0.16	0.68	1.13	
Rbmx2		-0.43	0.02	2.29	+	0.28	0.64	0.37		0.10	0.84	0.16		-0.61	0.23	1.21	
Rc3h1		0.53	0.02	2.16	+	0.06	0.89	0.12		-0.39	0.26	1.64		0.07	0.98	0.15	
Rcor1		-0.80	0.00	3.15	+	0.21	0.66	0.37		0.34	0.36	1.00		-0.33	0.84	0.37	
Rdh10		-1.16	0.00	2.95	+	-0.49	0.48	0.54		0.09	0.89	0.10		-0.45	0.59	0.67	
Recql5		-0.74	0.00	3.74	+	0.41	0.38	0.76		0.24	0.56	0.52		-0.76	0.11	1.75	
Rexo4		-0.31	0.15	0.71		0.25	0.57	0.48		0.06	0.93	0.07		-0.61	0.09	2.14	+
Rfc3		0.33	0.03	2.63	+	0.54	0.04	2.67	+	-0.18	0.32	1.80		-0.18	0.92	0.32	
Rgs12		-0.13	0.37	0.42		-0.57	0.03	3.58	+	-0.17	0.55	0.61		0.36	0.22	1.79	
Rhbdd1		-0.41	0.01	4.06	+	-0.12	0.59	0.62		0.23	0.32	1.57		0.01	1.00	0.05	
Rnf11		0.88	0.00	4.24	+	0.00	0.99	0.01		-0.16	0.55	0.63		0.87	0.05	3.03	+
Rnf126		0.74	0.00	3.92	+	0.14	0.60	0.54		-0.18	0.41	1.13		0.35	0.32	1.39	
Rnf157		0.43	0.04	1.67	+	-0.28	0.44	0.69		-0.35	0.36	0.99		0.23	0.79	0.55	
Rnf181		0.93	0.00	4.98	+	0.43	0.27	1.02		-0.33	0.26	1.77		0.08	0.98	0.13	
Rnf7		0.66	0.03	1.43	+	-0.10	0.83	0.18		-0.22	0.50	0.68		0.55	0.53	0.70	
Rpl14		-0.59	0.01	2.54	+	0.32	0.45	0.65		0.41	0.32	1.16		-0.48	0.20	1.53	
Rpl22		-0.59	0.00	4.00	+	0.06	0.84	0.19		0.30	0.29	1.59		-0.34	0.21	1.98	
Rpl30		-0.47	0.01	3.85	+	0.17	0.67	0.37		0.34	0.34	1.14		-0.27	0.55	0.99	
Rpl34		-0.40	0.01	3.65	+	0.35	0.22	1.28		0.33	0.30	1.44		-0.42	0.12	2.58	
Rpl35a		-1.49	0.01	6.91	+	0.38	0.60	0.40		0.84	0.28	1.57		-1.01	0.07	1.94	+
Rpl36		-0.48	0.01	3.58	+	-0.23	0.24	1.49		0.13	0.51	0.91		-0.14	0.81	0.88	
Rpl36a		-1.05	0.00	5.09	+	0.15	0.77	0.23		0.44	0.27	1.48		-0.74	0.08	2.09	+
Rpl37		1.14	0.00	2.69	+	0.15	0.81	0.18		-0.63	0.27	1.86		0.12	0.98	0.11	
Rpl37a		-1.33	0.00	6.01	+	0.26	0.69	0.30		0.60	0.27	1.33		-0.99	0.06	2.13	+
Rplp1		0.57	0.01	2.73	+	0.05	0.84	0.21		-0.14	0.36	1.75		0.47	0.18	1.72	
Rplp2		0.52	0.02	1.96	+	-0.07	0.85	0.16		-0.26	0.27	1.87		0.37	0.46	0.96	
Rps11		-0.46	0.01	4.19	+	0.19	0.57	0.53		0.26	0.37	1.08		-0.37	0.18	2.03	
Rps23		-0.63	0.00	4.93	+	0.19	0.59	0.50		0.36	0.27	1.59		-0.42	0.18	1.87	
Rps3		-0.46	0.00	5.17	+	0.08	0.75	0.33		0.29	0.26	1.90		-0.25	0.32	2.02	
Rps6ka2		0.43	0.04	1.67	+	-0.06	0.89	0.13		-0.02	0.95	0.06		0.23	0.89	0.34	

Rragd		-0.75	0.00	3.49	+	-0.29	0.21	1.45		0.12	0.61	0.56		-0.20	0.82	0.53	
Rundc3b		0.49	0.04	1.50	+	-0.04	0.92	0.08		-0.20	0.52	0.65		0.20	0.89	0.37	
Rusc1		0.71	0.02	1.82	+	0.28	0.29	1.11		-0.20	0.51	0.68		0.20	0.83	0.49	
S100a1		0.59	0.02	1.95	+	-0.27	0.46	0.67		-0.09	0.74	0.31		0.86	0.07	2.17	+
S100a6		0.43	0.02	2.19	+	0.08	0.81	0.23		-0.23	0.45	0.82		0.14	0.82	0.75	
S100a9		0.39	0.42	0.22		1.07	0.09	1.68	+	-0.17	0.80	0.18		-1.26	0.25	0.95	
S100b		0.43	0.01	2.98	+	0.13	0.64	0.48		-0.21	0.37	1.22		0.21	0.78	0.61	
Samd4a		-0.74	0.02	1.87	+	-0.26	0.67	0.33		0.41	0.44	0.71		0.12	0.97	0.15	
Scaf1		-0.55	0.01	2.78	+	-0.21	0.42	0.84		0.10	0.73	0.33		-0.05	0.99	0.09	
Scamp4		-0.64	0.02	1.69	+	0.32	0.52	0.52		0.55	0.25	1.51		-0.31	0.77	0.51	
Scd1		0.71	0.03	1.33	+	-0.05	0.82	0.25		0.00	1.00	0.00		0.62	0.12	1.79	
Scg2		0.70	0.01	3.14	+	-0.21	0.63	0.42		-0.27	0.28	1.73		0.45	0.51	0.78	
Scg5		1.13	0.00	3.82	+	-0.41	0.46	0.59		-0.38	0.29	1.36		1.10	0.09	1.74	+
Scn3a		0.61	0.01	2.14	+	0.13	0.76	0.27		-0.13	0.67	0.39		0.23	0.85	0.43	
Sco2	+	-0.52	0.01	3.20	+	-0.48	0.03	3.73	+	0.01	0.98	0.03		-0.05	0.97	0.36	
Scrg1		0.68	0.01	2.71	+	-0.30	0.25	1.24		-0.25	0.36	1.19		0.69	0.06	2.72	+
Sdhaf2	+	0.59	0.01	2.72	+	-0.17	0.74	0.28		-0.52	0.21	2.61		0.37	0.63	0.65	
Sdhd	+	-0.64	0.01	2.66	+	-0.09	0.81	0.20		0.54	0.27	1.86		-0.07	0.97	0.19	
Sdk2		0.64	0.03	1.53	+	-0.06	0.89	0.12		0.09	0.64	0.60		0.54	0.48	0.78	
Sdsl	+	0.42	0.01	3.05	+	0.26	0.30	1.11		0.00	0.99	0.01		0.03	1.00	0.08	
Selenoi		1.08	0.01	1.89	+	0.33	0.19	1.49		0.02	0.96	0.04		0.59	0.29	1.08	
Sergef		0.41	0.04	1.72	+	0.09	0.71	0.41		-0.17	0.47	0.87		0.14	0.85	0.60	
Serinc1		-0.50	0.01	2.99	+	0.04	0.92	0.09		0.38	0.26	1.92		-0.18	0.75	0.79	
Serinc5		-1.02	0.00	4.25	+	0.20	0.70	0.32		0.71	0.23	2.09		-0.68	0.17	1.45	
Serpina1b		-0.46	0.11	0.74		0.53	0.07	2.21	+	-0.12	0.77	0.24		-1.43	0.06	2.21	+
Serpina1c		0.97	0.02	1.40	+	1.05	0.15	1.26		-0.30	0.59	0.43		-0.41	0.76	0.47	
Serpina1d		-0.27	0.28	0.40		0.53	0.04	2.76	+	-0.25	0.51	0.62		-1.36	0.06	2.19	+
Serpina1e		-1.08	0.05	0.97		1.41	0.10	1.53		0.36	0.72	0.25		-2.33	0.04	2.86	+
Serpina3k		-0.50	0.10	0.80		0.60	0.09	1.89	+	0.00	0.99	0.00		-1.44	0.06	2.13	+
Serpina3m		-0.26	0.24	0.50		0.67	0.08	1.95	+	-0.16	0.72	0.29		-1.48	0.05	2.03	+
Serpina6		-0.37	0.22	0.47		0.56	0.30	0.88		-0.38	0.43	0.78		-1.59	0.06	1.97	+
Serpinc1		-0.53	0.07	0.96		0.64	0.03	3.08	+	0.05	0.88	0.12		-1.39	0.05	2.32	+
Serpind1		0.38	0.21	0.49		0.89	0.08	1.85	+	-0.05	0.94	0.06		-0.87	0.24	1.05	
Serpinf2		-0.44	0.11	0.76		0.51	0.07	2.30	+	-0.07	0.86	0.15		-1.31	0.06	2.11	+
Sf3b5		0.47	0.02	2.48	+	0.17	0.50	0.69		-0.20	0.33	1.57		0.31	0.69	0.62	
Sft2d2		-0.45	0.01	3.92	+	0.03	0.94	0.07		0.19	0.51	0.70		-0.34	0.23	1.82	
Sgce		-0.50	0.02	2.06	+	0.33	0.37	0.82		0.36	0.39	0.89		-0.25	0.83	0.46	
Sgsm3		0.41	0.04	1.56	+	-0.16	0.50	0.72		-0.25	0.41	0.96		0.26	0.52	1.09	

Sh2b2		1.04	0.00	4.27	+	-0.25	0.61	0.43		-0.52	0.29	1.31		0.76	0.05	2.58	+
Sh2d5		0.58	0.03	1.55	+	0.15	0.75	0.27		0.15	0.64	0.42		0.52	0.30	1.12	
Sh3pxd2a		0.72	0.03	1.50	+	0.12	0.63	0.52		0.00	0.99	0.00		0.41	0.57	0.73	
Shc2		-0.73	0.01	1.92	+	-0.64	0.09	1.88	+	0.47	0.42	0.76		0.38	0.23	1.63	
Shisa4		-0.60	0.03	1.52	+	0.19	0.41	0.92		0.43	0.31	1.23		-0.57	0.20	1.39	
Shpk		0.41	0.05	1.32	+	-0.02	0.97	0.03		-0.31	0.39	0.95		0.05	1.00	0.07	
Shprh		-0.44	0.03	1.77	+	0.18	0.54	0.58		0.11	0.65	0.45		-0.27	0.83	0.43	
Slc13a3		-0.70	0.00	4.66	+	0.19	0.64	0.41		0.38	0.26	2.21		-0.54	0.17	1.64	
Slc17a5		-0.99	0.02	1.66	+	-0.34	0.40	0.74		0.78	0.27	1.27		0.06	0.98	0.14	
Slc25a14	+	0.05	0.70	0.17		0.46	0.09	2.13	+	0.35	0.31	1.32		-0.06	0.95	0.56	
Slc25a21	+	-0.74	0.00	3.19	+	-0.03	0.96	0.04		0.23	0.58	0.50		-0.41	0.24	1.48	
Slc25a29	+	0.36	0.02	2.68	+	0.53	0.03	4.01	+	0.00	0.99	0.01		-0.01	1.00	0.03	
Slc25a33	+	-0.58	0.03	1.46	+	-0.55	0.16	1.42		0.25	0.56	0.51		0.17	0.88	0.40	
Slc25a44	+	-0.69	0.00	3.96	+	0.27	0.56	0.49		0.35	0.33	1.17		-0.45	0.45	0.89	
Slc29a2		-0.44	0.01	2.77	+	-0.07	0.79	0.28		0.32	0.25	1.86		-0.02	1.00	0.06	
Slc2a4		0.11	0.46	0.29		0.22	0.35	1.03		0.67	0.10	3.52	+	0.76	0.10	1.83	+
Slc2a6		0.49	0.03	1.68	+	-0.08	0.77	0.29		-0.09	0.70	0.41		0.42	0.25	1.42	
Slc30a6		-0.55	0.03	1.56	+	-0.55	0.14	1.48		-0.10	0.74	0.29		-0.18	0.92	0.31	
Slc30a7		-0.87	0.01	2.79	+	0.34	0.58	0.44		0.37	0.33	1.16		-0.85	0.22	1.11	
Slc30a9	+	0.63	0.00	5.55	+	0.55	0.01	6.30	+	-0.01	0.92	0.19		0.04	0.97	0.39	
Slc35f3		-0.60	0.01	2.24	+	-0.28	0.46	0.65		0.10	0.82	0.17		-0.12	0.93	0.35	
Slc43a2		-0.38	0.01	4.23	+	-0.07	0.64	0.78		0.48	0.05	7.14	+	0.20	0.46	1.81	
Slc47a1		-0.97	0.01	1.76	+	0.56	0.04	2.71	+	0.44	0.41	0.81		-1.15	0.02	4.48	+
Slc4a1		-0.68	0.07	0.86		0.58	0.03	3.63	+	0.00	0.99	0.01		-1.51	0.05	2.27	+
Slc5a5		-1.21	0.01	1.91	+	-0.24	0.68	0.33		0.54	0.43	0.71		-0.47	0.36	1.04	
Slc5a6		-1.02	0.02	1.42	+	-0.07	0.94	0.06		1.22	0.35	0.85		0.16	0.94	0.24	
Slc5a7		0.81	0.02	1.75	+	-0.04	0.94	0.06		0.18	0.61	0.47		0.65	0.49	0.72	
Slc6a20a		-0.53	0.08	0.89		0.17	0.84	0.15		-0.37	0.71	0.26		-0.93	0.07	2.05	+
Slc6a4		0.90	0.01	1.87	+	0.33	0.72	0.26		-0.12	0.87	0.11		0.03	1.00	0.02	
Slc7a6os		0.74	0.00	3.85	+	0.43	0.11	1.89		-0.21	0.30	1.78		0.08	0.96	0.24	
Slit2		-0.87	0.01	2.34	+	0.68	0.24	1.00		0.74	0.24	2.07		-0.73	0.23	1.13	
Slitrk1		1.00	0.00	3.30	+	0.42	0.14	1.61		-0.30	0.36	1.10		0.40	0.35	1.17	
Smc6		0.67	0.01	2.12	+	1.32	0.04	2.42	+	-0.04	0.94	0.06		-0.68	0.27	1.05	
Smg5		0.66	0.02	1.76	+	0.64	0.16	1.30		-0.11	0.78	0.22		-0.11	0.97	0.17	
Smim12		0.80	0.01	3.08	+	0.37	0.24	1.19		-0.14	0.64	0.43		0.31	0.46	1.09	
Smim8	+	0.51	0.04	1.42	+	0.22	0.65	0.39		-0.02	0.97	0.02		0.28	0.37	1.50	
Smpx		1.34	0.00	3.39	+	0.52	0.53	0.47		-1.05	0.22	1.96		-0.23	0.95	0.18	
Snap29	+	-0.48	0.01	4.29	+	0.05	0.87	0.16		0.11	0.63	0.53		-0.40	0.12	2.52	

Snapin		0.40	0.02	2.35	+	0.07	0.78	0.30		-0.06	0.74	0.41		0.23	0.57	1.06	
Sncb		-0.47	0.05	1.32	+	-0.20	0.45	0.76		0.14	0.71	0.32		-0.15	0.83	0.66	
Snn		1.00	0.00	2.98	+	-0.41	0.14	1.62		-0.27	0.33	1.33		0.97	0.06	2.32	+
Snrnp27		-0.72	0.02	1.56	+	-0.09	0.84	0.17		0.06	0.90	0.10		-0.57	0.22	1.30	
Snrpc		1.00	0.00	4.08	+	-0.09	0.89	0.11		-0.44	0.34	1.03		0.92	0.13	1.46	
Snrpd1		-0.63	0.00	4.21	+	0.04	0.93	0.08		0.18	0.46	0.86		-0.32	0.68	0.63	
Snrpf		-0.64	0.01	2.64	+	0.17	0.64	0.42		0.29	0.39	0.95		-0.35	0.56	0.80	
Snx33		-0.39	0.08	1.03		-0.52	0.04	2.98	+	0.09	0.74	0.32		0.15	0.91	0.37	
Snx7		-0.42	0.02	2.13	+	-0.43	0.43	0.65		-0.05	0.92	0.08		-0.16	0.93	0.26	
Sod1	+	0.53	0.01	3.25	+	0.01	0.98	0.02		-0.06	0.66	0.71		0.44	0.21	1.58	
Sox10		0.86	0.01	2.35	+	0.78	0.15	1.32		-0.20	0.63	0.42		-0.22	0.92	0.29	
Sparc		0.49	0.01	3.64	+	-0.02	0.96	0.04		-0.21	0.37	1.17		0.28	0.54	0.97	
Spns2		0.40	0.05	1.42	+	0.00	1.00	NaN		-0.55	0.46	0.63		0.00	1.00	NaN	
Spock3		0.80	0.02	1.53	+	0.05	0.87	0.16		-0.44	0.33	1.06		0.15	0.92	0.33	
Spry4		-1.16	0.01	1.84	+	-0.06	0.86	0.16		0.75	0.26	1.57		-0.20	0.80	0.57	
Spta1		-0.61	0.08	0.86		0.43	0.03	3.96	+	-0.10	0.77	0.25		-1.35	0.05	2.32	+
Srek1		-0.82	0.01	2.76	+	-0.09	0.80	0.23		0.37	0.32	1.24		-0.24	0.72	0.65	
Sri		0.55	0.01	3.52	+	-0.26	0.47	0.65		-0.43	0.26	1.70		0.45	0.20	1.60	
Sspn		1.79	0.02	1.45	+	1.37	0.16	1.16		-0.27	0.39	1.00		0.44	0.96	0.15	
Stard7	+	0.73	0.01	2.52	+	0.46	0.16	1.46		-0.20	0.57	0.53		0.09	0.95	0.27	
Stom	+	-0.48	0.03	1.58	+	0.27	0.12	2.29		0.06	0.72	0.49		-0.77	0.05	2.63	+
Stx1b		-0.54	0.01	4.20	+	0.05	0.90	0.12		0.32	0.26	1.94		-0.22	0.66	0.86	
Stx2		-0.41	0.03	1.97	+	-0.04	0.88	0.16		0.24	0.36	1.21		-0.12	0.85	0.71	
Stx7		-0.57	0.00	4.20	+	-0.04	0.93	0.08		0.33	0.30	1.44		-0.20	0.68	0.88	
Stxbp2		0.50	0.03	1.81	+	0.24	0.55	0.52		-0.43	0.30	1.27		-0.19	0.83	0.53	
Stxbp4		-0.62	0.01	2.92	+	-0.11	0.70	0.37		0.40	0.26	1.83		-0.08	0.95	0.34	
Stxbp5l		-0.45	0.00	5.44	+	0.02	0.97	0.04		0.25	0.33	1.39		-0.15	0.85	0.58	
Sumo3		0.42	0.02	2.45	+	0.30	0.44	0.70		-0.12	0.77	0.24		0.13	0.93	0.32	
Surf1	+	-0.62	0.00	3.99	+	-0.54	0.03	3.74	+	0.10	0.66	0.48		0.01	1.00	0.08	
Syde1		0.27	0.27	0.42		0.44	0.04	3.05	+	0.16	0.64	0.41		-0.11	0.96	0.19	
Sypl1		0.42	0.04	1.61	+	0.00	0.99	0.01		-0.08	0.84	0.16		0.24	0.68	0.77	
Syt13		-1.08	0.01	2.28	+	0.10	0.76	0.28		1.02	0.24	2.38		-0.31	0.56	0.86	
Taf6		0.37	0.04	1.79	+	0.69	0.05	2.61	+	-0.21	0.33	1.49		-0.53	0.19	1.52	
Tbc1d2b		0.03	0.88	0.04		0.95	0.07	1.86	+	0.17	0.73	0.27		-0.22	0.96	0.14	
Tbp		-0.75	0.01	2.19	+	-0.41	0.42	0.67		0.32	0.32	1.28		-0.03	1.00	0.03	
Tcf4		-0.44	0.02	2.06	+	-0.12	0.69	0.38		-0.07	0.79	0.24		-0.44	0.15	2.00	
Tdp2		-0.43	0.05	1.35	+	0.00	1.00	NaN		-0.28	0.63	0.39		0.00	1.00	NaN	
Tf		-0.04	0.82	0.07		0.52	0.03	3.29	+	-0.12	0.66	0.41		-0.96	0.10	1.67	

Tgfb1i1		0.61	0.01	2.81	+	0.20	0.28	1.39		-0.12	0.60	0.58		0.17	0.84	0.55	
Thap11		-1.45	0.00	4.74	+	-0.57	0.22	1.11		0.45	0.27	1.47		-0.08	0.99	0.06	
Thbd		0.00	1.00	NaN		0.41	0.10	2.06	+	0.00	1.00	NaN		-0.41	0.11	2.74	
Thoc3		0.29	0.09	1.13		0.54	0.09	1.99	+	0.03	0.88	0.15		-0.21	0.82	0.53	
Thra		-0.63	0.01	2.71	+	-0.16	0.72	0.31		0.34	0.45	0.73		-0.11	0.93	0.40	
Thsd1		0.98	0.01	2.09	+	0.68	0.14	1.43		-0.34	0.55	0.50		0.13	0.95	0.22	
Timm10	+	1.10	0.00	3.88	+	-0.14	0.75	0.27		-0.21	0.41	1.04		1.09	0.04	2.79	+
Timm10b	+	1.62	0.00	3.77	+	0.01	0.99	0.01		-0.51	0.26	1.62		1.15	0.05	2.49	+
Timm13	+	0.97	0.00	3.88	+	-0.16	0.69	0.35		-0.38	0.22	2.82		0.83	0.07	2.18	+
Timm23	+	-0.53	0.00	4.58	+	-0.15	0.66	0.40		0.24	0.40	1.02		-0.12	0.90	0.46	
Timm8a1	+	0.98	0.00	3.14	+	-0.16	0.69	0.35		-0.33	0.26	2.03		1.00	0.07	1.97	+
Timm8b	+	1.26	0.00	3.32	+	-0.03	0.96	0.04		-0.42	0.25	1.66		0.96	0.07	2.08	+
Timm9	+	0.88	0.00	3.22	+	-0.13	0.76	0.25		-0.35	0.27	2.08		0.73	0.12	1.76	
Tle4		-0.70	0.14	0.58		-0.27	0.26	1.21		1.44	0.27	2.16		1.34	0.07	1.83	+
Tle5		-0.41	0.04	1.52	+	-0.51	0.33	0.83		0.25	0.50	0.65		0.51	0.37	0.99	
Tm9sf1		0.76	0.03	1.31	+	0.68	0.09	1.85	+	-0.14	0.62	0.48		-0.17	0.95	0.20	
Tmbim6		0.30	0.22	0.50		0.92	0.04	2.63	+	0.52	0.26	1.72		-0.03	1.00	0.03	
Tmeff2		1.52	0.00	3.00	+	-0.12	0.84	0.17		-0.09	0.75	0.30		1.27	0.09	1.67	+
Tmem117		1.07	0.00	3.28	+	0.68	0.29	0.87		-0.37	0.52	0.54		0.00	1.00	0.00	
Tmem120a		0.50	0.03	1.77	+	-0.04	0.87	0.18		-0.21	0.27	2.21		0.33	0.42	1.16	
Tmem126b	+	-0.89	0.01	2.72	+	-0.14	0.39	1.22		0.89	0.13	3.27		0.21	0.58	1.14	
Tmem141		1.16	0.00	3.10	+	0.75	0.04	2.77	+	-0.07	0.76	0.31		0.34	0.68	0.61	
Tmem14c	+	0.55	0.11	0.72		0.97	0.03	2.83	+	0.07	0.92	0.08		-0.95	0.44	0.71	
Tmem175		0.36	0.03	2.39	+	0.52	0.03	3.33	+	-0.04	0.86	0.18		-0.18	0.65	1.14	
Tmem186	+	-1.12	0.00	4.92	+	-0.06	0.92	0.08		0.44	0.30	1.23		-0.61	0.12	1.84	
Tmem223		-0.99	0.00	3.21	+	-0.56	0.03	4.07	+	0.24	0.45	0.81		-0.08	0.95	0.29	
Tmem263		-0.66	0.00	5.26	+	0.24	0.45	0.71		0.36	0.27	2.22		-0.46	0.20	1.62	
Tmem35a		-0.68	0.00	5.46	+	0.00	0.99	0.01		0.29	0.30	1.49		-0.33	0.48	0.98	
Tmem38a		-0.65	0.01	2.60	+	0.06	0.92	0.09		-0.06	0.86	0.15		-0.61	0.22	1.25	
Tmem51		-1.08	0.00	3.18	+	0.26	0.76	0.23		0.63	0.33	1.03		-0.68	0.28	1.04	
Tmem68		0.24	0.25	0.48		0.47	0.06	2.55	+	0.13	0.61	0.53		-0.03	1.00	0.05	
Tmub1		0.46	0.01	3.06	+	-0.12	0.68	0.40		-0.16	0.52	0.72		0.63	0.16	1.59	
Tmub2		-0.30	0.47	0.20		1.34	0.09	1.58	+	1.01	0.31	1.02		-0.64	0.67	0.52	
Tomm22	+	0.62	0.01	2.46	+	0.12	0.76	0.27		-0.02	0.92	0.11		0.56	0.20	1.41	
Tomm40l	+	-0.50	0.01	2.48	+	0.17	0.60	0.49		0.39	0.27	1.50		-0.21	0.72	0.76	
Top1		-0.53	0.02	2.16	+	0.14	0.74	0.29		0.22	0.52	0.64		-0.23	0.87	0.37	
Tpbgl		0.86	0.02	1.73	+	0.61	0.45	0.59		-0.16	0.73	0.28		0.10	1.00	0.05	
Tph2		0.80	0.03	1.32	+	-0.11	0.88	0.11		0.30	0.56	0.48		0.87	0.31	0.91	

Trak1		0.71	0.00	4.39	+	0.56	0.10	1.84	+	-0.10	0.73	0.32		0.10	0.95	0.29	
Triap1	+	1.83	0.00	3.05	+	-0.14	0.80	0.20		-0.42	0.26	1.67		1.55	0.06	2.05	+
Trim65		-0.10	0.55	0.21		-0.49	0.06	2.55	+	-0.04	0.89	0.12		0.35	0.42	1.11	
Trmt112		0.45	0.02	2.64	+	-0.08	0.79	0.27		-0.21	0.29	2.02		0.35	0.28	1.49	
Tsc22d1		0.48	0.01	3.49	+	-0.08	0.76	0.32		-0.26	0.25	2.39		0.29	0.35	1.58	
Tsen15		0.79	0.01	2.43	+	0.46	0.33	0.84		-0.27	0.47	0.72		0.06	0.99	0.07	
Tspan33		-0.62	0.01	2.66	+	-0.09	0.87	0.13		-0.02	0.98	0.02		-0.36	0.52	0.85	
Ttr		-0.94	0.02	1.56	+	0.49	0.29	0.93		-0.28	0.57	0.49		-1.87	0.03	3.15	+
Tubal3		0.78	0.00	3.62	+	0.16	0.65	0.41		-0.14	0.64	0.45		0.46	0.17	1.78	
Tubb2a		0.56	0.03	1.49	+	0.00	1.00	0.00		-0.07	0.83	0.19		0.42	0.40	1.03	
Tubb4b		1.57	0.00	2.42	+	-0.89	0.40	0.63		-1.04	0.27	1.23		1.38	0.14	1.31	
Tubgcp5		0.50	0.04	1.51	+	0.08	0.89	0.11		-0.13	0.81	0.17		0.58	0.34	0.99	
Txn		0.60	0.00	4.31	+	0.02	0.97	0.04		-0.25	0.27	2.02		0.39	0.27	1.42	
Txndc17		1.11	0.00	4.31	+	0.03	0.96	0.04		-0.41	0.20	2.81		0.67	0.18	1.43	
Ube2a		0.47	0.01	3.30	+	0.07	0.83	0.19		-0.31	0.22	3.54		0.11	0.95	0.28	
Ube2e3		-0.53	0.03	1.71	+	-0.51	0.22	1.13		0.05	0.84	0.18		0.18	0.94	0.24	
Uchl1		0.76	0.00	3.65	+	-0.31	0.53	0.51		-0.42	0.29	1.38		0.53	0.36	0.99	
Uimc1		-1.19	0.00	2.94	+	-0.34	0.49	0.56		0.16	0.72	0.28		-0.69	0.16	1.48	
Ulk2		-0.16	0.45	0.26		-0.45	0.08	2.25	+	0.25	0.54	0.56		0.55	0.09	2.44	+
UPF0415		0.08	0.61	0.19		-0.51	0.07	2.21	+	-0.20	0.44	0.92		0.46	0.22	1.48	
Uqcc1	+	0.31	0.03	2.59	+	0.46	0.03	5.02	+	0.09	0.64	0.59		-0.05	0.95	0.98	
Uqcr10	+	-0.74	0.00	4.16	+	0.04	0.95	0.05		0.34	0.30	1.35		-0.46	0.26	1.29	
Uqcrh	+	1.60	0.00	4.56	+	-0.26	0.70	0.30		-0.54	0.26	1.60		1.39	0.05	2.40	+
Urm1		0.55	0.02	2.13	+	0.19	0.60	0.47		0.05	0.81	0.26		0.49	0.28	1.21	
Utp20		0.41	0.02	2.20	+	0.22	0.30	1.22		-0.06	0.84	0.18		0.20	0.56	1.35	
Vamp1		-0.65	0.00	3.64	+	0.04	0.96	0.05		0.36	0.41	0.83		-0.41	0.27	1.40	
Vamp2		-0.89	0.00	3.06	+	0.00	1.00	0.00		0.50	0.34	1.01		-0.40	0.51	0.82	
Vamp3		-1.15	0.00	3.90	+	0.23	0.77	0.22		0.55	0.41	0.76		-0.87	0.09	1.88	+
Vangl2		0.19	0.16	1.00		0.46	0.05	2.72	+	0.07	0.78	0.27		-0.17	0.68	1.06	
Vdac3	+	-0.50	0.01	3.31	+	0.14	0.70	0.34		0.37	0.29	1.45		-0.27	0.47	1.18	
Vtn		-0.32	0.16	0.67		0.41	0.11	1.95		-0.15	0.60	0.51		-1.18	0.06	1.98	+
Vwf		-0.24	0.11	1.21		0.60	0.09	1.91	+	0.17	0.52	0.70		-0.87	0.08	1.98	+
Wapl		0.24	0.15	0.88		0.41	0.05	2.80	+	-0.05	0.83	0.20		0.03	1.00	0.04	
Wbp4		0.69	0.03	1.55	+	0.74	0.07	1.99	+	-0.33	0.40	0.88		-0.38	0.61	0.68	
Wdr41		-0.48	0.01	2.73	+	-0.10	0.70	0.39		0.29	0.31	1.40		-0.13	0.85	0.68	
Wdr74		-1.29	0.02	1.55	+	0.77	0.77	0.20		1.21	0.44	0.63		-0.80	0.77	0.39	
Wdr92		-0.82	0.01	2.73	+	-0.16	0.49	0.75		0.52	0.27	1.86		-0.13	0.83	0.78	
Wdtc1		-0.70	0.01	1.99	+	-0.24	0.44	0.76		0.53	0.27	1.63		0.17	0.87	0.44	

Wipi2		-0.42	0.02	2.31	+	0.08	0.84	0.18		0.28	0.33	1.31		-0.21	0.74	0.70	
Xaf1		0.00	1.00	NaN		-0.99	0.09	1.68	+	0.00	1.00	NaN		0.62	0.59	0.60	
Xkr6		0.75	0.01	3.00	+	0.18	0.30	1.42		-0.12	0.50	0.96		0.49	0.12	2.25	
Xpr1		0.55	0.02	1.84	+	0.31	0.25	1.20		-0.04	0.89	0.14		0.17	0.88	0.42	
Zc3h13		0.03	0.83	0.07		-0.65	0.06	2.18	+	-0.53	0.27	1.97		0.25	0.69	0.69	
Zfand1		0.93	0.01	2.18	+	0.37	0.45	0.63		-0.06	0.87	0.13		0.49	0.55	0.70	
Zfand2b		0.40	0.02	2.29	+	-0.20	0.29	1.29		-0.26	0.28	2.53		0.26	0.52	1.07	
Zgpat		0.46	0.02	2.10	+	0.65	0.16	1.30		-0.14	0.46	1.04		-0.21	0.92	0.29	
Zhx1		0.44	0.01	2.85	+	0.04	0.91	0.10		-0.36	0.29	1.40		0.17	0.84	0.53	
Zmiz1		-0.72	0.02	1.77	+	-0.17	0.50	0.68		0.55	0.26	1.69		0.14	0.93	0.31	
Znf280c		-0.80	0.02	1.68	+	-0.61	0.28	0.92		-0.06	0.95	0.05		0.12	0.98	0.12	
Znf330		0.69	0.03	1.34	+	-0.33	0.56	0.46		-0.17	0.72	0.29		0.85	0.20	1.21	
Znf385b		-0.40	0.04	1.54	+	0.21	0.63	0.41		0.00	0.99	0.00		-0.12	0.99	0.08	
Znf428		0.82	0.01	2.42	+	0.27	0.33	1.01		-0.12	0.56	0.74		0.63	0.22	1.23	
Znf740		-0.58	0.02	1.87	+	0.25	0.50	0.60		0.14	0.66	0.39		-0.68	0.12	1.80	
Znf787		-0.42	0.02	2.17	+	0.35	0.40	0.74		0.15	0.59	0.55		-0.03	1.00	0.01	
Znrd2		0.65	0.01	2.40	+	-0.02	0.98	0.02		-0.21	0.58	0.51		0.45	0.35	1.10	
Znrf2		0.58	0.01	2.69	+	-0.09	0.84	0.18		-0.32	0.37	0.99		0.46	0.22	1.51	

Table S4. List of proteins found significatively altered in 28 weeks spinal cord proteomics. The comparisons among the different genotypes are highlighted by colors.
q value < 0.1, p value < 0.05, no FC cut-off applied. Table alphabetically sorted by gene name. Sig: significant

		DKO/WT				TKO/Sarm1KO				TKO/DKO				Sarm1KO/WT			
Gene name	**MitoCarta**	**Log2FC**	**q value**	**-log p value**	**Sig**	**Log2FC**	**q value**	**-log p value**	**Sig**	**Log2FC**	**q value**	**-log p value**	**Sig**	**Log2FC**	**q value**	**-log p value**	**Sig**
Actg2		0.11	0.96	0.05		-1.43	0.03	3.66	+	-0.81	0.50	0.77		0.72	0.52	0.75	
Afg3l2	+	-0.69	0.04	7.63	+	-0.67	0.02	7.22	+	-0.03	0.90	0.56		-0.05	0.90	0.61	
Alyref		0.09	0.89	0.52		0.11	0.96	0.62		-0.59	0.05	4.45	+	-0.61	0.09	3.34	+
Anxa2		0.68	0.10	3.22	+	0.04	0.99	0.09		-0.17	0.72	0.53		0.47	0.30	1.63	
Atox1		0.14	0.87	0.40		0.10	0.97	0.46		-0.64	0.13	2.54		-0.60	0.09	3.39	+
Aven		-0.02	0.97	0.04		0.01	0.99	0.03		-0.65	0.09	3.04	+	-0.68	0.17	2.07	
Ccdc124		0.06	0.93	0.29		0.07	0.98	0.41		-0.53	0.09	3.42	+	-0.54	0.11	4.11	
Ccdc51	+	-0.47	0.10	4.48	+	-0.48	0.05	5.97	+	-0.01	0.96	0.10		0.00	0.99	0.03	
Chchd2	+	-0.78	0.06	3.97	+	-0.67	0.11	3.05		-0.16	0.70	0.70		-0.26	0.55	1.14	
Chmp5		0.11	0.90	0.28		0.07	0.98	0.29		-0.54	0.09	3.50	+	-0.50	0.28	1.67	
Chp1		0.06	0.94	0.17		-0.03	0.99	0.21		-0.52	0.07	4.14	+	-0.42	0.32	1.70	
Ckm		-0.50	0.76	0.51		-1.05	0.38	1.47		-1.21	0.06	2.44	+	-0.67	0.62	0.57	
Clta		0.10	0.92	0.20		0.02	1.00	0.07		-0.91	0.04	4.03	+	-0.83	0.11	2.44	
Col11a1		0.00	1.00	NaN		-0.75	0.82	0.80		-1.20	0.09	2.20	+	0.00	1.00	NaN	
Col1a1		3.01	0.07	2.20	+	-0.78	0.83	0.81		-0.87	0.32	1.19		2.92	0.10	1.97	+
Col1a2		3.02	0.06	2.32	+	-0.98	0.66	1.01		-0.96	0.30	1.22		3.03	0.12	2.15	
Col2a1		1.03	0.66	0.61		-0.31	0.95	0.40		0.24	0.87	0.13		1.58	0.05	3.56	+
Cox18	+	0.60	0.19	2.27		0.82	0.09	2.93	+	-0.02	0.96	0.06		-0.23	0.75	0.53	
Crls1	+	-1.17	0.06	3.44	+	-0.67	0.07	3.82	+	0.40	0.44	1.29		-0.10	0.83	0.55	
Crym		-0.54	0.58	0.85		0.43	0.74	1.27		-0.18	0.77	0.32		-1.15	0.10	2.32	+
Csdc2		0.04	0.95	0.10		0.12	0.95	0.95		-0.44	0.29	1.88		-0.52	0.10	3.70	+
Dusp14		-0.04	0.95	0.14		0.08	0.98	0.18		0.57	0.07	3.74	+	0.46	0.38	1.31	
Edf1		-0.02	0.96	0.13		0.13	0.95	0.86		-0.31	0.37	2.01		-0.46	0.10	4.83	+
Ermn		-0.02	0.97	0.06		0.06	0.98	0.32		-0.45	0.07	4.99	+	-0.52	0.17	2.38	
Ewsr1		0.16	0.79	0.79		0.15	0.97	0.47		-0.71	0.05	4.20	+	-0.69	0.14	2.37	
Fam162a	+	-0.46	0.10	4.52	+	-0.38	0.10	5.47	+	0.06	0.81	0.80		-0.02	0.97	0.16	
Fhl3		0.77	0.51	0.89		-0.64	0.88	0.68		-1.25	0.05	2.66	+	0.15	0.95	0.09	
Fubp1		0.10	0.90	0.31		0.17	0.94	1.17		-0.62	0.05	4.82	+	-0.70	0.10	2.79	+
Fus		0.12	0.82	0.93		0.13	0.95	0.93		-0.53	0.04	4.79	+	-0.53	0.10	3.49	
Ghitm	+	-1.05	0.05	4.66	+	-0.93	0.01	8.29	+	0.17	0.65	0.98		0.05	0.88	0.72	
Glod4	+	0.03	0.94	0.46		0.04	0.98	0.47		0.51	0.04	7.11	+	0.50	0.12	5.11	
Gm11992		0.00	1.00	NaN		0.17	0.98	0.16		1.34	0.04	2.88	+	0.00	1.00	NaN	

Hdgfl3		0.15	0.86	0.43		0.04	0.99	0.26		-0.63	0.05	4.64	+	-0.53	0.23	1.96	
Hebp1	+	0.05	0.94	0.16		-0.08	0.99	0.08		-1.01	0.09	2.37	+	-0.88	0.17	1.78	
Hspb8		0.10	0.93	0.17		0.10	0.97	0.36		-0.70	0.04	3.75	+	-0.70	0.24	1.65	
Hspe1	+	0.10	0.92	0.19		0.11	0.98	0.39		-1.00	0.07	4.20	+	-1.00	0.10	2.71	+
Itga6		0.72	0.10	3.28	+	-0.02	0.99	0.03		-0.24	0.71	0.48		0.50	0.36	1.34	
Itgb4		1.40	0.08	2.48	+	-0.04	0.99	0.03		-0.55	0.59	0.65		0.89	0.33	1.16	
Lama4		0.81	0.10	2.76	+	-0.03	1.00	0.04		-0.41	0.47	1.06		0.43	0.54	0.83	
Lamtor5		-0.17	0.88	0.32		0.03	0.99	0.03		-1.06	0.17	1.71		-1.26	0.10	2.33	+
Mpc1	+	-1.36	0.19	1.65		-0.99	0.03	3.70	+	0.71	0.34	1.23		0.34	0.75	0.46	
Mpc2	+	-1.28	0.04	6.03	+	-1.09	0.02	4.68	+	0.14	0.71	0.74		-0.04	0.95	0.14	
Mpz		5.38	0.08	2.04	+	0.12	0.99	0.03		-1.35	0.60	0.51		3.90	0.26	1.07	
Mrpl34	+	-0.87	0.09	2.92	+	-0.31	0.89	0.97		0.41	0.30	1.81		-0.15	0.85	0.31	
Mrpl35	+	-1.40	0.06	2.92	+	-0.08	0.99	0.14		1.00	0.05	3.26	+	-0.32	0.74	0.49	
Mrps36	+	-0.17	0.78	0.89		-0.07	0.97	0.37		-0.52	0.09	3.46	+	-0.62	0.10	3.36	+
Ndufs6	+	0.02	0.97	0.08		-0.02	1.00	0.12		-0.66	0.05	4.64	+	-0.62	0.10	3.13	+
Nid1		0.87	0.10	2.69	+	-0.07	0.99	0.08		-0.40	0.60	0.69		0.55	0.44	1.01	
Nle1		0.00	1.00	NaN		-0.06	0.99	0.10		1.45	0.05	2.87	+	0.00	1.00	NaN	
Ovca2		0.02	0.97	0.08		0.08	0.98	0.38		0.78	0.05	4.07	+	0.72	0.12	4.11	
Parl	+	0.96	0.06	3.09	+	0.78	0.01	7.63	+	0.04	0.92	0.16		0.22	0.67	0.78	
Pdlim7		0.00	0.99	0.00		-1.30	0.09	2.46	+	-0.81	0.45	0.91		0.49	0.67	0.52	
Phb	+	-0.71	0.04	6.00	+	-0.70	0.02	6.28	+	-0.06	0.82	0.60		-0.07	0.85	0.86	
Phb2	+	-0.78	0.05	9.39	+	-0.79	0.01	8.84	+	-0.04	0.85	1.12		-0.04	0.92	0.74	
Pigz		-0.30	0.66	0.91		0.69	0.42	1.60		1.15	0.07	2.50	+	0.16	0.83	0.40	
Plgrkt	+	-0.55	0.21	2.28		-0.86	0.07	3.16	+	-0.21	0.67	0.65		0.09	0.88	0.29	
Pqbp1		0.08	0.91	0.35		0.02	1.00	0.10		-0.49	0.09	3.91	+	-0.43	0.21	2.46	
Ptges2	+	-0.58	0.06	5.00	+	-0.56	0.03	6.16	+	0.02	0.94	0.21		-0.01	0.98	0.06	
Rcsd1		0.17	0.79	0.81		-0.10	0.98	0.16		-0.85	0.07	2.82	+	-0.59	0.30	1.44	
Rps21		0.15	0.88	0.33		0.11	0.96	0.69		-0.85	0.06	4.54	+	-0.80	0.11	2.44	
Rps28		0.11	0.90	0.31		0.12	0.95	0.82		-0.59	0.05	4.39	+	-0.60	0.17	2.14	
Sgce		1.03	0.10	2.61	+	-0.08	0.99	0.08		-0.33	0.66	0.55		0.78	0.25	1.55	
Shfl		-0.11	0.87	0.55		0.10	0.97	0.47		-0.51	0.09	3.55	+	-0.72	0.11	3.51	
Slc25a33	+	-1.57	0.06	2.55	+	-1.14	0.03	3.67	+	0.60	0.46	0.92		0.17	0.74	0.76	
Slc30a9	+	0.51	0.06	6.13	+	0.46	0.05	6.59	+	-0.04	0.86	0.87		0.02	0.97	0.19	
Slit1		0.60	0.21	2.16		0.78	0.09	2.91	+	0.28	0.50	1.30		0.10	0.90	0.22	
Srsf2		0.18	0.78	0.78		0.11	0.95	1.17		-0.69	0.05	5.15	+	-0.61	0.10	3.08	
Srsf3		0.10	0.89	0.40		0.32	0.76	1.62		-0.55	0.07	3.71	+	-0.77	0.10	2.98	+
Srsf7		0.03	0.95	0.13		0.23	0.90	1.03		-0.44	0.22	2.38		-0.64	0.10	3.32	+
Surf1	+	-0.69	0.05	4.71	+	-0.60	0.03	6.27	+	0.11	0.71	1.01		0.03	0.95	0.27	

Syt10		0.54	0.31	1.68		1.02	0.03	4.10	+	0.98	0.14	4.25		0.51	0.33	1.47	
Szrd1		0.17	0.85	0.47		0.05	0.98	0.32		-0.53	0.09	3.51	+	-0.41	0.36	1.53	
Tcp11l2		2.37	0.51	0.75		-2.44	0.09	2.19	+	-2.17	0.30	1.06		2.64	0.30	1.02	
Timm10	+	-0.15	0.85	0.52		0.16	0.93	1.44		-0.32	0.35	2.01		-0.62	0.09	3.25	+
Timm50	+	-0.50	0.06	5.84	+	-0.44	0.09	4.99	+	0.06	0.81	0.88		0.00	0.99	0.03	
Tnks1bp1		0.10	0.87	0.59		-0.01	1.00	0.11		-0.47	0.05	5.71	+	-0.35	0.26	2.37	
Tssc4		0.54	0.58	0.85		0.35	0.94	0.41		-0.98	0.07	2.58	+	-0.79	0.56	0.65	
Uqcc1	+	0.35	0.20	3.69		0.46	0.08	5.18	+	0.11	0.67	1.97		0.01	0.99	0.04	
Uqcrb		0.03	0.97	0.06		0.10	0.98	0.29		-1.03	0.04	3.64	+	-1.09	0.11	3.02	
Vwa1		0.54	0.05	5.42	+	0.00	0.99	0.01		-0.26	0.63	0.78		0.28	0.64	0.72	
Washc2		0.09	0.90	0.38		0.07	0.98	0.44		-0.54	0.05	4.43	+	-0.52	0.14	2.74	
Wipf2		-0.09	0.92	0.23		0.10	0.97	0.35		-0.81	0.05	3.76	+	-1.00	0.13	3.48	
Wipf3		-0.02	0.98	0.04		-0.21	0.97	0.22		-1.28	0.05	2.63	+	-1.08	0.11	2.86	
Zfand2b		-0.04	0.96	0.08		0.16	0.97	0.36		-0.66	0.04	4.21	+	-0.86	0.17	1.83	
Zyx		0.18	0.81	0.59		0.03	1.00	0.10		-0.76	0.05	3.77	+	-0.60	0.13	2.68	

Table S5.1. Pathway analysis of the DKO/WT comparison performed with GSEA from the cerebellum proteomics at 28 weeks. NES: Normalization Enrichment Score. Pathways highlighted in green appear in graphs from Fig. 26. Table sorted by NES.

Pathway name	Size	NES	FDR q value
GOBP_OXIDATIVE_PHOSPHORYLATION	106	2.16	0.01
GOBP_PROTEIN_LOCALIZATION_TO_MITOCHONDRIAL_MEMBRANE	23	2.06	0.02
GOBP_SUPEROXIDE_METABOLIC_PROCESS	26	2.05	0.01
GOBP_RESPIRATORY_ELECTRON_TRANSPORT_CHAIN	91	2.02	0.02
GOBP_CELLULAR_RESPIRATION	165	1.96	0.04
GOBP_RESPONSE_TO_OXYGEN_RADICAL	17	1.95	0.04
GOBP_ENERGY_DERIVATION_BY_OXIDATION_OF_ORGANIC_COMPOUNDS	208	1.94	0.04
GOBP_MITOCHONDRIAL_ELECTRON_TRANSPORT_NADH_TO_UBIQUINONE	42	1.91	0.05
GOBP_NEUROPEPTIDE_SIGNALING_PATHWAY	20	1.88	0.06
GOBP_PROTEIN_INSERTION_INTO_MEMBRANE	43	1.87	0.06
GOBP_SENSORY_PERCEPTION_OF_PAIN	37	1.86	0.07
GOBP_INTRINSIC_APOPTOTIC_SIGNALING_PATHWAY	25	1.83	0.09
GOBP_TRANSLATIONAL_ELONGATION	37	1.82	0.09
GOBP_NUCLEOSIDE_TRIPHOSPHATE_BIOSYNTHETIC_PROCESS	49	1.81	0.10
GOBP_RESPONSE_TO_COPPER_ION	21	1.81	0.10
GOBP_RESPONSE_TO_AMINE	21	1.79	0.11
GOBP_RIBONUCLEOSIDE_TRIPHOSPHATE_BIOSYNTHETIC_PROCESS	42	1.78	0.11
GOBP_CELLULAR_RESPONSE_TO_TOXIC_SUBSTANCE	62	1.76	0.13
GOBP_GENERATION_OF_PRECURSOR_METABOLITES_AND_ENERGY	310	1.75	0.14
GOBP_PROTON_TRANSMEMBRANE_TRANSPORT	86	1.75	0.14
GOBP_DETOXIFICATION	66	1.73	0.16
GOBP_IRON_SULFUR_CLUSTER_ASSEMBLY	23	1.72	0.17
GOBP_REGULATION_OF_RYANODINE_SENSITIVE_CALCIUM_RELEASE	15	1.71	0.18
GOBP_HUMORAL_IMMUNE_RESPONSE	50	-1.82	0.191
GOBP_CARTILAGE_DEVELOPMENT	40	-1.83	0.187
GOBP_IMMUNOGLOBULIN_PRODUCTION	16	-1.85	0.193
GOBP_NUCLEOSOME_ASSEMBLY	28	-1.85	0.178
GOBP_CYTOPLASMIC_TRANSLATION	116	-2	0.095
GOBP_COMPLEMENT_ACTIVATION	26	-2.05	0.075
GOBP_NEGATIVE_REGULATION_OF_DNA_RECOMBINATION	17	-2.13	0.05

Table S5.2. Pathway analysis of the TKO/Sarm1KO comparison performed with GSEA from the cerebellum proteomics at 28 weeks. NES: Normalization Enrichment Score. Pathways highlighted in green appear in graphs from Fig. 26

Pathway name	Size	NES	FDR q value
GOBP_REGULATION_OF_COAGULATION	34	2.29	0.00
GOBP_REGULATION_OF_WOUND_HEALING	51	2.27	0.00
GOBP_NEGATIVE_REGULATION_OF_PEPTIDASE_ACTIVITY	94	2.11	0.00

GOBP_ACUTE_INFLAMMATORY_RESPONSE	33	2.03	0.00
GOBP_NEGATIVE_REGULATION_OF_PROTEOLYSIS	140	1.96	0.01
GOBP_HEMOSTASIS	108	1.96	0.01
GOBP_HUMORAL_IMMUNE_RESPONSE	19	1.92	0.02
GOBP_HYDROLASE_ACTIVITY	147	1.92	0.02
GOBP_HISTONE_H4_ACETYLATION	37	1.88	0.03
GOBP_POSITIVE_REGULATION_OF_PHAGOCYTOSIS	24	1.86	0.04
GOBP_EXTERNAL_ENCAPSULATING_STRUCTURE_ORGANIZATION	79	1.86	0.04
GOBP_REGULATION_OF_TUBE_SIZE	47	1.85	0.05
GOBP_DNA_GEOMETRIC_CHANGE	38	1.84	0.05
GOBP_COLLAGEN_FIBRIL_ORGANIZATION	18	1.83	0.06
GOBP_DNA_REPAIR	187	1.82	0.06
GOBP_TRANSCRIPTION_BY_RNA_POLYMERASE_I	23	1.8	0.07
GOBP_EXTRACELLULAR_MATRIX_ASSEMBLY	18	1.8	0.08
GOBP_B_CELL_MEDIATED_IMMUNITY	43	1.79	0.07
GOBP_REGULATION_OF_DNA_RECOMBINATION	52	1.79	0.07
GOBP_RECOMBINATIONAL_REPAIR	54	1.79	0.07
GOBP_PEPTIDYL_LYSINE_ACETYLATION	87	1.78	0.07
GOBP_NEGATIVE_REGULATION_OF_CELL_CELL_ADHESION	55	1.77	0.08
GOBP_PROTEIN_ACETYLATION	99	1.74	0.10
GOBP_ERYTHROCYTE_DEVELOPMENT	18	1.74	0.10
GOBP_CHEMOKINE_PRODUCTION	24	1.74	0.10
GOBP_CHROMATIN_REMODELING	88	1.74	0.10
GOBP_INTEGRIN_MEDIATED_SIGNALING_PATHWAY	55	1.72	0.11
GOBP_POSITIVE_REGULATION_OF_STEROL_TRANSPORT	19	1.71	0.12
GOBP_REGULATION_OF_STEROL_TRANSPORT	29	1.7	0.13
GOBP_RECEPTOR_MEDIATED_ENDOCYTOSIS	27	1.7	0.13
GOBP_PORPHYRIN_CONTAINING_COMPOUND_METABOLIC_PROCESS	27	1.69	0.14
GOBP_MRNA_CIS_SPLICING_VIA_SPLICEOSOME	17	1.68	0.15
GOBP_ORGANIC_CATION_TRANSPORT	17	1.68	0.15
GOBP_CHROMOSOME_ORGANIZATION	395	1.68	0.15
GOBP_NEGATIVE_REGULATION_OF_IMMUNE_SYSTEM_PROCESS	119	1.67	0.15
GOBP_PIGMENT_METABOLIC_PROCESS	38	1.67	0.16
GOBP_NEGATIVE_REGULATION_OF_CELL_ACTIVATION	58	1.67	0.16
GOBP_ LIPID_LOCALIZATION	41	1.67	0.16
GOBP_EPITHELIAL_CELL_MIGRATION	30	1.66	0.16
GOBP_RNA_SPLICING	259	1.66	0.16
GOBP_POTASSIUM_ION_TRANSPORT	15	1.62	0.20
GOBP_NEURAL_TUBE_FORMATION	40	1.62	0.20
GOBP_ PHOSPHOLIPASE_ACTIVITY	19	-1.92	0.09
GOBP_NEURAL_NUCLEUS_DEVELOPMENT	38	-1.94	0.08
GOBP_RIG_I_SIGNALING_PATHWAY	15	-1.97	0.07
GOBP_ACETYL_COA_METABOLIC_PROCESS	25	-2.1	0.02
GOBP_MITOCHONDRIAL_TRANSLATION	55	-2.26	0.00
GOBP_INNER_MITOCHONDRIAL_MEMBRANE_ORGANIZATION	32	-2.3	0.00
GOBP_MITOCHONDRIAL_GENE_EXPRESSION	71	-2.33	0.00

Table S5.3. Pathway analysis of the TKO/DKO comparison performed with GSEA from the cerebellum proteomics at 28 weeks. NES: Normalization Enrichment Score. Pathways highlighted in green appear in graphs from Fig. 26. Table sorted by NES

Pathway name	Size	NES	FDR q value
GOBP_ACTIN_CYTOSKELETON_REORGANIZATION	24	2.00	0.18
GOBP_CALCIUM_ION_DEPENDENT_EXOCYTOSIS	25	1.98	0.16
GOBP_TUMOR_NECROSIS_FACTOR_SUPERFAMILY_CYTOKINE_PRODUCTION	17	1.89	0.19
GOBP_REGULATION_OF_RUFFLE_ASSEMBLY	18	1.89	0.18
GOBP_NEUTRAL_AMINO_ACID_TRANSPORT	26	1.88	0.17
GOBP_ORGANELLE_MEMBRANE_FUSION	71	1.86	0.18
GOBP_PHOSPHATIDYLSERINE_METABOLIC_PROCESS	15	1.85	0.17
GOBP_CHEMICAL_SYNAPTIC_TRANSMISSION_POSTSYNAPTIC	55	1.84	0.17
GOBP_AMINE_TRANSPORT	49	1.84	0.16
GOBP_ENDOPLASMIC_RETICULUM_TUBULAR_NETWORK_ORGANIZATION	15	1.84	0.16
GOBP_SYNAPTIC_VESICLE_RECYCLING	55	1.84	0.15
GOBP_CALCIUM_ION_REGULATED_EXOCYTOSIS	41	1.84	0.14
GOBP_CYTOPLASMIC_TRANSLATION	116	1.83	0.14
GOBP_MODULATION_OF_EXCITATORY_POSTSYNAPTIC_POTENTIAL	27	1.83	0.13
GOBP_POSITIVE_REGULATION_OF_SYNAPTIC_TRANSMISSION	96	1.83	0.13
GOBP_RIBOSOMAL_LARGE_SUBUNIT_BIOGENESIS	46	1.83	0.12
GOBP_NEGATIVE_REGULATION_OF_T_CELL_PROLIFERATION	17	1.82	0.13
GOBP_CARBOHYDRATE_TRANSMEMBRANE_TRANSPORT	52	1.81	0.13
GOBP_NEUROTRANSMITTER_RECEPTOR_TRANSPORT	21	1.80	0.15
GOBP_REGULATION_OF_EXOCYTOSIS	121	1.79	0.17
GOBP_REGULATION_OF_POSTSYNAPTIC_MEMBRANE_POTENTIAL	72	1.78	0.17
GOBP_MEMBRANE_DOCKING	58	1.77	0.18
GOBP_CATECHOLAMINE_SECRETION	29	1.77	0.17
GOBP_AMINO_ACID_TRANSPORT	83	1.76	0.18
GOBP_RIBONUCLEOSIDE_TRIPHOSPHATE_BIOSYNTHETIC_PROCESS	42	-1.69	0.156
GOBP_SUPEROXIDE_METABOLIC_PROCESS	26	-1.69	0.152
GOBP_PROTON_TRANSMEMBRANE_TRANSPORT	86	-1.7	0.153
GOBP_RELEASE_OF_CALCIUM_BY_ENDOPLASMIC_RETICULUM	15	-1.7	0.156
GOBP_INTRINSIC_APOPTOTIC_SIGNALING_PATHWAY	16	-1.7	0.154
GOBP_KETONE_BIOSYNTHETIC_PROCESS	15	-1.7	0.15
GOBP_MITOCHONDRIAL_MEMBRANE_ORGANIZATION	81	-1.71	0.159
GOBP_INTERLEUKIN_1_PRODUCTION	18	-1.71	0.156
GOBP_POSITIVE_REGULATION_OF_DNA_BINDING	18	-1.71	0.152
GOBP_MRNA_METABOLIC_PROCESS	418	-1.75	0.142
GOBP_HYDROGEN_PEROXIDE_METABOLIC_PROCESS	20	-1.78	0.123
GOBP_RESPONSE_TO_TOXIC_SUBSTANCE	116	-1.8	0.11
GOBP_ENERGY_DERIVATION_BY_OXIDATION_OF_ORGANIC_COMPOUNDS	208	-1.82	0.105
GOBP_PROTEIN_LOCALIZATION_TO_MITOCHONDRIAL_MEMBRANE	24	-1.85	0.08
GOBP_MITOCHONDRIAL_ELECTRON_TRANSPORT_NADH_TO_UBIQUINONE	42	-1.86	0.081
GOBP_ACTIN_FILAMENT_BASED_MOVEMENT	16	-1.87	0.081

GOBP_ELECTRON_TRANSPORT_CHAIN	115	-1.92	0.05
GOBP_CELLULAR_OXIDANT_DETOXIFICATION	48	-1.92	0.049
GOBP_POSITIVE_CHEMOTAXIS	15	-1.93	0.048
GOBP_INNER_MITOCHONDRIAL_MEMBRANE_ORGANIZATION	32	-1.98	0.035
GOBP_CELL_COMMUNICATION_BY_ELECTRICAL_COUPLING	20	-1.98	0.031
GOBP_IRON_SULFUR_CLUSTER_ASSEMBLY	22	-2	0.038
GOBP_CELLULAR_RESPONSE_TO_TOXIC_SUBSTANCE	62	-2.03	0.047
GOBP_OXIDATIVE_PHOSPHORYLATION	106	-2.13	0.029

Table S5.4. Pathway analysis of the Sarm1KO/WT comparison performed with GSEA from the cerebellum proteomics at 28 weeks. NES: Normalization Enrichment Score. Pathways highlighted in green appear in graphs from Fig. 30. Table sorted by NES.

Pathway name	Size	NES	FDR q value
GOBP_ATP_SYNTHESIS_COUPLED_ELECTRON_TRANSPORT	73	2.23	0.00
GOBP_OXIDATIVE_PHOSPHORYLATION	108	2.17	0.00
GOBP_PROTEIN_LOCALIZATION_TO_MITOCHONDRIAL_MEMBRANE	23	2.14	0.00
GOBP_REGULATION_OF_SYNAPTIC_TRANSMISSION_GLUTAMATERGIC	45	1.99	0.02
GOBP_LEARNING	86	1.98	0.02
GOBP_INTRACILIARY_TRANSPORT	15	1.90	0.06
GOBP_NEUROPEPTIDE_SIGNALING_PATHWAY	21	1.89	0.06
GOBP_RESPONSE_TO_COLD	26	1.88	0.05
GOBP_MITOCHONDRIAL_ELECTRON_TRANSPORT_NADH_TO_UBIQUINONE	42	1.86	0.06
GOBP_SENSORY_PERCEPTION_OF_PAIN	37	1.85	0.06
GOBP_LONG_TERM_SYNAPTIC_DEPRESSION	17	1.85	0.06
GOBP_RESPONSE_TO_ACETYLCHOLINE	16	1.82	0.07
GOBP_ENERGY_DERIVATION_BY_OXIDATION_OF_ORGANIC_COMPOUNDS	210	1.82	0.06
GOBP_POSTSYNAPTIC_SIGNAL_TRANSDUCTION	20	1.82	0.06
GOBP_POSITIVE_REGULATION_OF_LONG_TERM_SYNAPTIC_POTENTIATION	16	1.82	0.06
GOBP_INNER_MITOCHONDRIAL_MEMBRANE_ORGANIZATION	32	1.81	0.06
GOBP_COGNITION	159	1.80	0.06
GOBP_NEGATIVE_REGULATION_OF_AXONOGENESIS	32	1.80	0.06
GOBP_REGULATION_OF_AMPA_RECEPTOR_ACTIVITY	18	1.80	0.06
GOBP_REGULATION_OF_TRANS_SYNAPTIC_SIGNALING	272	1.80	0.06
GOBP_ATP_METABOLIC_PROCESS	188	1.79	0.07
GOBP_PROTEIN_INSERTION_INTO_MEMBRANE	43	1.78	0.07
GOBP_MEMORY	63	1.70	0.14
GOBP_PROTEIN_TARGETING_TO_MITOCHONDRION	73	1.70	0.14
GOBP_NEGATIVE_REGULATION_OF_DEVELOPMENTAL_GROWTH	41	1.69	0.14
GOBP_NEUROMUSCULAR_PROCESS	77	1.68	0.14
GOBP_NEUROTRANSMITTER_METABOLIC_PROCESS	18	1.66	0.17
GOBP_TRANSMISSION_OF_NERVE_IMPULSE	31	1.66	0.16
GOBP_CENTRAL_NERVOUS_SYSTEM_NEURON_DEVELOPMENT	42	1.65	0.16
GOBP_PROTON_TRANSMEMBRANE_TRANSPORT	87	1.65	0.16

GOBP_REGULATION_OF_CATION_CHANNEL_ACTIVITY	80	1.65	0.16
GOBP_PROTEIN_LOCALIZATION_TO_CILIUM	33	1.63	0.18
GOBP_IRON_SULFUR_CLUSTER_ASSEMBLY	23	1.63	0.18
GOBP_POSITIVE_REGULATION_OF_SYNAPTIC_TRANSMISSION	96	1.63	0.18
GOBP_NEURONAL_MORPHOGENESIS	299	1.63	0.18
GOBP_CELL_CELL_ADHESION	321	-1.75	0.04
GOBP_REGULATION_OF_FATTY_ACID_METABOLIC_PROCESS	31	-1.75	0.04
GOBP_RESPONSE_TO_CORTICOSTEROID	65	-1.75	0.04
GOBP_APOPTOTIC_CELL_CLEARANCE	25	-1.75	0.04
GOBP_PRODUCTION_OF_MOLECULAR_MEDIATOR_OF_IMMUNE_RESPONSE	58	-1.75	0.04
GOBP_ENDOTHELIAL_CELL_MIGRATION	87	-1.75	0.04
GOBP_CELL_SUBSTRATE_ADHESION	160	-1.76	0.04
GOBP_BIOLOGICAL_PROCESS_INVOLVED_IN_SYMBIOTIC_INTERACTION	123	-1.76	0.04
GOBP_NEUTRAL_LIPID_METABOLIC_PROCESS	54	-1.76	0.04
GOBP_REGULATION_OF_CELL_MORPHOGENESIS_INVOLVED_IN_DIFFERENTIATION	64	-1.76	0.04
GOBP_POSITIVE_REGULATION_OF_PHAGOCYTOSIS	24	-1.76	0.04
GOBP_REGULATION_OF_RESPONSE_TO_EXTERNAL_STIMULUS	324	-1.77	0.03
GOBP_VASCULATURE_DEVELOPMENT	254	-1.77	0.03
GOBP_ESTABLISHMENT_OF_MITOTIC_SPINDLE_LOCALIZATION	18	-1.77	0.04
GOBP_REGULATION_OF_TUBE_SIZE	47	-1.78	0.03
GOBP_SNRNA_PROCESSING	17	-1.79	0.03
GOBP_PORPHYRIN_CONTAINING_COMPOUND_METABOLIC_PROCESS	27	-1.79	0.03
GOBP_REGULATION_OF_PROTEOLYSIS	327	-1.79	0.03
GOBP_NEGATIVE_REGULATION_OF_CELL_CELL_ADHESION	55	-1.79	0.03
GOBP_POSITIVE_REGULATION_OF_CELL_SUBSTRATE_ADHESION	60	-1.79	0.03
GOBP_PRIMARY_ALCOHOL_METABOLIC_PROCESS	40	-1.79	0.03
GOBP_EXTRACELLULAR_MATRIX_ASSEMBLY	19	-1.79	0.03
GOBP_LIPID_HOMEOSTASIS	32	-1.80	0.03
GOBP_REGULATION_OF_LIPID_LOCALIZATION	61	-1.80	0.03
GOBP_CELLULAR_RESPONSE_TO_VASCULAR_ENDOTHELIAL_GROWTH_FACTOR_STIMULUS	24	-1.80	0.03
GOBP_NEUTROPHIL_CHEMOTAXIS	24	-1.81	0.02
GOBP_ARTERY_MORPHOGENESIS	18	-1.81	0.02
GOBP_RETINOL_METABOLIC_PROCESS	17	-1.81	0.02
GOBP_MESONEPHROS_DEVELOPMENT	20	-1.81	0.02
GOBP_NEGATIVE_REGULATION_OF_EXTRINSIC_APOPTOTIC_SIGNALING_PATHWAY_VIA_DEATH_DOMAIN_RECEPTORS	16	-1.81	0.03
GOBP_REGULATION_OF_VASOCONSTRICTION	20	-1.81	0.03
GOBP_INTERLEUKIN_8_PRODUCTION	21	-1.82	0.02
GOBP_IMMUNOGLOBULIN_PRODUCTION	38	-1.82	0.02
GOBP_EXTRINSIC_APOPTOTIC_SIGNALING_PATHWAY_VIA_DEATH_DOMAIN_RECEPTORS	37	-1.82	0.02
GOBP_ESTABLISHMENT_OF_SPINDLE_ORIENTATION	19	-1.82	0.02
GOBP_MYELOID_CELL_DEVELOPMENT	34	-1.82	0.02
GOBP_REGULATION_OF_MONOOXYGENASE_ACTIVITY	21	-1.83	0.02
GOBP_INFLAMMATORY_RESPONSE	219	-1.83	0.02
GOBP_POSITIVE_REGULATION_OF_IMMUNE_SYSTEM_PROCESS	260	-1.83	0.02
GOBP_CELLULAR_HORMONE_METABOLIC_PROCESS	39	-1.83	0.02

GOBP_RESPONSE_TO_BACTERIUM	179	-1.88	0.02
GOBP_TERPENOID_METABOLIC_PROCESS	34	-1.88	0.02
GOBP_POSITIVE_REGULATION_OF_CELL_CELL_ADHESION	84	-1.88	0.02
GOBP_MUSCLE_CELL_MIGRATION	38	-1.89	0.01
GOBP_INTERLEUKIN_1_PRODUCTION	29	-1.89	0.01
GOBP_POSITIVE_REGULATION_OF_LIPASE_ACTIVITY	23	-1.90	0.01
GOBP_BONE_MORPHOGENESIS	23	-1.90	0.01
GOBP_REGULATION_OF_PHAGOCYTOSIS	40	-1.94	0.01
GOBP_COLLAGEN_METABOLIC_PROCESS	26	-1.94	0.01
GOBP_PROTEIN_LIPID_COMPLEX_ASSEMBLY	19	-1.95	0.01
GOBP_REGULATION_OF_SUBSTRATE_ADHESION_DEPENDENT_CELL_SPREADING	39	-1.95	0.01
GOBP_REGULATION_OF_STEROID_METABOLIC_PROCESS	37	-1.97	0.01
GOBP_NEGATIVE_REGULATION_OF_PROTEOLYSIS	143	-1.98	0.01
GOBP_LYMPHOCYTE_MEDIATED_IMMUNITY	73	-1.99	0.01
GOBP_DEFENSE_RESPONSE_TO_OTHER_ORGANISM	300	-1.99	0.01
GOBP_REGULATION_OF_PLATELET_ACTIVATION	23	-1.99	0.01
GOBP_REGULATION_OF_CELL_CELL_ADHESION	135	-1.99	0.01
GOBP_NEGATIVE_REGULATION_OF_HYDROLASE_ACTIVITY	149	-2.04	0.00
GOBP_ANTIMICROBIAL_HUMORAL_RESPONSE	15	-2.05	0.00
GOBP_EXTERNAL_ENCAPSULATING_STRUCTURE_ORGANIZATION	80	-2.06	0.00
GOBP_INTEGRIN_MEDIATED_SIGNALING_PATHWAY	55	-2.07	0.00
GOBP_PROTEIN_LIPID_COMPLEX_SUBUNIT_ORGANIZATION	24	-2.09	0.00
GOBP_CHOLESTEROL_EFFLUX	26	-2.10	0.00
GOBP_REGULATION_OF_LIPASE_ACTIVITY	32	-2.11	0.00
GOBP_B_CELL_MEDIATED_IMMUNITY	43	-2.14	0.00
GOBP_NEGATIVE_REGULATION_OF_PEPTIDASE_ACTIVITY	96	-2.15	0.00
GOBP_CYTOPLASMIC_TRANSLATION	116	-2.15	0.00
GOBP_ADAPTIVE_IMMUNE_RESPONSE	100	-2.16	0.00
GOBP_DEFENSE_RESPONSE_TO_BACTERIUM	53	-2.18	0.00
GOBP_REGULATION_OF_STEROL_TRANSPORT	29	-2.20	0.00
GOBP_ACUTE_INFLAMMATORY_RESPONSE	34	-2.22	0.00
GOBP_REGULATION_OF_PLASMA_LIPOPROTEIN_PARTICLE_LEVELS	34	-2.24	0.00
GOBP_ACUTE_PHASE_RESPONSE	17	-2.27	0.00
GOBP_COLLAGEN_FIBRIL_ORGANIZATION	18	-2.32	0.00
GOBP_PLASMINOGEN_ACTIVATION	17	-2.34	0.00
GOBP_HETEROTYPIC_CELL_CELL_ADHESION	24	-2.36	0.00
GOBP_REGULATION_OF_WOUND_HEALING	52	-2.57	0.00
GOBP_HUMORAL_IMMUNE_RESPONSE	48	-2.60	0.00
GOBP_COMPLEMENT_ACTIVATION	25	-2.63	0.00
GOBP_REGULATION_OF_COAGULATION	35	-2.66	0.00

Table S6.1. Pathway analyses of the DKO/WT comparison performed with GSEA from the spinal cord proteomics at 28 weeks. NES: Normalization Enrichment Score. Pathways highlighted in green appear in graphs from Fig. 26. Table sorted by NES.

Pathway name	Size	NES	FDR q value
GOBP_EXTERNAL_ENCAPSULATING_STRUCTURE_ORGANIZATION	89	2.78	0.00
GOBP_COLLAGEN_FIBRIL_ORGANIZATION	18	2.42	0.00
GOBP_INTEGRIN_MEDIATED_SIGNALING_PATHWAY	55	2.34	0.00
GOBP_BASEMENT_MEMBRANE_ORGANIZATION	16	2.26	0.00
GOBP_HEMOSTASIS	121	2.26	0.00
GOBP_CELL_MATRIX_ADHESION	103	2.17	0.00
GOBP_WOUND_HEALING	194	2.17	0.00
GOBP_REGULATION_OF_COAGULATION	38	2.15	0.00
GOBP_CELL_ADHESION_MEDIATED_BY_INTEGRIN	35	2.07	0.00
GOBP_EXTRACELLULAR_MATRIX_ASSEMBLY	21	2.07	0.00
GOBP_CELL_SUBSTRATE_ADHESION	170	2.07	0.00
GOBP_COLLAGEN_METABOLIC_PROCESS	26	2.05	0.00
GOBP_ENDOTHELIAL_CELL_PROLIFERATION	48	2.04	0.01
GOBP_CONNECTIVE_TISSUE_DEVELOPMENT	61	2.03	0.01
GOBP_UROGENITAL_SYSTEM_DEVELOPMENT	107	2.02	0.01
GOBP_BLOOD_VESSEL_MORPHOGENESIS	212	2.01	0.01
GOBP_NEURON_PROJECTION_GUIDANCE	106	2	0.01
GOBP_APPENDAGE_DEVELOPMENT	50	1.99	0.01
GOBP_FORMATION_OF_PRIMARY_GERM_LAYER	36	1.98	0.01
GOBP_MORPHOGENESIS_OF_AN_EPITHELIAL_SHEET	29	1.97	0.01
GOBP_CIRCULATORY_SYSTEM_DEVELOPMENT	378	1.96	0.01
GOBP_REGULATION_OF_EMBRYONIC_DEVELOPMENT	24	1.96	0.01
GOBP_ODONTOGENESIS	29	1.95	0.01
GOBP_SKIN_DEVELOPMENT	70	1.95	0.01
GOBP_MESENCHYMAL_CELL_DIFFERENTIATION	81	1.95	0.01
GOBP_POSITIVE_REGULATION_OF_STEROL_TRANSPORT	17	1.94	0.01
GOBP_CORTICAL_ACTIN_CYTOSKELETON_ORGANIZATION	30	1.94	0.01
GOBP_POSITIVE_REGULATION_OF_T_CELL_PROLIFERATION	29	1.94	0.01
GOBP_RESPONSE_TO_CAMP	36	1.93	0.01
GOBP_TAXIS	224	1.93	0.01
GOBP_RESPONSE_TO_GROWTH_FACTOR	271	1.93	0.02
GOBP_ANIMAL_ORGAN_MORPHOGENESIS	284	1.92	0.02
GOBP_CELL_CHEMOTAXIS	96	1.91	0.02
GOBP_GLAND_MORPHOGENESIS	36	1.9	0.02
GOBP_ENDODERM_DEVELOPMENT	22	1.9	0.02
GOBP_NEGATIVE_REGULATION_OF_PEPTIDASE_ACTIVITY	103	1.89	0.02
GOBP_SUBSTRATE_ADHESION_DEPENDENT_CELL_SPREADING	71	1.88	0.02
GOBP_MEIOTIC_CELL_CYCLE	51	1.88	0.02
GOBP_POSITIVE_REGULATION_OF_LOCOMOTION	229	1.88	0.02
GOBP_TUBE_DEVELOPMENT	354	1.88	0.02
GOBP_ENDOTHELIAL_CELL_MIGRATION	91	1.88	0.02
GOBP_REGULATION_OF_CELL_ADHESION	284	1.87	0.02

GOBP_RHO_PROTEIN_SIGNAL_TRANSDUCTION	71	1.87	0.02
GOBP_EXOCRINE_SYSTEM_DEVELOPMENT	18	1.87	0.02
GOBP_CORTICAL_CYTOSKELETON_ORGANIZATION	42	1.86	0.02
GOBP_CARTILAGE_DEVELOPMENT	42	1.84	0.03
GOBP_GASTRULATION	61	1.84	0.03
GOBP_NEURAL_CREST_CELL_MIGRATION	22	1.84	0.03
GOBP_ACUTE_INFLAMMATORY_RESPONSE	38	1.84	0.03
GOBP_NEGATIVE_REGULATION_OF_HYDROLASE_ACTIVITY	163	1.84	0.03
GOBP_PROTEIN_HYDROXYLATION	15	1.83	0.03
GOBP_HISTONE_PHOSPHORYLATION	21	1.83	0.03
GOBP_CELLULAR_RESPONSE_TO_ACID_CHEMICAL	45	1.82	0.03
GOBP_T_CELL_ACTIVATION	69	1.82	0.03
GOBP_SEMAPHORIN_PLEXIN_SIGNALING_PATHWAY	22	1.82	0.03
GOBP_POSITIVE_REGULATION_OF_ENDOTHELIAL_CELL_PROLIFERATION	28	1.82	0.03
GOBP_TRANSMEMBRANE_RECEPTOR_PROTEIN_SIGNALING_PATHWAY	120	1.82	0.03
GOBP_DIGESTIVE_SYSTEM_PROCESS	30	1.82	0.03
GOBP_REGULATION_OF_VASCULATURE_DEVELOPMENT	98	1.81	0.03
GOBP_POSITIVE_REGULATION_OF_LEUKOCYTE_PROLIFERATION	42	1.81	0.03
GOBP_RNA_DEPENDENT_DNA_BIOSYNTHETIC_PROCESS	42	1.81	0.03
GOBP_HETEROTYPIC_CELL_CELL_ADHESION	26	1.81	0.03
GOBP_MESENCHYME_DEVELOPMENT	93	1.81	0.03
GOBP_RESPONSE_TO_TRANSFORMING_GROWTH_FACTOR_BETA	90	1.81	0.03
GOBP_TELOMERE_MAINTENANCE_VIA_TELOMERE_LENGTHENING	45	1.81	0.03
GOBP_MEMBRANE_RAFT_ORGANIZATION	18	1.8	0.03
GOBP_TUBE_MORPHOGENESIS	279	1.8	0.03
GOBP_REGULATION_OF_PEPTIDASE_ACTIVITY	182	1.8	0.03
GOBP_NEGATIVE_REGULATION_OF_RESPONSE_TO_EXTERNAL_STIMULUS	150	1.8	0.03
GOBP_BONE_CELL_DEVELOPMENT	15	1.79	0.03
GOBP_REGULATION_OF_CELL_SHAPE	87	1.79	0.03
GOBP_ENDOCRINE_PROCESS	22	1.79	0.03
GOBP_MYOBLAST_FUSION	16	1.78	0.04
GOBP_POSITIVE_REGULATION_OF_ENDOTHELIAL_CELL_MIGRATION	45	1.78	0.04
GOBP_LEUKOCYTE_CELL_CELL_ADHESION	112	1.78	0.04
GOBP_NEURON_PROJECTION_REGENERATION	30	1.78	0.04
GOBP_REGULATION_OF_CHEMOTAXIS	78	1.77	0.04
GOBP_SKELETAL_SYSTEM_DEVELOPMENT	150	1.77	0.04
GOBP_HEART_MORPHOGENESIS	66	1.77	0.04
GOBP_NEGATIVE_REGULATION_OF_DNA_METABOLIC_PROCESS	49	1.77	0.04
GOBP_REGULATION_OF_PLASMA_LIPOPROTEIN_PARTICLE_LEVELS	37	1.77	0.04
GOBP_EPITHELIAL_TO_MESENCHYMAL_TRANSITION	53	1.77	0.04
GOBP_PLASMINOGEN_ACTIVATION	16	1.76	0.04
GOBP_ANTIMICROBIAL_HUMORAL_RESPONSE	16	1.76	0.04
GOBP_ALPHA_BETA_T_CELL_DIFFERENTIATION	21	1.76	0.04
GOBP_REGULATION_OF_EPITHELIAL_TO_MESENCHYMAL_TRANSITION	34	1.76	0.04
GOBP_DNA_METHYLATION	18	1.76	0.04
GOBP_RESPIRATORY_SYSTEM_DEVELOPMENT	65	1.76	0.04

GOBP_GRANULOCYTE_CHEMOTAXIS	34	1.75	0.04
GOBP_ENZYME_LINKED_RECEPTOR_PROTEIN_SIGNALING_PATHWAY	346	1.75	0.04
GOBP_LYMPHOCYTE_ACTIVATION_INVOLVED_IN_IMMUNE_RESPONSE	52	1.75	0.04
GOBP_KIDNEY_EPITHELIUM_DEVELOPMENT	37	1.75	0.04
GOBP_CD4_POSITIVE_ALPHA_BETA_T_CELL_ACTIVATION	19	1.74	0.05
GOBP_GLOMERULUS_DEVELOPMENT	19	1.74	0.05
GOBP_NEURAL_CREST_CELL_DIFFERENTIATION	35	1.74	0.05
GOBP_RESPONSE_TO_ESTROGEN	21	1.73	0.05
GOBP_NEGATIVE_REGULATION_OF_PROTEIN_KINASE_B_SIGNALING	19	1.73	0.05
GOBP_REGULATION_OF_INSULIN_SECRETION	22	-1.7	0.10
GOBP_PROTEIN_TRANSMEMBRANE_IMPORT	28	-1.75	0.07
GOBP_RELEASE_OF_CYTOCHROME_C_FROM_MITOCHONDRIA	32	-1.75	0.07
GOBP_POSITIVE_REGULATION_OF_PHOSPHOLIPASE_ACTIVITY	19	-1.77	0.06
GOBP_TRICARBOXYLIC_ACID_CYCLE	26	-1.77	0.06
GOBP_INTRACELLULAR_PROTEIN_TRANSMEMBRANE_TRANSPORT	41	-1.79	0.05
GOBP_GLUTAMATE_METABOLIC_PROCESS	21	-1.81	0.04
GOBP_ORGANELLE_DISASSEMBLY	81	-1.81	0.04
GOBP_DICARBOXYLIC_ACID_METABOLIC_PROCESS	62	-1.82	0.04
GOBP_MITOCHONDRIAL_RESPIRATORY_CHAIN_COMPLEX_ASSEMBLY	76	-1.82	0.04
GOBP_APOPTOTIC_MITOCHONDRIAL_CHANGES	63	-1.83	0.04
GOBP_AMIDE_BIOSYNTHETIC_PROCESS	478	-1.84	0.04
GOBP_NADH_DEHYDROGENASE_COMPLEX_ASSEMBLY	50	-1.84	0.03
GOBP_PROTON_TRANSMEMBRANE_TRANSPORT	88	-1.86	0.03
GOBP_INTRACELLULAR_STEROID_HORMONE_RECEPTOR_SIGNALING_PATHWAY	16	-1.86	0.03
GOBP_MITOCHONDRIAL_CALCIUM_ION_HOMEOSTASIS	20	-1.93	0.02
GOBP_BRANCHED_CHAIN_AMINO_ACID_METABOLIC_PROCESS	19	-1.94	0.02
GOBP_RIG_I_SIGNALING_PATHWAY	15	-2	0.01
GOBP_NUCLEOSIDE_BISPHOSPHATE_BIOSYNTHESIS	75	-2.03	0.01
GOBP_PHOSPHATIDYLGLYCEROL_METABOLIC_PROCESS	22	-2.06	0.00
GOBP_RECEPTOR_SIGNALING_PATHWAY_IN_RESPONSE_TO_VIRUS	17	-2.09	0.00
GOBP_MITOCHONDRION_ORGANIZATION	344	-2.12	0.00
GOBP_ACETYL_COA_BIOSYNTHETIC_PROCESS	16	-2.16	0.00
GOBP_ENERGY_DERIVATION_BY_OXIDATION_OF_ORGANIC_COMPOUNDS	210	-2.2	0.00
GOBP_OXIDATIVE_PHOSPHORYLATION	108	-2.22	0.00
GOBP_THIOESTER_BIOSYNTHETIC_PROCESS	35	-2.22	0.00
GOBP_ATP_SYNTHESIS_COUPLED_ELECTRON_TRANSPORT	73	-2.27	0.00
GOBP_RESPIRATORY_ELECTRON_TRANSPORT_CHAIN	92	-2.28	0.00
GOBP_MITOCHONDRIAL_TRANSMEMBRANE_TRANSPORT	80	-2.3	0.00
GOBP_MITOCHONDRIAL_TRANSLATION	53	-2.33	0.00
GOBP_CELLULAR_RESPIRATION	167	-2.37	0.00
GOBP_MITOPHAGY	23	-2.37	0.00
GOBP_MITOCHONDRIAL_GENE_EXPRESSION	69	-2.39	0.00
GOBP_INNER_MITOCHONDRIAL_MEMBRANE_ORGANIZATION	32	-2.41	0.00

Table S6.2. Pathway analyses of the TKO/Sarm1KO comparison performed with GSEA from the spinal cord proteomics at 28 weeks. NES: Normalization Enrichment Score. Pathways highlighted in green appear in graphs from Fig. 26. Table sorted by NES.

Pathway name	Size	NES	FDR q value
GOBP_MITOCHONDRIAL_TRANSLATION	53	-2.27	0.00
GOBP_MITOCHONDRIAL_GENE_EXPRESSION	69	-2.26	0.00
GOBP_MITOCHONDRIAL_CALCIUM_ION_HOMEOSTASIS	20	-2.18	0.00
GOBP_FATTY_ACID_BETA_OXIDATION	55	-2.17	0.00
GOBP_LIPID_OXIDATION	72	-2.15	0.00
GOBP_INNER_MITOCHONDRIAL_MEMBRANE_ORGANIZATION	32	-2.14	0.00
GOBP_ OXIDATIVE_PHOSPHORYLATION	119	-2.09	0.01
GOBP_COLLAGEN_FIBRIL_ORGANIZATION	24	-2.08	0.01
GOBP_THIOESTER_METABOLIC_PROCESS	63	-2.06	0.01
GOBP_ORGANIC_ACID_CATABOLIC_PROCESS	152	-2.06	0.01
GOBP_MITOCHONDRIAL_TRANSMEMBRANE_TRANSPORT	81	-2.04	0.01
GOBP_MONOCARBOXYLIC_ACID_CATABOLIC_PROCESS	79	-2.03	0.01
GOBP_ACETYL_COA_METABOLIC_PROCESS	26	-2.03	0.01
GOBP_MITOCHONDRIAL_MEMBRANE_ORGANIZATION	79	-2.01	0.01
GOBP_PHOSPHATIDYLGLYCEROL_METABOLIC_PROCESS	22	-1.99	0.02
GOBP_RIG_I_SIGNALING_PATHWAY	15	-1.97	0.02
GOBP_POSITIVE_REGULATION_OF_IMMUNOGLOBULIN_PRODUCTION	17	-1.96	0.02
GOBP_RECEPTOR_SIGNALING_PATHWAY_IN_RESPONSE_TO_VIRUS	17	-1.96	0.02
GOBP_RESPIRATORY_ELECTRON_TRANSPORT_CHAIN	92	-1.93	0.03
GOBP_NUCLEOSIDE_BISPHOSPHATE_METABOLIC_PROCESS	75	-1.92	0.03
GOBP_NADH_DEHYDROGENASE_COMPLEX_ASSEMBLY	50	-1.91	0.03
GOBP_POSITIVE_REGULATION_OF_PHOSPHOLIPASE_ACTIVITY	20	-1.89	0.04
GOBP_KETONE_BIOSYNTHETIC_PROCESS	15	-1.88	0.04
GOBP_POSITIVE_REGULATION_OF_STEROL_TRANSPORT	17	-1.88	0.04
GOBP_SMALL_MOLECULE_CATABOLIC_PROCESS	220	-1.87	0.04
GOBP_PROTEIN_TARGETING_TO_PEROXISOME	16	-1.86	0.05
GOBP_PEROXISOMAL_TRANSPORT	19	-1.84	0.05
GOBP_GENERATION_OF_PRECURSOR_METABOLITES_AND_ENERGY	315	-1.84	0.05
GOBP_MITOPHAGY	23	-1.83	0.06
GOBP_LIPID_MODIFICATION	131	-1.81	0.07
GOBP_REGULATION_OF_PHOSPHOLIPASE_C_ACTIVITY	15	-1.81	0.07
GOBP_MITOCHONDRION_ORGANIZATION	346	-1.8	0.07
GOBP_EXTERNAL_ENCAPSULATING_STRUCTURE_ORGANIZATION	97	-1.79	0.08
GOBP_INTRACELLULAR_STEROID_HORMONE_RECEPTOR_SIGNALING_PATHWAY	17	-1.78	0.08
GOBP_CELLULAR_RESPONSE_TO_OXYGEN_LEVELS	78	-1.78	0.08
GOBP_COLLAGEN_METABOLIC_PROCESS	31	-1.76	0.09
GOBP_MITOCHONDRIAL_FISSION	26	-1.76	0.09
GOBP_POSITIVE_REGULATION_OF_IMMUNE_EFFECTOR_PROCESS	68	-1.75	0.10
GOBP_MITOCHONDRIAL_FUSION	27	-1.74	0.10
GOBP_AMIDE_BIOSYNTHETIC_PROCESS	481	-1.73	0.11
GOBP_PROTEIN_TRANSMEMBRANE_IMPORT	28	-1.71	0.12

Table S6.3. Pathway analyses of the TKO/DKO comparison performed with GSEA from the spinal cord proteomics at 28 weeks. NES: Normalization Enrichment Score. Pathways highlighted in green appear in graphs from Fig. 26. Table sorted by NES.

Pathway name	Size	NES	FDR q value
GOBP_MEMBRANE_LIPID_BIOSYNTHETIC_PROCESS	52	2.04	0.10
GOBP_NEUROTRANSMITTER_SECRETION	100	1.97	0.14
GOBP_GLYCOLIPID_BIOSYNTHETIC_PROCESS	15	1.94	0.14
GOBP_SYNAPTIC_VESICLE_EXOCYTOSIS	76	1.94	0.11
GOBP_NEUROTRANSMITTER_TRANSPORT	139	1.91	0.12
GOBP_REGULATION_OF_ENDOPLASMIC_RETICULUM_UNFOLDED_PROTEIN_RESPONSE	17	1.89	0.11
GOBP_SYNAPTIC_VESICLE_PRIMING	15	1.85	0.16
GOBP_CATECHOLAMINE_SECRETION	28	1.85	0.15
GOBP_POSITIVE_REGULATION_OF_EXOCYTOSIS	46	1.83	0.16
GOBP_CELLULAR_CARBOHYDRATE_METABOLIC_PROCESS	23	1.81	0.17
GOBP_VESICLE_MEDIATED_TRANSPORT_IN_SYNAPSE	140	1.81	0.16
GOBP_SYNAPTIC_VESICLE_MEMBRANE_ORGANIZATION	19	1.8	0.16
GOBP_DOPAMINE_TRANSPORT	23	1.78	0.16
GOBP_CERAMIDE_BIOSYNTHETIC_PROCESS	24	1.78	0.16
GOBP_SPHINGOLIPID_BIOSYNTHETIC_PROCESS	42	1.78	0.15
GOBP_MONOAMINE_TRANSPORT	37	1.76	0.17
GOBP_CALCIUM_ION_REGULATED_EXOCYTOSIS	40	1.76	0.16
GOBP_POSITIVE_REGULATION_OF_REPRODUCTIVE_PROCESS	17	1.76	0.15
GOBP_RIBOSOMAL_LARGE_SUBUNIT_ASSEMBLY	16	1.76	0.15
GOBP_BRAIN_MORPHOGENESIS	18	1.75	0.15
GOBP_OXIDATIVE_PHOSPHORYLATION	109	-1.59	0.20
GOBP_ATP_SYNTHESIS_COUPLED_ELECTRON_TRANSPORT	73	-1.64	0.20
GOBP_CENTROSOME_DUPLICATION	27	-1.81	0.12
GOBP_INTEGRIN_MEDIATED_SIGNALING_PATHWAY	56	-1.81	0.11
GOBP_MRNA_CIS_SPLICING_VIA_SPLICEOSOME	17	-1.82	0.11
GOBP_COLLAGEN_METABOLIC_PROCESS	32	-1.84	0.10
GOBP_REGULATION_OF_COAGULATION	38	-1.84	0.10
GOBP_PROTEIN_LOCALIZATION_TO_NUCLEUS	18	-1.84	0.10
GOBP_REGULATION_OF_RNA_SPLICING	85	-1.85	0.13
GOBP_EXTRACELLULAR_MATRIX_ASSEMBLY	23	-1.85	0.12
GOBP_ACTIN_FILAMENT_BASED_MOVEMENT	66	-1.85	0.12
GOBP_REGULATION_OF_PROTEIN_IMPORT	34	-1.85	0.11
GOBP_MUSCLE_ORGAN_MORPHOGENESIS	20	-1.85	0.11
GOBP_RESPONSE_TO_VITAMIN	27	-1.86	0.12
GOBP_NEGATIVE_REGULATION_OF_INTRACELLULAR_TRANSPORT	32	-1.87	0.14
GOBP_POSITIVE_REGULATION_OF_WOUND_HEALING	24	-1.87	0.13
GOBP_NEGATIVE_REGULATION_OF_INTRACELLULAR_PROTEIN_TRANSPORT	27	-1.89	0.11
GOBP_POSITIVE_CHEMOTAXIS	15	-1.92	0.10
GOBP_VASCULAR_ENDOTHELIAL_GROWTH_FACTOR_SIGNALING_PATHWAY	15	-1.92	0.09
GOBP_MRNA_SPLICE_SITE_SELECTION	23	-1.93	0.11
GOBP_CELL_ADHESION_MEDIATED_BY_INTEGRIN	36	-1.93	0.10

GOBP_CELLULAR_RESPONSE_TO_ACID_CHEMICAL	46	-1.95	0.11
GOBP_POSITIVE_REGULATION_OF_RESPONSE_TO_WOUNDING	32	-1.97	0.11
GOBP_EXTERNAL_ENCAPSULATING_STRUCTURE_ORGANIZATION	97	-2.07	0.03
GOBP_COLLAGEN_FIBRIL_ORGANIZATION	24	-2.37	0.00

Table S6.4. Pathway analyses of the Sarm1KO/WT comparison performed with GSEA from the spinal cord proteomics at 28 weeks. NES: Normalization Enrichment Score. Pathways highlighted in green appear in graphs from Fig. 28. Table sorted by NES.

Pathway name	Size	NES	FDR q value
GOBP_COLLAGEN_FIBRIL_ORGANIZATION	18	2.38	0.00
GOBP_EXTERNAL_ENCAPSULATING_STRUCTURE_ORGANIZATION	89	2.26	0.00
GOBP_BONE_DEVELOPMENT	76	2.13	0.01
GOBP_CARTILAGE_DEVELOPMENT	42	2.08	0.01
GOBP_VASOCONSTRICTION	28	1.98	0.06
GOBP_STEROL_BIOSYNTHETIC_PROCESS	41	1.97	0.05
GOBP_PLASMINOGEN_ACTIVATION	16	1.96	0.05
GOBP_REGULATION_OF_EMBRYONIC_DEVELOPMENT	24	1.90	0.11
GOBP_SKELETAL_SYSTEM_DEVELOPMENT	149	1.90	0.09
GOBP_MEMBRANE_RAFT_ORGANIZATION	18	1.87	0.12
GOBP_ISOPRENOID_METABOLIC_PROCESS	43	1.87	0.11
GOBP_CONNECTIVE_TISSUE_DEVELOPMENT	61	1.86	0.11
GOBP_T_CELL_PROLIFERATION	29	1.86	0.11
GOBP_PROTEOGLYCAN_METABOLIC_PROCESS	15	1.86	0.10
GOBP_CORTICAL_ACTIN_CYTOSKELETON_ORGANIZATION	30	1.85	0.10
GOBP_STEROL_METABOLIC_PROCESS	75	1.83	0.11
GOBP_LYMPHOCYTE_COSTIMULATION	15	1.83	0.11
GOBP_POSITIVE_REGULATION_OF_REPRODUCTIVE_PROCESS	17	1.82	0.10
GOBP_LONG_CHAIN_FATTY_ACID_METABOLIC_PROCESS	55	1.82	0.10
GOBP_SECONDARY_ALCOHOL_METABOLIC_PROCESS	75	1.82	0.10
GOBP_SUBSTRATE_ADHESION_DEPENDENT_CELL_SPREADING	71	1.81	0.11
GOBP_NEGATIVE_REGULATION_OF_CELL_CELL_ADHESION	60	1.80	0.11
GOBP_GLAND_MORPHOGENESIS	36	1.80	0.10
GOBP_FATTY_ACID_BIOSYNTHETIC_PROCESS	77	1.80	0.10
GOBP_RNA_PHOSPHODIESTER_BOND_HYDROLYSIS_EXONUCLEOLYTIC	27	1.79	0.10
GOBP_WOUND_HEALING	193	1.79	0.10
GOBP_STEROID_METABOLIC_PROCESS	119	1.79	0.10
GOBP_ATP_METABOLIC_PROCESS	188	-1.77	0.13
GOBP_MRNA_SPLICE_SITE_SELECTION	23	-1.77	0.12
GOBP_ENERGY_DERIVATION_BY_OXIDATION_OF_ORGANIC_COMPOUNDS	210	-1.78	0.12
GOBP_POSITIVE_REGULATION_OF_PROTEIN_POLYMERIZATION	55	-1.79	0.11
GOBP_CALCIUM_ION_TRANSMEMBRANE_TRANSPORT	17	-1.80	0.12
GOBP_MICROTUBULE_POLYMERIZATION_OR_DEPOLYMERIZATION	75	-1.80	0.12
GOBP_NEUROPEPTIDE_SIGNALING_PATHWAY	24	-1.85	0.08
GOBP_MICROTUBULE_NUCLEATION	21	-1.85	0.08

GOBP_REGULATION_OF_RNA_SPLICING	83	-1.87	0.07
GOBP_REGULATION_OF_LYASE_ACTIVITY	20	-1.93	0.04
GOBP_INNER_MITOCHONDRIAL_MEMBRANE_ORGANIZATION	32	-1.94	0.04
GOBP_PROTEIN_LOCALIZATION_TO_MITOCHONDRIAL_MEMBRANE	24	-1.97	0.03
GOBP_MITOCHONDRIAL_ELECTRON_TRANSPORT_NADH_TO_UBIQUINONE	43	-2.06	0.01
GOBP_AEROBIC_RESPIRATION	141	-2.14	0.00
GOBP_OXIDATIVE_PHOSPHORYLATION	108	-2.20	0.00
GOBP_ATP_SYNTHESIS_COUPLED_ELECTRON_TRANSPORT	73	-2.21	0.00

Acknowledgements

My PhD has been full of emotions. I remember the excitement at the beginning, when I just wanted to learn as much as possible, do science and take the most out of every moment. Then things started getting tougher and tougher, and then covid hit. If pursuing a PhD is already challenging, spending most of it while the word is facing a pandemic did not make it any easier. I am very grateful that in spite of that I was able to keep my head down and give my best while staying true to myself. I would like to thank all the people who, one way or another, were part of this journey with me.

First and foremost, I am very thankful to Prof. Elena Rugarli, for the mentorship and guidance since the very first moment, for all the fruitful scientific discussions and for giving me the opportunity to learn so much from you. I would also like to thank my TAC members; Prof. Natalia Kononenko and Prof. Manolis Pasparakis, for your valuable feedback and ideas. My sincere gratitude goes to the RTG-NCA people, particularly Katerina Vlantis and Kathy Joergens, for being always so helpful and caring when I needed it.

To all of you Rugarli lab members, current and formers: Lennart, Matteo, Mujeeb, Desi, Marie, Esther, Alex, Giovanna, Thibaut, Irene, Marta, Tim, Giada and Claudia. I will always remember our funny lunch times, lab trips, carnival and Christmas parties! Lennart and Matteo, you were the first to welcome me to the HSP team! I enjoyed so much our HSP trips, all the time we spend pre-covid sharing offices… it was so much easier to work having you around mocking everyone and laughing to one another :D Really guys, thank you for always being there for me! Gio, I would like to make a special mention to you, I am so glad you join the lab! I did not feel alone with my project anymore. I loved our discussions and all the times we hung out. Thanks a lot for everything! Thibaut, despite having landed in the lab just few months ago, I have a lot to thank you. I appreciate all the advice you gave me, your support and your willingness to help me with whatever task I have, but also for all the fun and laughs we had together :)

Por último, me gustaría destacar el apoyo de mi familia y amigos. Estaré eternamente agradecida a mis padres, dos de los pilares más importantes de mi vida. Gracias por no cortarme las alas, por animarme a conseguir mis metas, sean las que sean, y además acompañarme en el proceso. Si soy como soy, es también gracias a vosotros. Pao, gracias por tu luz, por escucharme siempre y por ser una gran amiga además de hermana. Alba y Sergio, gracias por estar siempre ahí a pesar de la distancia, por no dudar en venir a visitarme y por todos los buenos momentos juntos. Álvaro, esta tesis no hubiera sido posible sin tu ayuda. Gracias por tu comprensión, por animarme cada día para seguir adelante y por tu confianza incondicional en mí, eres el mejor compañero de vida.

Erklärung zur Dissertation
gemäß der Promotionsordnung vom 12. März 2020

„Hiermit versichere ich an Eides statt, dass ich die vorliegende Dissertation selbstständig und ohne die Benutzung anderer als der angegebenen Hilfsmittel und Literatur angefertigt habe. Alle Stellen, die wörtlich oder sinngemäß aus veröffentlichten und nicht veröffentlichten Werken dem Wortlaut oder dem Sinn nach entnommen wurden, sind als solche kenntlich gemacht. Ich versichere an Eides statt, dass diese Dissertation noch keiner anderen Fakultät oder Universität zur Prüfung vorgelegen hat; dass sie - abgesehen von unten angegebenen Teilpublikationen und eingebundenen Artikeln und Manuskripten - noch nicht veröffentlicht worden ist sowie, dass ich eine Veröffentlichung der Dissertation vor Abschluss der Promotion nicht ohne Genehmigung des Promotionsausschusses vornehmen werde. Die Bestimmungen dieser Ordnung sind mir bekannt. Darüber hinaus erkläre ich hiermit, dass ich die Ordnung zur Sicherung guter wissenschaftlicher Praxis und zum Umgang mit wissenschaftlichem Fehlverhalten der Universität zu Köln gelesen und sie bei der Durchführung der Dissertation zugrundeliegenden Arbeiten und der schriftlich verfassten Dissertation beachtet habe und verpflichte mich hiermit, die dort genannten Vorgaben bei allen wissenschaftlichen Tätigkeiten zu beachten und umzusetzen. Ich versichere, dass die eingereichte elektronische Fassung der eingereichten Druckfassung vollständig entspricht."

Köln, 10/07/2022 Carolina Montoro Gámez